The 3D Structure and Stellar Content of the Outer Parts of the Small Magellanic Cloud

by Lance T. Gardiner

A thesis submitted for the degree of *Doctor of Philosophy.*

Edinburgh University 1991.

This thesis is an account of work carried out at the University of Edinburgh between October 1988 and October 1991. It consists entirely of my own work, except where specifically indicated in the text. Some of the results presented in Chapters 2, 3 and 4 have been published in *Mon.Not.R.astr.Soc*, **251**, 174, under the joint authorship of M.R.S. Hawkins. A paper incorporating some of the results presented in Chapters 7, 8, 9 and 10 was submitted to *Mon.Not.R.astr.Soc* in July 1991, under the joint authorship of D. Hatzidimitriou. Results from the thesis have also been presented at several conferences and published in conference proceedings. These include the IAU Symposium No.148 held in Sydney in 1990 and the Conference on Digital Optical Sky Surveys held in Edinburgh in 1991.

Department of Astronomy
University of Edinburgh
Blackford Hill

November 1991.

Abstract

This study is directed towards investigating the structure and stellar content of the Small Magellanic Cloud (SMC), the second nearest external galaxy, with the aim of understanding its evolutionary development in the context of its interactions with the Large Magellanic Cloud and our own Galaxy. The study extends the work done by D. Hatzidimitriou on the north-eastern and south-western parts of the SMC, which was presented in her PhD thesis (1988), to cover the rest of the outer area lying beyond about 2 kpc from the SMC centre.

Including the plate material utilised by D. Hatzidimitriou, the observational material for this project consists of 38 good quality blue and red photographic plates taken with the UK Schmidt Telescope in Australia. The plates were digitised by the COSMOS automatic measuring machine and calibrated by CCD sequences obtained at the Danish 1.5-m telescope at ESO in Chile. The resulting database consists of positional and colour-magnitude data for 1.1 million objects covering nearly the whole of the outer area of the SMC.

The scientific analysis involved the study of the properties of colour-magnitude diagrams in conjunction with surface distribution plots of different stellar populations in order to derive the detailed positional dependence of the line-of-sight depth and the past star formation history of the outer parts of the SMC. This has led to confirmation that the depth of the SMC exceeds its tidal radius in the eastern projected areas and supports current ideas suggesting the disintegration of the SMC.

Supplementary CCD observations of the south-eastern outlying SMC cluster NGC 643 and the surrounding field region, obtained at the South African Astronomical Observatory 1-m telescope, are reported. A wide area search for RR-Lyrae candidates using the available plate material was also conducted which yielded 95 candidates in the northern outer parts of the SMC. A detailed study of the Wing region of the SMC has also been made.

Acknowledgements

I would like to express my sincere gratitude to Mike Hawkins and David Emerson for their valuable supervision and encouragement during my three and a bit years in Edinburgh. I would also like to thank Despina Hatzidimitriou for her continued support for and interest in this project. I gratefully acknowledge numerous people with whom I had fruitful scientific discussions, among them S. Beard, P. Brand, D. Buckley, R. Cannon, C. Collins, A. Heavens, Professor P.Hodge, H. MacGillivray, L. Miller, R. Nichol, Q. Parker and T. Yamagata.

I would like to thank the UK Schmidt Telescope Unit for providing the excellent photographic plate material for this project, and the COSMOS unit for carrying out the plate measurements. I also wish to acknowledge the STARLINK group for provision of astronomical software, and the local site manager, John Barrow, for being extremely helpful on many occasions. I would like to thank the staff of the South African Astronomical Observatory for their assistance with my observations at the SAAO 1-m telescope.

I gratefully acknowledge the financial support during the past three years of the Science and Engineering Research Council, who kindly waived home status eligibility criteria in my case, and who provided financial assistance for my observing and conference trips.

I am privileged to have known, worked with and even lived with (Bob Mann) a fine group of young astronomers who comprised my fellow postgraduate students. Their warm friendship and collective camaraderie will be fondly remembered. I mention particularly the fellow students in my year — Brian Williams, Bob Nichol, Chris Davies and Andy Connolly, who also shared with me the trials and tribulations of writing-up (somebody has to finish first, Bob!). I am grateful to the older (ex-)students, who helped me settle in during my first year, and especially mention Paul Mitchell, Karl Glazebrook, Stuart Lumsden, Phil Blanco and Neil Heydon-Dumbleton for assisting me with their computing expertise. It has also been my pleasure to share an office

with some pleasant personalities, namely Phillippe Eenens, Donata Guanieri, Dave Buckley, Suzanne Ramsay, Ruth Doherty and Hugh Jones.

I would like to deeply thank my parents whose unceasing love and encouragement has been a constant source of inspiration. The support of the rest of my family is also greatly valued. Finally, I would like to thank Siew Lian for her love and devotion and making such a wonderful difference in my life.

Contents

List of Figures

List of Tables

CHAPTER

— 1 —

INTRODUCTION

The Large and Small Magellanic Clouds (LMC and SMC), "the gems of the southern skies", according to Bok (1966), appear to the naked eye as detached portions of the Milky Way lying well out of the galactic plane. Abbe (1867) was the first to propose that the Magellanic Clouds, or the two *Nubeculae* as he called them, are merely *nebulae* (or galaxies) which lie near to us. Detailed research on the Magellanic Clouds began when the Harvard College Observatory established its southern station in 1889. As a result of these pioneering investigations, Miss H. Leavitt (1912) discovered the period-luminosity relation for Cepheid variables, establishing a crucial role for the Magellanic Clouds in determining the extragalactic distance scale. This 'Harvard period', which was dominated by the efforts of Harlow Shapley and his collaborators, ended in the mid-1950s. In the 1950s and 60s research on the Magellanic Clouds continued to expand with major progress being achieved in mapping the neutral hydrogen distribution. The modern period of research on the Magellanic Clouds can be said to

have begun about 25 years ago with the construction of large telescopes at the new southern observatories located in Chile (ESO and CTIO) and Australia (AAO). Together with the availability of multi-wavelength detection facilities (x-ray, ultra-violet, infrared, submm spectral ranges), these facilities enabled a very efficient period of research to ensue. The recent IAU Symposium on the Magellanic Clouds held in Sydney (1990) demonstrated the extent to which the full range of modern instrumentation has been turned towards attacking fundamental questions in astronomical research posed by the Magellanic Clouds.

The history of the Magellanic Clouds themselves, as opposed to the history of research on the Magellanic Clouds, has been a subject of ardent debate in the past two decades. As pointed out by Mathewson & Ford (1984) the existence of a galaxy as bright as the LMC in the neighbourhood of a large spiral galaxy such as our own Milky Way is very probably a unique phenomenon. Even more unusual is that, while several *isolated* pairs of Magellanic-type galaxies are known to exist, a pair of Magellanic galaxies should be found in association with a large spiral. We are naturally drawn to surmise on the origins of the Magellanic Clouds in the local environment of our Galaxy. In this regard, three competing views have been proposed:—

(1) The Magellanic Clouds are in a hyperbolic orbit around the Galaxy, and just happen to be passing by (see Mathewson & Ford 1984).

(2) They have always been satellites of our Galaxy, having formed as part of our Hypergalaxy (Einasto *et al.* 1976).

(3) They were formed as part of the Local Group of galaxies but were at some point captured by our Galaxy.

Westerlund (1989) pointed out that possibility (2) is unlikely because the Magellanic Clouds are so gas rich, in contrast to other more remote dwarf elliptical satellites of our Galaxy, which appear to have been stripped completely of their gas content. It is generally accepted today that the Magellanic Clouds are satellites of the Milky Way according to possibility (3), as a result of independent orbital computations by Murai & Fujimoto (1980), Lin & Lynden-Bell (1982) and Mathewson *et al.* (1987). Different

workers are, however, not in agreement on precisely when the Magellanic Clouds were captured by the Galaxy, the first two of the above sets of authors favouring sometime before 10^{10} yr ago and the last a few 10^8 yr ago, while in the revised computations of Murai & Fujimoto (1986) the SMC was found to have been independently orbiting the Galaxy and captured by the LMC about 1.7×10^9 yr ago. The dynamical relationship between the Magellanic Clouds and the Galaxy will be investigated more thoroughly in Chapter 6.

The rest of this introductory chapter will be devoted to establishing the astronomical value of Magellanic Clouds research (Section 1), describing the background to this project (Section 2) and stating the aims and content of this present research (Section 3).

1 The Importance of Magellanic Clouds Research

The importance of Magellanic Clouds research in attacking many problems of fundamental astronomical interest derives predominantly from their proximity, combined with the fact that, unlike our own Galaxy, its constituent objects may be considered to lie effectively at the same distance. At distances of about 45 kpc (LMC) and 60 kpc (SMC) they are about ten times closer to us than the Andromeda galaxy (M31) and therefore provide in many ways an ideal astrophysical laboratory for the study of numerous problems ranging from stellar evolution to the dynamical effects of galaxy-galaxy interactions. Below we summarise several areas of research in which the Magellanic Clouds make an important contribution to wider astrophysical questions.

(i) The Extragalactic Distance Scale

Since the pioneering work of Miss Leavitt on Cepheids, variable stars have played an important role in establishing the distances to the Magellanic Clouds and in calibrating the extragalactic distance scale. The discovery by Thackeray and Wesselink of RR-Lyrae variables in the Magellanic Clouds, announced at the 1952 Rome IAU

General Assembly, with apparent magnitudes 1.5 mag fainter than expected led to a doubling of the extragalactic distance scale. Cepheid variables, owing to their greater luminosity, play a more important role in estimating distances to galaxies within about 5 Mpc and the period-luminosity relation is continually being refined with the Magellanic Clouds as a very important testbed. Sandage (1958) extended the period-luminosity relation for Cepheids to a period-luminosity-colour relation and applied it to the Magellanic Clouds. Research on the dependence of the period-luminosity relation on metallicity is presently being conducted (see Freedman & Madore 1991) using the Magellanic Clouds and M31. Mould (1991) anticipates that interferometric measurements of the angular diameters of Cepheids in the solar neighbourhood will lead to a more accurate distance calibration in the Milky Way. The Magellanic Clouds will then enable the period-luminosity relation to be extended from short to long periods allowing further refinement of the extragalactic distance scale.

(ii) Star Formation

The existence of current star formation (Gatley, Hyland & Jones 1982) and young 'globular' clusters in the Magellanic Clouds provides unparalleled opportunities for research on the problems of star formation. The LMC contains the 30 Doradus giant H II complex in which a dramatic burst of star formation is taking place. Bok (1966) states that if this giant nebula were at the distance of the Orion nebula it would subtend an angle of about 30° on the sky and cast permanent shadows on the earth! According to Walborn (1991), 30 Doradus is the "Rosetta Stone" for the interpretation of starburst regions in more distant galaxies, providing valuable information on the stellar content, initial mass functions, protostars and high-energy phenomena in such complexes. Kennicutt (1991) described the importance of the study of H II regions in the Magellanic Clouds for the investigation of global star formation properties of galaxies. The clusters of the Magellanic Clouds are a valuable tool for studies of the stellar initial mass function over a large mass range (see Mateo 1988) enabling testing of theories of star formation via cloud collapse and fragmentation.

(iii) Stellar Evolution

> "The Magellanic Clouds are like a well-stocked laboratory for the study of star birth and evolution." (B.J. Bok 1966)

Owing to the greater metal deficiency of the Magellanic Clouds with respect to the galactic disk and the existence of 'globular' clusters in the Magellanic Clouds spanning a much larger age range than those in the Galaxy, the Magellanic Clouds have presented many interesting problems for research on stellar evolution. Several topics on which Magellanic Cloud research has had a major impact are mentioned below:—

• The observation of a red giant 'clump' feature in the colour-magnitude diagrams of intermediate age Magellanic clusters resembling that found in galactic open cluster diagrams paved the way to its identification by Cannon (1970) as being due to the more massive equivalents of the core-helium burning horizontal branch stars found in galactic globular clusters. Subsequent modelling of this phase of stellar evolution by several workers (e.g. Faulkner & Cannon 1973; Seidel, Demarque & Weinberg 1987) has led to a detailed theoretical understanding and ultimately to the use of 'clump' stars as distance indicators (see Chapter 4).

• The detection of RR-Lyrae variables in the $\sim$ 12 Gyr old SMC cluster NGC 121 and their non-detection in the $\sim$ 10 Gyr old cluster Lindsay 1 sets a lower limit on the ages of RR-Lyrae variables at around 10-12 Gyr (see Stryker, Da Costa & Mould 1985; Olszewski, Schommer & Aaronsen 1987). Therefore, these old 'Population II' indicators do not necessarily possess ages of the order of galactic globular clusters (14-16 Gyr) with important consequences for the age-dating of populations in galaxies containing RR-Lyraes (e.g. most dwarf elliptical satellites of our Galaxy).

• Studies of the asymptotic giant branch (AGB) in Magellanic Cloud clusters have stimulated theoretical understanding of the properties of the AGB and of carbon stars. The AGB represents an advanced evolutionary phase in which double-shell burning takes place above a degenerate carbon-oxygen core. Carbon stars are thought to be

in the AGB phase and Iben (1984) was able to deduce the minimum and maximum ages that could be possessed by carbon stars from comparative studies of Magellanic clusters. Mould & Aaronsen (1980) established a relation between the maximum luminosity of the AGB and the age of the stellar population to which they belong. A theoretical and empirical understanding of the properties of the AGB has recently assumed a major role in studies of the population synthesis of high-redshift galaxies with a view to identifying the epoch of galaxy formation (see Renzini 1991).

• Stellar evolutionary models involving overshoot from convective cores have been developed by Bertelli, Bressan, & Chiosi (1985) and applied to age determinations of Magellanic Clusters. These non-classical stellar models generally predict larger ages for a given main sequence turn-off luminosity than classical isochrones, e.g. the Revised Yale Isochrones of Green, Demarque & King (1987), but show better agreement with ages derived from the AGB 'tip' luminosity according to the calibration by Mould & Aaronsen (1985). The availability of several independent age estimators for Magellanic Cloud clusters makes them a valuable testbed for ideas on stellar evolution.

The topics listed above are by no means exhaustive and there are numerous ways in which the Magellanic Clouds provide opportunities for understanding unusual types of stars e.g. Cepheids, long-period variables, Wolf-Rayet stars, OH/IR stars to name but a few. Again, the proximity of the Magellanic Clouds combined with their diversity of stellar populations makes such studies extremely worthwhile.

(iv) The Magellanic Clouds as Prototype Galaxies

Hubble (1926) classified irregular galaxies as those exhibiting chaotic, non-symmetrical blue light distributions in contrast to the axial symmetry of 'regular' galaxies. Later classification schemes divided irregular galaxies into two major groups: Magellanic systems (type Irr I or Im) which resemble the Magellanic Clouds and peculiar, often amorphous galaxies classified as Irr II or I0 systems (Gallagher & Hunter 1984). De Vaucouleurs & Freeman (1972) consider that the Magellanic irregulars represent an extension of the spiral sequence with spiral structure decaying along the sequence

Sa...Sd, Sm, Im. According to Freeman (1984), "The basic structure shared by these barred Magellanic systems is the strong asymmetry of the spiral structure about the bar axis", in addition to asymmetry in the rotation curves. These systems are also thought to be disk-like (Freeman 1984; Gallagher & Hunter 1984), although in the case of the SMC this statement must be qualified in light of the remark by Westerlund (1991) that: "Early efforts to define the SMC as a rotating galaxy with a spiral structure (de Vaucouleurs & Freeman 1972) have been replaced by intense efforts to understand its extension in depth and possible fragmentation." Although recent work has generally emphasised the study of the Magellanic Clouds as individual galaxies, nevertheless it is clear that they represent the prototype systems in efforts to understand the dynamics and the organisation of star formation in irregular systems.

(v) Galaxy-Galaxy Interactions

The Magellanic Clouds are interacting with each other and with the Galaxy. The results of these interactions can be seen in the existence of the stellar and H I Bridge between the Clouds, the asymmetric prominence or 'Wing' of the SMC, and the Magellanic Stream. Owing to the proximity of the Magellanic Clouds such features can be examined in detail and subjected to extensive modelling. In general, the three-body interaction between the Galaxy, LMC and SMC will result in more complicated features than the two-body interactions more commonly seen in distant interacting systems, but the success in modelling major features of these interactions (see e.g. the tidal models of Murai & Fujimoto 1980) appear to confirm the essential correctness of approaches involving particle simulations used in order to model the more general two-body interaction.

This short review confirms the major impact of research on the Magellanic Clouds on many diverse fields of astronomical endeavour. Besides being challenging objects in their own right, the Magellanic Clouds represent one of the primary testbeds for astronomical theories concerning star formation, stellar evolution and dynamical interactions between galaxies. They also play a major role in cosmology via their crucial position in the extragalactic distance scale and via population synthesis studies di-

rected towards modelling the spectra of high-redshift galaxies.

2 Background to the Present Study

Having discussed the general importance of research on the Magellanic Clouds, we will now establish the background for this present study by referring to the broad picture that has emerged concerning the structure and stellar content of the SMC. In Fig. 1.1, a photograph of the SMC, a digital reproduction of Fig. 13 from de Vaucouleurs & Freeman (1972), is presented with the main SMC features identified. The prominent Population I component associated with the 'Bar', 'Arms' and luminous inner 'Wing' of the SMC (Stryker 1984b) has been the focus of most of the existing studies of the structure, kinematics and stellar content of the SMC. The youngest stellar generations, the formation of which began some 50 Myr ago, are represented by early- and late-type supergiants, blue clusters and emission nebulae, while an older group (of the order of a few 10^8 yr or less) are exemplified by Cepheid variables and relatively older clusters. While these young populations dominate the appearance of the SMC on deep optical photographs, as remarked by Bok (1966), "In all likelihood Population II stars determine the gravitational and rotational properties of the SMC, and the spectacular Population I component represents only the frosting on a beautiful cake". Intermediate-age and old stellar populations occupy a much larger area in projection than the younger populations, extending well beyond the boundaries of the photograph in Fig. 1.1 to some 7° from the SMC optical centre ($RA = 00^h51^m$, $DEC = -73°$, 1950) (see e.g. de Vaucouleurs & Freeman 1972). The older populations in the general field of the SMC, which are the subject of investigation of this work, can only be seen as an excess density of stars over the foreground population of the Galaxy in these parts of the sky. The intermediate-age populations in the SMC are represented by the carbon stars, whose ages range between 0.8 and 8 Gyr according to Iben (1984), as well as several clusters within this age range (see Fig. 1.2). The oldest populations (older than 10 Gyr), which most probably form a continuum in age with the intermediate-age populations, are characterised by two old clusters L 1 and NGC 121, as well as

RR-Lyraes in the general field. A more extensive review of the stellar generations of the Magellanic Clouds can be found in the article by Westerlund (1990). The detailed stellar age distribution of the SMC outer regions will be investigated in Part III of this work.

The terms Population I and II have been used above in a stellar evolutionary sense only and do not infer the dynamical properties exhibited by such populations in the Galaxy. In fact, owing to the complicated structure of the SMC and the lack of kinematical data on the intermediate-age and older stellar content of the SMC we cannot apply the terms 'disk' and 'halo' populations, associated in the Galaxy with Populations I and II respectively, to the stellar content of the SMC in a meaningful way at present. The term SMC 'halo' has often been used to describe the outer area of the SMC located beyond the optically luminous central regions, but in view of this uncertainty we will largely avoid this practice in the present work.

The structure of the SMC delineated by studies of the young stellar component in the central regions (see the review by Feast 1989) is still a controversial subject. Early indications that the stellar distribution within the bright central regions defined a regular disk-like system (see de Vaucouleurs 1955) have given way to more complicated interpretations with the accumulation of evidence that the young populations of the SMC have a considerable depth along the line-of-sight, combined with H I data indicating complex bulk motions (e.g. Torres & Carranza 1987; Martin, Maurice & Lequeux 1989; Mathewson & Ford 1984). The actual extent of the depth has been hotly disputed (see e.g. Welch *et al.* 1987), but there seems little doubt that the line-of-sight extension of the young populations is at least three times the projected dimensions of these populations. The gravitational influence of the LMC is strongly suspected to have given rise to the observed large depths and complex kinematical behaviour, and this has led Mathewson and his collaborators (1984; 1986; 1988) to claim that the SMC is in the process of 'irreversible disintegration' due to a recent close encounter with the LMC. The structure of the SMC outer regions delineated by the older stellar component of the SMC is investigated in Part II of this work.

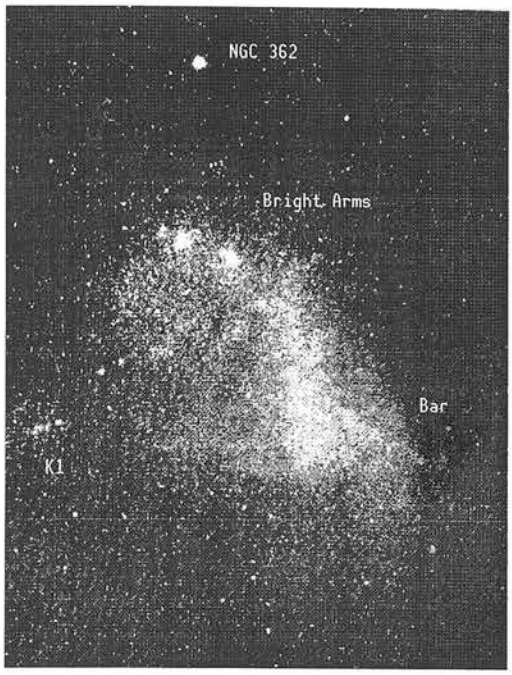

Figure 1.1: Digital reproduction of a photograph of the SMC from Fig. 13 of de Vaucouleurs & Freeman (1972). Several main features of the central SMC area are identified. The K1 knot is the stellar condensation in the luminous inner Wing of the SMC and NGC 362 is a foreground galactic globular cluster. The area covered by this photograph is $4 \times 5°$. North is at the top and east is to the left.

Turning our attention to the predominantly older stellar content of the SMC outer regions, which is the purview of this project, the most important attempts to understand the stellar content of the outer regions have been directed towards obtaining high-quality CCD observations of a handful of prominent clusters located in the outer regions of the SMC. These observations have enabled the construction of deep colour-magnitude diagrams down to the main sequence turnoff, yielding ages and metallicities. A bibliography of these studies is presented in Table 1.1, and we will refer to them hereafter using the reference codes listed in this table. The locations and derived ages (where available) of prominent intermediate-age and old clusters in the outlying regions of the SMC including those studied using deep CCD photometry are shown in Fig 1.2, reproduced from Fig. 4 of Olszewski (1988). The use of clusters to probe the star formation history of the outlying regions of the SMC, however, is unsatisfactory in two main respects. Firstly, the number of clusters amenable to such study is small, which may lead to a rather unrepresentative view of the overall star formation history, and secondly, the conditions favouring formation of relatively massive globular clusters surviving disruption to the present day may be substantially different from those conducive to star formation in the general field. Furthermore, the problem of the 3D structure of the SMC has been scarcely tackled by such studies, again due to poor statistics. This project has been designed to overcome these limitations by embarking on the study of the general field populations of the outer regions of the SMC, located approximately beyond 2° from the SMC optical centre.

The forerunning studies to this project were the series of publications by workers based at the Royal Observatory, Edinburgh (Brück & Marsoglu 1978; Brück 1978; 1980; Hawkins & Brück 1982; 1984; Brück, Cannon & Hawkins 1985), in which the stellar content of the SMC outer regions ('halo') was investigated on the basis of colour-magnitude diagrams, and with a limiting visual magnitude of 21. This present project was begun in 1985 when M.Hawkins and D.Hatzidimitriou initiated a systematic investigation of the stellar content of the outer regions of the SMC to eventually cover virtually the entire outer area of the SMC and encompass six standard ESO/SERC survey fields. The observational material was to consist of sets of blue and red photo-

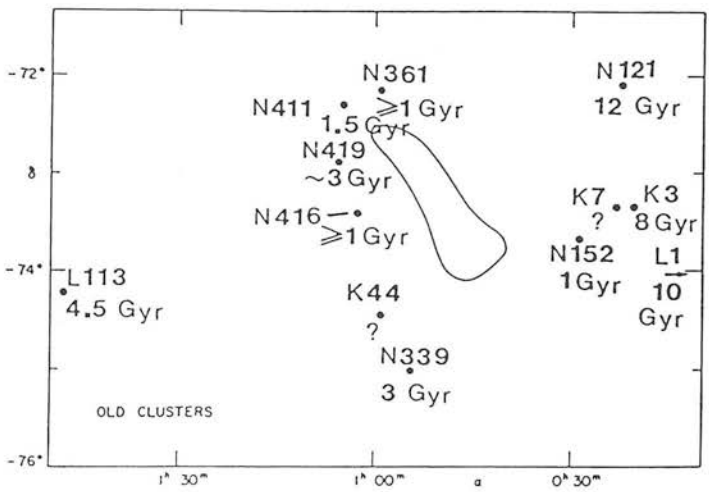

Figure 1.2: Locations and derived ages (where available) of prominent intermediate-age and old SMC clusters with respect to the Bar of the SMC. Figure reproduced from Fig. 4 of Olszewski (1988).

graphic plates obtained by the 1.2-m UK Schmidt Telescope of the Anglo-Australian Observatory at Siding Springs, Australia. The extraction of the colour-magnitude information of the images on these plates was to be accomplished using the COSMOS plate measuring machine at the Royal Observatory, Edinburgh (see Chapter 3). CCD sequences were also obtained on two separate observing runs at the Danish 1.5-m telescope at ESO in Chile, and were used to calibrate the photographic photometry (see Chapter 2). The first stage of the project involved the study of the stellar populations and large-scale structure of the north-eastern and south-western outer regions of the SMC in two standard ESO/SERC fields, numbers 52 and 28. These investigations formed the basis of the PhD thesis by D.Hatzidimitriou (1989). An enormous debt is acknowledged towards this body of work, which laid the groundwork for this project. Some of the results from the above thesis were published in two articles by Hatzidimitriou, Hawkins & Gyldenkerne (1989) and Hatzidimitriou & Hawkins (1989), which comprised Papers I and II in the series. The PhD thesis by Hatzidimitriou (1989) (hereafter H-thesis) will be solely referenced in this present work since the content of these two papers is incorporated within it.

Cluster	Author(s)/Year	Short Code
NGC 411	Da Costa & Mould, 1986	GC1
L 113	Mould *et al.*, 1984	GC2
Kron 3	Rich *et al.*, 1984	GC3
L 1	Olszewski *et al.*, 1987	GC4
NGC 121	Stryker *et al.*, 1985	GC5
NGC 362	Bolte, 1987	GC6
NGC 152	Melcher & Richtler, 1989 & private communication	GC7
L 11	Buttress *et al.*, 1988	GC8

Table 1.1: Bibliography of deep CCD studies of SMC clusters and adjacent field areas.

Observational material for the remaining four project fields covering the outer area of the SMC (Fields 50, 51, 29 and 30) were acquired in the period 1988-1991 and together with that used in H-thesis, comprised the complete material for this present work. Results on the structure of the northern and north-western outer regions of the SMC based on Fields 51 and 50 were published in an article by Gardiner & Hawkins (1991) (Paper III in the series). The fourth paper in the series, on the age distribution of the SMC outer regions, was submitted for publication in July 1991 (Gardiner & Hatzidimitriou 1991). In this present work, some attempt was made to avoid repetition of the content of H-thesis, and on many occasions where topics were discussed comprehensively in H-thesis the reader is referred to the latter work. However, the nature of scientific research means that the body of knowledge is continually being updated, and recent progress in areas related to this project has not been ignored. Although keeping within the basic framework of the research methods presented in H-thesis, a number of new methods of analysis were employed in order to extract results of scientific importance. The observational data for Fields 52 and 28, which formed the basis of the investigations in H-thesis, have also been re-analysed using these new techniques, and to the greatest extent possible the data from all six project fields have been treated as a homogeneous data set.

The basic method of the scientific investigations of this project comes under the heading of optical sky surveys. Indeed, results from this project were presented at the conference on Digital Optical Sky Surveys held in Edinburgh in 1991, and we conclude this section by discussing the significance of this project in relation to this mode of astronomical investigation. Until the use of CCD detectors became common, the vast majority of broadband investigations of the stellar content of star clusters and Local Group galaxies was undertaken using photographic plates as the raw observational material. However, the linearity and greater sensitivity of CCDs enabled deeper and more accurate colour-magnitude diagrams to be constructed and revolutionised research on the stellar populations of galaxies. Nevertheless, photographic plates have retained the advantage of wider areal coverage with respect to CCDs, and for the study of the overall structure of stellar systems as well as searches for variable stars in these systems, photographic material is still the ideal tool.

The following considerations illustrate the suitability of using photographic plates for investigating the outer parts of the SMC:—

• The SMC covers a fairly small number of standard UKST survey fields (~ 6) and therefore represents a feasible prospect for a project based on photographic data. The LMC, on the other hand, covers a projected area in the sky of about 5-6 times that of the SMC.

• The SMC is an irregular galaxy possessing large-scale non-uniformities in the distribution of its stellar populations. The earlier investigations of the Edinburgh group described above confirmed that the structure and stellar content of the outer regions of the SMC was sufficiently unusual to merit a study of the *whole* of the outer area. Hodge *et al.* (1991) recently demonstrated by their the study of the Local Group dwarf irregular galaxy IC 1613 the usefulness of photographic photometry in mapping stellar populations in irregular galaxies.

• Owing to the proximity of the SMC, photographic photometry can reach faint enough to allow the investigation of horizontal branch populations as well as main sequence

populations aged up to about 2 Gyr.

• The fairly low surface densities of images in the outer regions of the SMC render the photographic material very suitable for automated methods of measurement leading to the construction of an extensive database with a reasonably high level of completeness (see Chapter 3).

Another two-colour photographic study of part of the Magellanic System has been conducted by Irwin, Demers & Kunkel (1990). These authors, by their discovery of a stellar 'bridge' linking the Magellanic Clouds, demonstrated the power of automated measuring methods combined with large area sky coverage. As regards the more distant galaxies of the Local Group, the remoteness of these galaxies means that most detailed work is done using CCD imaging, with photographic photometry providing useful preliminary data as in the case of the investigation of the stellar content of the recently discovered Sextans dwarf spheroidal satellite galaxy (Irwin *et al.* 1990). The proximity of the Magellanic System, however, is the characteristic which makes it almost uniquely suitable among resolved stellar systems for the application of photographic survey techniques in the modern era of linear CCDs.

3 Aims and Content of the Thesis

The scientific aims of this project can be stated as follows:—

(1) The determination of the 3D structure of the outer regions of the SMC. This would enable us to:—

• investigate the effect of the tidal interaction with the LMC and the Galaxy on the structure of the SMC.

• establish whether the SMC exceeds its tidal radius and is in a state of 'irreversible disintegration' as suggested by Mathewson, Ford & Visvanathan (1986; 1988).

(2) The investigation of the stellar age distribution in the outer regions of the SMC. In so doing, the following questions will be considered:—

• What is the age of the bulk of the stellar population in the outer regions?

- How are populations of different ages distributed with respect to one another, and what does this tell us about the organisation of star formation in irregular galaxies?
- What is the role of external interactions in the star formation history of the SMC?
- What is the nature and origin of the stellar populations in the Wing region?

The main body of the thesis (excluding the Introduction and Conclusions chapters) consists of nine chapters divided into three *Parts*. Part I (Chapters 2 and 3) deals with the database for the project.

In Chapter 2, the CCD observations and reductions, used for the calibration of the photographic photometry, are presented.

In Chapter 3, the construction of the photographic database is described, including an assessment of its accuracy and completeness.

Part II (Chapters 4-6) deals with the investigation of the 3D structure of the SMC.

In Chapter 4, the 3D structure of the SMC outer regions is investigated based on the surface and luminosity distribution of stars belonging to the HB/clump.

In Chapter 5, we describe follow-up CCD observations obtained at the SAAO 1-m telescope of the prominent south-eastern cluster NGC 643 and the surrounding area, with the aim of obtaining very accurate data for the study of the depth of the SMC.

In Chapter 6, the interacting Milky Way-Magellanic system is discussed from the viewpoint of existing numerical simulations of the system and the overall geometry of the SMC.

Part III (Chapters 7-10) investigates the stellar age distribution.

In Chapter 7, the relatively young (less than about 2 Gyr old) populations of the SMC outer regions are investigated using the surface distribution and luminosity functions of the main sequence populations.

In Chapter 8, the older stellar content represented by the horizontal branch populations (HB/clump, red horizontal branch, blue horizontal branch and RR-Lyrae variables) are analysed to reconstruct the earlier star formation history of the SMC outer regions.

In Chapter 9, the detailed morphology and age composition of the Wing region are

considered, and the origin of the Wing is discussed.

In Chapter 10, there is a discussion of the star formation history of the SMC based on the results of Chapters 7, 8 and 9 in conjunction with existing studies of the stellar populations of the SMC.

Finally, in Chapter 11, the main conclusions are stated.

PART I: *THE DATABASE*

CHAPTER

— 2 —

THE CCD PHOTOMETRY

It is recommended practice for magnitude parameters produced by automated measuring machines from scans of photographic plates to be externally calibrated using sequences of stellar magnitudes established via photoelectric or CCD photometry (MacGillivray & Stobie 1984). The establishment of a zeropoint for conversion of instrumental photographic magnitudes to the standard system is not sufficient; the poor linearity and limited dynamical range of a photographic plate necessitates a calibration as a function of magnitude. Hence, calibration sequences with a good distribution of magnitudes are required to define the transformation of the photographic magnitudes to the standard system.

Two of the project ESO/SERC survey fields, Fields 28 and 52, have already been calibrated (see H-thesis p.12ff) using CCD sequences obtained at the Danish 1.5-

ish telescope in 1987 and Siding Spring Observatory in 1987 using the 3.9-m Anglo-Australian Telescope (during service time). In order to calibrate the photographic photometry for the remaining four project fields, CCD sequences for Fields 50, 51, 29 and 30 were obtained on the nights of Sept.30–Oct.3, 1988, at the Danish 1.5-m telescope at La Silla, Chile. In this chapter we describe the acquisition and reduction of the CCD observations obtained for the purpose of providing photometric sequences for the calibration of the photographic photometry.

1 CCD Characteristics and Calibration Observations

CCD observations of flat fields, standard stars and sequence fields were obtained during four photometric nights at the Danish 1.5-m telescope, during which the seeing varied from about 1.5 to 3 arcsec. The detector used was ESO CCD RCA#5; it is a thinned, back-illuminated CCD, with an active area of 512×320 pixels and a bias strip at the edge of the frame consisting of 512×16 pixels. Each pixel is of size 30μm which corresponds to a scale of 0.47 arcsec per pixel at the Cassegrain focus. The conversion factor is 14 e^- per ADU (analogue-to-digital unit) and the readout noise is 49 e^-. For all the long exposure observations the principal source of noise was due to the sky brightness. The dark current, which is 100 $e^- pix^{-1} hr^{-1}$, makes a negligible contribution to the noise level for exposure times less than a few hours. The saturation level of the chip is about 16000 ADU (analogue-to-digital units), but linearity is affected above 10000 ADU. The observations were obtained using Johnson B and Gunn R filters. I-band observations were also obtained during the run for the purpose of calibrating near infrared photographic plates, but will not be described here.

The preliminary reductions of the science frames comprised bias-subtraction, trimming worthless rows and columns, and flatfielding to compensate for the response pattern of the CCD chip. These manipulations were performed with standard routines in

the STARLINK FIGARO package. A fixed bias level offset is added by the CCD to the signal to avoid feeding negative values to the analogue-to-digital converter. All CCD exposures were bias subtracted using the mean ADU value of the bias strip at the edge of each exposure, which was then removed from the CCD frame by trimming.

Sensitivity variations in the CCD chip cause a characteristic response pattern which introduces extra noise into the raw CCD pixel data if not removed by flatfielding. The variations arise from pixel-to-pixel changes in the size and quantum efficiency per pixel (Mackay 1986), and possibly from geometrical vignetting and distortions in the telescope optics. To compensate for the response pattern, flat fields comprising 'blank' uniformly illuminated exposures were obtained through the different filters. A small number of flatfield frames were taken with B and R filters and consisted of short exposures of the telescope dome illuminated by the leaking twilight. The flat fields were stable and exhibited variations, measured by the standard deviation of the pixel counts over the whole frame, of less than 3 per cent. Representative B and R flat fields were selected, normalised to unity and then used as the standard flat fields for the entire run. They left no residual gradients when the science frames were divided by them.

The existence of fringe patterns on CCD frames can be a problem since their removal requires long-exposure blank sky frames (or carefully constructed images from which astronomical objects have been removed) in order to define the fringe pattern. Such patterns are caused by deviations from perfect planar geometry in the CCD's silicon layer which may give rise to an interference pattern as the thickness of the layer is comparable to the wavelength of light. The emission features of the night sky, which are more prominent towards longer wavelengths, may give rise to a strong time-varying fringe pattern which may be very difficult to remove. Although several I-band frames, which were also obtained during the run, showed interference-fringing, the B and R frames did not.

No attempt was made to patch up cosmetic defects in the chip due to individual bad pixels and one bad column. The photometry routine used for the reduction of the

CCD sequence stars was able to identify such pixels and essentially ignore them.

2 The Standard Stars

16 standard stars, ranging from 9th to 16th magnitude, were observed, selected from the lists of Landolt (1983), Menzies, Banfield & Laing (1980) and Graham (1981;1982). Table 2.1 lists the standard stars, their references and our own ID numbers. As well as defining the photometric zeropoints, the standard star observations were used to determine the colour transformations to the standard $UBVRI$ system. Standard extinction coefficients for the site were used to reduce the observations to the same airmass.

The standard star exposures were short, i.e. between 10 and 60 seconds. Most stars were observed at least two times on different nights in order to monitor changes in photometric conditions. The frames were reduced with the FIGARO program AFOTO, a simple aperture photometry routine, which applies a circular annulus centred on the stellar image to evaluate the sky counts to be subtracted from the total counts within the aperture. A compromise between a large aperture, including all the stellar flux but giving a low signal-to-noise ratio, and a small aperture, which includes a variable proportion of the stellar flux due to seeing and focussing variations was chosen for the reductions. Fig. 2.1 shows an example of a growth curve for the instrumental magnitude as a function of the aperture size. It can be seen that the turnover of the instrumental magnitude beyond which the magnitude is fairly constant occurs at a radius of about 8 pixels. Beyond a radius of 10 pixels the intrinsic error due to the increasing sky contribution is seen to increase. On this basis, an aperture of radius 10 pixels (4.7 arcsec), which includes at least 95 per cent of the stellar flux, was selected for the standard star photometry reductions.

Two of the standard stars (numbers 7 and 18 in Table 2.1) were subsequently discovered to be saturated in B, while in R, three stars (numbers 12, 28 and 18) were saturated, so these observations were discarded. Furthermore, one standard star

ID	Reference/ID	B (mag)	R (mag)	N_{obs} B/R	Deleted?
1	L / −12.134	11.481	11.863	1/1	BR
2	L / −11.162	11.109	11.140	3/3	
4	L / F16	12.395	12.414	3/3	R
8	L / F108	12.735	13.07	2/2	
9	L / 96.83	11.902	11.631	1/1	B
12	MBL / CPD7344	10.238	9.508	1/2	BR
18	MBL / CPD 66350	10.332	9.501	1/2	BR
22	G82 / E1:49-V	12.204	11.308	5/5	
25	G82 / E2:o	14.660	13.778	6/5	
26	G82 / E2:I	16.638	15.239	4/2	BR
27	G82 / E3:o	15.356	14.490	3/2	
28	G81 / 5	12.20	10.63	3/4	R
29	G81 / 11	16.23	14.74	2/2	
82	G82 / E1:i	14.675	13.245	1/1	
83	G82 / E2:s	15.323	14.224	6/5	BR
84	G82 / E3:v	16.763	15.942	3/2	BR

Table 2.1: List of standard stars used for determining the zeropoints and colour transformations to the standard $UBVRI$ photometric system. *Column 1* gives our own star ID number and *Column 2* gives the standard star list / ID number from which they were derived. (L refers to Landolt 1983, MBL to Menzies, Banfield & Laing 1980, and G81 and G82 to Graham 1981;1982). *Column 3* gives the B and R magnitudes. *Column 4* indicates the number of observations of each standard star made in the B and R wavebands. *Column 5* indicates whether the stars were deleted from the list of observations used in the zeropoint determinations (e.g. because of saturation or the existence of close double components), with B indicating that the B observation was omitted, and R indicating that the R observation was omitted.

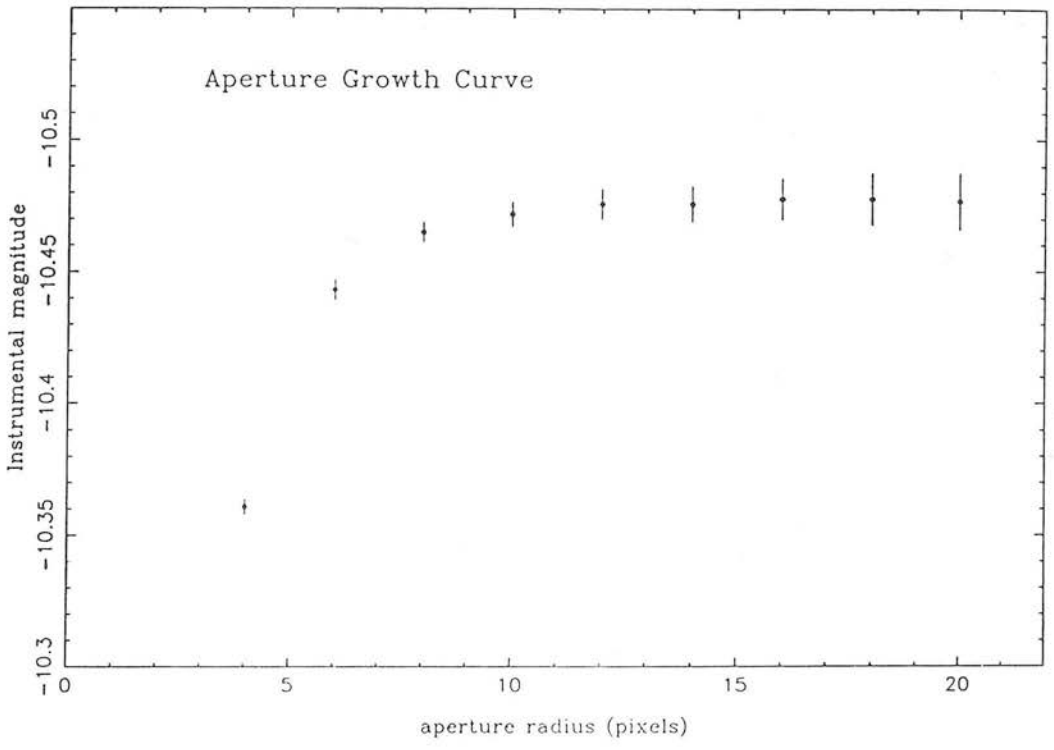

Figure 2.1: An example of a curve of growth for the instrumental magnitude as a function of aperture size for a standard star. Photometry errors determined by the aperture photometry program are also shown.

(number 4) was a close double, while another (number 1) had a double component which was judged to affect the flux of the standard star at the level of a few percent. Another star (number 26), in both B and R wavebands had a very large discrepancy (> 1 mag) with respect to the known magnitude; it was judged to be either variable or a misidentification. Two fainter stars (numbers 83 and 84) in the standard star sample, each located on the same frame as a brighter standard star, were also discarded due to significantly larger intrinsic errors than the other stars. Plots of the magnitude difference between the known and instrumental quantities (which were averaged if several separate observations were made of the same standard star) against $B-R$ colour were used to determine the colour coefficients and zeropoints for both B (10 remaining standard stars) and R (9 remaining standard stars) and are produced in Fig. 2.2. Two more standard stars (numbers 9 and 12), whose instrumental magnitudes were based on a single observation, were removed from the fit for the B data due to large ($> 2.5\sigma$) discrepancies with respect to the least-squares fit to all the data.

The final equations obtained were:

$$B = B_{inst} + 0.122(B-R) - 0.215\chi + 2.5\log_{10}T + Z_B$$

$$R = R_{inst} + 0.070(B-R) - 0.091\chi + 2.5\log_{10}T + Z_R$$

where the instrumental magnitudes are calculated according to:—
$B_{inst} = -2.5\log_{10}(signalcounts - skycounts)$
and χ = airmass, T = exposure time, Z_B and Z_R are the respective zeropoints. The standard errors in the zeropoints were 0.037 mag in B and 0.032 mag in R, while the errors in the colour coefficients were 0.007 for B and 0.010 for R. Pedersen (private communication, 1987) gives a colour transformation:

$$B = B_{inst} + 0.15(B-V) + const. \qquad (1)$$

Using the relation determined by H-thesis (p.20) between the colour indices $B-R$ and $V-R$ from photoelectric standards in the Graham (1982) E-regions we obtain:

$$B - V = 0.642(B-R). \qquad (2)$$

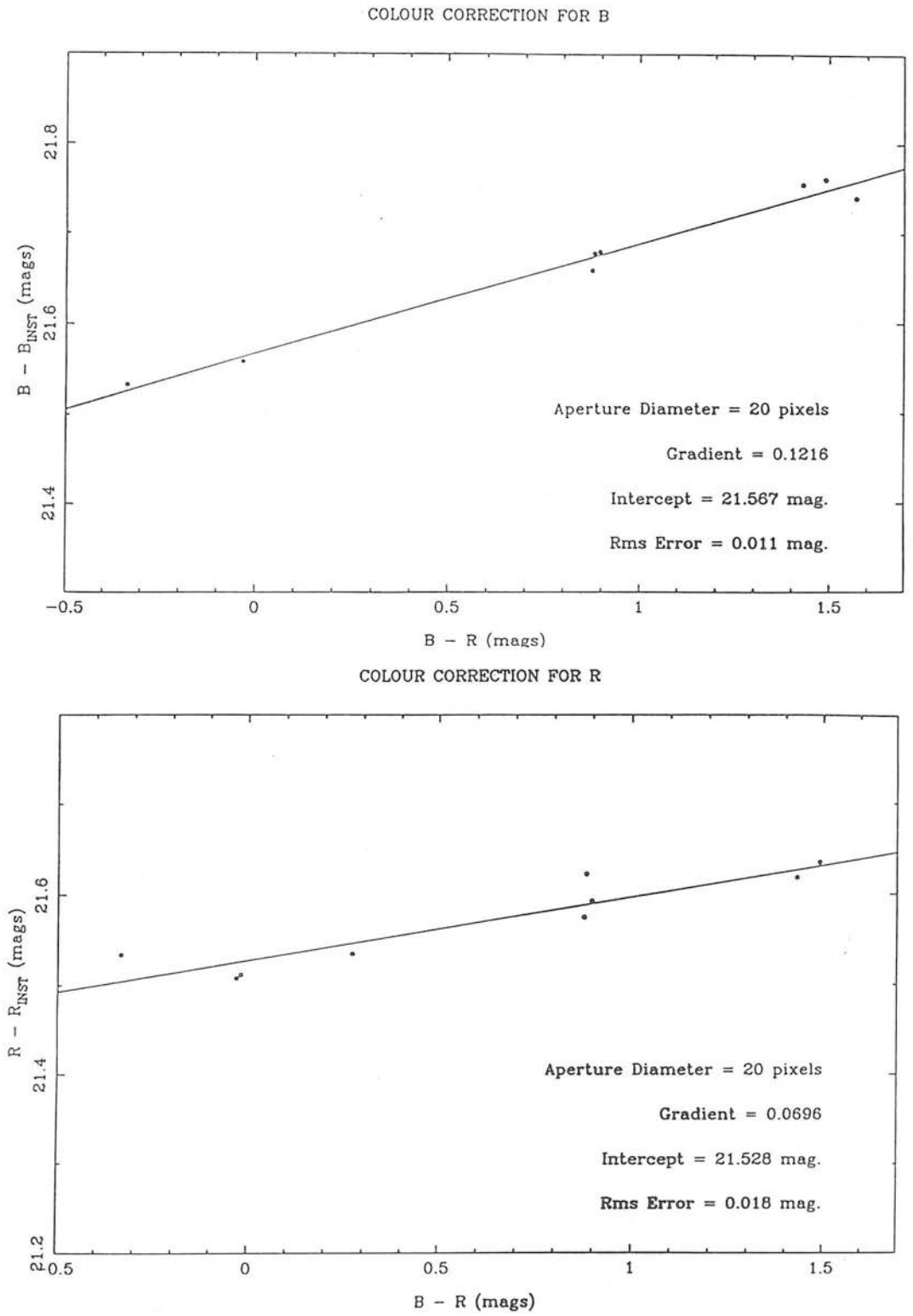

Figure 2.2: Determination of the colour corrections and photometric zeropoints for B (top) and R (bottom).

Substitution of eqn.(2) into eqn.(1) gives a colour term of $0.096(B-R)$ compared to our $B-R$ colour coefficient of 0.122. This discrepancy amounts to a few hundredths of a magnitude over the full range of stellar $B-R$ colours. However, the significance of this difference is low given that a previous determination of the $B-V$ colour coefficient differs by 15 per cent from the 1987 determination.

No systematic variation of the zeropoints with night of observation, airmass or $B-R$ colour was observed. Fig. 2.3 shows, for the individual standard star observations, the difference between the known and instrumental magnitudes corrected to the standard system as a function of magnitude with different symbols indicating low, intermediate and large airmasses. Fig 2.4 is the same plot with the symbols representing different colour ranges and in Fig. 2.5 the symbols indicate the night of observation. From the absence of any systematic trends in these plots it can be seen that (a) the extinction coefficient supplied for the site is not in error; (b) second-order terms in the colour equation can be neglected; and (c) there was no significant shift of the photometric zeropoint from night to night which may occur due to extinction by cloud or very variable seeing conditions.

3 The CCD Sequences

A total of ten locations were selected in Fields 29, 30, 50 and 51 for the CCD sequences. Two of the locations were selected to be in the overlapping areas between Fields 29/30 and 50/51 so could each be used for calibrating two fields. Of the remaining eight sequence locations, two each were in Field 50 and Field 51, three lay in Field 30 and one in Field 29. Altogether there were three calibrating sequences for Fields 50 and 51, four for Field 30 and three in Field 29. For Field 29 we included an additional calibration sequence from Field 28 (sequence F28R1 from H-thesis p.30) which lies in the overlap region between Fields 28 and 29. In Fig. 2.6 the locations of the eleven sequences used for the calibration of the four fields are indicated.

For each location, a bright ($<$ 17th mag) sequence, and a faint sequence (down

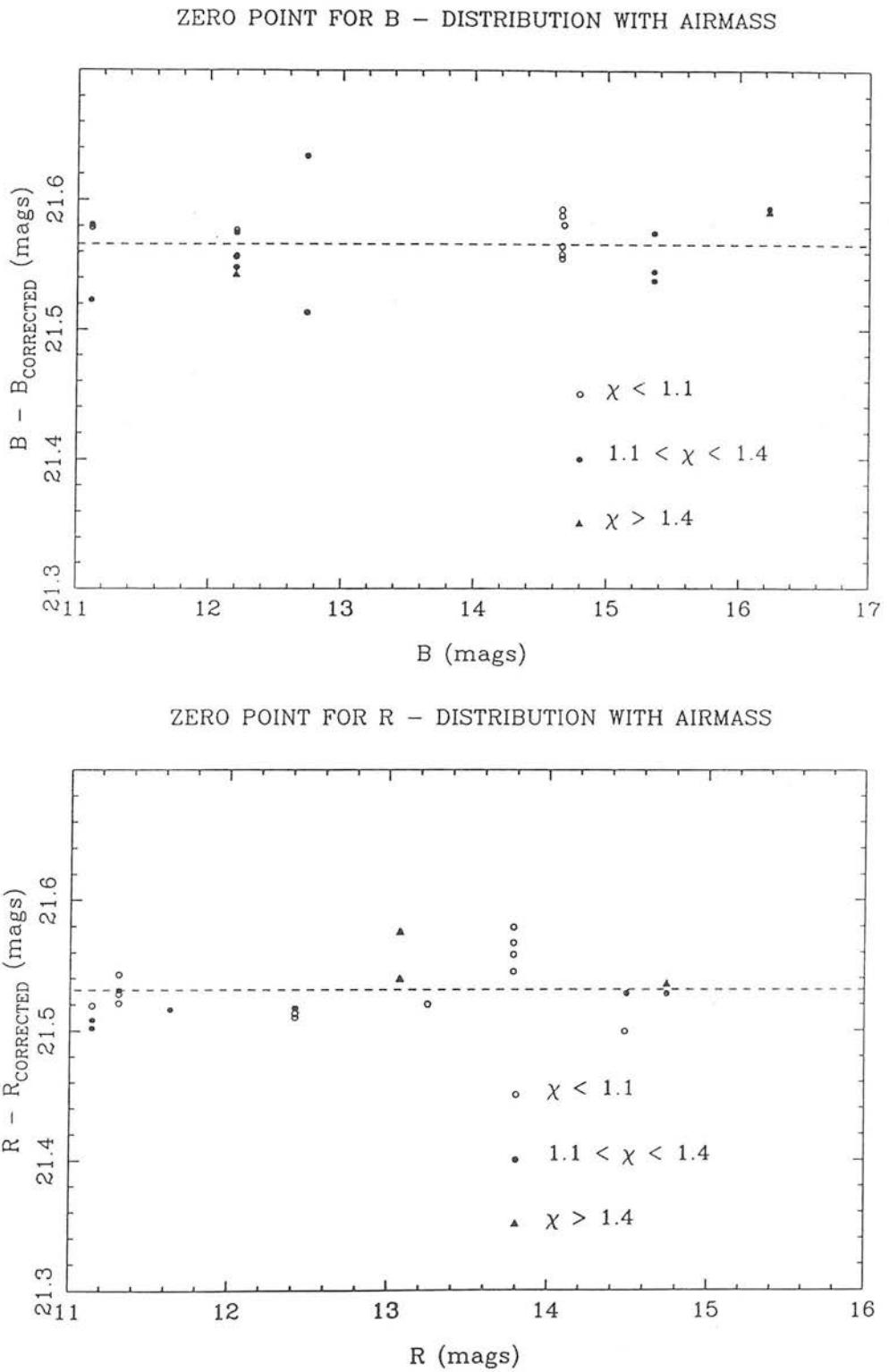

Figure 2.3: A check on the variation of the B and R photometric zeropoints with the airmass of the observation.

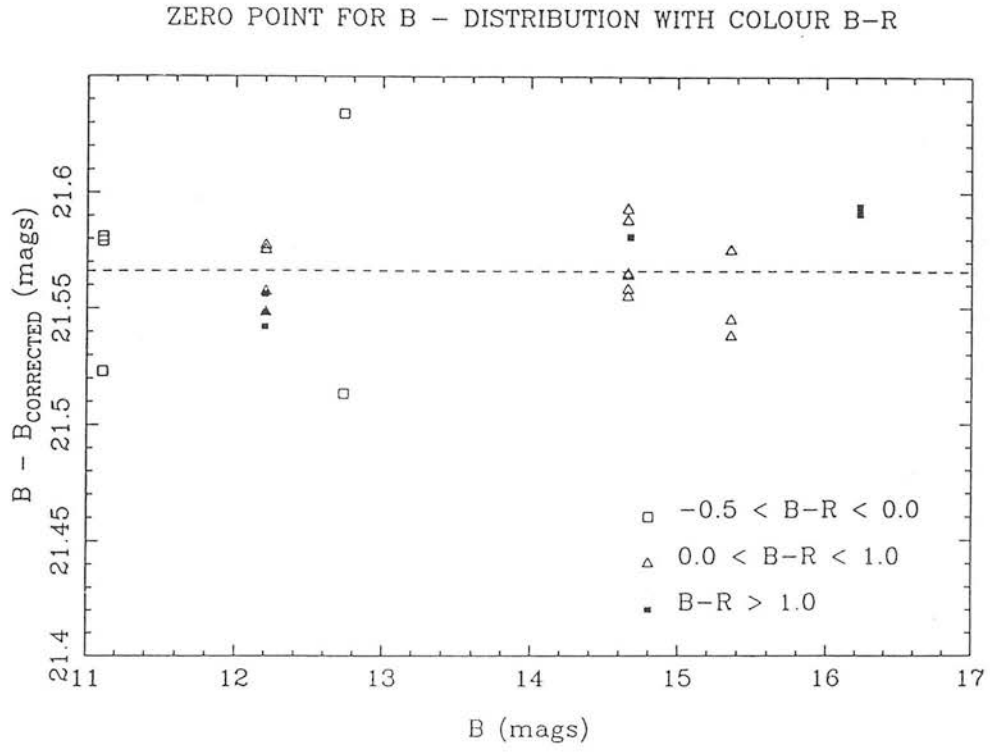

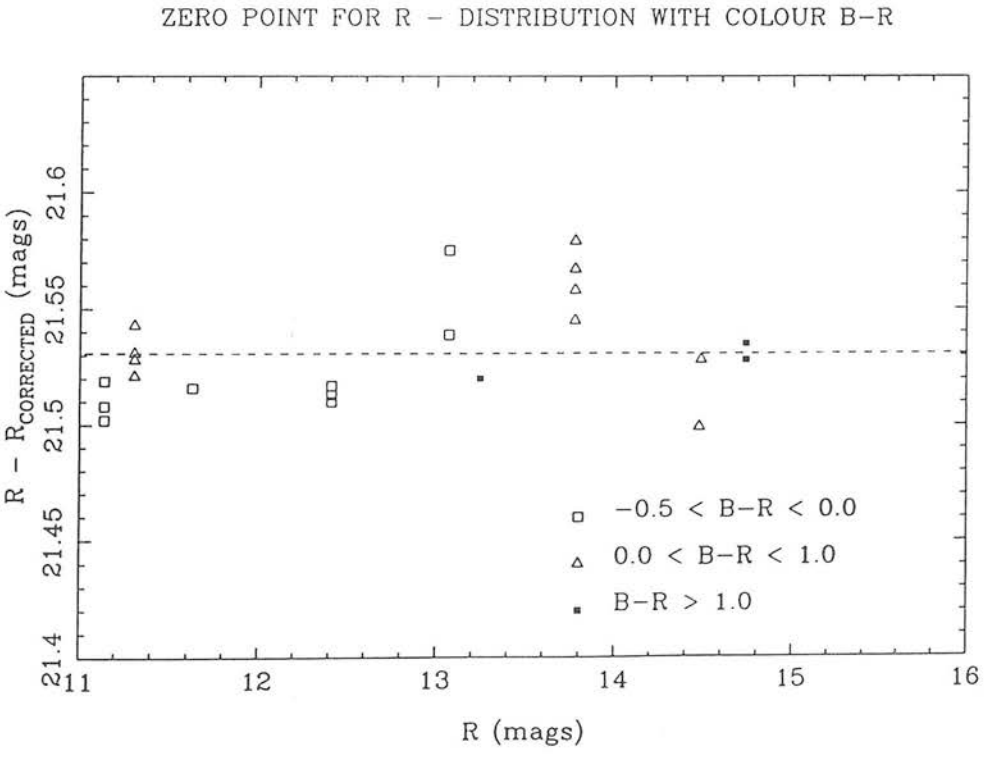

Figure 2.4: A check on the variation of the B and R photometric zeropoints with different colour ranges.

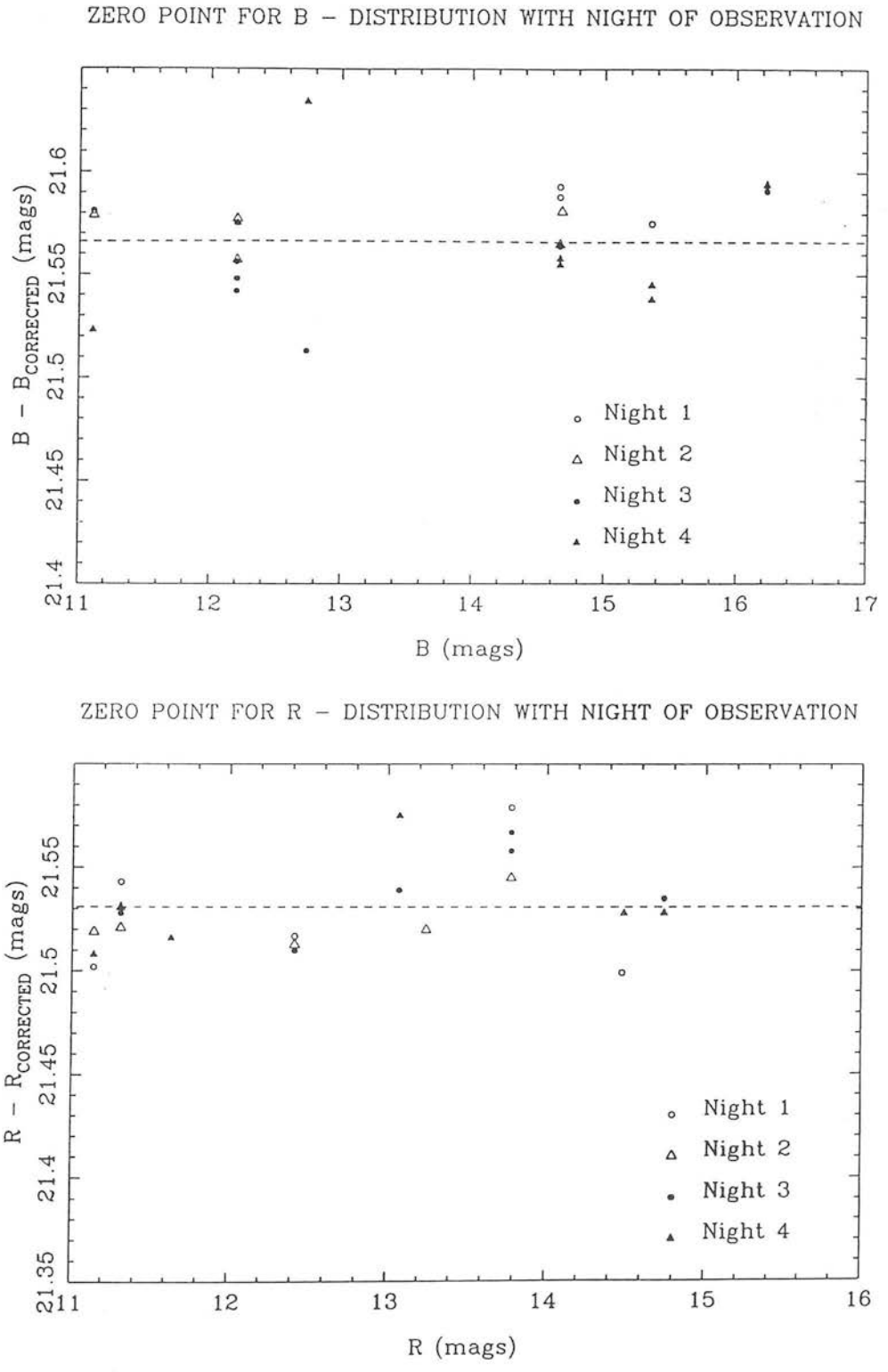

Figure 2.5: A check on the variation of the B and R photometric zeropoints with night of observation.

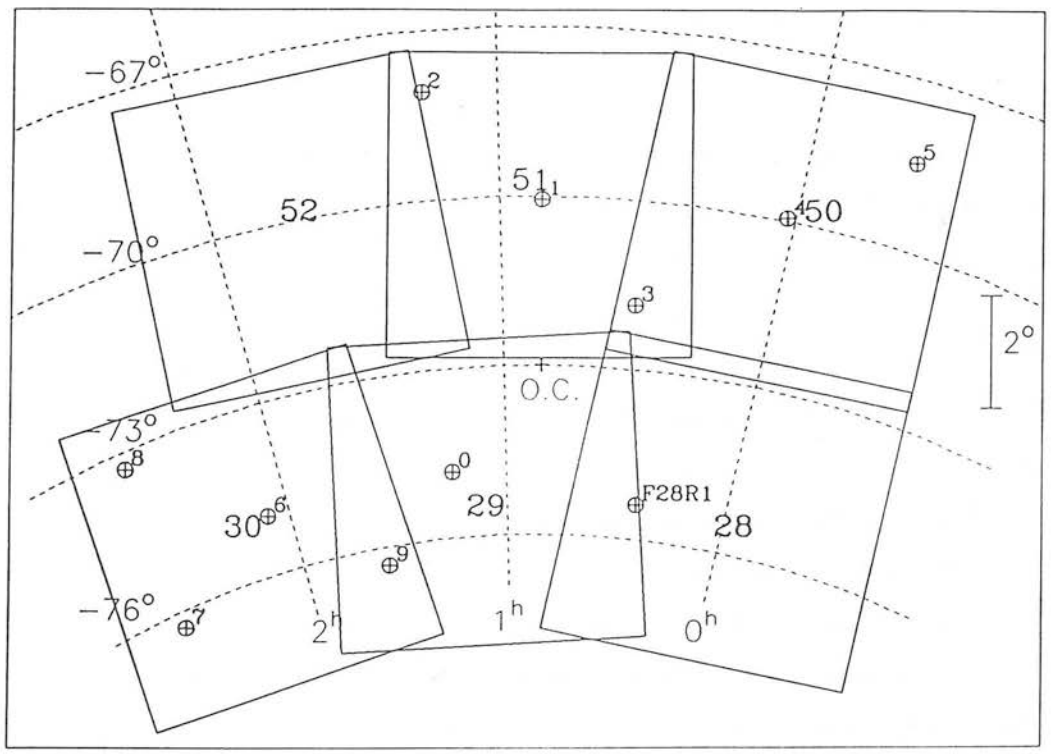

Figure 2.6: The positions of the CCD sequence locations. The ESO/SERC field numbers are shown and the SMC optical centre is marked.

to the limit of the photographic magnitudes) were observed, requiring both long and short exposures to cover a large range of magnitudes while avoiding image saturation. The short exposures were mostly of duration 1 min for R and 2 min for B, with even shorter exposures for very bright stars, while the long exposures were of duration 10 min for R and 20 min for B with additional shorter exposures for the brightest stars which were saturated on the long exposure frames.

In deciding which photometry program was to be used for the reduction of the programme frames, two considerations mitigated against the use of simple aperture photometry routines and instead favoured the use of some sort of profile-fitting stellar photometry package. The first consideration was the level of crowding of stellar images on long exposure frames, which at first sight does not pose a serious problem since merged images would not be separated by the COSMOS software applied to photographic plates and thus even if it were possible to accurately measure their magnitudes they would be useless for the plate calibration. However, serious difficulties result from the evaluation of the sky background in a relatively crowded area if the photometry package determines the sky level from a circular annulus centred on the stellar image as in the case of the AFOTO program. In this regard the STARLINK aperture photometry program PHOTOM allows the user to select the area to be used for the sky level evaluation by enabling a circular sky aperture to placed on a blank sky region. The more serious consideration, however, is the question of photometric accuracy at low signal-to-noise levels. Profile-fitting techniques give smaller intrinsic errors by effectively giving more weight to the pixels with the highest ADU values and less weight to pixels with a large sky contribution. Based on the above considerations, it was decided to use the DAOPHOT code (see Stetson 1987) which employs a 2-dimensional point-spread function fitting method to determine the stellar magnitudes. The improvement in the photometric accuracy for the profile-fitting technique compared to aperture photometry is demonstrated in Fig. 2.7, where the errors estimated by the profile-fitting program (DAOPHOT) and the aperture photometry program (in this case PHOTOM) are plotted as a function of magnitude for B and R using sample long exposure frames. The improvement in accuracy given by the

adoption of profile-fitting is about 0.02 mag at $R = 20$ and $B = 21$.

The DAOPHOT code enables the construction of a model 2-dimensional point-spread function (PSF) from the brightest isolated stars on a particular frame, which is then scaled and fitted to the other images on the frame. The form of the PSF is stored in two components, consisting of an analytic bivariate Gaussian profile, which is a good approximation to the core of the image, and a look-up table of residuals. Thus the PSF is ultimately an empirical one which avoids the problems associated with non-matching of an assumed stellar profile to the true image profile, which can result in magnitude errors of a few per cent (Walker 1984). A useful feature of the program is its star-finding routine which allows automatic detection of objects whose peak brightness is above a threshold specified by the user, while rejecting bad pixels and cosmic ray events (isolated 'hot' pixels). As an intermediate step between the identification of possible stellar objects and the final profile-fitting stage, the program performs aperture photometry on these objects using a set of user-specified radii. After defining the PSF from the brightest isolated stars on the frame, the profile-fitting routine produces instrumental magnitudes related to the magnitude, previously determined by aperture photometry, of the first star selected for the construction of the PSF. This allows the photometry to be related to the zeropoints already determined for a fixed aperture, in this case an aperture of radius 10 pixels as for the photometric reductions of the standard stars.

Multiple observations of a few CCD regions were obtained on different nights (including both long and short exposures), allowing a check on the zeropoint fluctuations from night to night. These did not exceed 0.02 mag and are smaller than the actual uncertainties in the zeropoints. A supporting programme was written to pair up the B and R frames, and transform the magnitudes to the standard system, simultaneously eliminating spurious identifications. The CCD sequences included stars ranging in brightness from 12th magnitude to well beyond the plate limit in both B and R. The standard errors, incorporating errors in the zeropoints as well as the instrumental errors determined by DAOPHOT, were acceptably small: equal to 0.04 mag for B

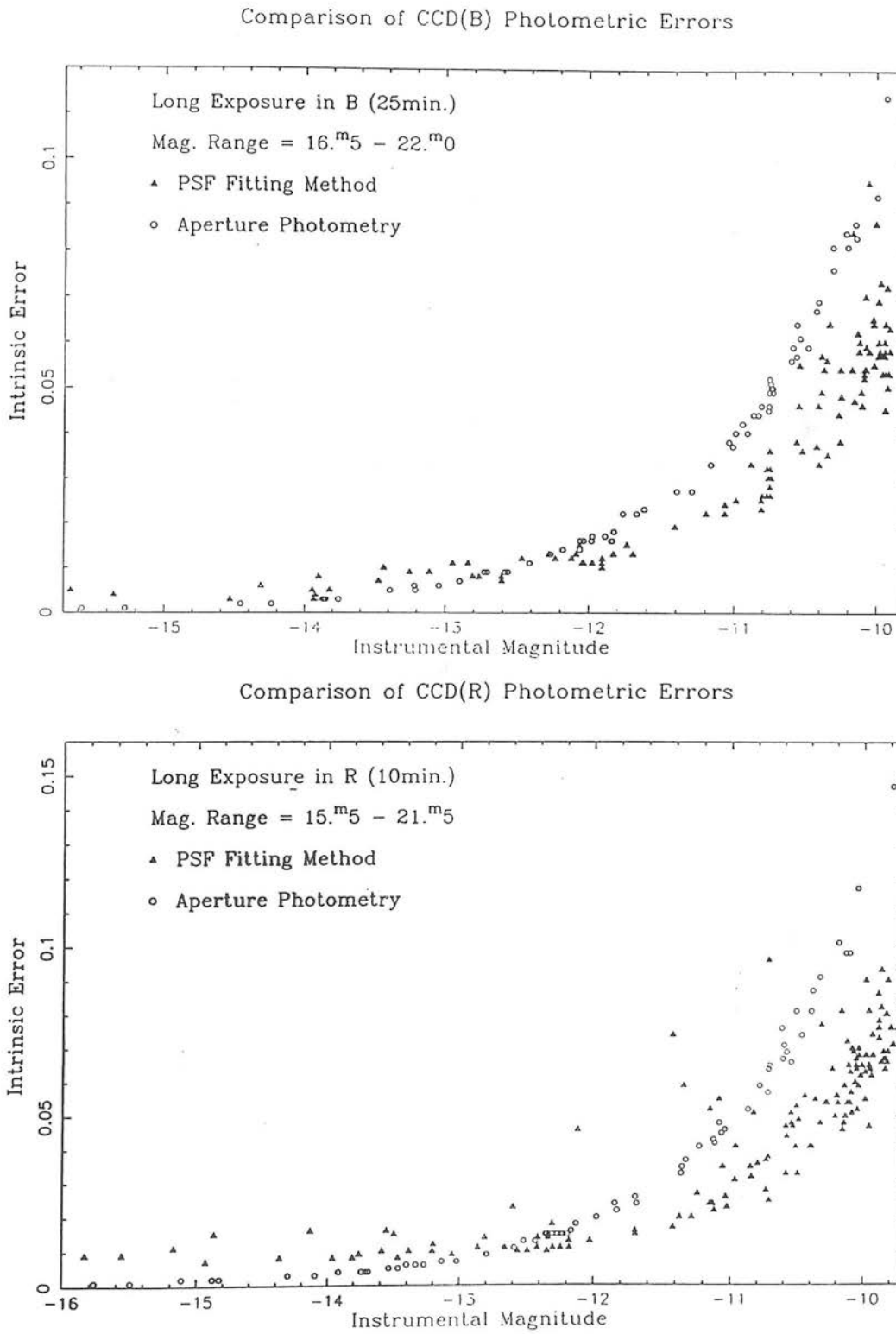

Figure 2.7: Comparison of intrinsic photometric errors obtained with aperture and profile-fitting photometry methods for a sample CCD region — B (top) and R (bottom).

magnitudes between $B = 12$ and $B = 20$, rising to 0.06 mag at $B = 21.5$ (the B photographic plate limit for reliable COSMOS measurements), and for R magnitudes equal to 0.03 mag for the range $R = 12$ to $R = 19.5$, rising to 0.05 mag at $R = 20.5$ (the equivalent limit in R).

The final CCD sequences used in calibrating the photographic plate material are listed in Appendix A. The first digit of the star ID numbers refer to the numbered sequence locations in Fig. 2.5, and the suffix B or F indicates whether the magnitudes were derived from bright (short exposures) or faint (generally long exposures) sequences. The coordinates of each star were determined by applying the STARLINK utility ASTROM to COSMOS data using reference stars from the astrometric catalogue accessed by the CHART utility, and are accurate to within a few arcseconds. Not all the stars listed have both B and R magnitudes for various reasons, which included the existence of faint stars of extreme colour, high rms errors in the photographic calibration, and most commonly the presence of large errors associated with some stars whose magnitudes were derived only from short exposures.

PART I: *THE DATABASE*

CHAPTER

— 3 —

THE PHOTOGRAPHIC PHOTOMETRY

This chapter describes the photographic plate material and COSMOS measurements upon which the project is based. In Section 1, the plate material, which comprises the raw observational data for the project, is reviewed. Section 2 describes the COSMOS measurements and calibration, including an evaluation of the photometric accuracy and completeness of the project database. Section 3 gives an overview of the methods of analysis used in Parts II and III to perform the investigation of the structure and stellar content of the outer regions of the SMC. Finally, in Section 4, the main features of the colour-magnitude diagrams constructed from the database are discussed as a preliminary to a full scientific analysis.

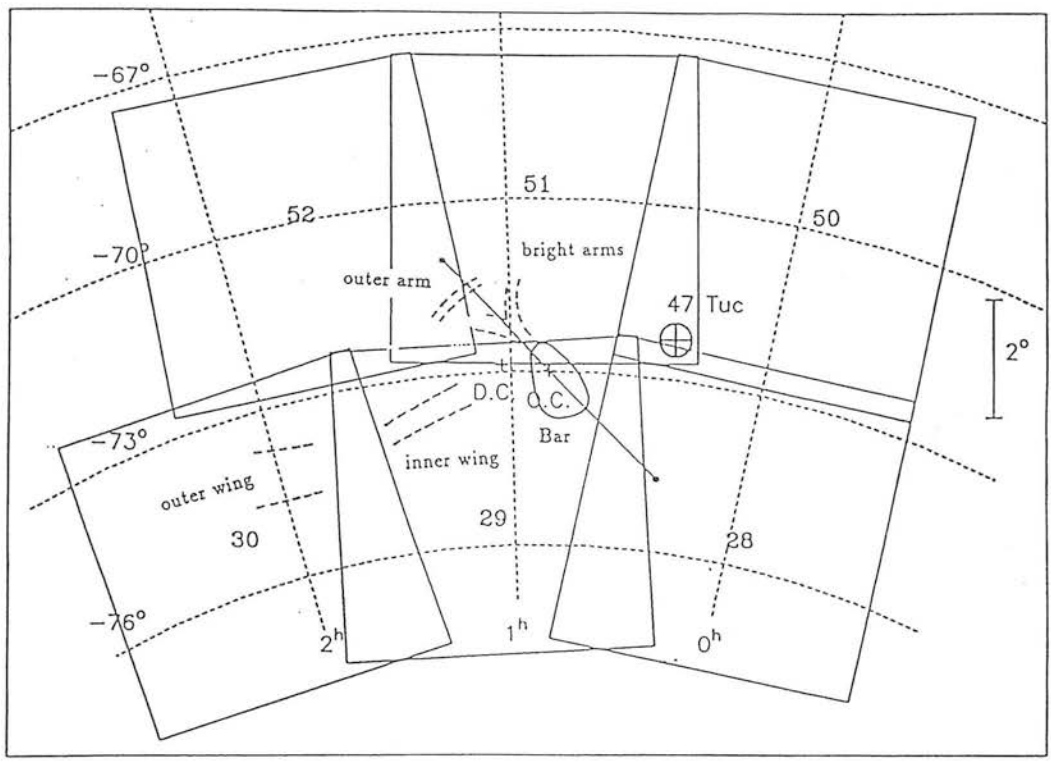

Figure 3.1: The locations of the ESO/SERC standard survey fields used in the project together with prominent SMC features. The optical centre (O.C.), dynamical centre (D.C.) and the SMC major axis are also marked.

1 The Plate Material

The full data set comprises six ESO/SERC fields (numbers 28, 29, 30, 50, 51, 52) in and around the Small Magellanic Cloud, covering a total measured area of 130 square-degrees. Fig. 3.1 shows the overall area included in the study, showing the location of the various fields with respect to the main features of the Small Magellanic Cloud. The plate material for Fields 28 and 52 is described in H-thesis (pp.36-38); however, an extra plate in Field 52 has been added to the plate material and a revised calibration carried out.

In all, 38 blue (B_J — filter/emulsion combination IIIa-J/GG395) and red (OR — IIIa-F/OG590 or R — IIIa-F/OG630) plates from all six project fields taken with the

1.2-m UK Schmidt Telescope (UKST) at Siding Spring Observatory, Australia, were used. The plates were all sky-limited with exposures between 40 and 115 min. They possessed acceptable image quality with UKST-unit quality grades between A and C (survey grades) or α (non-survey grading system). Three or four plates per filter combination and per field were used, except for Field 29 which has three red plates but only two blue plates. The rationale for the use of several plates per filter per field lies in the improvement in the accuracy of the photographic photometry. Firstly, random errors are reduced by a factor $1/\sqrt{n}$ by combining data from several plates, where n is the number of plates, and secondly, position dependent systematic errors within individual plates (see Section 3) are minimised. The list of the plates used is given in Table 3.1, along with the coordinates of the centres of the fields, the dates of acquisition and the quality classification of each plate (UKST-Unit classification system).

The plate material used for the project was obtained over a period of several years (1974 to 1990) during which several changes to the operation of the UK-Schmidt Telescope and plate processing procedures were made (see UKSTU Handbook, Appendix 4, 1983). The most important of these was the introduction of the nitrogen-flushing technique in 1982 which has the effect of reducing differential desensitisation at the edges of the plate due to moist air trapped between the flat filter and the curved plate. Plate material taken before 1982 may suffer from field effects due to differential desensitisation, the extent varying mainly with the air humidity during exposure, and in general such plates were removed from the calibration (though not from the database).

Plate non-uniformities may introduce systematic errors into the global calibration of the plates. Besides the problem of differential desensitisation described above, such non-uniformities include geometrical vignetting affecting the edges of the plates and changes of image structure across a plate. The latter effect can be caused by differential atmospheric extinction and affects blue plates more significantly than red plates due to the higher refractive index of the atmosphere in the B_J passband. In

Plate No.	Date UT	Emulsion	Filter	Exp. Time (min)	Grade
Field 28: $00^h00^m : -75°00'$					
J 1935*	75-11-29	IIIaJ	GG 395	50.9	BUX2
J 3675	77-10-13	IIIaJ	GG 395	80.0	AI3
J 9553	84-08-29	IIIaJ	GG 395	70.0	aI
R 7220	81-09-28	IIIaF	RG 630	100.0	CIU6
R 9587*	84-09-20	IIIaF	RG 630	90.0	aH
R 9600	84-09-23	IIIaF	RG 630	95.0	a
Field 29: $01^h06^m : -75°00'$					
J 1940	75-11-30	IIIaJ	GG 395	60.0	BIS2
J 1948*	75-12-03	IIIaJ	GG 395	60.0	A2
OR11406*	86-10-01	IIIaF	OG 590	45.0	BEI3
OR13439	89-11-21	IIIaF	OG 590	65.0	A3
OR13908	90-10-11	IIIaF	OG 590	75.0	a
Field 30: $02^h12^m : -75°00'$					
J 1805	75-09-08	IIIaJ	GG 395	60.0	BE2
J 8844*	83-10-08	IIIaJ	GG 395	60.0	A2
J13917	90-10-13	IIIaJ	GG 395	80.0	a
OR13260*	89-08-29	IIIaF	OG 590	75.0	BI3
OR13500	89-12-18	IIIaF	OG 590	60.0	BIE4
OR13834	90-09-16	IIIaF	OG 590	60.0	aI
Field 50: $00^h00^m : -70°00'$					
J 905	74-09-11	IIIaJ	GG 395	40.0	B
J 3670*	77-10-12	IIIaJ	GG 395	75.0	A2
J12700	88-08-11	IIIaJ	GG 395	85.0	BEI4
J12720	88-08-19	IIIaJ	GG 395	100.0	CIU5
OR10385	85-08-17	IIIaF	OG 590	75.0	BUIE4
OR11282	86-08-10	IIIaF	OG 590	70.0	BID3
OR12192*	87-09-24	IIIaF	OG 590	85.0	AUE3
OR12728	88-08-20	IIIaF	OG 590	95.0	AI3
Field 51: $00^h52^m : -70°00'$					
J 1800	75-09-07	IIIaJ	GG 395	60.0	BIE3
J 1829	75-10-03	IIIaJ	GG 395	70.0	BI3
J 1877*	75-10-31	IIIaJ	GG 395	70.0	A1
J13369	89-10-05	IIIaJ	GG 395	60.0	BI4
OR10440*	85-09-08	IIIaF	OG 590	75.0	BI4
OR12821	88-10-30	IIIaF	OG 590	95.0	BI4
OR13318	89-09-24	IIIaF	OG 590	75.0	AEI3
Field 52: $001^h44^m : -70°00'$					
J 1825	75-10-02	IIIaJ	GG 395	70.0	AIF3
J 2566*	76-09-01	IIIaJ	GG 395	60.0	AI2
J 3671	77-10-12	IIIaJ	GG 395	75.0	BE2
R10516	85-10-17	IIIaF	RG 630	95.0	a
R10640*	86-01-02	IIIaF	RG 630	115.0	aT
OR12169	87-09-20	IIIaF	OG 590	90.0	BEI4

Table 3.1: List of the photographic plate material used in the study together with the coordinates of the field centres. *Columns 1–5* are self-explanatory. The plates used as master-plates are followed by an asterisk. In *Column 6* the quality of the plates is described using the UKSTU grading system. **E**: emulsion fault; **F**: fogging; **I**: image size $> 35\mu$m; **U**: underexposed; **UX**: although underexposed, no obvious difference from the survey plate; **H**: haze halos (affecting only the brightest stars); **T**: trail

the following section these effects are considered in relation to systematic errors in the COSMOS photometry measurements.

2 The COSMOS Measurements

The photographic plates were digitised using the high-speed microdensitometer COSMOS at the Royal Observatory, Edinburgh (see e.g. Stobie 1986). In this section we first describe the operation of the COSMOS machine (subsection 2.1); secondly (subsection 2.2), we describe the calibration of the COSMOS instrumental magnitudes using the CCD sequences described in the previous chapter; thirdly, we consider the photometric accuracy of the COSMOS measurements (subsection 2.3); and finally, we investigate the completeness of the data set (subsection 2.4).

2.1 The COSMOS Measuring Machine

The COSMOS machine is a computer-controlled, high-speed microdensitometer, capable of digitising photographs of size 356 × 356 mm, although the actual area that can be scanned is limited to 287 × 287 mm. Its basic principle is the same as all microdensitometers and operates by focussing a microspot onto the photographic emulsion and measuring the amount of transmitted light. The scanning system uses a flying spot scanner which deflects the spot in the x-direction while the machine carriage drifts in the y-direction, effectively producing a raster scan of the photographic plate. A pixel size of 16 μm in combination with a spot size of 32 μm FWHM was used, allowing most of the information to be extracted from the images recorded on the photographic plate. The scanning system is described fully by MacGillivray & Stobie (1984). A notable feature is the use of a dual-beam system to monitor the spot brightness and response across the light-emitting cathode-ray tube enabling variations to be effectively eliminated. The transmitted light is registered by a photomultiplier and the integrated signal is fed into an analogue-to-digital (A/D) converter which outputs

a 14-bit transmission value (i.e. 16384 transmission levels). This is converted into a relative intensity using a calibration curve obtained from the step wedge at the edge of each plate, which possesses steps of known relative intensity.

The threshold mapping mode (TM) of COSMOS was used to extract data on the astronomical objects recorded on each plate. Instead of outputting all the pixel data onto disk, which is the case in mapping mode (MM), only pixels with transmission values above a fixed percentage of the night sky background level are utilised, apart from the determination of the local sky background. The sky background is evaluated by prescanning the plate at low resolution (32 μm) and obtaining a 2D array of median transmission values covering the scanned area. The array is subject to 2D median-filtering and the sky background for each pixel is estimated by interpolating between this coarse grid. The median filtering procedure removes bad sky values caused, for example, by a very bright star whose pixels dominate the pixel transmission histogram in a single array element. The intensity threshold used was 6-8 per cent of the local sky value and was chosen to ensure detection of images very nearly down to the plate limit. The pixels with transmission values above the threshold are subsequently analysed by the pattern algorithm of Thanisch, McNally & Robin (1984) which connects up the pixels into discrete objects. The application of moment analysis to the pixel data for each object results in twenty parameters being output to magnetic tape, including X and Y position in 0.1 μm, image area A in pixels 8 μm square, a photometric parameter defined as COSMAG= $-2.5 \log \Sigma I$ where ΣI is the sum of the intensities above the sky background of the pixels within the image area, and the major and minor axes and orientation of the fitted ellipse.

The software used for the object analysis was non-deblending, i.e. the algorithms assume that each object is isolated. A new deblending software package has recently been developed for crowded field analysis (see Beard, MacGillivray & Thanisch 1990) which has been extensively tested on simulated data but has yet to be fully tested on real photographic plates. Since the photographic plates covering the SMC area become increasingly crowded towards the SMC centre, ideally deblending techniques

should be used to achieve high levels of completeness. The interpretation of our colour-magnitude data places a high premium on photographic accuracy and therefore non-deblending software was considered more reliable than the deblending software package until such time as the deblending software was adequately tested on real data. Nevertheless, the tests on simulated data described by Beard *et al.* (1990) provide promising indications that the deblending software may be appropriate for analysis of relatively crowded fields of stellar objects. The effects on the overall completeness of the non-deblending software used in this project are considered in subsection 2.4.

2.2 The Plate Pairing and Calibration of the COSMOS Magnitudes

The same procedure for processing the data produced by COSMOS described in H-thesis (pp.44-46) was followed, using software developed by Hawkins (1983; 1984). Briefly, after pairing of the data sets of each colour, the magnitudes were calibrated using CCD sequences, and then merged with the data set of the other colour.

For the pairing process a master plate in each waveband was selected, which was usually the best quality plate with the faintest effective magnitude limit. A least-squares rotation, translation and scale-change transformation was evaluated from the positions on the master plate to each one of the other plates using the 1000 brightest images on each plate. For each image on the master plate the nearest image on the secondary plate to the transformed position was adopted as a match provided it lay within an error box of specified size. The photometric, positional and geometrical information of each image on the master plate is retained, but only the COSMOS magnitude information from the secondary is retained after the pairing process. If no match was found for a master image a zero entry is made for the magnitude of the secondary plate 'image'. For the scientific analysis only those images matched on all the plates in each field were included.

The percentage of images matched on a single pairing is sensitive to the effective magnitude limits of the master and the secondary plates but for images with magni-

tudes at least a magnitude brighter than the magnitude limit of the secondary plate the efficiency of pairing was typically greater than 95 per cent for relatively uncrowded areas (see the discussion on incompleteness in the following section). The plate pairing process removes spurious images as well as faint images due to the different limiting magnitudes of the various plates, adjacent images which were merged into one image on one plate but resolved on another, and objects of extreme colour at faint magnitudes. Close pairs or groups of images which may be registered as a single image due to thresholding effects were often unpaired due to random errors in their coordinates.

After the creation of the paired data set in each waveband for a given field the COSMOS magnitudes were calibrated using the CCD sequences in Appendix A. The matching of the sequence stars with the COSMOS data for each CCD frame was performed using a semi-automated procedure which relies on visual identification of two CCD sequence stars on the COSMOS data to define the transformation from the CCD frame to the COSMOS coordinate system. The remaining stars on the CCD frame are then matched up automatically. Fig. 3.2 shows the matching of CCD sequence stars with COSMOS data for a representative faint CCD sequence in Field 51.

The calibration is carried out by evaluating a least-squares fit of a fourth-order polynomial relation between the CCD sequence magnitudes and the mean of the COSMOS instrumental magnitudes. Prior to the evaluation of the transformation, the standard Johnson B magnitudes from CCD photometry were converted to IIIa-J/GG395 (B_J) magnitudes using (from H-thesis p.45) the relation

$$B_J = B - 0.25(B - R).$$

For the scientific analysis, however, the calibrated B_J magnitudes were transformed back to standard Johnson B magnitudes by applying the inverse relation

$$B = B_J + 0.3333(B_J - R).$$

Fig. 3.3 shows an example of a polynomial fit between the COSMOS instrumental magnitudes and the true (CCD) magnitudes of the sequence stars for one filter/field

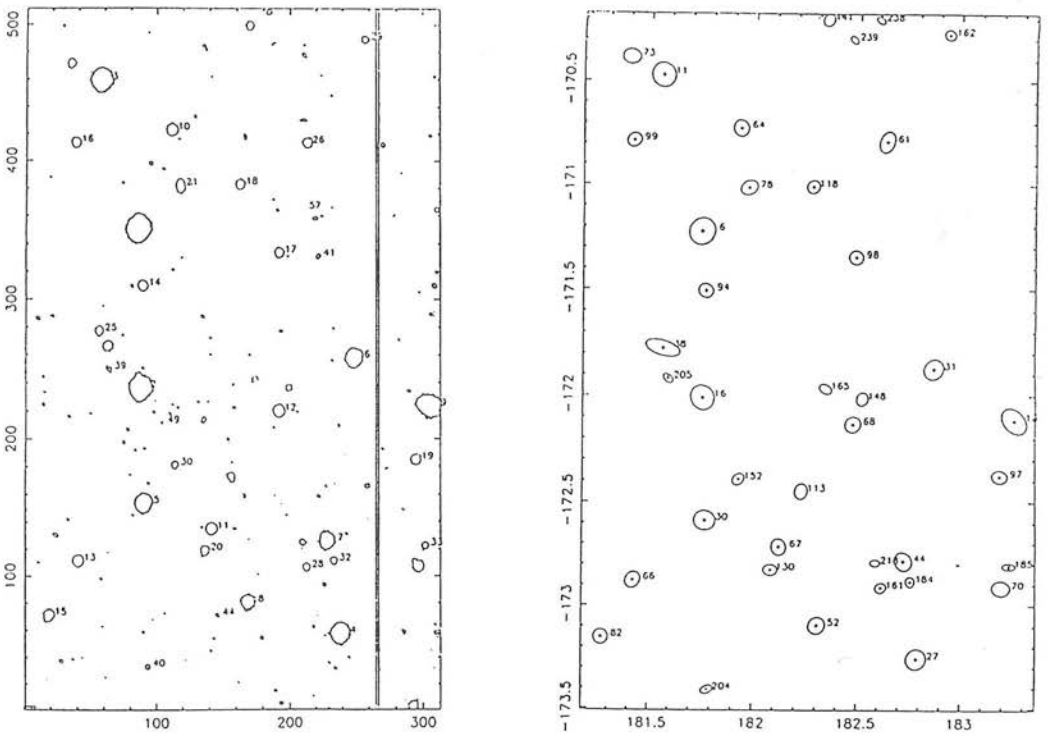

Figure 3.2: Matching of a CCD sequence to COSMOS data for the calibration of COSMOS instrumental magnitudes. This example is from a sequence location in Field 51. On the left is a contour map of the CCD frame, and on the right the corresponding COSMOS data map is shown. COSMOS images matched with CCD sequence stars are indicated with a central dot.

combination. This figure clearly shows that the relation between COSMOS magnitude and true stellar magnitude is not linear due to saturation of the photographic emulsion at brighter magnitudes. In Fig. 3.4 the transformed COSMOS magnitudes (i.e. that produced by application of the polynomial transformation to the COSMOS instrumental magnitudes) are plotted against the CCD magnitudes of the sequence stars. The scatter plot accurately defines a straight line, confirming the suitability of a fourth-order polynomial in determining the transformation. The resulting residuals between the sequence magnitudes and the transformed COSMOS magnitudes were about 0.1 mag for all the filter/field combinations, which is comparable to the value expected from the random error from the average of 3-4 individual plate measurements (see next subsection) combined with the standard error associated with the CCD sequence magnitudes.

In order to make comparisons between the magnitudes of images on different plates all the COSMOS instrumental magnitudes were reduced to the same scale by evaluating a least-squares polynomial transformation of the individual plate measurements to the mean of the COSMOS measurements. The polynomial transformation was then applied to each individual plate magnitude in the remainder of the image list in a position-dependent manner as described in Hawkins (1983; 1984) in order to correct for field effects peculiar to individual plates. Finally, in each field the calibrated data sets for each waveband were paired using the same procedure followed for the single-waveband plate pairings.

2.3 The Accuracy of the Photographic Magnitudes

The analysis of the photometric data obtained from the photographic photometry is critically dependent on the systematic and random errors in the photometry. Conclusions drawn from the data analysis are subject to these errors which may limit the significance of the derived results. There are two kinds of errors — random and systematic — both of which need quantification for the various scientific investigations in the following chapters. We deal with these two aspects separately.

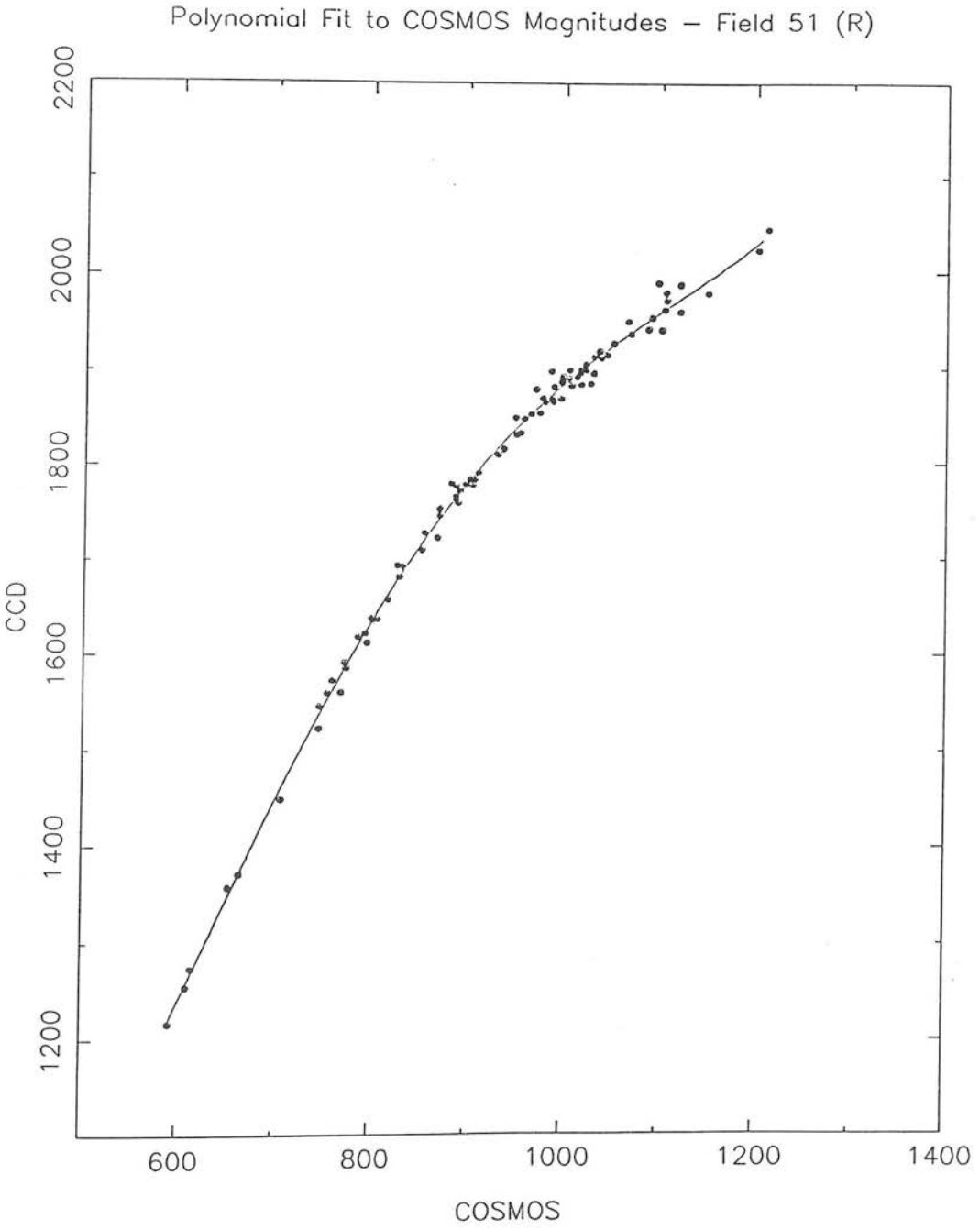

Figure 3.3: COSMOS calibration plot showing CCD magnitude versus COSMOS instrumental magnitude for sequence stars in Field 51 (R-band photometry). The units are in hundredths of a magnitude. The fitted curve represents a fourth-order polynomial relation used subsequently to define the transformation from COSMOS instrumental magnitudes to the standard system.

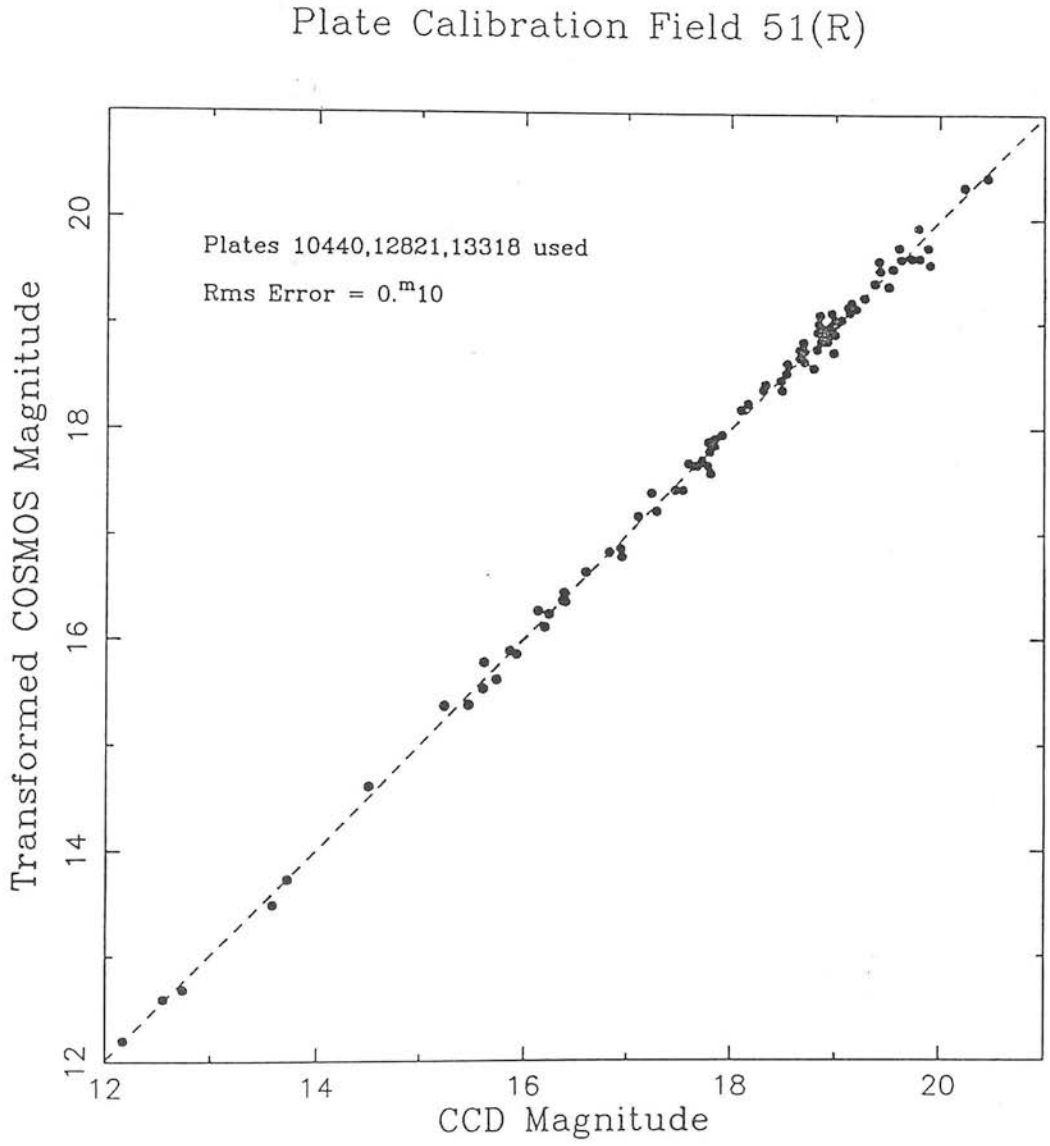

Figure 3.4: COSMOS calibration plot showing transformed COSMOS magnitude versus CCD magnitude for sequence stars in Field 51 (R-band photometry). The points define a straight line relation which confirms that a fourth-order polynomial transformation for the COSMOS instrumental magnitudes is adequate.

(i) Random Errors

Random errors in the photometry of objects on a single plate are due to the intrinsic photometric uncertainty corresponding to the signal-to-noise ratio of the data for any given image. These errors can be estimated by considering the rms variation of separate measurements of the same object on several photographic plates. It is assumed that systematic variations (due to field effects) affecting individual plates have been eliminated by the position-dependent calibration process of Hawkins (1983; 1984). Histograms of the distribution of the rms errors due to individual measurements with respect to the mean of all the measurements for a given filter/field combination indicate that the peak of the error distribution increases from about 0.05 mag at bright magnitudes (less than 15th mag) to 0.10 mag near the plate limit. In Fig. 3.5, the distribution of rms errors is shown for the B_J measures in Field 51 for several different magnitude ranges, illustrating the above trend. The histograms also show a non-Gaussian tail due to genuinely variable objects or objects affected by emulsion flaws and other defects (e.g. diffraction spikes due to nearby bright stars) on one or more plates. For n plates the size of the random error can be expected to be reduced by a factor $1/\sqrt{n}$.

A further exercise in assessing the random accuracy of the photometry was undertaken by comparing the rms errors between independently derived magnitudes of the same objects in the overlapping area between Fields 50 and 51, which was chosen as a representative case. (Systematic errors in the photometry in the overlapping areas between different fields will be investigated later.) Fig. 3.6 shows the variation of random errors (i.e. rms errors after removing the systematic discrepancy) as a function of magnitude for all stars with two independently derived magnitudes. The points represent the mean quantities per 0.1 mag bin. For both B_J and R the random errors lie between 0.06 mag and 0.10 mag per field, generally increasing towards fainter magnitudes. We therefore conclude that the random errors in the photometry are less than 0.10 mag.

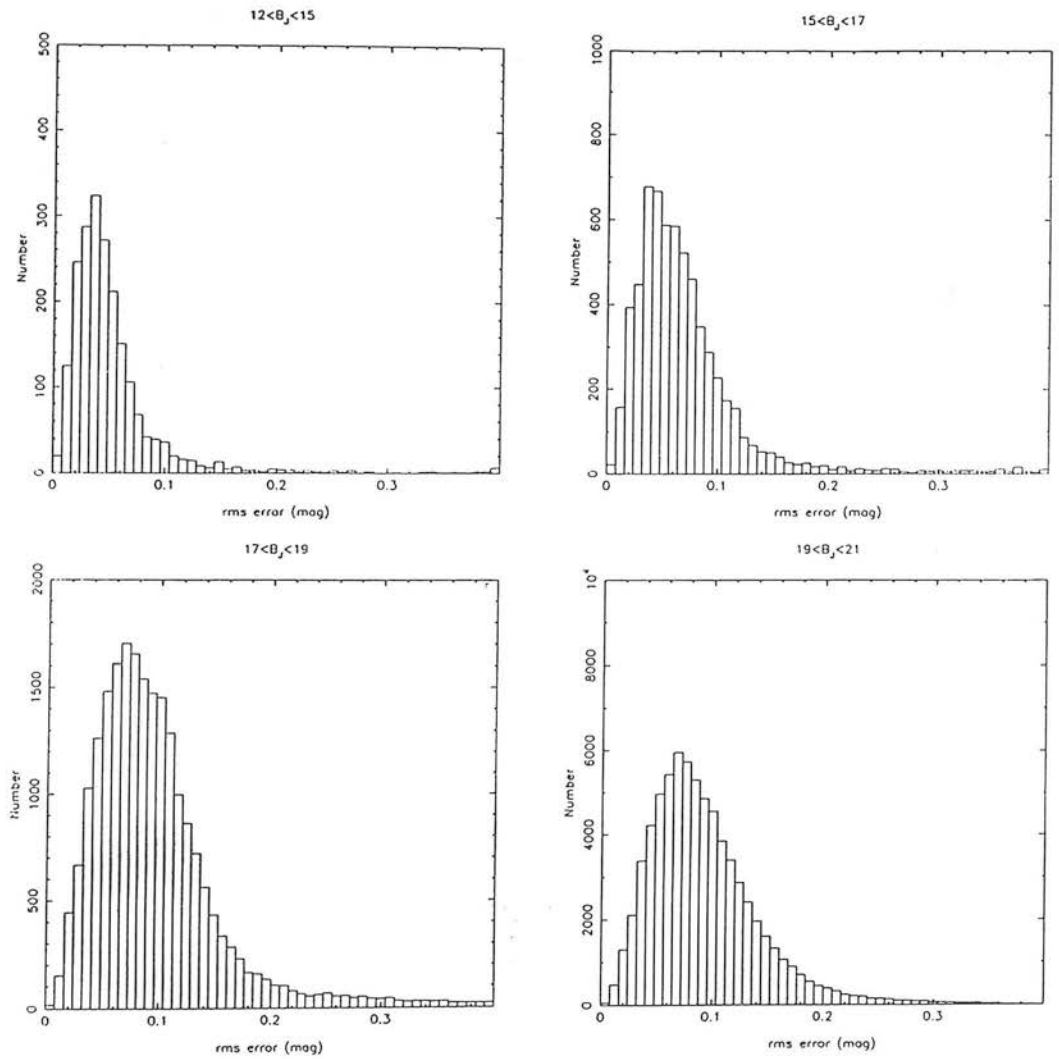

Figure 3.5: Plots of the distribution of rms magnitude errors for different magnitude ranges based on four B_J plates in Field 51. The peak of the error distribution gives an estimate of the random error of a measurement derived from a single plate.

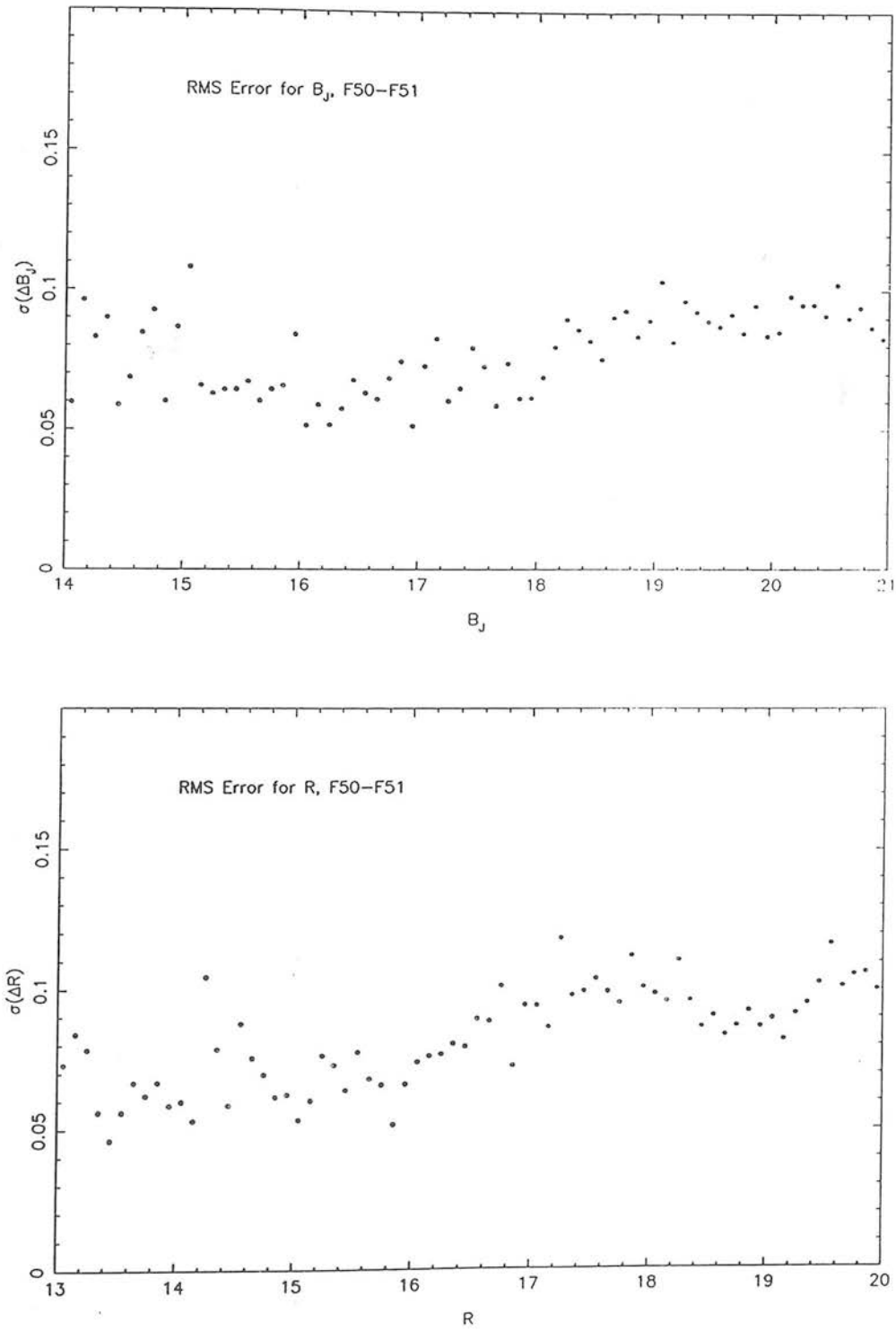

Figure 3.6: Random photometric errors (i.e. rms errors after removing the systematic magnitude discrepancy) derived from matched images in the overlapping plate area between Fields 50 and 51 as a function of magnitude for B_J and R.

(ii) Systematic Errors

Plate non-uniformities such as those discussed in Section 1 can give rise to systematic errors of up to about 0.3 mag over the area of a single plate. The effects of these non-uniformities are generally reduced by combining data from several plates but global non-uniformities affecting all plates may still give rise to significant systematic errors towards plate edges. As an indicator of the size of systematic errors on a single plate, the deviations of the magnitude of images for individual plates from the mean magnitude of all the plates for a given filter/field combination was monitored as a function of position on the plate. Fig. 3.7 shows the pattern of residuals for four R plates in Field 50 for a bright range ($12 < R < 17$) and a faint range ($17 < R < 22$) of magnitudes. There is a similar pattern for all the plates, namely larger deviations from the mean up to 0.2 mag for the brighter magnitudes and considerably smaller deviations, in most cases less than 0.1 mag, for the fainter range. This effect is due to variations in emulsion sensitivity or image structure more critically affecting brighter saturated images.

The application of the position-dependent calibration process corrects the variations from the mean for each individual plate but cannot remove global field effects affecting all plates, of which vignetting at the edges of plates is probably the most significant. In principle, the CCD sequences should define upper limits for the systematic magnitude variations by monitoring the applicability of the transformation at different locations. Large residuals are produced for areas significantly affected by global field effects. In practice, however, there are generally too few sequence stars at each location, particularly at fairly bright magnitudes (less than about 16th mag) to give quantitative information on significant trends. Fig. 3.8 shows a plot of the residuals between the transformed COSMOS magnitudes and the CCD magnitudes of the sequence stars in Field 51 (R) as a function of magnitude with stars from different locations indicated by different symbols. It is evident that, fainter than $R = 16$, there are no clear systematic trends which would indicate the presence of plate non-uniformities.

RESIDUALS FOR PLATE 12192 IN 0.01 MAGS

BRIGHT IMAGES, 12 < MAG < 17

-15	-13	-9	-9	-8	-7	-4	-4	-2	0	1	2	0	-5	-5	-9
-11	-7	-5	-8	-7	-5	0	1	3	2	2	0	2	0	4	1
-8	1	-1	-3	0	-3	2	6	2	5	9	3	2	1	5	-1
-6	0	-2	0	1	-3	3	7	8	11	12	9	8	5	5	2
-3	1	0	2	2	4	2	5	7	14	14	8	10	5	5	4
-8	-3	0	0	4	3	9	7	6	15	10	14	6	6	0	-3
1	0	-1	2	6	7	6	4	6	13	15	11	8	6	3	7
2	6	5	3	8	9	8	10	10	17	15	15	15	16	9	8
2	7	8	3	2	9	9	12	13	8	16	15	13	13	11	3
2	4	4	9	10	7	10	11	17	19	19	17	17	12	10	8
0	1	1	10	13	12	15	15	15	14	16	15	13	14	12	9
-1	5	3	7	7	11	11	16	14	14	21	19	16	14	11	14
-2	-1	1	4	7	10	13	9	10	20	20	22	17	17	16	13
-7	-3	-1	3	3	13	13	16	14	18	16	17	16	6	3	11
-13	-7	-4	0	5	9	14	15	8	12	16	17	4	2	-7	3
-14	-10	-6	0	0	4	11	10	13	14	12	9	4	-5	-12	-12

FAINT IMAGES, 17 < MAG < 22

-9	-10	-8	-7	-7	-7	-6	-4	-3	-2	-1	-3	-4	-5	-6	-5
-9	-6	-6	-8	-7	-4	-3	-2	-1	-2	0	-1	-2	-3	-2	-4
-6	-3	-5	-5	-6	-4	-4	-3	0	0	1	-1	-2	-1	0	-2
-7	-3	-3	-2	-1	-5	-3	-1	0	0	2	0	0	0	0	-1
-7	-4	-3	-3	-4	-3	-2	-1	0	0	1	2	1	0	-2	-2
-7	-6	-5	-3	-3	-1	0	0	0	0	1	2	-1	0	-3	-2
-4	-2	-3	-1	0	1	0	0	0	1	2	2	0	-2	-2	0
-3	0	0	-1	0	2	2	0	1	1	1	0	2	3	0	0
-2	0	0	0	0	1	1	2	0	0	0	2	3	2	0	0
-3	-4	0	1	3	0	2	1	3	2	2	2	2	1	0	0
-2	-3	-1	0	2	2	3	4	3	0	4	2	0	1	1	0
-3	0	-2	0	1	2	2	2	2	1	5	4	3	2	1	0
-5	-4	-1	-1	0	2	2	2	2	4	5	5	3	2	2	0
-5	-5	0	0	-1	1	2	2	3	3	4	6	5	2	0	1
-8	-6	-3	-2	0	0	2	0	2	2	4	3	3	3	-2	0
-11	-8	-6	-3	-2	-3	0	0	1	1	1	1	1	-3	-5	-2

RESIDUALS FOR PLATE 10385 IN 0.01 MAGS

BRIGHT IMAGES, 12 < MAG < 17

23	16	13	11	12	14	11	9	6	6	5	4	1	0	-1	0
19	13	10	10	10	10	9	7	6	2	2	1	-2	-3	-3	-3
13	9	6	7	7	7	5	4	5	0	0	0	-2	-4	-4	-6
10	10	6	3	2	4	4	4	3	0	0	0	-4	-4	-5	-6
9	9	5	2	1	2	3	5	3	-1	-2	-1	-4	-7	-9	-7
11	9	6	2	1	2	2	1	2	1	-2	-1	-2	-4	-7	-8	-9	-8
9	10	5	2	1	3	3	2	0	0	-3	-4	-7	-9	-10	-12
11	10	4	1	0	1	3	1	-2	-2	-2	-4	-9	-11	-11	-11
10	8	2	1	1	1	0	0	-1	0	-4	-6	-9	-10	-12	-11
11	9	4	1	1	1	2	2	-1	-3	-5	-6	-10	-9	-10	-11
12	9	5	1	0	0	1	-1	-1	-5	-5	-7	-8	-12	-11	-10
11	10	6	3	1	1	1	-1	-2	-4	-5	-7	-9	-10	-10	-11
11	9	6	2	0	0	-1	-1	-2	-6	-6	-9	-11	-12	-14	-14
12	8	5	4	2	0	-1	-5	-3	-7	-9	-9	-12	-12	-13	-16
15	10	7	5	3	0	0	-2	-2	-6	-9	-11	-12	-11	-14	-14
15	12	9	4	2	3	1	0	-2	-5	-8	-9	-12	-12	-12	-12

FAINT IMAGES, 17 < MAG < 22

15	13	10	8	8	7	7	6	5	3	4	3	2	0	1	3
12	9	7	6	6	6	5	5	4	3	3	2	0	0	0	0
10	7	5	5	6	5	3	3	4	2	2	2	0	0	0	-1
6	5	3	3	2	3	4	3	3	2	2	3	0	-1	-1	0
4	4	2	3	2	4	3	4	3	2	1	1	-1	-1	-2	-1
4	4	3	3	2	3	3	2	3	2	0	0	-3	-3	-4	-2
3	3	3	3	1	3	3	2	2	1	0	0	-3	-4	-4	-5
4	4	3	2	2	4	3	1	0	0	0	-1	-5	-5	-5	-6
4	3	3	2	2	3	2	2	0	0	-1	-2	-4	-4	-4	-5
5	4	3	4	2	2	3	1	1	-2	-1	-2	-5	-4	-5	-5
5	3	3	3	2	4	2	2	0	-1	0	0	-4	-5	-4	-3
7	6	3	3	4	3	3	2	1	0	0	-1	-3	-4	-5	-4
9	7	4	3	2	2	2	1	0	-2	-1	-1	-4	-5	-6	-6
10	7	6	5	4	2	0	0	0	0	-2	-3	-5	-6	-7	-5
12	9	8	5	5	4	1	0	0	-3	-3	-4	-6	-7	-7	-2
16	13	10	8	6	7	4	2	0	-1	-2	-2	-4	-4	-4	2

RESIDUALS FOR PLATE 11282 IN 0.01 MAGS

BRIGHT IMAGES, 12 < MAG < 17

-6	0	1	3	1	-5	-6	-6	-4	-8	-9	-6	-2	2	3	6
-2	1	2	2	-1	-5	-9	-9	-9	-6	-9	-5	-1	1	-3	-1
3	0	2	1	-3	-3	-6	-10	-11	-10	-12	-9	-7	-2	-4	2
11	2	3	2	0	-1	-6	-10	-13	-13	-16	-14	-8	-4	-2	0
14	5	2	0	1	-1	-5	-9	-10	-13	-14	-12	-9	-1	2	0
14	8	3	3	0	-4	-8	-7	-10	-15	-12	-13	-4	-2	4	4
10	5	1	0	-1	-7	-8	-7	-8	-14	-16	-10	-5	-2	2	2
9	1	0	1	-2	-8	-10	-10	-5	-16	-16	-13	-10	-8	0	1
8	1	0	-1	-2	-7	-7	-10	-10	-11	-14	-10	-8	-5	0	3
8	6	1	-3	-6	-4	-10	-11	-12	-15	-13	-10	-9	-4	0	1
8	9	3	-3	-7	-7	-12	-8	-11	-9	-14	-7	-8	-1	-1	-1
9	3	3	0	-1	-6	-8	-7	-7	-7	-14	-8	-6	-1	0	0
9	7	5	3	1	-2	-3	-3	-1	-11	-13	-8	-2	-2	0	2
12	10	7	1	0	-6	-5	-3	-5	-7	-6	-4	-1	2	6	6
14	13	8	5	0	0	-4	-1	-1	0	-3	-1	5	-1	13	11
16	14	9	8	7	1	0	1	0	0	1	4	6	8	16	26

FAINT IMAGES, 17 < MAG < 22

-5	-2	0	0	-1	-3	-2	-3	-1	-2	-4	-1	1	4	5	3
-1	-1	0	0	-1	-3	-4	-4	-2	-2	-4	-1	2	3	3	5
-2	-3	0	0	-2	-2	-1	-1	-4	-5	-5	-2	0	1	0	4
2	0	0	0	0	1	0	-2	-5	-4	-6	-4	-1	1	1	3
2	1	1	1	2	0	-1	-3	-3	-4	-6	-3	0	1	5	4
3	2	2	3	2	-2	-3	-2	-3	-2	-4	-3	3	3	7	4
1	0	-1	-1	0	-4	-4	-3	-1	-3	-5	-1	2	5	7	6
2	-3	-3	0	-1	-4	-5	-2	0	-2	-4	0	1	0	5	7
3	-1	-2	-2	0	-4	-3	-3	0	0	0	0	1	0	6	6
0	0	-1	-3	-3	-2	-4	-2	-3	0	-2	0	1	3	6	6
1	2	0	-2	-3	-3	-4	-4	-3	0	-5	-1	2	4	5	4
0	-1	1	-1	-2	-2	-4	-2	-2	-3	-5	-2	1	4	5	6
2	0	1	1	2	-2	0	-1	0	-3	-5	-3	1	4	6	8
1	2	0	-1	0	-2	-1	0	-1	-2	-2	0	1	4	8	7
2	2	1	0	0	-1	-2	0	0	1	0	1	4	1	8	5
3	2	2	1	1	0	-1	0	1	0	1	3	4	5	10	9

RESIDUALS FOR PLATE 12728 IN 0.01 MAGS

BRIGHT IMAGES, 12 < MAG < 17

0	-1	-4	-4	-3	0	1	2	2	3	3	0	3	5	4	4
-4	-5	-5	-2	0	1	2	2	1	3	5	4	2	4	4	4
-7	-10	-6	-3	-1	1	0	0	4	6	4	6	8	6	5	6
-14	-11	-6	-5	-2	2	0	0	3	3	5	6	6	4	4	4
-18	-15	-6	-3	-4	-3	0	1	1	2	4	5	5	4	2	3
-16	-13	-8	-4	-4	0	-1	0	2	2	6	4	6	6	5	9
-20	-15	-4	-4	-4	-2	0	2	2	3	6	5	5	7	5	4
-22	-17	-8	-4	-4	-1	0	0	0	2	5	4	6	5	3	2
-20	-16	-9	-2	0	-1	-1	0	0	5	3	3	5	3	2	6
-20	-18	-9	-5	-3	-2	-1	0	-1	1	1	1	2	3	2	4
-20	-18	-9	-6	-5	-4	-3	-3	-1	1	4	0	4	0	1	3
-18	-18	-11	-8	-6	-6	-3	-5	-3	-1	0	-1	0	-1	0	0
-16	-14	-12	-8	-7	-6	-6	-3	-4	-1	0	-3	-1	-1	-1	0
-15	-13	-10	-7	-4	-5	-5	-5	-4	-1	0	-1	0	5	4	0
-14	-14	-11	-8	-7	-8	-7	-9	-3	-3	-1	-2	3	12	10	1
-16	-14	-10	-10	-8	-8	-12	-10	-9	-6	-4	-2	3	11	10	0

FAINT IMAGES, 17 < MAG < 22

0	0	0	1	1	4	3	3	1	3	2	2	1	1	0	0
0	0	0	3	4	3	3	2	1	2	2	1	1	0	0	1
0	0	2	2	3	3	3	2	1	3	2	2	3	1	1	1
0	0	1	0	0	2	1	2	3	2	3	3	2	3	1	0
1	0	1	0	0	1	1	2	2	3	4	1	2	2	0	1
1	1	1	0	0	1	0	1	1	2	3	2	3	2	1	1
1	0	2	0	0	1	1	3	1	2	4	1	2	3	0	0
-1	0	2	0	0	0	1	2	0	2	4	1	2	3	1	0
-2	0	0	0	0	1	1	0	0	2	3	1	1	1	0	1
-1	0	0	0	0	0	0	0	0	2	2	1	1	1	0	0
-2	-1	0	0	0	-1	0	0	0	2	3	1	2	1	0	0
-3	-2	-1	0	-1	-1	0	0	0	2	2	0	0	0	0	-1
-5	-1	-3	-1	-3	-1	-2	-1	0	2	3	0	1	0	0	-1
-4	-2	-2	-1	-1	0	0	-1	-1	1	1	0	0	0	0	-1
-5	-4	-4	-2	-2	0	0	0	0	0	0	0	0	0	4	2	-2
-7	-6	-3	-4	-4	-2	-1	0	-1	0	1	0	0	3	1	-7

Figure 3.7: Magnitude deviations for individual plates from the mean magnitude of all the plates for a sample field (Field 50 R-band photometry) as a function of plate position. The residuals are given for a bright ($12 < R < 17$) and a faint ($17 < R < 22$) magnitude range.

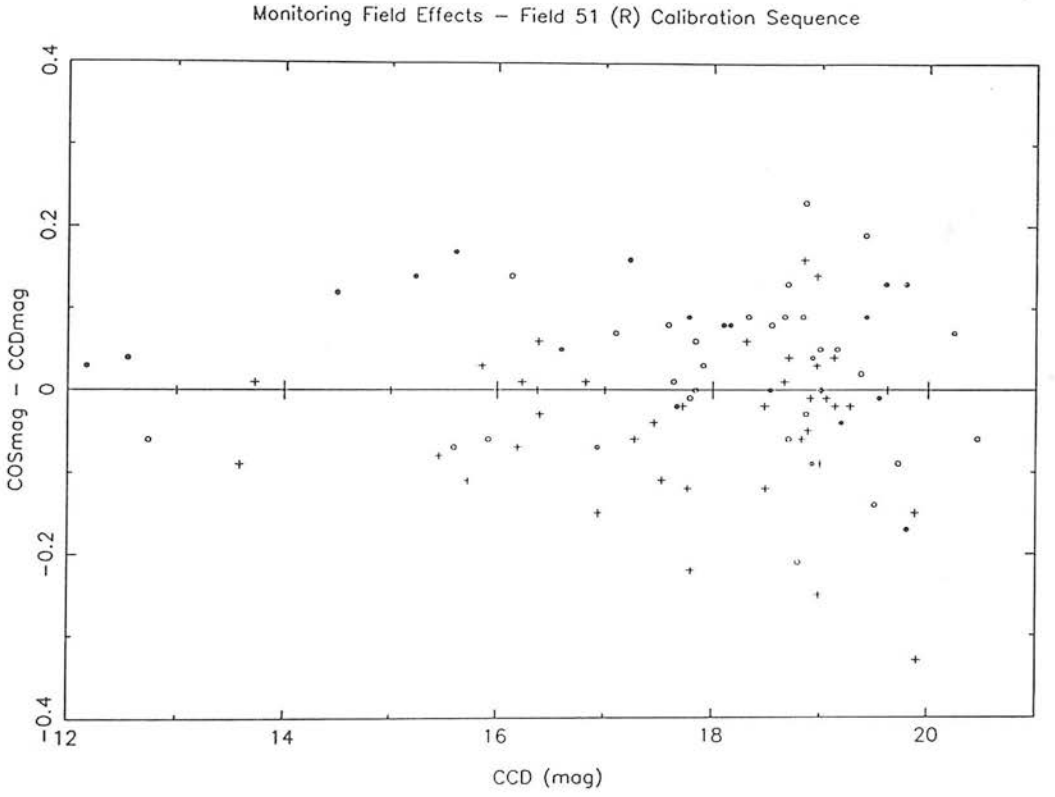

Figure 3.8: Plot of residuals between transformed COSMOS magnitudes and CCD magnitudes as a function of CCD magnitude for CCD sequence stars in Field 51 (R-band photometry). Sequence stars from three different locations in two corners and the centre of the field are shown by different symbols in order to monitor the presence of field effects which would give rise to systematic errors in the photometry.

Systematic errors in the photometry within a given field and between fields can best be monitored by comparing the photometry in the overlapping regions of neighbouring fields. Photometry comparisons were performed between all pairs of neighbouring fields, i.e. between Fields 30-52, 52-51, 50-51, 50-28, 29-28 and 30-29. Figs 3.9 (a,b) show the magnitude differences for paired stars in the aforementioned field overlaps for the B_J and R filters respectively. Figs 3.10 (a,b) likewise show the *mean* differences between the photometry in the field overlaps which essentially define the size of the systematic differences in the photometry between adjacent fields. In general, the mean differences between the photometry in overlapping fields are less than 0.2 mag and are generally smaller for fainter magnitudes than brighter magnitudes, reflecting the greater systematic magnitude residuals at bright magnitudes for individual plates discussed above. Thus, the probable value for the maximum systematic discrepancy between *any* two fields is 0.2 mag; however, the reported errors are upper limits for the errors in the central parts of the plates, due to larger systematic errors at the plate edges.

The size of these systematic discrepancies is fairly satisfactory for much of the scientific analysis in the following chapters. However, for the investigation of the structure of the SMC, where we use core-helium burning clump giants as distance indicators, a more accurate quantification of the size of systematic errors is essential. The clump stars in the SMC have luminosities generally around $R = 18.9$. From examination of Fig. 3.10 (b) at this magnitude, the maximum discrepancy between any two adjacent fields is 0.13 mag, which is the discrepancy for both 30-52 and 50-28. Therefore, we can make the more general conclusion that it is unlikely that the systematic discrepancy in the photometry between *any* two fields is greater than 0.13 mag. An estimate of the maximum systematic variation in the photometry at the magnitude level of the clump giants *within* a field may be obtained by considering the sum of the overlap differences for all six field overlaps. If the differences in the photometry between neighbouring fields were due entirely to the zeropoint differences in the photometric calibration of each field, this sum would be zero. The sum of these differences at the magnitude level of the HB/clump was found to be 0.08 mag. We can

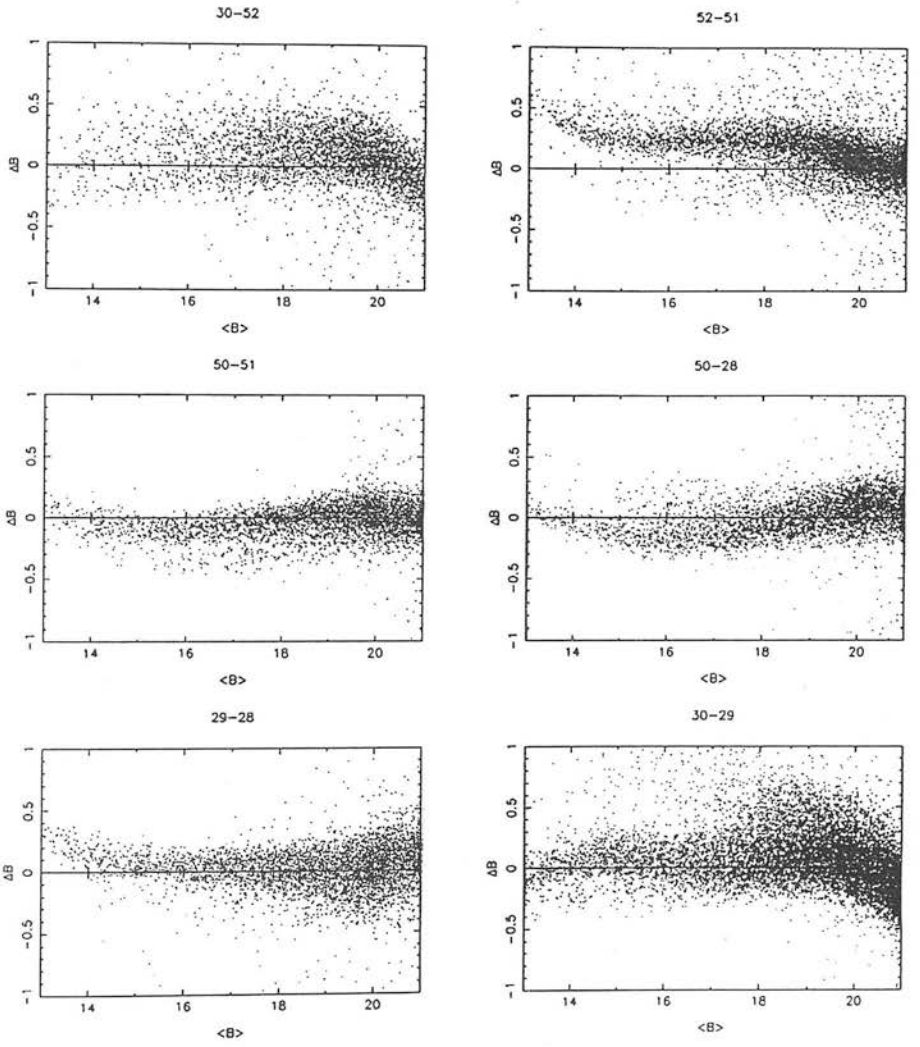

Figure 3.9: (a) Photometry comparisons in the overlap areas between the fields. The differences between photometry of individual images from different fields for the overlapping fields 30-52, 52-51, 50-51, 50-28, 29-28 and 30-29 are shown for the B_J waveband.

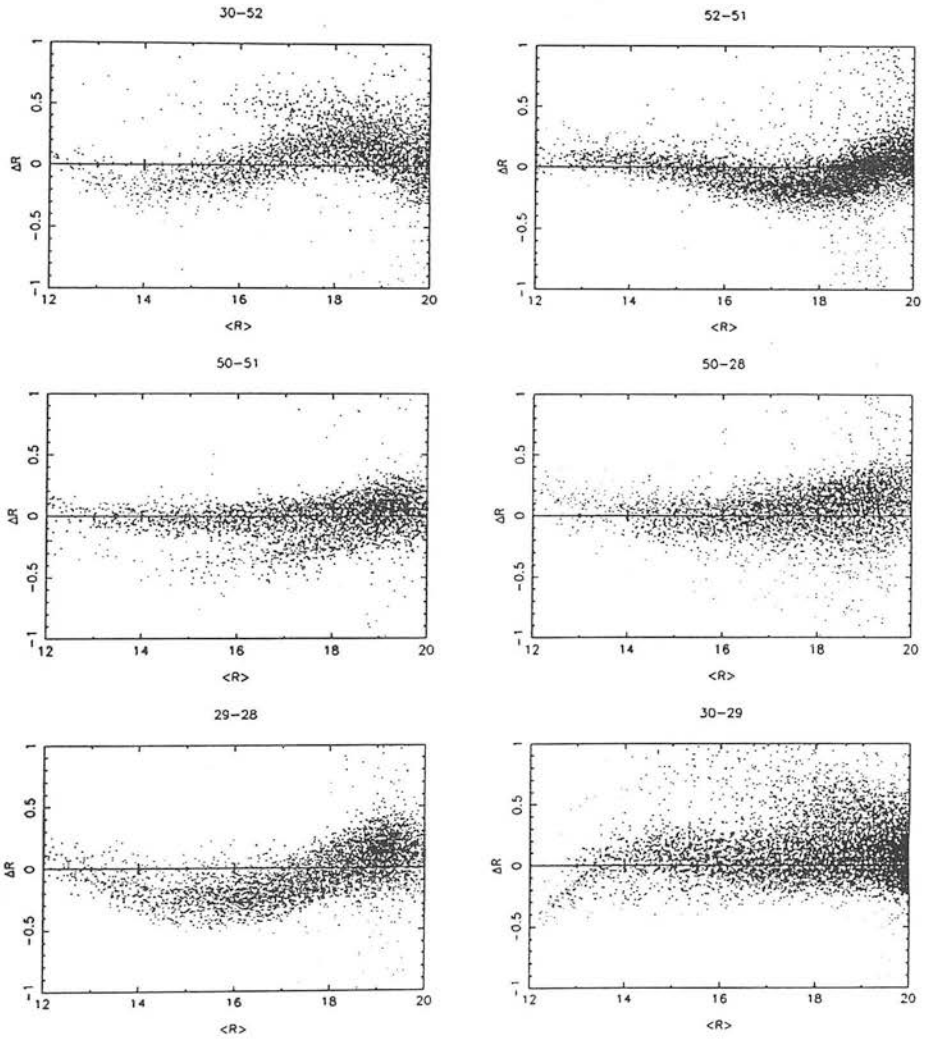

Figure 3.9: (b) The same as Fig. 3.9 (a) for the R waveband.

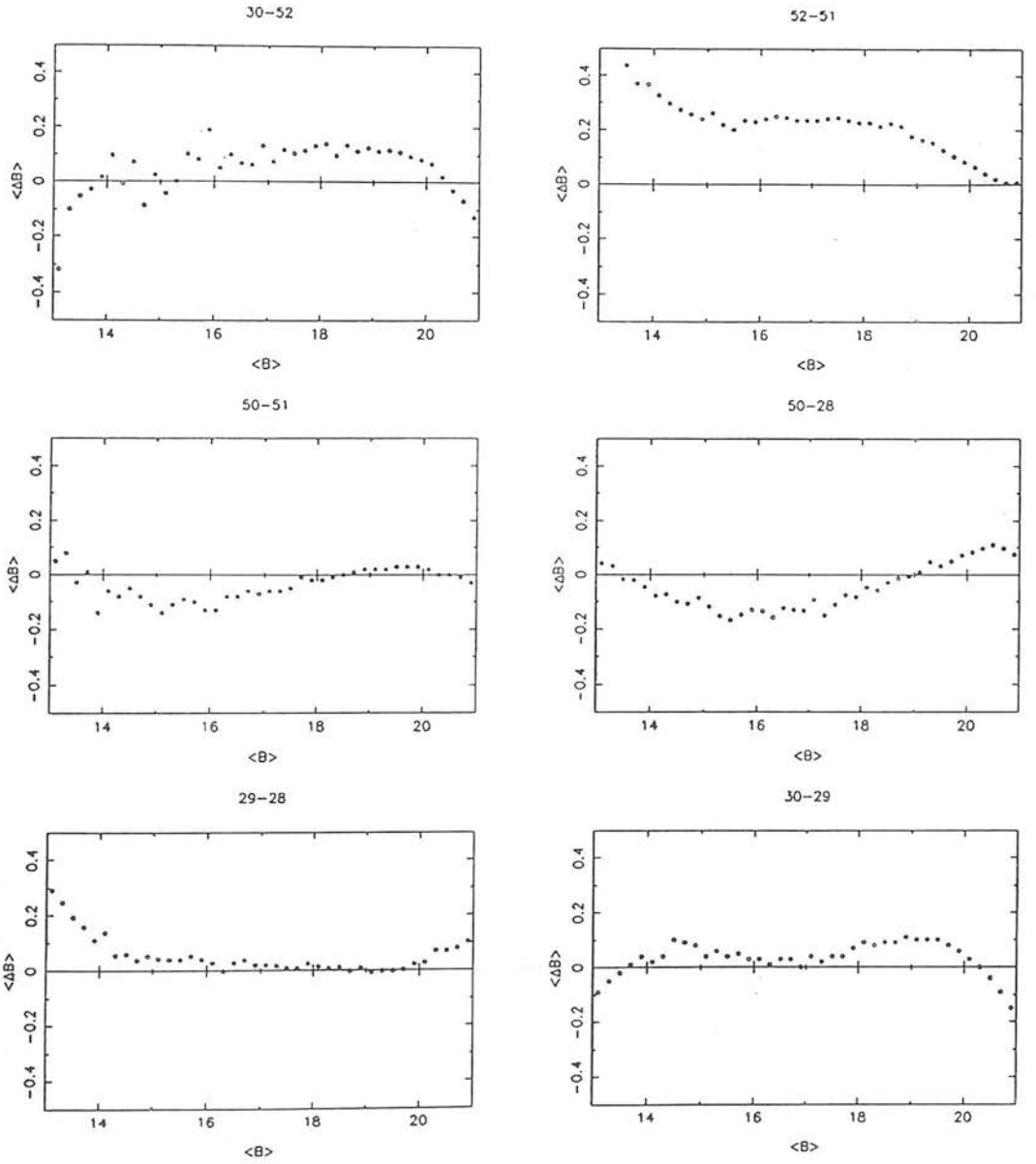

Figure 3.10: (a) Mean differences in the photometry between different fields in the overlap areas for the B_J waveband. The plots are based on data plotted in Fig. 3.9 (a).

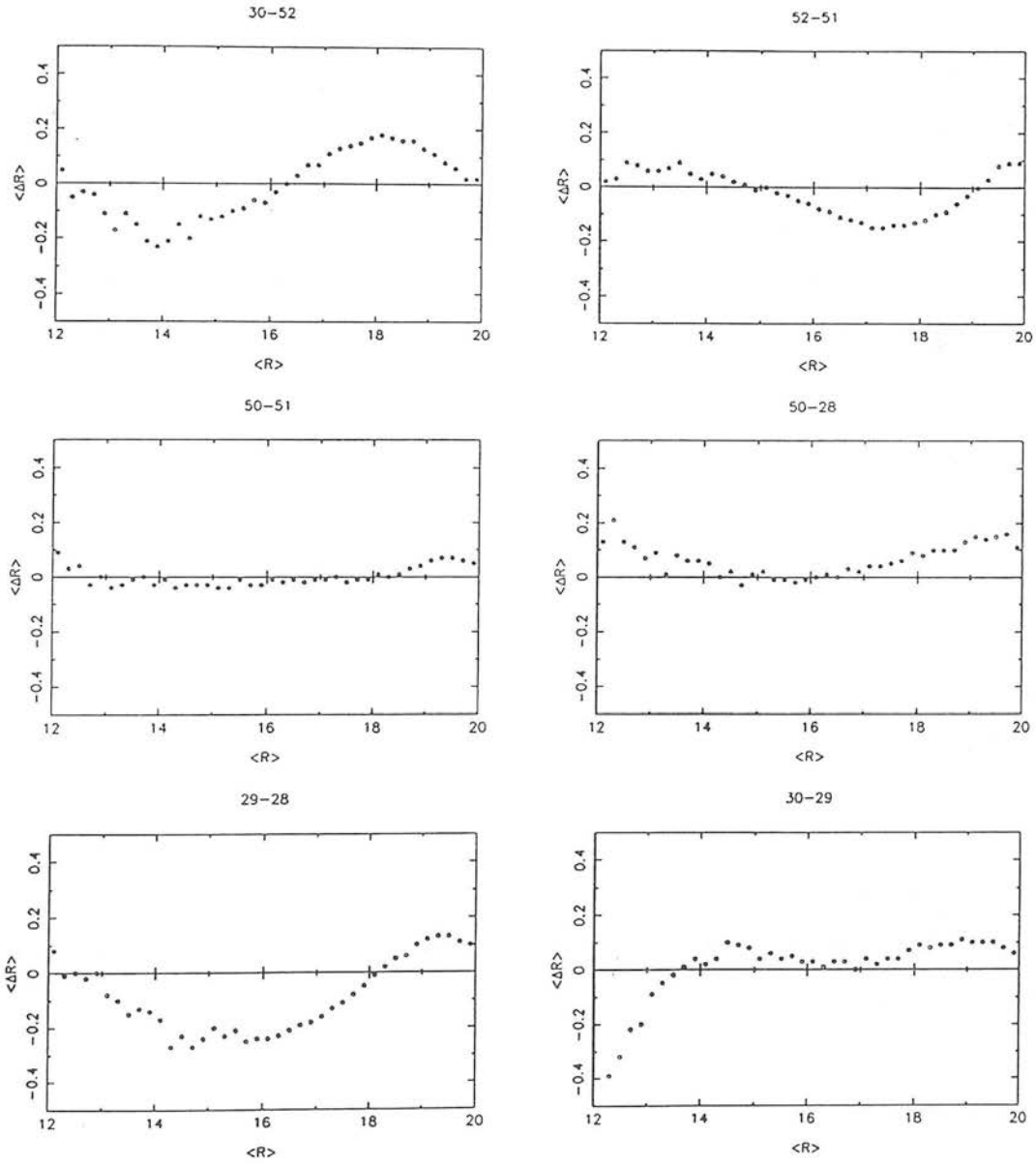

Figure 3.10: (b) The same as Fig. 3.10 (a) for the R waveband.

therefore conclude that this is the likely size of the maximum systematic photometric variation occurring within a single field at the magnitude level of the HB/clump.

To conclude the assessment of the accuracy of the data set we can say that the random photometric errors are below 0.10 mag for the whole range of magnitudes, while the size of the largest systematic errors between any two fields is 0.2 mag. However, for the magnitude regime in which the clump giants are found, these errors are probably less than 0.13 mag for the R-band photometry. In general, these errors do not pose great problems for the treatment of all six survey fields as a homogeneous data set; nevertheless care has been taken in the scientific analysis to take due account of photometric discrepancies between different fields.

2.4 The Completeness of the Data Set

Without external information on the numbers and magnitude distributions of images to be expected, an assessment of the completeness of the data set is a difficult undertaking. In H-thesis (pp.50-55), the completeness was mainly investigated by studying the efficiency of the pairing process, which, however, does not quantify very well the loss of images with increased crowding, and at best can only be a qualitative indicator of increasing incompleteness near the effective magnitude limit. The other method used was comparison with CCD sequence frames, but the small total number of images on a CCD frame (less than about 50 stars brighter than $R \sim 20$) does not allow a conclusive study to be conducted.

There are two aspects to the incompleteness problem which can be dealt with separately. The first is loss of images near the effective magnitude limit due to lower signal-to-noise levels and different limiting magnitude of each plate. The second is increasing incompleteness in crowded fields due to merging and non-matching of close pairs or groups of images. This is evidently a greater problem with increasing image density approaching the SMC centre.

(i) Incompleteness at Faint Magnitudes

Our approach to this problem is to study the percentage of stars detected on the master plate that are matched on all plates as a function of magnitude for a given filter/field combination. Evidently, the point at which the matching efficiency deteriorates indicates the magnitude at which the level of incompleteness becomes significant. In Figs 3.11 (a,b) we have plotted the percentage of stars identified on the master plate (usually the deepest plate in the plate set) not matched on all plates as a function of magnitude in each field for B_J and R. It can be seen from this figure that for magnitudes well above the effective magnitude limit the numbers of unmatched images are less than 10 per cent of the total, and that for a given filter/field combination the matching efficiency does not appear to vary significantly with magnitude. However, about half a magnitude above the magnitude limit the percentage of unmatched images begins to rapidly increase. For all fields, the percentage of unmatched images does not begin to rise until after $B_J = 20$, and at $B_J = 21$ most fields have a matching success rate of at least 80 per cent. For the analysis of the clump giants, a satisfactory level of completeness is required down to $B_J = 20.5$ and this condition is satisfied by all the fields. For the R-band data, significant incompleteness begins to occur fainter than $R = 19.5$ for some fields, which is satisfactory from the point of view of the analysis of clump giant stars. These results on the limiting magnitudes defined by the completeness will be taken into account in the scientific analysis in the following chapters.

(ii) Incompleteness in Crowded Fields

As the surface density of images increases, the proportion of overlapped images rises and the percentage of images detected and matched on all the plates in a given field is reduced. Results of tests on simulated data for both non-deblending and deblending software giving the percentages of images recovered as a function of image surface density may serve as a guide to the kind of incompleteness levels we can expect. These results are presented in by Beard, MacGillivray & Thanisch (1990) in their Fig. 5. This figure shows that for surface densities less than 2 objects arcmin^{-2}

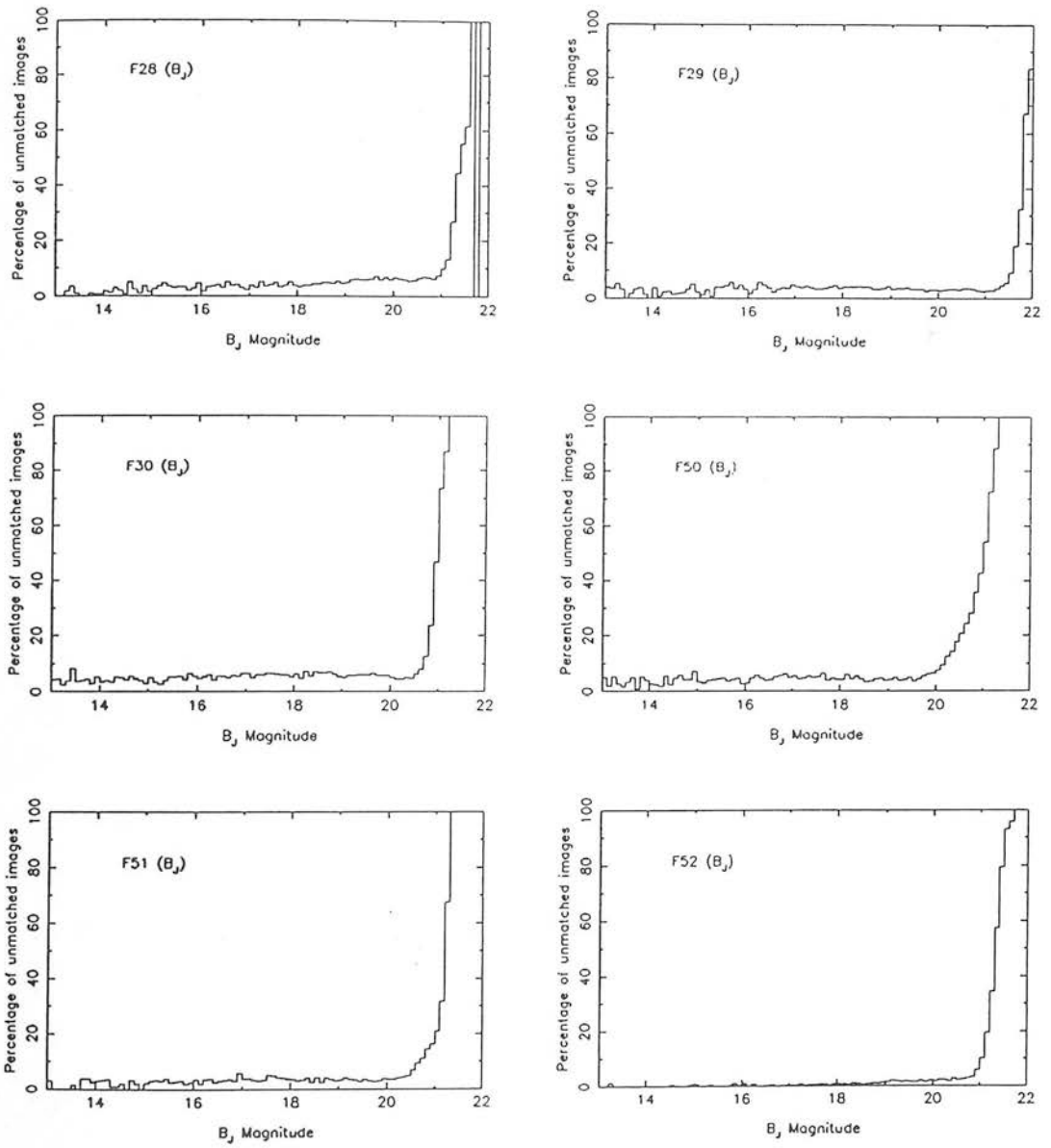

Figure 3.11: (a) Plots of the percentage of unmatched images with respect to the total number of master images as a function of B_J magnitude for each of the six project fields. The onset of significant incompleteness (loss of faint images) is indicated by a steep rise in the percentage of unmatched images.

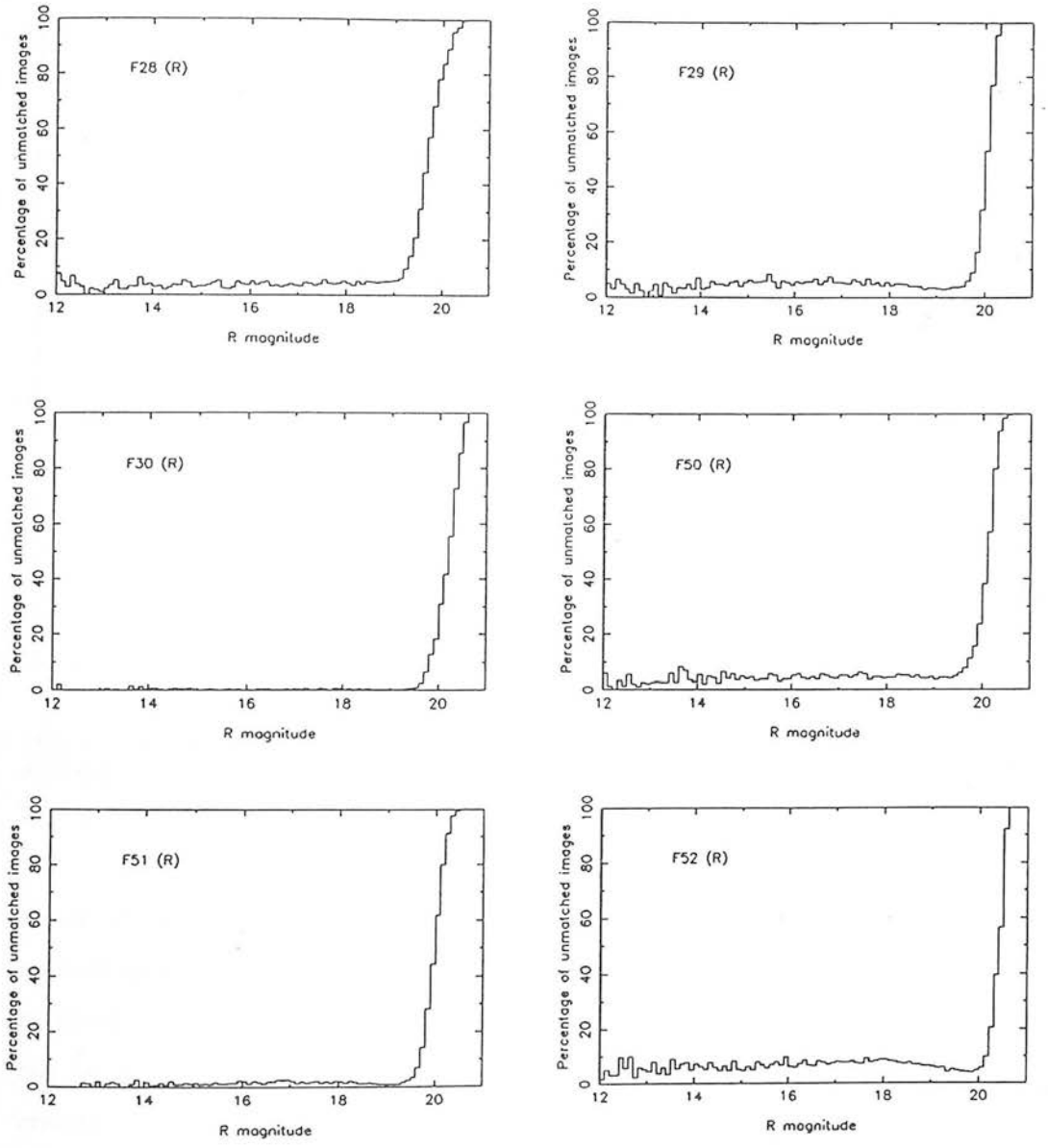

Figure 3.11: (b) The same as Fig. 3.11 (a) for the R waveband.

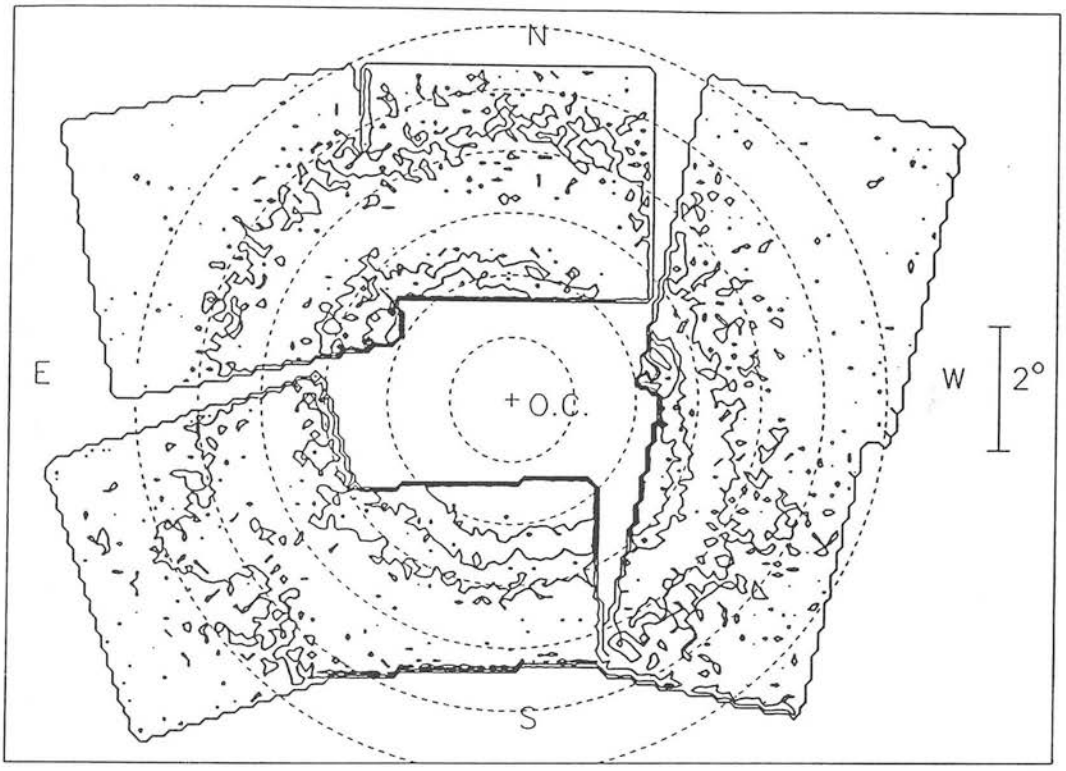

Figure 3.12: Contour plot of the surface density of images brighter than $R = 20$ using data from all six project fields. The contour levels increase towards the SMC optical centre (O.C.) and represent 1.6, 3.0, 4.0 and 6.0 images arcmin^{-2}.

about 95 per cent of the stars are detected by the non-deblending software. The percentage drops to about 90 per cent at about 3 objects arcmin^{-2} and 65 per cent at about 10 objects arcmin^{-2}. To examine the level of incompleteness expected for our database, in Fig. 3.12 we have plotted a surface contour map, using the database created from all six fields, of the number density of images brighter than $R = 20$. The counts were made in pixels 5 mm square and no smoothing has been applied. The contour level for 3 objects arcmin^{-2} encompasses a considerable area within 3° of the SMC centre, and within this region the incompleteness should be in excess of 10 per cent. The highest recorded image density outside a radius of 2° from the SMC centre is 6 images arcmin^{-2} corresponding to an incompleteness of around 20 per cent. However, our measured image densities are not total object densities and therefore

the level of incompleteness is somewhat larger as we will see below.

As a crude check on the levels of incompleteness, direct comparisons of the detected images with photographic prints were made in two areas in Field 51. Photographic enlargements ($\times 18$) of areas of size 5.8×4.5 arcmin on a B_J plate were made and a map of the images from the same area matched on all the plates in Field 51 was overlaid. Different magnitude ranges were indicated by different symbols on the overlaid map to allow an eye estimate of the magnitudes of undetected stellar images. The first area was located at a distance of 2.35° from the SMC optical centre and half a degree east of the foreground galactic globular cluster, NGC 362. The image density was 3.3 images arcmin^{-2}. Based on the numbers of stars which were not detected, the completeness was estimated to be about 80 per cent. The actual surface density of images was reckoned to be 4.1 objects per arcmin^2 taking into account the incompleteness and a comparison can be made with the estimated 90 per cent completeness from the Beard *et al.* tests for this object density. The second area investigated was located exactly 2° from the SMC centre near the densely populated northern 'outer arm' feature (see Brück 1980) and lay a third of a degree to the south-east of NGC 362 (the cluster itself does not extend into this area). The detected image density was 4.5 objects arcmin^{-2} and the field is visibly more crowded than the other area. The image counts indicated that the level of incompleteness is around 40 per cent. The corrected image density is then 7.5 objects arcmin^{-2}. The estimated incompleteness for this surface density is 25 per cent according to the Beard *et al.* (1990) tests. Larger values for the incompleteness are therefore suggested by our own test, which will be verified by one further means of checking the completeness to be presently described.

Surface counts of red foreground stars belonging to the galactic disk component (see Section 4), defined by the colour-magnitude limits $20 < R < 18$, $B - R > 2.2$, should be relatively invariant with respect to position in a given field if the data are complete. The actual counts obtained should therefore indicate the level of completeness assuming high levels of completeness in areas possessing low surface densities. The method is subject to real fluctuations in the number counts as well as systematic

photometric errors; however, the trend towards lower number counts for the disk population towards the SMC central regions with high image densities is apparent. These counts confirm the levels of incompleteness suggested by comparing the COSMOS data with photographic prints, and indicate less than 20 per cent incompleteness for object densities below 3 images arcmin^{-2} and about 40 per cent incompleteness in the densest regions.

An important aspect of the incompleteness problem is differential loss of images with magnitude. At first sight, in areas of high image density, a magnitude dependence in the incompleteness manifested as preferential loss of faint images would be expected for two reasons: (a) a faint image close to a bright one will make the bright one brighter together with the result of the non-detection of the faint image and (b) two faint images close to each other may result in a single image detection with a brighter magnitude. Inspection of photographic prints of the two sample areas mentioned above does not seem to indicate that this is a significant problem, since generally multiple objects tend to be removed from the data set altogether by the pairing procedure (random errors in the image centroids occur, or stars are merged on some plates and not on others). Multiple images are paired on all plates only in cases where the object centroids are located within a few arcseconds of each other, and such cases did not amount to more than a few per cent of the total number of images in the more crowded sample region of our completeness study. The numbers of multiple images lost completely do not appear to depend significantly on the magnitude; Penny & Dickens (1986) confirm that loss of images in crowded fields is evenly distributed with respect to magnitude. Therefore we conclude that the differential loss of faint images with respect to bright images is not very significant.

Overdense regions with high surface densities, typically greater than 10 images arcmin^{-2}, were either not scanned by COSMOS or excluded from the analysis. Such areas include the central regions of the SMC in Fields 51, 29 and 28, and regions near the galactic globular clusters 47 Tuc and NGC 362 which are not of interest for the project.

To conclude the discussion on completeness of the database, we can state that in regions of low image density (less than 2 objects arcmin^{-2}), the data are about 95 per cent complete down to $B_J = 20.5$ and $R = 19.5$. Based on tests involving visual examination of sample areas of photographic plates and separate tests using number counts of galactic disk component stars, it appears that greater than 20 per cent incompleteness occurs (at magnitudes considerably brighter than the faint magnitude limit) in much of the central 3° of the SMC area with image densities in excess of 3 objects arcmin^{-2}. The densest areas included in our study, lying within 2.5° of the SMC centre, probably have an incompleteness of around 40 per cent. Most of the studied area therefore possesses an incompleteness of less than 20 per cent and, on the whole, the level of incompleteness does not present undue difficulty for the scientific analysis. However, the absolute numbers of stellar counts must be treated with caution. Finally, there is no evidence that differential loss of faint images is significant.

3 Data Organisation and Analysis Methods

After application of the calibration processes described above, positional and colour-magnitude data for a total of 1.1 million images comprised the database for the study of the stellar populations in the outer parts of the SMC. This section describes the organisation of the data for the scientific analysis. The principal method adopted was division of the area of each field into grid regions allowing an array of colour-magnitude diagrams to be constructed upon which the study of the positional dependence of the line-of-sight structure and distribution of stellar populations could be based. The other main method involves the production of contour maps in order to gain an overview of the population distribution. Both these methods are described below. One more method, used mainly to study the main sequence luminosity functions (see Chapter 7) involves the use of circular grid regions centred on the SMC optical centre for each field.

(i) The Square Grid Regions

The majority of grid regions consist of squares of size 50×50 mm (0.93° × 0.93°, i.e. 0.87 deg^2), but the southernmost regions in Field 51 are half this size. Fig. 3.13 shows the division of the area of each field into square grid regions. The shaded areas indicate areas which were excluded from the analysis due to excessive crowding of stellar images. The central RA, DEC coordinates for those grid regions used for the study of the structure of the SMC are given in Chapter 4. Regarding the completeness of the data for the individual grid regions, counts of the foreground galactic disk component were used to determine estimates (see previous subsection). Four grid regions (F52:15; F28:31,41; F29:12), with grid centres lying within or near the contour level for 4 images arcmin^{-2} (Fig. 3.12), apparently possess a level of incompleteness greater than 30 per cent. Most of the remaining regions contain data which are more than 80 per cent complete.

(ii) Construction of Contour Maps

This method allows the detailed surface distribution of different types of stellar populations, e.g main sequence or clump giants, to be studied by means of number counts in small-sized pixels. Although levels of incompleteness in the database due to crowding become significant within the central 3° area of the SMC, the level of incompleteness appears to be a function of the surface density of stellar images only and does not vary from field to field as will be confirmed by the good matching between neighbouring fields in the contour plots produced for different stellar populations. The technique involves performing number counts using pixels of size 5 mm square (5.6 arcmin square) and subsequent transformation of the pixel positions to RA, DEC coordinates. The final pixel grid comprising data from all six project fields consists of 180 × 130 pixels. This array was smoothed with a Gaussian filter with $\sigma = 9.7$ arcmin before contouring.

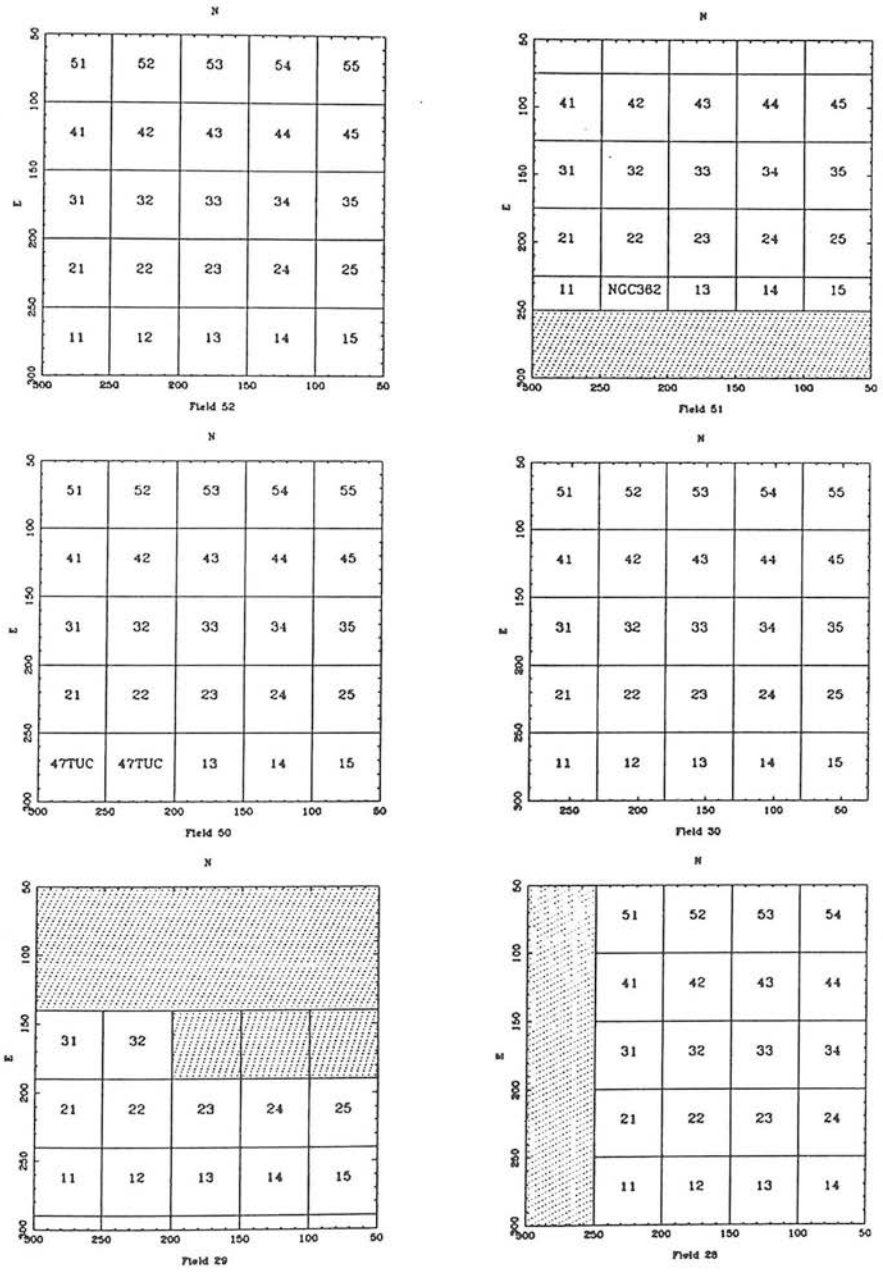

Figure 3.13: Division of the plate area of each field into grid regions measuring 50×50 mm or $0.93° \times 0.93°$ except for five half-sized regions in Field 51. The shaded areas in Fields 51, 29 and 28 were either not measured or not included in the analysis due to excessive crowding of stellar images. The orientation is north at the top and east to the left.

4 The Colour-Magnitude Diagrams

A colour-magnitude diagram (CMD) in R vs $B-R$ was constructed for each of the square grid regions shown in Fig. 3.13. In Appendix B the entire grid of CMDs for each field are presented in compact form, with all the CMDs for a single field produced on a single page. In Appendix C, we present, in a larger format, representative CMDs in each of the six project fields. In this section we discuss the main features of the colour-magnitude diagrams and review briefly the reddening and SMC distance modulus determinations adopted for the project in H-thesis (pp.75-81) which are relevant to the interpretation of the CMDs.

Fig. 3.14 shows an example of a CMD, Field 51:13, which we will use to discuss the main features of the CMD of the SMC field outer regions. Two isochrones are overlaid from the Revised Yale Isochrones of Green, Demarque & King (1987) both for $Z = 0.001$ and $Y = 0.2$, but with different ages of 200 Myr and 10 Gyr. Our purpose here is not to carry out a detailed age analysis but to employ these isochrones to illuminate certain features of the CMD of the SMC field. The main features of the CMD are labelled on the figure and comprise a main sequence comprising relatively young stars, a well-defined red giant branch, a densely populated red horizontal branch or clump and a subgiant branch. The two ridges of the galactic foreground population are also noticeable on the CMD: the 'red' and 'blue' ridges due respectively to the disk and spheroidal components of the Galaxy. We briefly discuss each of these features in turn.

(i) The Main Sequence

Main sequence populations are seen to extend from the effective magnitude limit to brighter luminosities at a constant colour of around $B-R=-0.1$. They consist of stars still burning hydrogen in their cores and except for the Wing region their numbers are seen to fade rapidly beyond about 3° from the SMC centre. The limiting ages of the main sequence populations that can be detected are defined by the effective magnitude limit, since the more massive stars of older stellar populations would

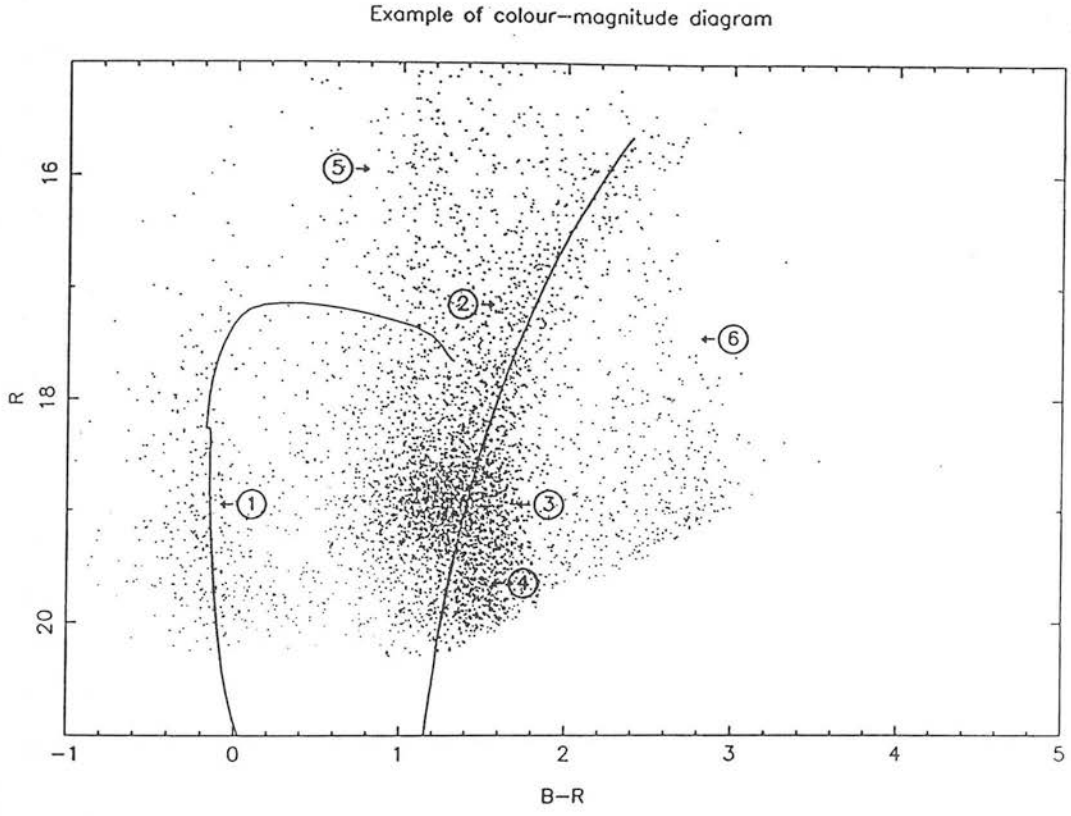

Figure 3.14: An example of a colour-magnitude diagram from Field 51 (Region 51:13) showing the various stellar populations. (1) Main Sequence. (2) Red Giant Branch. (3) HB/Clump. (4) Subgiant Branch. (5) Galactic Foreground — 'blue ridge'. (6) Galactic Foreground — 'red ridge'. Isochrones for 200 Myr (to the left) and 10 Gyr (to the right) for Z=0.001, Y=0.2 with SMC distance modulus = 18.8, $E_{B-R} = 0.045$ and $A_R = 0.07$ are superimposed.

have already evolved off the main sequence. From consideration of the Revised Yale Isochrones for metallicities appropriate for the SMC, the upper age limit for main sequence populations to be detected above the effective magnitude limit at $R = 20$ is about 2 Gyr. The isochrone shown in the CMD example is for 200 Myr and is seen to agree fairly well with the observed main sequence locus. The main sequence surface distributions and luminosity functions, to be analysed in Chapter 7, enable a comprehensive study of relatively young stellar populations in the SMC field to be undertaken.

(ii) The Red Giant Branch (RGB)

The first ascent giant branch consists of evolved stars burning hydrogen in a shell surrounding an inert helium core. The first ascent giant branch extends from the base of the HB/clump feature at about $R = 19, B-R = 1.4$ upwards and redwards to luminosities of $R \sim 16$ and $B - R$ colours of around 2.5. The second ascent giant branch, comprising double shell-burning stars which have completed the horizontal branch phase of their evolution, forms a bright and red extension of the red giant branch and may be identified with the asymptotic giant branch as described by Aaronsen & Mould (1982).

Stars possessing a wide range of ages up to to the ages of galactic globular clusters may evolve onto the red giant branch after evolving off the main sequence. Evolutionary tracks of the red giant phase (e.g. the Revised Yale Isochrones) indicate that RGB morphology is mainly dependent on metallicity. Metal poor globular clusters, and Magellanic Cloud clusters are known to have tall, almost vertical giant branches, while galactic open clusters and metal rich globular clusters have fainter, sloping giant branches. The 10 Gyr isochrone for Z=0.001 is seen to agree very well with the shape of the RGB in the figure. This metal abundance corresponds to [Fe/H]= -1.3 given a solar abundance of Z=0.02, and is similar to the metallicities obtained for several outlying SMC clusters from metallicity indicators derived from CCD photometry (see Table 1.1 for references).

(iii) The Horizontal Branch/Clump

The HB/clump is the most conspicuous feature of the CMDs in areas with significant numbers of SMC stars. It is located at around $R = 19, B - R = 1.3$ and has a considerable range in luminosity due to intrinsic luminosity scatter arising from evolutionary effects as well as geometrical factors. The clump consists of core-helium burning stars which are the more massive equivalents of the horizontal branch stars found in galactic globular clusters. Clump stars possess a wide range of ages from a few 10^8 yr up to about 10 Gyr where theoretical models indicate a transition to horizontal morphology. Empirical evidence (see Cannon 1970, Mateo & Hodge 1985) indicates that the luminosity of the HB/clump is fairly constant with age. This can be understood theoretically (see Faulkner & Iben 1966) by considering that the helium core behaves as an independent star of fixed mass determined by the critical mass at which helium burning is ignited in an electron-degenerate core. The clump feature is considered in more detail with respect to evolutionary model predictions in the following chapter.

(iv) The Subgiant Branch

A subgiant branch is seen on the CMDs populated by SMC stars extending below the HB/clump at a roughly constant colour of $B-R = 1.6$. Owing to the deteriorating level of completeness fainter than $R = 19.5$ the properties of the subgiant branch are not used very much in the scientific analysis in the following chapters. According to Hardy *et al.* (1984), the subgiant branch begins to be populated at an age of around 3-4 Gyr. This fact was used in that paper and also by Hodge (1987b) to argue that the bulk of the stellar population in the LMC field is aged less than 3-4 Gyr based on the apparently small numbers of subgiant stars in the observed CMDs. The comparative strength of the subgiant branch in the SMC field is evident from our CMDs and also from the CMDs near the SMC Wing region produced by Hardy & Durand (1984). This is an indication of an older age profile for SMC field populations compared to the LMC field populations and confirms the existence of significant SMC populations with a minimum age of 3 Gyr.

(v) The Contribution from the Galactic Foreground and Background Galaxies

In the outermost regions beyond about 7° from the SMC centre the CMDs do not appear to have any trace of populations belonging to the SMC. The CMDs in these regions can be considered to consist purely of galactic foreground objects and background galaxies. In H-thesis (pp.41-44), a study of the completeness of the database at low image densities was carried out by comparing the numbers of objects in these outermost CMDs with the predictions of counts from galactic structure models (Ratnatunga & Bahcall 1985) and galaxy count studies (Jarvis & Tyson 1981; Shanks *et al.* 1984). Good agreement of the actual counts was found with the predicted figure of 4200 objects $\deg^{-2}$ (3100 stars and 1100 galaxies) down to a limiting magnitude of $B = 21.2$. According to previous starcount studies, reviewed by Yamagata & Yoshii (1991), the various components of the Galaxy (thin-disk, thick-disk and spheroid) can be separated on the basis of their observed colours. Thin-disk stars dominate at bright magnitudes but fainter than about $R = 17$ the colour distribution splits into two pronounced peaks — the red peak consisting of thin-disk stars and the blue peak consisting of both thick-disk and spheroid component stars. The blue peak can be seen in our CMDs at $B - R \sim 1.0$ and the red peak at $B - R \sim 2.6$.

The technique of foreground/background subtraction to construct 'pure' SMC CMDs was used in H-thesis (pp.69-73) but will not be applied to the remainder of this project. In most cases, direct statistical subtraction of the estimated foreground/background contribution was sufficient. In general, it was found that systematic errors in the photometry and differential completeness between the outermost and inner CMDs made it difficult to construct 'clean' subtracted CMDs for all the project fields, some of which did not have any CMDs without a contribution from the SMC field.

Finally, we discuss the reddening and distance modulus scales which will be adopted in the scientific analysis and which were used to apply the isochrones in Fig. 3.14 to the case of the SMC outer regions.

(i) Reddening

Extinction and reddening in the outer regions of the SMC is extensively discussed in H-thesis (p.77-81), where a compilation of reddening determinations towards the SMC is listed. There are no direct reddening determinations towards the *outlying* regions of the SMC which would be of relevance to our study. However, even for the inner regions the colour excess is quite small, determined to be $E_{B-V} = 0.054$ on the basis of BVI reddenings (Caldwell & Coulson 1985). Following H-thesis (p.80) we adopt a colour excess, $E_{B-R} = 0.045$, and extinction, $A_R = 0.07$, for the outer regions of the SMC possessing very low H I surface densities and therefore little reddening intrinsic to the SMC. These parameters were used for the isochrones in Fig. 3.14. Areas of the SMC Wing region possessing higher H I densities may have a slightly higher reddening. The above-quoted result on the BVI reddenings applies to the Wing region, giving an extinction, $A_R = 0.13$. Given the various uncertainties in the distance modulus and the photometry, the difference between the reddenings of the Wing region and the other outer regions is not significant.

(ii) The SMC Distance Modulus

An extensive discussion of the distance moduli for the Magellanic Clouds is presented in H-thesis (pp.75-77), which reviewed evidence for two different distance modulus scales, a short (dm= 18.8 for the SMC) and a long (19.3) scale. The short distance modulus scale for the Magellanic Clouds has come to be favoured recently based on isochrone fits to well-studied deep CCD colour-magnitude diagrams and theoretical predictions of the luminosities of clump giants (see Seidel, Da Costa & Demarque 1987) and has been adopted for this project.

PART II: *THE 3D STRUCTURE*

CHAPTER

— 4 —

THE HB/CLUMP AND THE GEOMETRY OF THE SMC

1 Introduction

The present state of our knowledge of the geometry of the SMC was discussed in a recent review of studies of the structure of the Magellanic Clouds by Feast (1989). The complex geometry of the central SMC area is evident from various studies employing young stellar objects such as red and blue supergiants and Cepheid variables. The geometry of the SMC has defied a simple analysis, unlike the LMC, for which a thin disk model has yielded fruitful explanations of its large-scale structure. Taken together

with kinematical information, these studies led to extensive debate on the extent of the influence of dynamical interactions with the LMC and the Galaxy with which the SMC forms a triple interacting system. The SMC has been influenced to a greater extent by the gravitational forces due to its more massive neighbours; the SMC Wing, H I Bridge and Magellanic Stream providing evidence of a turbulent history as a result of a series of intergalactic encounters.

Much controversy has accompanied determinations of the line-of-sight depth of the SMC central regions (including the Bar and Arms), and different authors have obtained conflicting results. The debate has centred on whether the dimensions of the SMC exceed its tidal radius and whether indeed the SMC is breaking up into separate fragments. The tidal diameter itself is uncertain; estimates range from 8 to 19 kpc (Welch *et al.* 1987), depending on the adopted value of the mass of the Galaxy. The very large depths, well in excess of the upper estimate of the tidal diameter, reported by Mathewson, Ford & Visvanathan (1986) from Cepheid observations have been challenged by other workers (e.g. Caldwell & Coulson 1986, Laney & Stobie 1986 and Welch *et al.* 1987), also using Cepheids. Studies of the kinematics of gas and young objects have led to the suggestion by Mathewson & Ford (1984) that the SMC is disintegrating into two fragments, but as yet no clear picture has emerged of a correlation between distance and velocity to lend conclusive support to the hypothesis.

This work attempts to resolve outstanding questions concerning the present structure and future state of the SMC by extending the area of study to the field populations clear of the central area. In this chapter, most of the outer area beyond 2° in projection from the SMC centre has been systematically investigated using the properties of the luminosity distribution of HB/clump stars. We focus here on the techniques used to investigate the structure of the SMC and on the geometry indicated by the observational results, leaving a discussion of the implications of the observed structure for understanding the interactions of the Milky Way-Magellanic System until Chapter 6. In Section 2 the morphology of the HB/clump populations which provide a distance indicator in the SMC outer regions is discussed. Section 3 describes the methodology

employed to determine the structural indicators used for the study of the 3 dimensional geometry. Sections 4 and 5 present the results on the 2D and 3D structure yielded by the application of these methods. Finally Section 6 presents a geometrical interpretation of the complex structure of the SMC revealed by the observational results.

2 HB/Clump Morphology

According to the discussion in the previous chapter, SMC stars belonging to the red horizontal branch/clump (hereafter simply referred to as clump stars) are core-helium burning stars with ages between a few 10^8 yr and 10 Gyr. We make extensive use of the properties of the clump in what follows. As discussed fully in H-thesis (pp.124-127), observational work and theoretical results derived from the stellar evolutionary tracks of Seidel, Demarque & Weinberg (1987) (SDW) indicate that the mean luminosity of the clump is largely independent of age or metallicity for the stellar populations in question. Seidel, Da Costa & Demarque (1987) (SDD) examined the application of these models to the colour-magnitude diagrams of Magellanic Cloud clusters and converted the theoretical quantities M_{bol}, T_{eff} produced by the SDW models into the observational $R, B-R$ plane. Evolutionary tracks reproduced in the observational plane by SDD with Z=0.001 show a progressive brightening of the mean clump magnitude by a total of about 0.2 mag with increasing mass from 0.74 to 1.00 $M_{\odot}$. However, with the exception of the old cluster NGC 121 with an age of 11 ± 2 Gyr, they showed that all the clusters in their study, which range in age from 1 to 8 Gyr, have clump stars with masses between 0.8 and 0.9 $M_{\odot}$. The narrow range in clump mass can be accounted for by large mass loss (about 0.5-0.6 $M_{\odot}$) on the red giant branch for the clusters younger than 2 Gyr and smaller mass loss (about 0.15 $M_{\odot}$) for older clusters, an explanation which the authors point out also explains the discrepancy between cluster ages and the observed asymptotic giant branch tip luminosities of several clusters (see Mould & Aaronsen 1985). It is therefore likely that the mean clump magnitude for the dominant intermediate aged populations of the SMC does not vary by more

than 0.1 mag which is the difference predicted by the SDW models for masses between 0.8 and 0.9 $M_{\odot}$. SDD did not extensively discuss the effect of metallicity variations on the predicted clump luminosities since the SDW models were evaluated only for Z=0.001 and 0.01, of which only the former is appropriate for the SMC, and in any case the metallicity spread in the cluster sample was not very significant.

The relatively broad range in luminosities of the clump feature, which gives it its name and distinguishes it from the 'flat' horizontal branch of old galactic globular clusters, is due to evolution of clump stars from their zero-age horizontal branch locations. Since our depth determinations depend on the evaluation of the spread in luminosity of the clump stars it is vital to know how much of this spread is due to this intrinsic luminosity dispersion. This question was examined in detail in H-thesis (pp.126-127) from the point of view of the theoretical models, with the conclusion that the clump size for a coeval population is smaller than 0.6 mag and does not vary significantly with metallicity or age except in the neighbourhood of 10 Gyr where there is an indication of transition to a horizontal morphology. Examination of the evolutionary tracks produced in the observational $R, B-R$ plane by SDD indicates that the length of the tracks is about 0.4 mag, but that the clump stars spend most of their HB lifetime in a luminosity range only about 0.15 mag wide. Study of the colour-magnitude diagram of the SMC cluster Kron 3 (GC3), whose clump feature is well populated, indicates that the dispersion (1σ) of clump magnitudes for a coeval, chemically homogeneous population is about 0.1 mag, which compares well with the length of the theoretical HB track, 0.4 mag, if this length is equivalent to the 4σ clump dispersion. The existence of an extra cosmic scatter in the clump luminosities of a mixture of non-coeval populations in the SMC general field is very likely, but as mentioned earlier the change in the mean clump magnitude, which will also affect the overall clump size, due mainly to age variations is probably not much greater than 0.1 mag. Therefore, we expect an intrinsic clump size (2σ) somewhere between 0.2 and 0.4 mag, depending on the extra scatter due to the presence of non-coeval populations. In the following section we will derive a value for an intrinsic clump size which falls near 0.4 mag, and thus our geometrical depth determinations will produce conservatively

small lower limits.

3 Determination of the Structural Indicators

After application of the calibration process described in Part I, positional and colour-magnitude data for 1.1 million images in six survey fields comprised the database for the study of the 3D structure of the outlying regions of the SMC. This database could be used to produce surface number counts for the study of the 2D appearance of the SMC seen in projection using the method described in Chapter 2 (Section 3). To obtain information on the depth and distance of the stellar population, i.e. the third dimension, the investigative methods are more complex and are discussed in detail in this section.

To investigate the 3D properties of the stellar population the 0.87 deg^2 grid regions described in the previous chapter were used. The fundamental structural indicators for each grid region can be derived from the mean clump magnitude, yielding the mean distance modulus, and the size (scatter in luminosity) of the HB/clump feature, which yields an estimate of the depth along the line-of-sight direction. Improvements have been made to the methods used in H-thesis (described in pp.183-186) for evaluating these structural indicators and the revised method is described below.

Firstly, the mean distance modulus evaluated for each region is given by

$$\overline{(m-M)}_o = \overline{R}_{clump} - M_{R,clump} - A_R \qquad (1)$$

where A_R is the reddening correction ($A_R = 0.07$ — Chapter 3), and $M_{R,clump} = 0.05$ mag given the mean clump magnitude for well studied SMC clusters, $\overline{R} = 18.92 \pm 0.04$ (Olszewski, Schommer & Aaronson 1987) and using the short distance modulus for the SMC, $(m-M)_o = 18.8$.

Secondly, the thickness along the line-of-sight is derived from the luminosity distribution of the clump stars. The observed number-magnitude relation for the clump

stars is a convolution of that due to the geometrical distribution of distance moduli, the photometric error distribution and the number-magnitude relation associated with the intrinsic size of the clump feature.

We may assume that the magnitudes of a group of clump stars having zero effective depth are normally distributed. This seems reasonable as the number-magnitude profile for clump stars for areas where the clump appears most narrow is well fitted by a Gaussian profile. Although we will also assume a normal distribution for the distribution of distance moduli along the line-of-sight, this may not necessarily be true. Since the observed number-magnitude relations essentially have a central peak with wings on either side, we are justified in assuming the normal distribution as an approximation. This question of course is related to the problem of what we mean by the depth along the line-of-sight. The determination of a Gaussian width gives us a measure of the depth in which the bulk of the stellar population is contained and allows a meaningful comparison between results from different regions. The number-magnitude histogram, in itself, is worth looking at and this approach will also be adopted in the discussion of the observed structure of the SMC.

Given that the distributions of each of the contributions to the convolution are Gaussian, the thickness along the line-of-sight is obtained by applying

$$\sigma_{geo}^2 = \sigma_{total}^2 - (\sigma_{int}^2 + \sigma_{err}^2) \tag{2}$$

where the quantity σ represents a dispersion measure equivalent to the deviation from the mean within which 68.3 per cent of the data points lie and we define 'size' as twice this quantity. Specifically, σ_{geo} is the contribution to the overall luminosity dispersion, σ_{total}, due to the dispersion in line-of-sight distance moduli, while σ_{int} is the intrinsic luminosity scatter for a collection of stars possessing zero line-of-sight depth, and σ_{err} represents the associated random errors in the photometry ($\sigma_{err} = 0.06 \sim 0.10$mag. as shown in Section 2).

An estimate of the geometric line-of-sight distance spread can thus be gained after converting the quantity $2\sigma_{geo}$ into a physical depth. The depth thus obtained is not the

total range of distance along the line-of-sight of all the stars but represents the depth over which the bulk of the SMC population may be found. Feast (1989) considers $4\sigma_{geo}$ to be a good estimate of the full range of distance moduli; however, we will generally use the 2σ depth as the robust structural indicator.

The number-magnitude relation obtained from the colour-magnitude data consists not only of the contribution of the clump stars but also of that due to the galactic foreground population as well as stars belonging to the red giant branch and subgiant branch extension. None of these populations can be separated from true clump stars on the basis of their colours and magnitudes. Hence in determining the true size of the clump of red HB stars we have adopted the technique of fitting a Gaussian function to the number-magnitude relation (with 0.1 mag bin size) for stars in the magnitude range $18.0 < R < 20.0$, and colour range $0.6 < B - R < 1.8$, by minimising χ^2 for four free parameters. The number-magnitude relation of the galactic foreground contribution was calculated by averaging data from four grid regions located beyond the outer contour of the SMC and represents a fixed offset which was subtracted from the total number-magnitude relation before performing the fit. Since the number-magnitude relation for the galactic foreground contribution can be expected to change with galactic longitude and latitude, and also since the level of completeness at magnitudes fainter than $R = 19.5$ varies from field to field, in most cases a separate 'background' number-magnitude relation was derived for each field. This was done for each of Fields 28, 30, 50 and 52, but in Fields 29 and 51 where a pure 'background' number-magnitude relation could not be derived because of the presence of SMC stars out to the edges of the fields, the 'background' number-magnitude relation from Field 50 was used. Fig. 4.1 shows the 'background' number-magnitude relations derived from Fields 28, 30, 50 and 52.

The errors used in the minimisation are derived from the Poissonian errors of the number counts with an additional contribution, also assumed Poissonian, from the foreground/background subtraction process. The fitted curve is of the form

$$N = Hexp(-(x - x_c)^2/2\sigma^2) + B. \qquad (3)$$

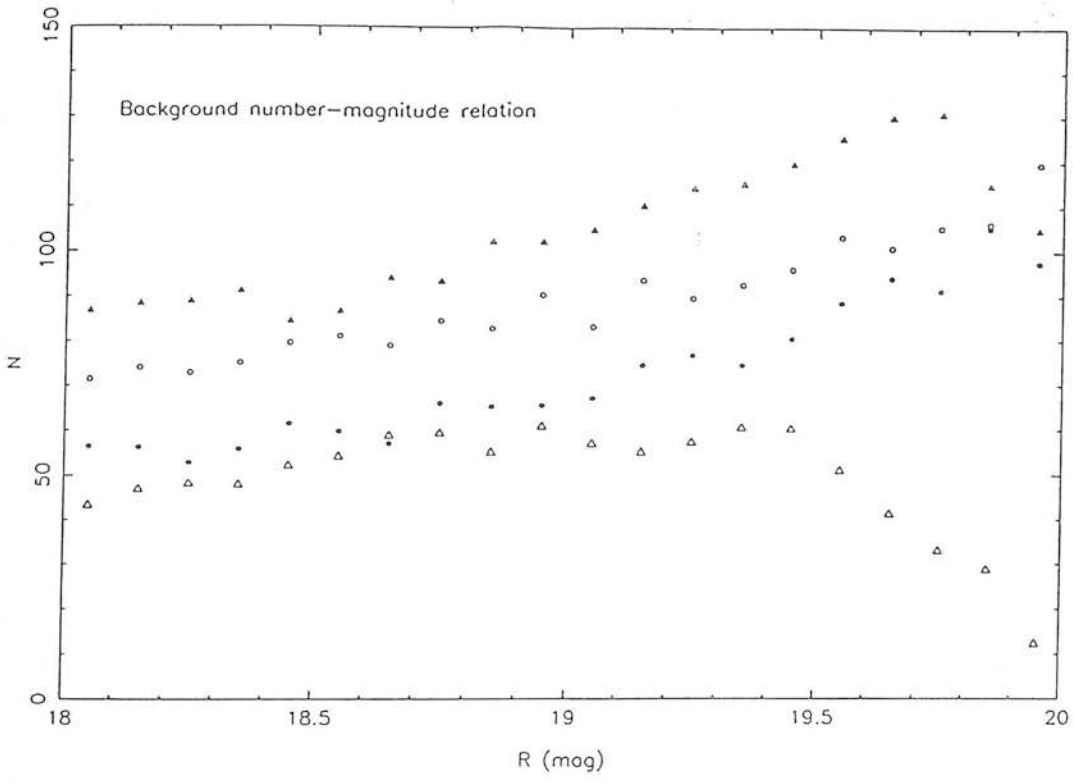

Figure 4.1: 'Background' (i.e. galactic foreground and background galaxies) number-magnitude relations (with arbitrary offsets) for the region of the CMD populated by clump stars. The relations were constructed by averaging data within colour limits $0.6 < R < 1.8$ from four grid regions in each field with apparently no SMC contribution. The symbols represent: Field 30 — filled triangle, Field 52 — open circle, Field 50 — filled circle, Field 28 — open triangle. The falloff in counts fainter than $R = 19.5$ for the Field 28 relation is due to increasing incompleteness near the effective magnitude limit.

The parameters for the fit are the height of the Gaussian function, H, the Gaussian dispersion (σ_{total} as defined above), the magnitude of the centre of the Gaussian, x_c, and the background offset, B. The parameter B is basically the correction for the red giant branch contamination, where the fixed offset implies that the giant branch luminosity function is assumed to be flat. The parameter x_c is actually the best estimate of the mean clump magnitude, $\overline{R}_{clump}$, since this quantity is corrected for the effects of red giant branch contamination. Fig. 4.2 shows the fit to the number-magnitude relation for two regions in Field 51 with a 'broad' and a 'narrow' clump feature.

The quantities x_c (i.e. $\overline{R}_{clump}$) and σ_{total} are used in eqns (1) and (2) respectively to derive the mean distance modulus and depth for each grid region. Estimates of the standard errors for $\overline{R}_{clump}$ and σ_{total} can be obtained from the properties of the χ^2 function in four-parameter space. The statistical method described by Avni (1976) has been used to determine the 68.3 per cent confidence limits for x_c and σ_{total}, providing results which are equivalent to the standard error. These standard errors are generally small ($\leq$ 0.03mag.) for the mean clump magnitude given by x_c. The standard error for the clump dispersion represents the total contribution of errors from the fore/background statistical subtraction, Poisson noise statistics and the assumption of a Gaussian profile for the clump number-magnitude relation.

To determine the geometrical spread of the distance moduli we need to have an estimate of the intrinsic luminosity dispersion of the clump, σ_{int}, (i.e. for a group of stars of zero effective depth). Earlier we mentioned that the value of σ_{int} for a coeval, chemically homogeneous population may be as small as 0.1 mag, but the figure for a non-coeval mixture may be up to 0.1 mag larger in size. Our approach to the determination of σ_{int} appropriate for the field populations in the SMC is based on the following. We require an area with an independently determined value for σ_{geo} for which we can provide a corresponding estimate of σ_{total}, and we use the study of Graham (1975) for this purpose. He studied SMC RR-Lyrae stars in a $1° \times 1.3°$ area which also contained the foreground galactic globular cluster 47 Tuc and the SMC

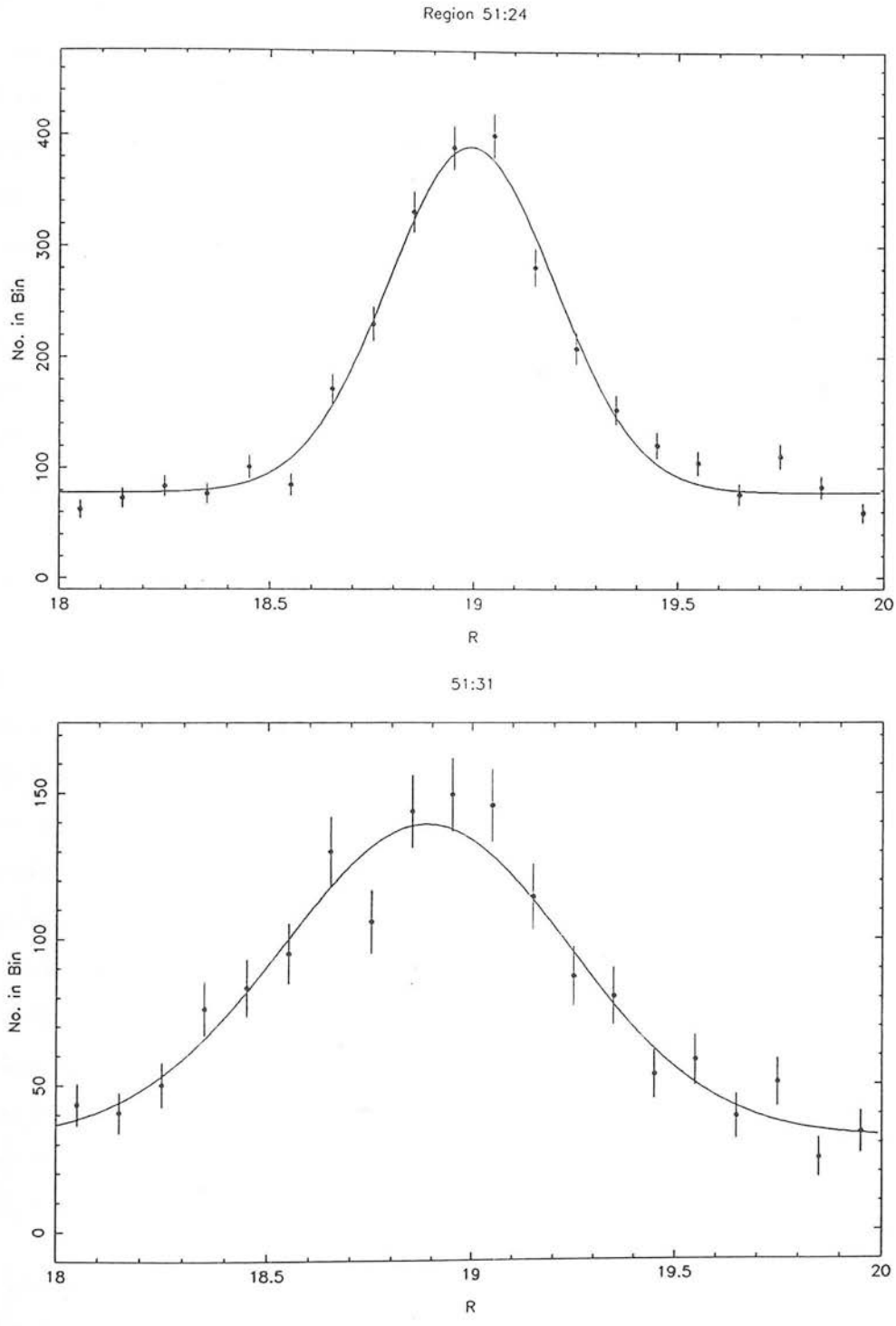

Figure 4.2: Gaussian fits to the number-magnitude relation for clump stars. *Top:* A 'narrow' clump (region F51:24) and *Bottom:* A 'broad' clump (region F51:31).

cluster NGC 121. We make the assumption that the SMC field clump stars and RR-Lyraes have a similar line-of-sight extension. For two groups of RR-Lyraes, one for RR-Lyraes within 17 arcmin of the plate centre and the other outside this radius, the dispersion in the apparent mean magnitudes of the sample was 0.14 mag and 0.09 mag respectively. We choose the latter figure, 0.09 mag equivalent to a 2σ depth of 5kpc, as more reliable due to the larger sample of stars involved. The lower value is also preferable as the figures have not been corrected for dispersions due to photometric errors (probably small due to the large number of plates used) and metallicity effects (possibly non-zero). We then use the clump half-size, $\sigma_{total} = 0.224 \pm 0.016$, evaluated for the grid region just north of the area of the RR-Lyrae study (to avoid 47 Tuc). It is more convenient to work with the quantity $\sqrt{(\sigma_{int}^2 + \sigma_{err}^2)}$, i.e. the dispersion of the Gaussian function resulting from the intrinsic luminosity scatter combined with photometric errors, since σ_{err} is an approximately constant quantity. The resulting value for the error-broadened intrinsic dispersion is 0.205 mag (from eqn. (2)), which is adopted for the subsequent analysis. The possibility remains that the size of σ_{int} (which is 0.18 mag after removing the contribution from photometric errors) may vary due to differences in the age and metallicity distributions of populations in other outer areas compared to that which we have used to derive a value of σ_{int}. We consider this to be unlikely given efficient dynamical and orbital mixing of the stellar populations of the outer regions of the SMC. A variation in the clump size as a function of distance from the SMC may occur as a result of the aging trend towards the periphery of the SMC (see Chapter 8), but we note that the value we have derived is close to the maximum value (0.2 mag as shown in the previous section) expected from consideration of observational results on well-observed SMC clusters and the theoretical models of SDW. Therefore the global adoption of this value for the whole of the SMC outer area should not lead us to overestimate our derived depths.

Lastly we discuss the effects of differential incompleteness in the data set, described in Chapter 3, on the determination of the structural indicators, since the 'background' number-magnitude relation is constructed from data which has a greater degree of completeness than that for the more crowded inner SMC regions. In particular, four

grid regions (F52:15; F28:31,41; F29:12) are believed to be affected by an incompleteness of around 40 per cent. By modifying the 'background' number-magnitude relation by a completeness factor of 40 per cent for these four grid regions, an attempt was made to see if there was any significant difference in the results for the mean clump magnitude and clump size compared to the results given assuming no differential incompleteness. Since these regions have very large numbers of SMC stars compared to galactic foreground stars, a major difference in the results is not expected. The mean clump magnitude showed a variation of less than 0.01 mag, while a small increase in the clump size, whose size was less than the 1σ errors on the clump size determinations, was seen with the use of a completeness correction. For the sake of uniformity and since it was difficult to obtain reliable completeness estimates for each grid region, no completeness corrections were applied to the 'background' number-magnitude relation. Most of the other regions have data which are at least 80 per cent complete and it was found that for these regions the application of an estimated completeness correction altered the results very little.

4 Results on the 2D Distribution

Before considering the results on the 'third dimension', i.e. the depth in the line-of-sight direction, let us examine the 2D projected distribution of HB/clump stars. Using the full database, i.e. without foreground/background subtraction, we isolated stars within the range defined by $18.2 < R < 19.5$, $0.6 < B - R < 1.8$, thus selecting mostly clump stars, and constructed a smoothed contour plot based on the method described in Chapter 2 (Section 3). The plot is shown in Fig. 4.3. From the fixed level of the counts beyond the apparent radius of the SMC, there appears to be a contribution of approximately 7.5 counts per 5 mm square pixel from the galactic foreground. In addition, red giant branch stars are also included in the clump number counts since the RGB locus intersects the clump feature on the CMD. Their numbers amount to about 40 per cent of the clump numbers over the range of magnitudes used to define the clump population. This figure has been calculated from the number-magnitude

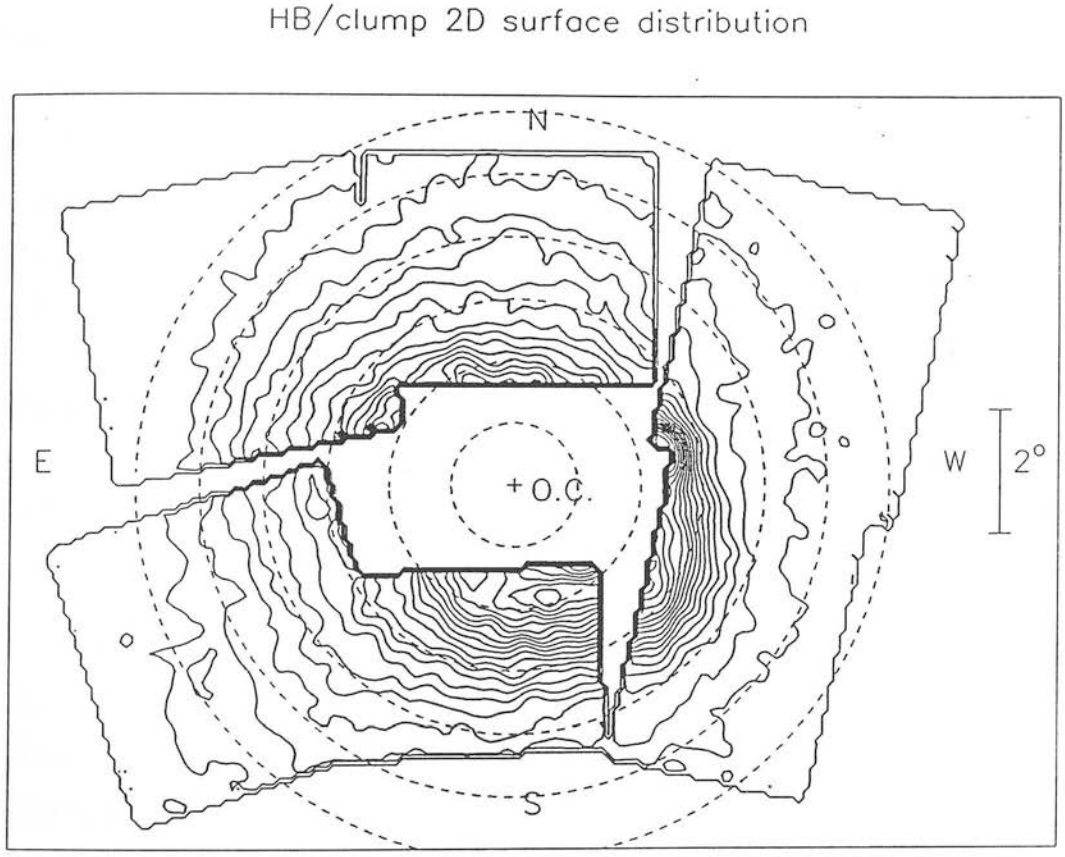

Figure 4.3: Contour plot of the surface distribution of HB/clump stars defined by the colour-magnitude limits $0.6 < B - R < 1.8$, $18.2 < R < 19.5$ for all six survey fields. Concentric radii at 1,2,3,4,5,6 degrees from the SMC optical centre are shown. The contour levels increase towards the SMC centre and consist of levels of 9,13,17,21 etc. stars per pixel. The contribution from galactic foreground stars is about 7.5 counts per pixel. To obtain the number of stars per square degree multiply by 115. The galactic globular cluster 47 Tuc is located about 2° to the WNW of the optical centre, distorting the number counts in its vicinity.

histogram of clump stars after subtraction of the galactic foreground contribution (see Appendix D for examples of histograms). Cannon (1983) has pointed out that the ratio of the numbers of stars in the upper RGB to those in the HB phase may depend on the age of the stellar population. However, studies of the ratio of the numbers of stars in the upper red giant branch to those belonging to the HB/clump as a function of position in the SMC using our database (details are described in H-thesis pp.141-144) did not show any systematic variations of this quantity. It was also shown in H-thesis (p.141-143), from published data on Magellanic Cloud clusters, that this ratio is not a particularly sensitive indicator of age for clusters older than 1-2 Gyr. Lastly, although the number counts are affected by increasing levels of incompleteness towards the SMC centre as described in Chapter 2, the contour levels between neighbouring fields appear to be matched quite well, indicating that the levels of incompleteness are uniform from field to field.

We describe here the overall appearance of the surface distribution of clump stars. There is apparently an inner elliptical component roughly aligned with the SMC major axis with its centre located about half a degree to the south-west of the optical centre. This component extends to about 4° from the optical centre in the south-west and to about 3° in the north-east and may possibly be identified with the tilted SMC disk system described by Brück (1980). Another explanation is that the inner elliptical component resembles a Fornax-type dwarf elliptical galaxy which was suggested by Johnson (1961) for the old stellar population of the SMC on the basis of the appearance of an infrared photograph. The distribution and kinematics of carbon stars (Azzopardi & Rebeirot 1991) also suggest that such a component may be present in the SMC.

The outermost contours appear to be more nearly circular than the inner contours, but the shape still deviates significantly from radial symmetry. It has been pointed out that the dynamical centre of the SMC, defined by the H I rotation curve (Hindman 1967), which is located 50 arcmin to the east of the optical centre, might represent a better centre of symmetry of the SMC 'halo' if the bulk of the mass of the SMC were to be contained in the intermediate aged and old stellar population (Brück 1980).

However, the overall radial symmetry of the clump contours is not improved with the use of this centre instead of the optical centre. The E-W centre of symmetry lies somewhere in between the optical and dynamical centres but the irregular overall appearance of the outer clump contours renders the definition of a true centre of symmetry for these populations problematic.

The contour plot shows that the outermost contours are more extended in the N-S direction than the E-W direction confirming the asymmetry of the SMC halo noted by Brück (1980). Brück suggested that the western limit of the SMC might represent the tidal limit of the Magellanic system as a whole and may therefore be tidally truncated by the gravitational field of the Galaxy. This does not, however, explain the divergence from circular symmetry with respect to the optical centre of the outermost contours to more northerly and southerly directions in the easternmost regions. Alternatively, the action of the tidal field of the Galaxy may be responsible for the greater N-S extension of the SMC. It is interesting to note that the Magellanic Stream extends from galactic coordinates $l \sim 298°, b \sim 69°$ (i.e. 20° north of the northern edge of Field 51) northwards past the South Galactic Pole to the Galaxy. According to the tidal models of Murai & Fujimoto (1980, 1986) (see also Fujimoto & Murai 1984) the Stream was formed from gas removed in a close encounter with the LMC 2×10^8yr ago and extended by the tidal field of the Galaxy. If we assume that the stellar content of the SMC was also affected by these interactions we may establish a link between the interaction responsible for the formation of the Stream and the distorted shape of the SMC.

Finally, we present in Fig. 4.4 radial profiles of the surface number counts for selected position angles centred on the SMC optical centre. (The position angle increases from zero at due north towards the east). The galactic foreground contribution to the counts has been directly subtracted from the total counts. Owing to incompleteness in the data of greater than 20 per cent at total image densities above 3 images arcmin^{-2}, the radial profiles are unreliable for $r_{oc} < 3°$. Beyond this radius, the counts are subject to an incompleteness amounting to less than 0.1 (20 per cent in the actual

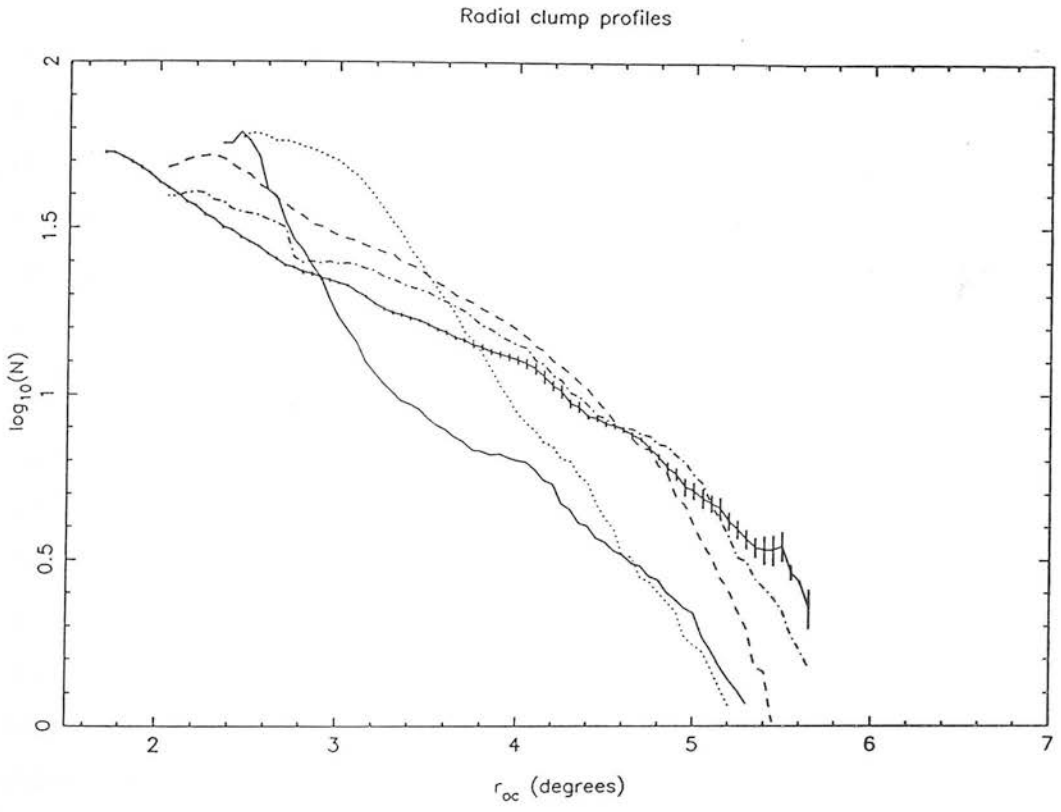

Figure 4.4: Plot of log (number counts-background counts) vs. distance from the SMC centre for selected position angles centred on the SMC centre. The profiles have been smoothed by averaging number counts from directions lying within $\pm 10°$ of the specified directions. Poissonian error bars for the measurements are indicated on one of the curves. Data for $r_{oc} < 3°$ are unreliable due to incompleteness of ≥ 20 per cent. To obtain the number of clump stars per deg^2 add 2.06 to the logarithmic number count data. The curves represent: $p.a. = -10°$ — solid line plus error bars; $p.a. = 60°$ — dashed line; $p.a. = 120°$ — dash-dotted line; $p.a. = -120°$ — dotted line; $p.a. = -60°$ — solid line.

counts) in the logarithm and are therefore fairly close to the 'true' curves that would be expected from complete data.

The asymmetrical nature of the distribution of the intermediate aged and old stellar populations represented by the HB/clump stars is apparent from the marked differences between the radial profiles in different directions. The radial extent of the SMC indicated by these profiles is between 5° and 6° for the more easterly and westerly directions and probably beyond 6° for the more northerly directions where the SMC extends beyond the northern edge of Field 51. The figure of 5-6 kpc is close to the lower estimate of the tidal radius proposed by Welch *et al.* (1987).

Radial profiles based on stellar number counts or integrated unresolved light in galaxies have been used to establish the underlying three-dimensional structure and dynamical states of galaxies. For instance, Hodge (1962) has used such profiles to determine the tidal radii of Local Group dwarf elliptical galaxies, and Hughes, Wood & Reid (1991) (hereafter HWR) have investigated whether the radial distribution of long-period variables in the LMC can either be represented by a power law profile indicative of a spheroidal halo system or an exponential profile corresponding to an exponential disk. The wide range of profiles for our SMC clump number counts means that such investigations will not yield unique answers, and in any case, as we shall see when we consider the depth structure of the SMC, the structure of the SMC is too complicated to be analysed in terms of such simple models. Nevertheless we do comment here briefly on the appearance of these radial profiles.

For two directions, $p.a. = -10°$ (roughly north) and $p.a. = -120°$ (roughly south-west) beyond 3° from the optical centre, the log(number counts) versus radial distance curve is approximately a straight line, representing an exponential falloff with distance from the optical centre, but with different scale lengths in each case. The exponential scale length for the south-west direction is about 0.5° while that for the northern direction is about 2°. As pointed out by Hodge *et al.* (1991), over a large range of radial distances an exponential light distribution is almost indistinguishable from a distribution possessing a King (1962) model profile characteristic of dynamically

relaxed systems such as most globular clusters and dwarf elliptical galaxies. Therefore, the existence of exponential profiles in some directions does not necessarily indicate the presence of an exponential disk system. We note that the exponential scale length ($\sim$ 2 kpc) found for the northern direction is similar to that found for the radial surface distribution of intermediate-aged and old long-period variables in the LMC by HWR, who found values of around 1.7 kpc for both populations.

The profiles in the more easterly directions, 60° (roughly north-east) and 120° (roughly south-east) are fairly similar to each other with an approximately exponential decrease in number counts with distance from the optical centre out to about 4.5° from the SMC centre and a steeper fall in the outermost areas. These areas possess the largest depths in the line-of-sight direction (see following section), and the unusual radial distribution in the surface number counts also suggests that these areas are tidally disrupted. It is apparent than none of the radial profiles can be well represented by a power law profile, which declines steeply at small radial distances followed by a a very gentle decrease (see the power law profiles shown in HWR). This fact argues against the existence of a spheroidal halo population possessing a power law distribution similar to that of the galactic halo (see Frenk & White 1980).

5 Results on the 3D Distribution

The contour plot of the surface densities of clump stars (Fig. 4.3) is a useful guide for determining which grid regions of each field possessed good enough statistics for accurate evaluation of the geometrical depth and mean distance modulus. In most cases reliable determinations could be achieved in the areas encompassed by the 13 counts per pixel contour. However, the accuracy of the determinations decreases with increasing clump dispersion due to the lower 'signal to noise ratio' of true clump stars to galactic foreground and red giant branch stars per magnitude bin, and therefore reliable determinations could not be obtained for some south-eastern regions located within this contour but which possess very large depths. The situation is analogous to

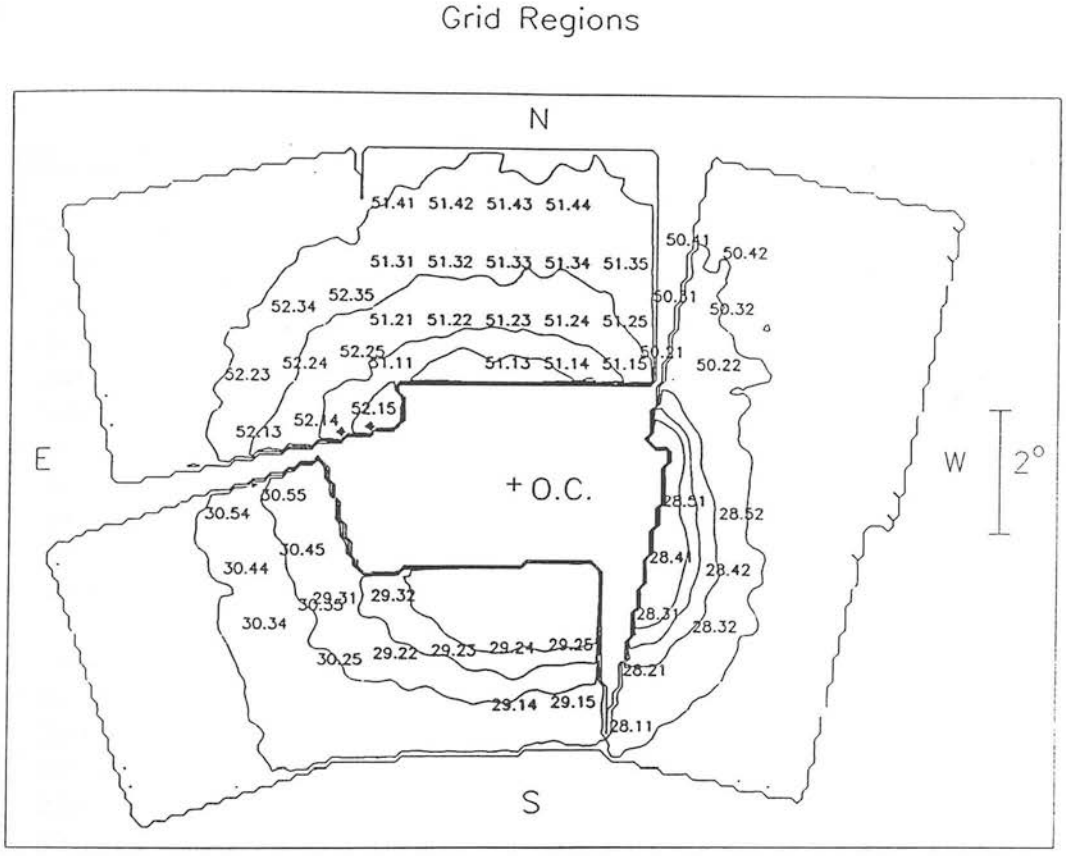

Figure 4.5: Location of the grid regions for which the structural indicators were determined, superimposed on a contour plot of the clump surface distribution. The central RA, DEC coordinates of these regions are given in Table 4.1. The contours for the HB/clump population consist of levels 12,24,36,48 stars per 5.6 × 5.6 arcmin pixel.

the different signal to noise ratios obtained in good seeing and bad seeing with CCD photometry. Table 4.1 lists the central coordinates and distance from the optical centre for each grid region for which reliable mean distance moduli and depths could be determined. Fig. 4.5 identifies the locations of these regions in relation to the surface distribution of HB/clump stars.

The methods for determining the structural indicators described in Section 3 were applied to the clump population of each grid region. At the distance modulus of the SMC (18.8) a difference of 0.2 mag in the distance modulus represents about 5 kpc,

Region	$RA : DEC$ (1950)	r_{oc} (deg)	Region	$RA : DEC$ (1950)	r_{oc} (deg)
28:11	00 16 49 : -76 50 53	4.42	**51:11**	01 15 35 : -71 03 28	2.70
28:21	00 15 42 : -75 55 02	3.73	**51:13**	00 52 33 : -71 08 56	1.85
28:31	00 14 43 : -74 59 10	3.17	**51:14**	00 41 00 : -71 07 42	2.01
28:32	00 00 18 : -75 00 58	4.00	**51:15**	00 29 31 : -71 03 48	2.53
28:41	00 13 51 : -74 03 17	2.82	**51:21**	01 14 47 : -70 21 41	3.22
28:42	00 00 15 : -74 04 59	3.73	**51:22**	01 03 41 : -70 25 36	2.75
28:51	00 13 05 : -73 07 23	2.75	**51:23**	00 52 32 : -70 26 58	2.54
28:52	00 00 13 : -73 08 59	3.68	**51:24**	00 41 23 : -70 25 46	2.67
29:31	01 34 08 : -74 41 15	3.43	**51:25**	00 30 17 : -70 22 01	3.08
29:32	01 20 02 : -74 46 42	2.67	**51:31**	01 13 47 : -69 25 58	3.99
29:22	01 21 06 : -75 42 29	3.37	**51:32**	01 03 10 : -69 29 42	3.62
29:23	01 05 59 : -75 44 45	2.91	**51:33**	00 52 31 : -69 31 00	3.47
29:24	00 50 50 : -75 43 27	2.71	**51:34**	00 41 51 : -69 29 51	3.56
29:25	00 35 49 : -75 38 35	2.82	**51:35**	00 31 13 : -69 26 16	3.88
29:14	00 49 59 : -76 39 18	3.64	**51:41**	01 12 53 : -68 30 13	4.82
29:15	00 33 57 : -76 34 06	3.72	**51:42**	01 02 42 : -68 33 47	4.52
30:25	01 35 41 : -75 40 35	4.01	**51:43**	00 52 29 : -68 35 02	4.40
30:35	01 37 50 : -74 45 14	3.67	**51:44**	00 42 16 : -68 33 56	4.48
30:45	01 39 44 : -73 49 48	3.56	**52:13**	01 43 53 : -71 50 10	4.14
30:55	01 41 25 : -72 54 19	3.68	**52:14**	01 31 56 : -71 49 12	3.30
30:34	01 51 59 : -74 51 34	4.58	**52:15**	01 20 02 : -71 45 30	2.51
30:44	01 53 05 : -73 55 46	4.49	**52:23**	01 43 48 : -70 54 11	4.57
30:54	01 54 05 : -72 59 58	4.59	**52:24**	01 32 25 : -70 53 16	3.82
50:21	00 22 25 : -70 48 04	3.11	**52:25**	01 21 04 : -70 49 45	3.17
50:22	00 11 05 : -70 52 05	3.74	**52:34**	01 32 51 : -69 57 20	4.48
50:31	00 21 23 : -69 52 19	3.90	**52:35**	01 22 00 : -69 53 59	3.94
50:32	00 10 33 : -69 56 09	4.41			
50:41	00 20 27 : -68 56 32	4.74			
50:42	00 10 05 : -69 00 13	5.17			

Table 4.1: Central coordinates and distance from the SMC optical centre (r_{oc}) for grid regions used for determining the structural indicators.

and hence the systematic errors in the photometry should be small enough to derive mean distance moduli which can provide useful distance information. Summarising the results of the investigation of the photometric accuracy at the magnitude level of the HB/clump stars discussed in Chapter 2 (Section 3), the systematic difference in the photometry between any two fields is unlikely to exceed 0.13 mag, corresponding to about 3.5 kpc at the distance of the SMC. Within a given field, systematic drifts in the photometry are limited to about 0.08 mag (2 kpc along the line-of-sight). The 2σ clump size depends to some extent on the size of random errors, which are fairly small (less than 0.10 mag) and comparable from field to field, and should not depend significantly on systematic differences between the photometry of different fields.

Table 4.2 lists the regions and the values of the structural indicators ($\overline{R}_{clump}$, mean distance modulus, 2σ clump size and 2σ depth) and the associated standard errors. In Fig. 4.6 we present a plot of the difference between the mean distance modulus and SMC short distance modulus (18.8) showing the variation of this quantity over the surface of the SMC by overlaying a contour map of the HB/clump distribution. Fig. 4.7 is a similar plot showing the variation of the 2σ depth over the surface of the SMC.

First, we remark on the main trends apparent from examination of the plots of the structural indicators as a function of projected position in the SMC and comment on these in more detail subsequently. The important observational results can be summarised as follows:—

(1) The western half of the SMC has small depths and a fairly constant mean distance modulus.

(2) The eastern half of the SMC is characterised by large depths, with the largest depths occurring in the south-eastern area.

(3) There is a continuous trend of decreasing mean distance moduli from west to east.

We discuss each of these points in turn.

(1) In the western half of the SMC, most of the depth determinations are below 10 kpc and the visual appearance of the HB/clump feature in the CMDs is quite

Region	$\overline{R}_{clump}$ (mag)	Mean dm	Clump Size (2σ) (mag)	2σ Depth (kpc)
28:11	19.01 ± 0.02	18.89	0.65 ± 0.04	14.0 ± 1.6
28:21	19.07 ± 0.01	18.95	0.47 ± 0.03	6.5 ± 2.0
28:31	18.98 ± 0.01	18.86	0.40 ± 0.02	0.0 ± 2.7
28:32	19.07 ± 0.01	18.95	0.43 ± 0.03	3.3 ± 3.3
28:41	18.97 ± 0.01	18.85	0.42 ± 0.01	2.2 ± 2.2
28:42	18.99 ± 0.01	18.87	0.44 ± 0.02	4.5 ± 1.8
28:51	18.94 ± 0.01	18.82	0.47 ± 0.02	6.1 ± 1.2
28:52	18.93 ± 0.02	18.81	0.39 ± 0.03	0.0 ± 2.4
29:11	19.03 ± 0.02	18.91	0.68 ± 0.08	15.2 ± 2.8
29:12	19.09 ± 0.01	18.97	0.63 ± 0.05	13.8 ± 1.9
29:22	19.07 ± 0.02	18.95	0.89 ± 0.10	22.7 ± 3.4
29:23	19.07 ± 0.02	18.95	0.57 ± 0.04	11.2 ± 1.5
29:24	19.08 ± 0.01	18.96	0.49 ± 0.02	7.8 ± 1.3
29:25	19.09 ± 0.01	18.97	0.42 ± 0.02	3.1 ± 3.1
29:34	19.11 ± 0.02	18.99	0.77 ± 0.09	18.8 ± 3.3
29:35	19.16 ± 0.02	19.04	0.54 ± 0.06	10.4 ± 3.3
30:25	19.08 ± 0.03	18.96	0.99 ± 0.04	25.8 ± 1.2
30:35	18.96 ± 0.02	18.84	0.85 ± 0.15	20.3 ± 4.8
30:45	19.00 ± 0.02	18.88	0.64 ± 0.05	13.5 ± 1.8
30:55	18.87 ± 0.02	18.75	0.58 ± 0.03	10.5 ± 1.3
30:34	18.96 ± 0.03	18.84	0.71 ± 0.07	15.6 ± 2.4
30:44	18.87 ± 0.02	18.75	0.62 ± 0.06	12.2 ± 2.0
30:54	18.83 ± 0.02	18.71	0.56 ± 0.06	9.6 ± 2.5
50:21	19.05 ± 0.01	18.93	0.45 ± 0.03	5.1 ± 3.1
50:22	19.10 ± 0.03	18.98	0.50 ± 0.08	8.3 ± 5.2
50:31	19.09 ± 0.02	18.97	0.49 ± 0.04	7.9 ± 2.1
50:32	18.99 ± 0.03	18.87	0.44 ± 0.04	4.2 ± 4.2
50:41	19.05 ± 0.02	18.93	0.29 ± 0.04	0.0 ± 0.0
50:42	18.98 ± 0.03	18.86	0.41 ± 0.08	1.1 ± 6.5
51:11	18.87 ± 0.02	18.75	0.62 ± 0.06	12.1 ± 2.1
51:21	18.83 ± 0.02	18.71	0.61 ± 0.04	11.5 ± 1.4
51:31	18.89 ± 0.02	18.77	0.71 ± 0.06	15.1 ± 2.0
51:41	18.91 ± 0.02	18.79	0.61 ± 0.07	12.0 ± 2.6
51:22	18.93 ± 0.01	18.81	0.48 ± 0.03	6.9 ± 1.4
51:32	18.94 ± 0.02	18.82	0.58 ± 0.06	11.0 ± 2.3
51:42	18.90 ± 0.02	18.78	0.59 ± 0.05	11.2 ± 2.1
51:13	18.96 ± 0.01	18.84	0.46 ± 0.02	5.8 ± 1.3
51:14	18.99 ± 0.01	18.87	0.39 ± 0.02	0.0 ± 0.0
51:15	19.00 ± 0.01	18.88	0.51 ± 0.03	8.5 ± 1.5
51:23	18.95 ± 0.01	18.83	0.43 ± 0.02	3.1 ± 3.1
51:24	18.99 ± 0.01	18.87	0.41 ± 0.03	0.0 ± 4.1
51:25	19.01 ± 0.01	18.89	0.50 ± 0.03	7.9 ± 1.8
51:33	18.97 ± 0.01	18.85	0.46 ± 0.02	5.8 ± 1.4
51:34	18.98 ± 0.02	18.86	0.47 ± 0.04	6.5 ± 2.6
51:35	18.98 ± 0.02	18.86	0.55 ± 0.04	9.9 ± 1.6
51:43	18.92 ± 0.02	18.80	0.53 ± 0.05	8.7 ± 2.3
51:44	18.95 ± 0.01	18.83	0.49 ± 0.03	7.1 ± 1.8
52:13	18.60 ± 0.03	18.48	0.49 ± 0.05	6.3 ± 2.2
52:14	18.76 ± 0.02	18.64	0.64 ± 0.04	12.1 ± 1.2
52:15	18.85 ± 0.02	18.73	0.64 ± 0.03	12.6 ± 1.0
52:23	18.57 ± 0.02	18.45	0.47 ± 0.05	5.4 ± 2.6
52:24	18.65 ± 0.02	18.53	0.55 ± 0.05	8.7 ± 1.7
52:25	18.72 ± 0.02	18.60	0.58 ± 0.04	9.8 ± 1.4
52:34	18.77 ± 0.05	18.65	0.62 ± 0.12	11.5 ± 4.6
52:35	18.83 ± 0.02	18.71	0.63 ± 0.05	12.1 ± 1.8

Table 4.2: Results on the structural indicators for the grid regions.

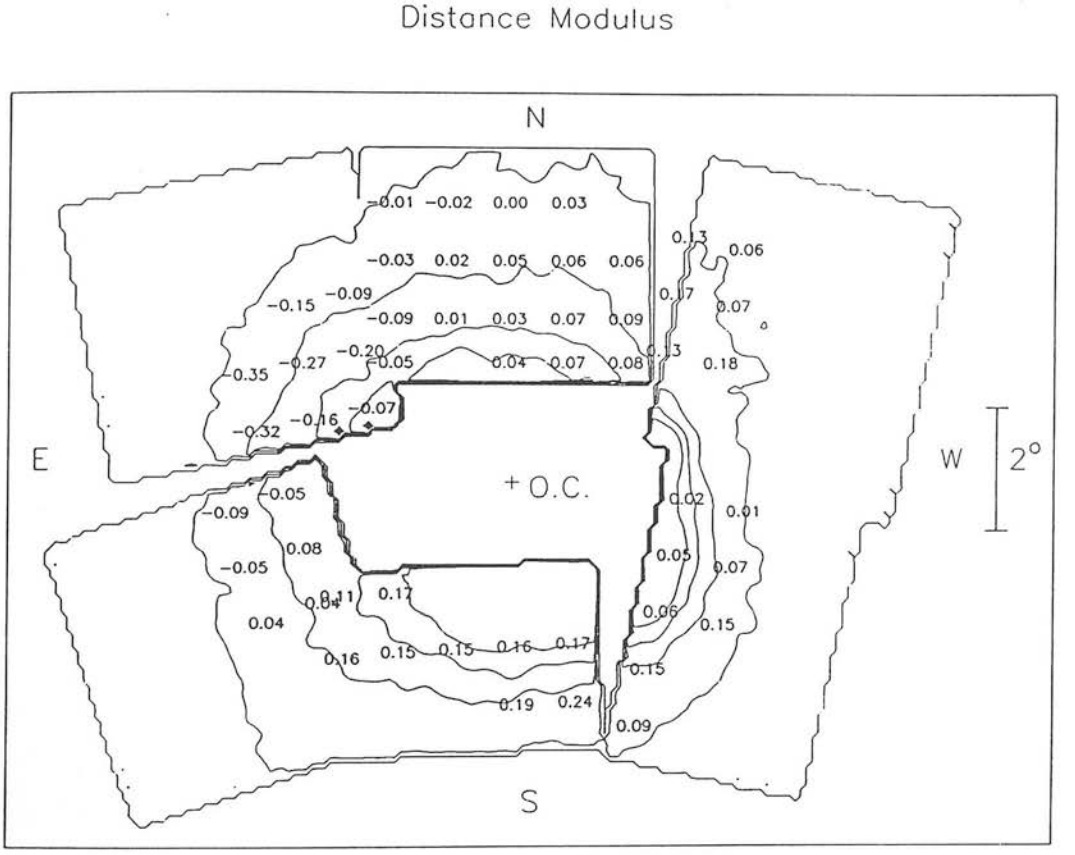

Figure 4.6: The mean distance moduli of each grid region, relative to the SMC short distance modulus (18.8). They are shown superimposed on a contour plot of the clump surface distribution. Clump contour levels are the same as in Fig. 4.5.

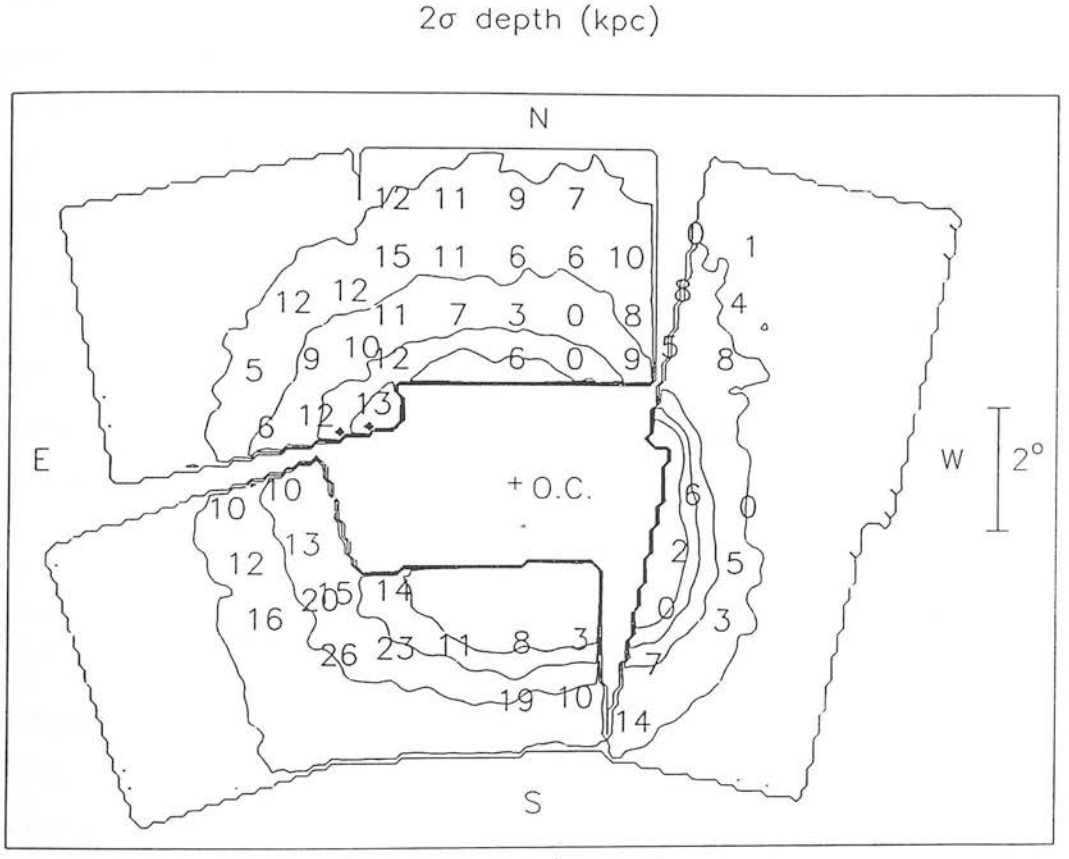

Figure 4.7: The 2σ depth of each grid region. They are shown as a function of projected position in the SMC as in Fig. 4.6.

compact with respect to that seen in the eastern half. There is a fairly large scatter in the depth determinations between neighbouring regions, this being partly due to the sensitivity of the calculated depth to small changes in the value of the observed clump size, particularly for depths below 5 kpc. If we consider all the grid regions in Field 28 and 50 plus the 11 westernmost regions in Field 51, the mean distance modulus ranges from 0.00 to +0.18 with respect to the SMC short distance modulus, representing an actual distance along the line-of-sight direction of about 5 kpc. Since the size of systematic errors in the photometry may be as much as 0.13 mag, the true range of mean distance moduli may in fact be considerably smaller than this. From Fig. 3.10 it can be seen that the systematic discrepancies in the photometry in the overlap regions at around R = 18.9 are 50-51=0.05 mag and 50-28=0.13 mag. Examination of Fig. 4.6 shows that these discrepancies have resulted in increased discontinuity between the mean distance modulus determinations in grid regions near the overlap regions.

We can estimate an average depth and distance modulus for each of the Fields 28 and 50 and Field 51 (west) by combining the colour-magnitude data from all the grid regions for which individual depth and distance modulus determinations were performed. For Field 28, data from 8 grid regions were combined; for Field 50, 6 regions, and for Field 51 (west), 11 regions were combined. The clump number-magnitude relations for the combined data in these fields were all extremely well fitted by Gaussian curves and the resultant standard errors for the clump size and mean clump magnitude were smaller than for any of the individual grid regions. The results for the mean clump magnitude were 18.98 (mean dm with respect to SMC short dm of +0.06) for Field 28, 19.05 (+0.13) for Field 50, and 18.98 (+0.06) for Field 51 (west). These results confirm the small variation in the mean distance modulus of the western areas of the SMC, giving an average distance modulus of 0.08 $\pm$ 0.03 for the western area with respect to the SMC short distance modulus. The mean clump magnitudes can be compared to values of R = 18.9 and R = 19.0 obtained respectively from CCD CMDs of the SMC field near Kron 3 (see GC3), lying just outside the eastern edge of the scanned area in Field 28, and near NGC 121 (see

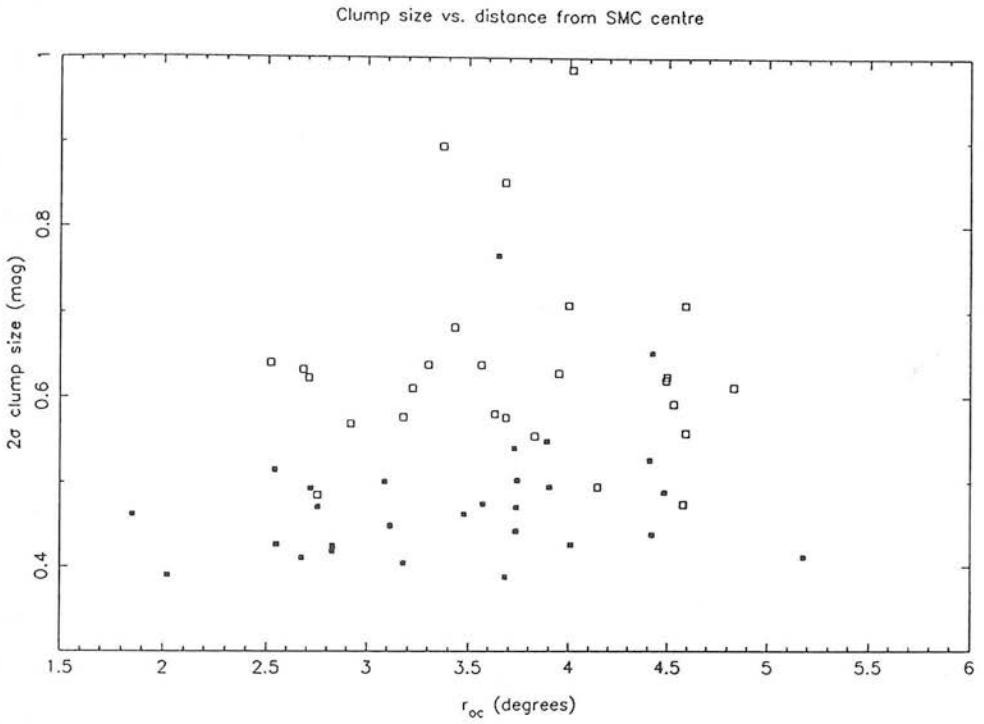

Figure 4.8: Plot of 2σ clump size versus distance from the SMC centre for all grid regions for which structural indicators were evaluated. The eastern regions (Fields 52, 30, the 7 easternmost regions in Field 51 and the 4 easternmost regions in Field 29) are represented by open squares, the western regions by filled squares.

GC5), lying at the eastern edge of Field 50. The 2σ depths determined for the three fields were 4.4 ± 0.9 kpc for Field 28, 4.3 ± 1.5 kpc for Field 50 and 5.7 ± 0.6 kpc for Field 51 (west). These determinations suggest that in the western area the depth is comparable to the projected dimensions of the SMC (diameter around 12 kpc) if the 4σ depth is close to the total depth of the SMC in a given area.

(2) In contrast to the western areas of the SMC, the majority of grid regions in the eastern areas (i.e Field 52, Field 30, the 7 easternmost regions in Field 51 and the 4 easternmost regions in Field 29) have 2σ depths greater than or equal to 9 kpc. Fig. 4.8 shows a plot of 2σ clump size against distance from the SMC centre with data for the eastern and western regions represented by different symbols. The segregation

of values between the eastern and western regions is apparent. In the eastern areas the depths lie between 9 and 16 kpc with the exception of smaller depths in the two easternmost regions in Field 52 and larger depths in the south-eastern regions close to the boundary between Fields 30 and 29. In Field 51, apart from the anomalously larger values in the 3 westernmost regions, the depths are seen to increase from west to east across the field independent of distance from the SMC centre. A similar trend towards increasing depths in the eastern regions can be seen in Field 29, where the depths for the western regions F29:24 and 25 are comparable to the small depths in the adjacent Field 28 and the easternmost regions possess much larger depths.

The trend towards increasing depths towards the east is not, however, continuous across the whole of the SMC outer area. The two easternmost regions in Field 52 have smaller depths (5 and 6 kpc) than the rest of the field, and the trend towards smaller values for the depth at the eastern extremity seems also to be indicated by the depths determined for Field 30. Given the size of the standard errors associated with the depth determinations, the significance is not very great, especially for the Field 30 regions, but this observation is apparently related to the trend towards shorter distance moduli in the east to be discussed later.

Very large depths of 20 kpc or greater are seen in three regions (F30:14,15, F29:22) located in the south-east in the overlapping area between Fields 30 and 29. The fact that these large depths are seen based on data in both Fields 30 and 29 attests to their reality. Within Field 30, the 2σ depths are seen to increase continuously towards the southern edge of the field from 10 kpc in the north to 26 kpc in the south and this increase is associated with a corresponding increase in the mean distance modulus towards the south of the field which is of the order of 0.2 mag and in excess of the largest expected systematic errors in the photometry.

(3) The trend towards smaller mean distance moduli in the east is seen across Fields 51, Field 52, Field 30 and to a certain extent in Field 29, and is ill-defined in the westernmost Fields 28 and 50. Across Field 51 the size of the change is at least 0.13 mag from regions F51:15,25 in the west to F51:11,21 in the east and is therefore

unlikely to be due to systematic errors in the photometry. The sharpest decrease of the mean distance modulus occurs in Field 52, with the mean dm decreasing by about 0.1 mag per grid region moving eastwards. In Field 30 the mean distance modulus is also seen to be smaller in the easternmost regions than the adjacent regions to the west.

There is apparently a sharp discontinuity between the mean distance moduli derived for the northernmost regions in Field 30 and the nearby regions in Field 52 of at least 0.2 mag. However, part of this difference may be attributed to the systematic discrepancy in the photometry between the two fields, which is about 0.13 mag at the magnitude level of the clump stars (see Fig. 3.10). Even so, it does appear that the true mean distance moduli for the southernmost regions in Field 52 are smaller by about 0.1 mag than those for the northernmost regions in Field 30. However, this is consistent with the trend of decreasing distance modulus from south to north in Field 30 mentioned earlier. The mean distance moduli for the two easternmost regions of Field 52 are the smallest in the entire outer area of the SMC and are probably related to the unusually small depths found in these regions compared to the rest of the eastern area.

6 The Geometry of the SMC

It is clear from the results on the 2D and 3D structure that the geometry of the SMC is rather complicated and cannot be interpreted by means of a straightforward geometrical model. Another handicap is that we cannot know the detailed distribution of clump stars along the line-of-sight — to accomplish this would require the deconvolution of the observed number-magnitude relation of clump stars into geometrical and 'intrinsic' components, which cannot be attempted because of the large statistical errors in our data. This leads to some confusion regarding what we mean by the depth along the line-of-sight direction. For a purely Gaussian distribution of distance moduli for stars in given grid region, the interpretation of the 2σ depth is that it is the depth

within which 68.3 per cent of the stars lie, but for more complicated non-Gaussian distributions this may not be exactly true. The actual 'background-corrected' number-magnitude histograms may provide more information for the interpretation of the geometry of the SMC beyond that provided by the structural indicators and are presented for the grid regions of all six project fields (including regions where the statistics are too poor for the determination of the structural indicators) in Appendix D.

The geometrical model which best describes the structure revealed by the depth and distance modulus information is a two-component model consisting of a far component of small thickness covering most of the outer area of the SMC and a near component in the eastern area superimposed along the line of sight. Large depths occur along lines of sight where both components are present, while smaller depths occur where only one component is present along any given line-of-sight. In the western half, the near component is absent, while in the easternmost areas of Field 52 the far component appears to be absent. We may derive the distance modulus difference between the two components by considering these two cases. As discussed above, the average distance modulus in the western areas of the SMC is $+0.08 \pm 0.03$ with respect to the SMC short distance modulus, while the distance moduli of the two easternmost grid regions in Field 52 (i.e. F52:13,23) are -0.32 and -0.35. The systematic discrepancies in the photometry between Fields 52 and the neighbouring Fields 30 and 52 (see Fig. 3.10) indicate that the photometry of Field 52 is more likely to be systematically brighter than that of other fields. Therefore, assuming a maximum discrepancy in the photometry between Field 52 and the other fields of 0.13 mag, the distance modulus difference between the two proposed components is between 0.30 mag (systematic photometric discrepancy of 0.13 mag) and 0.43 mag (no systematic photometric discrepancy) or 7-11 kpc along the line-of-sight. Since the maximum distance modulus separation between the two components is close to twice the value of the intrinsic clump luminosity dispersion, $\sigma_{int} = 0.205$, we would not expect a double-peaked structure in the clump number-magnitude histogram to be clearly seen if either of the components has a significant extension along the line-of-sight direction.

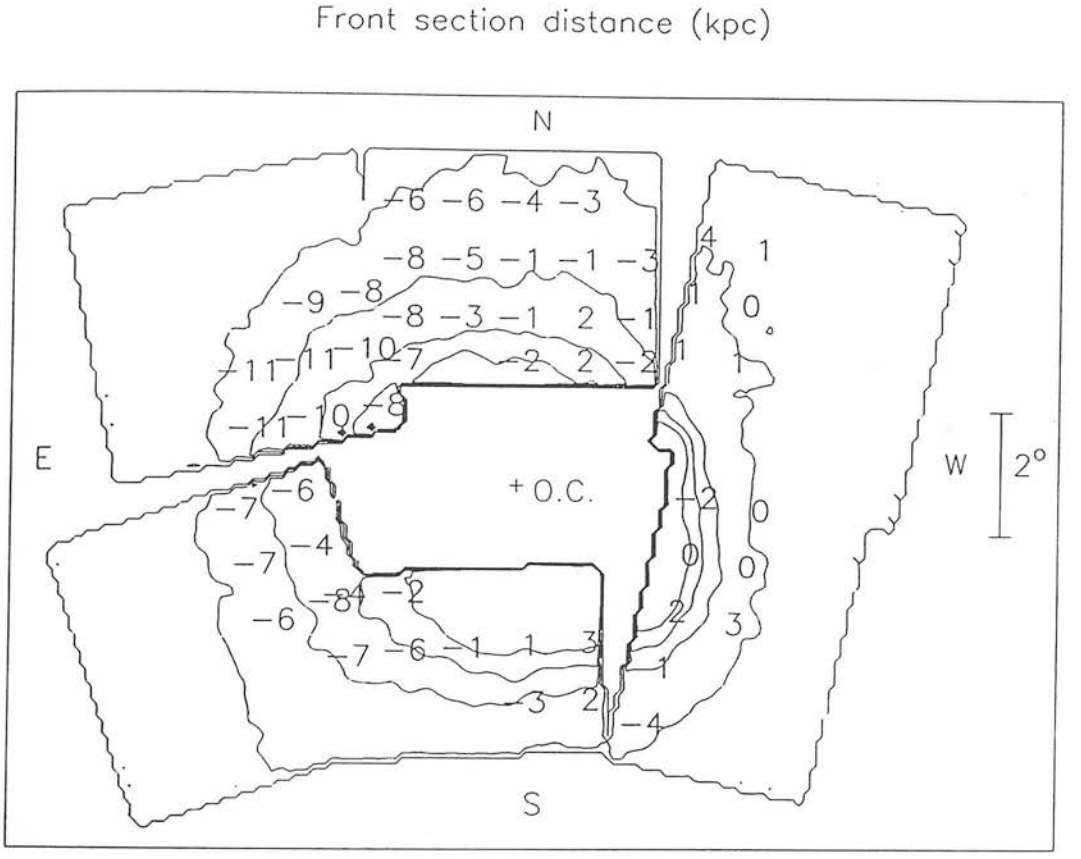

Figure 4.9: The distance of the front section of the SMC relative to the standard distance of the SMC (57.5 kpc) for each grid region. The distances are shown as a function of projected position in the SMC as in Fig. 4.6.

The practicality of the two-component model can be seen with the help of Figs 4.9 and 4.10, where we have plotted the estimated distances of the 'front' end and 'back' end of the SMC by respectively subtracting and adding the 1σ 'depth' to the distance given by the mean distance modulus, at the position of each grid region. The distances are given with respect to the distance of the SMC (57.5 kpc) given by the short distance modulus.

The two-component model satisfactorily explains some major observational trends described in the previous section. Firstly, it explains the trend towards smaller mean distance moduli in the east *not* in terms of an overall tilt of the system but by the

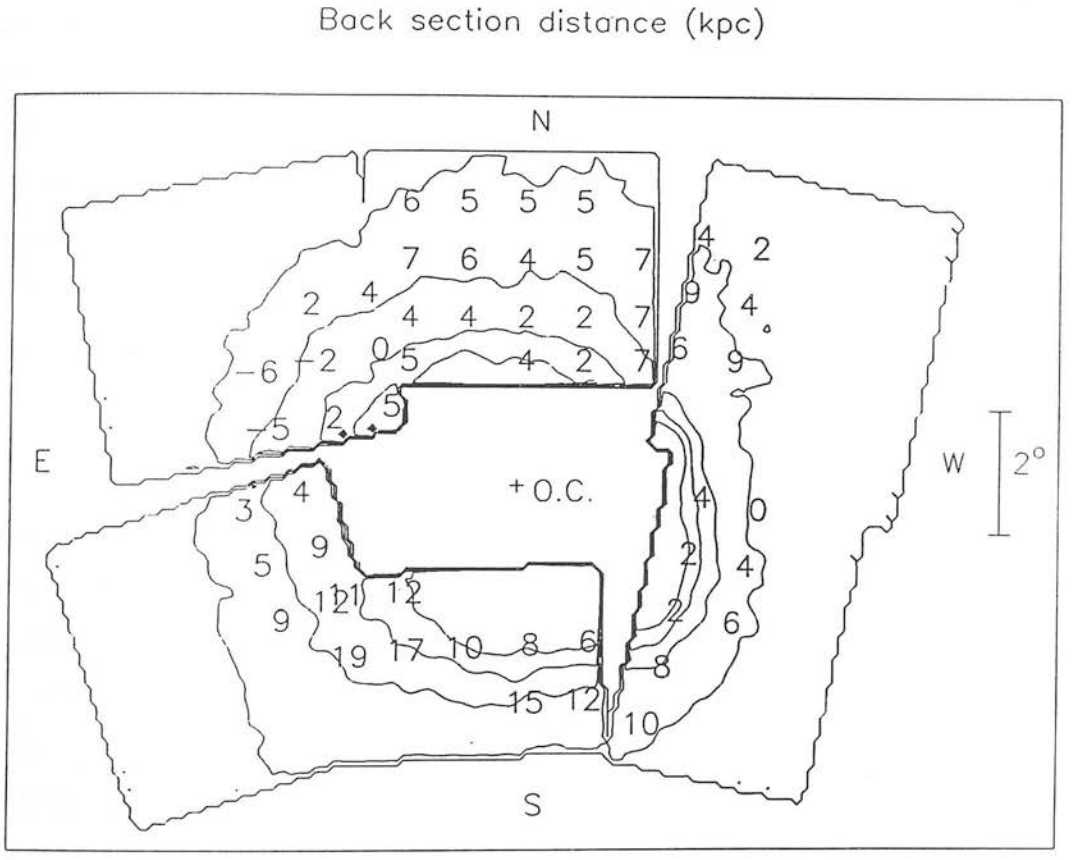

Figure 4.10: The distance of the back section of the SMC relative to the standard distance of the SMC for each grid region. The distances are shown as a function of projected position in the SMC as in Fig. 4.6.

increasing prominence of the nearer component with respect to the far component moving from west to east. Fig. 4.9 indicates that in Fields 52 and 30 the front section of the SMC remains at a fairly constant distance moving from west to east, while the back section appears to become progressively closer to us, demonstrating the inadequacy of a simple tilt model. In fact, allowing for the systematic difference between the photometry in Fields 30 and 52, the distance of the front section of the SMC appears to be fairly constant over the whole eastern area (Fields 30 and 52 and the easternmost regions of Fields 29 and 51) with no systematic trends. Secondly, the two-component model accounts for the trend towards smaller depths in the extreme east in both Fields 52 and 30 since the strength of the far component diminishes more rapidly than that of the near component with increasing distance from the SMC centre, leaving the near component the dominant one at the eastern extremity.

Two further observations based on Figs 4.9 and 4.10 can be explained in terms of the two-component model. Firstly, there is an abrupt decrease of the distance of the front section in the eastern regions of Field 51 moving from west to east and a similar change occurs in Field 29. Examination of the CMDs in Fields 51 and 29 in Appendix B indicates a fairly abrupt increase in the size of the clump feature in the eastern regions. These sudden changes are apparently due to the near component possessing a fairly sharp western boundary. Secondly, the small variation of the distance of the back section of the SMC in Field 51 and the westernmost regions in Field 52 suggests that the far component extends over the whole of this area despite the increased depths towards the boundary between Fields 51 and 52.

So far we have avoided mention of the huge depths ($\geq$ 20 kpc) in a few regions in the south-east of the SMC which do not fit easily into the two-component model. Nearly all of the other depth determinations are below 15 kpc and thus the bulk (about 70 per cent) of the SMC population probably lies within a range of distances similar to the projected dimensions of the SMC. However, in these south-eastern areas, the depths are greater than 20 kpc and thus considerably exceed the projected dimensions of the SMC. In these areas, the front section has approximately the same distance as

the remainder of the eastern area and therefore it is probable that the near component is still present. The 'extra' depth appears to lie at the far end of the SMC, where the most distant populations seem to be located at distances of almost 20 kpc behind the main body of the SMC. For the two-component model still to be applicable, we must invoke either a large depth (> 15 kpc) for the far component, or an extra component lying beyond the far component in this area. The 2D projected distribution of clump stars in the south-eastern area is quite unusual, the contours being distorted towards the south-east instead of being radially symmetric with respect to the SMC centre. This is a hint that the structure of the SMC has been substantially altered by external forces, but these enormous depths appear to be quite localised and may thus be due to some tail-like extension from the SMC.

Examination of the clump number-magnitude histograms in Appendix D supports the two-component geometrical interpretation. In particular, there are some histograms (e.g. F30:55; F51:21,31,41; F29:21,31,22) where a double-peaked structure is visible despite the fact that with a separation of 7-11 kpc between the two components, the individual peaks would be separated by only about twice the Gaussian intrinsic luminosity dispersion of the clump. Although the size of statistical errors indicate that in some cases the peaks are random, the flat-topped histogram of these regions, which contrasts with the sharply peaked histograms of many regions in Fields 28, 50 and 51, indicates that the underlying geometrical distribution strongly departs from Gaussian form. Furthermore, the CMD for F29:11 (see Appendix C) gives a strong impression of a bimodal clump feature, there being a conspicuous depopulated zone around $R = 18.9$ between two concentrations lying above and below in luminosity. Other evidence which may support a two-component model are the numerous clump histograms showing distributions which are not symmetrical with respect to the peak. This would be expected for regions where both components are present but with significantly different relative strengths.

In conclusion, the overall 2D surface distribution of clump stars and the structure along the line-of-sight direction has been shown to be very complex, demonstrating signs of having been severely affected by external forces. A two-component model is the most natural explanation for the observed structure of the SMC, although the very large depths observed in the south-east present some difficulties for this picture. In Chapter 6 we consider the origin of this structure in terms of the tidal interactions between the SMC and its neighbours, the LMC and the Galaxy, while the following chapter describes further CCD observations obtained in order to test the two-component hypothesis of SMC structure.

PART II: *THE 3D STRUCTURE*

CHAPTER

— 5 —

THE SAAO CCD OBSERVATIONS

The motivation for obtaining CCD observations of an area for which we already possessed photographic photometry was to employ the greater photometric accuracy of a linear CCD to determine whether two components existed in the SMC along our line-of-sight according to the model described in Chapter 4. In the end, our results were suggestive rather than conclusive, since ultimately we did not attain the areal coverage required to provide adequate statistics for a decisive analysis. The other scientific motivation was the study of the cluster NGC 643 (at $RA = 1^h34^m13^s, DEC = -75°48'39''$, 1950), a prominent cluster in the south-eastern outer regions located 4.0° from the SMC centre which has received little previous attention. In Section 1, the observations and reductions are described, while in Sections 2 and 3 the colour-magnitude diagrams of NGC 643 and the adjacent field regions are presented and analysed.

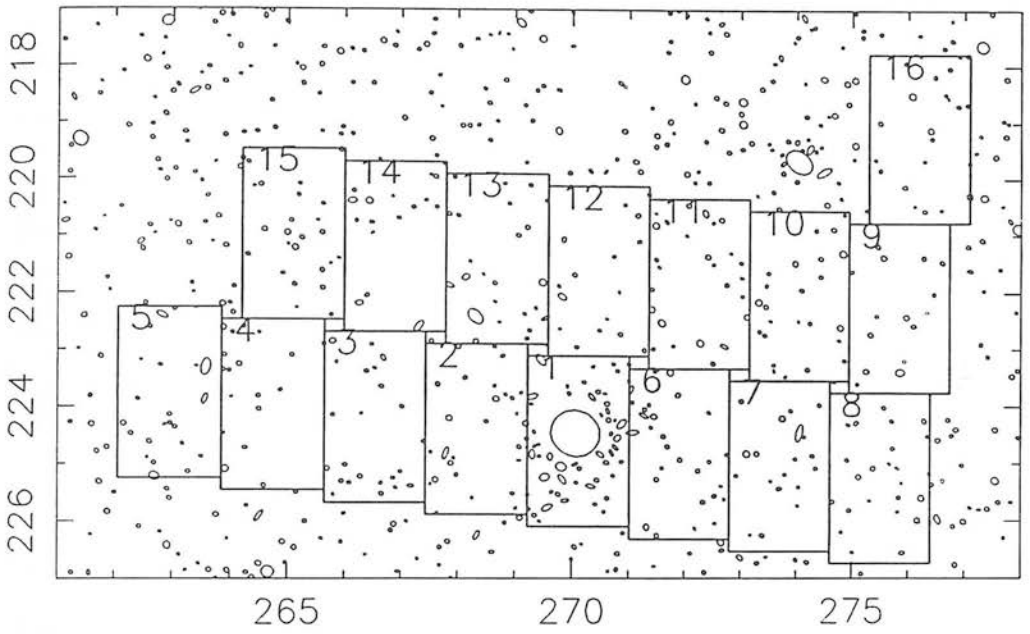

Figure 5.1: COSMOS map of the area imaged using CCD observations. The CCD regions are numbered 1-16, with CCD region 1 centred on the cluster NGC 643. North is at the top, east is to the *right*.

1 The Observations

One week of observing time at the South African Astronomical Observatory 1-m telescope (located at Sutherland, Cape Province, South Africa) was allocated from 13-19 November 1990. There was one completely photometric night, the 17-18 November, which was used to determine photometric zeropoints by establishing secondary standards for the long CCD exposures of each CCD region. No observations were obtained on the first night of the run due to adverse weather conditions and the final night was also largely clouded over. Observations under varying photometric conditions were obtained during most of the other five nights. In all, usable long exposure CCD observations were obtained in two wavebands, V and R, in 15 adjacent CCD regions, as indicated in Fig. 5.1, which shows the digitised COSMOS map of the area covered by the CCD observations.

1.1 CCD Characteristics and Preliminary Reductions

The detector is an RCA CCD mounted at the Cassegrain focus of the telescope. It consists of a 512 × 320 pixel array giving an active area of 3.3 × 2.0 arcmin with a pixel size of 0.39 arcsec. Other principal characteristics of the detector from the list contained in the SAAO Facilities Manual (1987) are the conversion factor of 11.5 e^- per ADU (analogue-to-digital unit), saturation level at 21700 ADU, readout noise of 73 e^- rms, and very low dark current of 4 $e^- pix^{-1} min^{-1}$. Standard V (Johnson) and R (Cousins) filters were used for the observations.

The observations consisted of:—

(1) very short exposures ($\leq$ 10 s) of bright (V < 10 mag) standard stars to derive the photometric zeropoints and monitor changes in these zeropoints due to non-photometric observing conditions;

(2) long exposure programme frames (1200 s in V and 1800 s in R) of the cluster NGC 643 and the surrounding field region;

(3) shorter exposure programme frames (120 s in V and 60 s in R) to establish secondary photometric standards;

(4) exposures of similar duration to (iii) taken before and after the long exposures to monitor changes in the photometric zeropoints.

A number of calibration frames, i.e. preflash frames and flat fields were also obtained.

The preliminary reductions were performed using standard routines in the STARLINK FIGARO package to manipulate the data arrays containing the raw CCD data. These reductions consisted of bias-subtracting and trimming all calibration and science frames, subtraction of the preflash frames and flatfielding of all the science frames.

There is a bias-strip at the edge of each CCD frame consisting of 512 × 40 pixels from which the mean bias value was calculated and subtracted from each frame. A separate bias exposure showed that there was no variation in the bias level over the frame, justifying the subtraction of a constant mean bias value. The resulting frames were then trimmed to remove the bias strip.

All the science exposures were preflashed in order for the sky level to exceed the readout threshold of 500 e^- (43 ADU), although for the long exposures this was not strictly necessary. Two long preflash-only frames towards the beginning and end of the observing run were obtained in order to determine the preflash counts to be subtracted from the science frames and flat fields. Unfortunately, it was found subsequently that the characteristics of the preflash illumination pattern differed between the two long preflash exposures and had also varied during the run. In particular, after subtracting the preflash counts from the science frames, some of the science frames had noticeable east-west gradients in the sky background, amounting to about 60 counts over 300 pixels. This did not introduce significant errors into the photometry as the variation in the level of the sky counts across the stellar seeing disk amounted to only about 1-2 ADU. The first long preflash was used for removing the preflash counts for all frames taken up till the night of 16-17 November, while the second long preflash was used for the remaining frames.

A series of flat fields were obtained in the first two nights of active observing which were used to eliminate the effects of variations in the pixel-to-pixel sensitivity in the science frames. Five flat field exposures in V and three in R of duration $10-30$ s were taken by imaging the twilight sky at dusk. The flat fields were stable from night to night and the sensitivity variations measured by the rms error of the count distribution were less than 7% for all flat field exposures with mean count levels greater than 4000 ADU. The flat fields in each waveband were coadded, normalised to unity and used as the standard flat fields for the science exposures. After division by the standard flat fields the only residual background gradients were due to the preflash contribution not being properly subtracted.

1.2 The Photometric Zeropoints

The absolute photometric zeropoints for V and R were determined by observations of seven standard stars selected from the revised E-Region and Magellanic Cloud lists of Menzies *et al.* (1989). Extinction coefficients for the site were furnished by

J.W.Menzies (private communication) and were used to reduce the observations to the same airmass. The colour corrections used to transform the instrumental V and R magnitudes to the standard $UBVRI$ system were effectively zero from the following considerations. The colour equations given by Menzies (1990) are:

$$V = v - 0.006(b - v)$$

and

$$(V - R) = 1.007(v - r)$$

where the standard passbands are represented by the uppercase letters and the instrumental quantities are represented by the lowercase letters. The ranges in the quantities $B-V$ and $V-R$ for our standard stars were $0.0 < B-V < 1.5$ and $0.0 < V-R < 0.8$, so according to these transformations the additional inaccuracies in the observational quantities V and $V - R$ introduced by assuming that the instrumental passbands are identical to the standard system do not exceed 0.01 mag, which is a satisfactory level of precision.

The aperture photometry routine in the DAOPHOT program (see also Chapter 2) was used to derive the instrumental magnitudes for the standard stars and secondary standards. This program simply adds up the counts within a specified aperture and then subtracts the sky contribution from a circular annulus between two specified radii outside the seeing profile of the stellar image. The flux due to the star is thus evaluated and an instrumental magnitude is derived. The instrumental magnitude is calculated by DAOPHOT according to

$$M_{inst} = 25.0 - 2.5 \log_{10}(signalcounts - skycounts).$$

An aperture of radius 10 pixels (3.9 arcsec) was chosen since it included about 95% of the stellar flux and for larger apertures the errors due to the greater sky contribution begin to increase.

The absolute photometric zeropoints were determined from observations of standard stars achieved in photometric conditions. The final equations relating the instru-

mental magnitudes to the standard system via the photometric zeropoints were:

$$V = V_{inst} - 0.15\chi + 2.5\log_{10} T + Z_V$$
$$R = R_{inst} - 0.10\chi + 2.5\log_{10} T + Z_R \quad (1)$$

where and χ = airmass, T = exposure time, $Z_V = -4.514 \pm 0.013$ and $Z_R = -4.233 \pm 0.018$ are the respective zeropoints. These zeropoints agree within the errors with the values given by Menzies (1990) of -4.507 for V and -4.221 for R (after subtracting 25.0 which is added by the DAOPHOT program).

Numerous exposures of standard stars were obtained during each night of observing as checks on the photometric conditions. In general, the extinction corrections due to cloud or poor seeing ($\geq$ 4 arcsec) varied considerably up to a maximum of 0.4 mag, although for most of the observations it was less than 0.2 mag. The observing conditions were seen to vary over short timescales (about half an hour) and therefore it was considered important to observe fairly bright ($\leq$ 16 mag) secondary standards to establish zeropoints for each CCD region. We took advantage of the one completely photometric night to obtain relatively short exposures (120 s in V and 60 s in R) of each CCD region. The magnitudes of the secondary standards were used to determine zeropoint corrections to the long exposure magnitude lists by means of comparison with the instrumental long exposure magnitudes of the same standards.

The use of secondary standards introduced additional errors into the definition of the zeropoints for each CCD region. The additional zeropoint errors were due to lower signal-to-noise ratios for observations of fairly bright stars obtained from relatively short exposures. Including the uncertainty in the absolute zeropoints of 0.013 mag for V and 0.018 mag for R, 11 out 16 CCD regions had zeropoints which could be defined to within an error of 0.05 mag. The zeropoints of the remaining regions could be defined to within an error of 0.1 mag. In a few cases where the magnitudes of the secondary standards (taken in photometric conditions) were actually fainter than the magnitudes of the same stars in the long exposures it was concluded that the conditions had been photometric during the long exposures and that the zeropoint discrepancy was due to the larger random error of the shorter exposure determination. Two of the

CCD regions did not possess stars bright enough to act as secondary standards so in these cases zeropoint corrections were estimated by interpolating from the zeropoint corrections indicated by the standard star exposures taken at times near these long programme frames. Table 5.1 lists the zeropoint corrections and associated zeropoint errors applied to the long exposure frames in each CCD region with notes on how the correction was determined.

1.3 The Programme Frames

Pairs of long exposure frames in $V$and R of duration 1800 s and 1200 s were obtained of NGC 643 (Region 1) and 15 adjacent field regions (Regions 2-16). The locations of the CCD regions are shown superimposed on the COSMOS image map in Fig. 5.1.

After performing the preliminary reductions described earlier, these frames were analysed using the DAOPHOT photometry routine, which is more fully described in Chapter 2, and the reductions were performed in the same manner as described there. As explained in Chapter 2, DAOPHOT determines a point-spread-function (PSF) from the brightest isolated stars on a frame and determines the magnitudes of other stars by fitting this PSF profile. Its capacity for simultaneous reduction of multiple images in crowded fields makes it suitable for the reduction of the observations of the cluster, but it also enables more accurate determinations of the magnitudes of faint stars with low signal-to-noise than aperture photometry methods. The same aperture size (10 pixel radius) as that used for the standard star reductions was specified, allowing the instrumental magnitudes produced by DAOPHOT to be directly related to the zeropoints determined above. Since the PSF-fitting method gives less weight to the flux recorded at the extremities of a stellar image, the intrinsic error is not significantly affected by the inclusion of a large sky contribution within the aperture.

The DAOPHOT magnitude lists are tied into the aperture magnitude system via the magnitude, determined by aperture photometry, of the first star selected for the construction of the PSF, which is normally the brightest isolated star on the frame. The

Region/Filter	Correction (mag)	Error (mag)	Method
1 R	0.0	0.033	2
1 V	-0.090	0.028	1
2 R	-0.005	0.077	1
2 V	-0.005	0.061	3
3 R	0.0	0.1	4
3 V	-0.1	0.1	4
4 R	-0.198	0.047	1
4 V	-0.082	0.050	4
5 R	-0.089	0.030	1
5 V	-0.091	0.024	1
6 R	-0.035	0.043	1
6 V	-0.040	0.049	1
7 R	0.0	0.048	2
7 V	0.0	0.049	2
8 R	-0.083	0.059	1
8 V	0.0	0.084	2
9 R	-0.372	0.035	1
9 V	-0.038	0.029	1
10 R	-0.033	0.033	1
10 V	0.0	0.028	2
11 R	-0.036	0.040	1
11 V	-0.027	0.036	1
12 R	-0.057	0.074	1
12 V	-0.194	0.080	1
13 R	0.0	0.025	2
13 V	0.0	0.050	2
14 R	0.0	0.065	2
14 V	0.0	0.054	2
15 R	0.0	0.025	2
15 V	0.0	0.018	3
16 R	0.0	0.025	2
16 V	0.0	0.018	2

Table 5.1: Zeropoint corrections applied to the long exposures in each CCD region. *Column 1* gives the CCD region name (see Fig. 5.1 for details of locations) and the observational passband. *Column 2* gives the zeropoint correction applied and the associated error in the zeropoint is given in *Column 3*. *Column 4* indicates the way in which the zeropoint correction was determined: 1 indicates a correction determined from comparing the magnitude of the secondary standard with the instrumental magnitude determined from the long exposure; 2 indicates that no correction is applied due to the long exposure magnitude being brighter (but within the random photometric errors) than the magnitude of the secondary standard; 3 indicates the case when the zeropoint was taken from the R data when the V magnitude of the secondary standard could not be determined — the assumption is made that photometric conditions were not altered between sequential V and R exposures; 4 indicates corrections determined from interpolating from observations of standard stars obtained at times close to the long exposures in cases where there were no stars bright enough in the CCD region to be used as secondary standards.

magnitude lists produced by DAOPHOT for each long exposure frame were converted to apparent magnitudes in the standard system by application of eqn.(1) with an additional zeropoint correction listed in Table 5.1 which was derived from comparison with the magnitudes of secondary standards as explained above. The V and R magnitude lists were then paired together, thus removing spurious detections and faint stars of extreme colour. The intrinsic errors in the stellar magnitudes for each CCD frame are very small: at $R = 19$ the error is just 0.02 mag but rises to about 0.05 mag at $R = 20$. The intrinsic errors in the magnitudes estimated by the DAOPHOT program are shown as a function of V and R magnitudes in Fig. 5.2 from data from Region 1 (the cluster CCD region). The major contribution to the random errors for the *whole* sample of observed stars is derived from the errors in the definition of the individual zeropoints for each CCD region, which can be as large as 0.1 mag. As an independent check on the R-band photometry the differences between the CCD magnitudes and photographic magnitudes for stars possessing both sets of magnitudes have been plotted in Fig. 5.3. It can be seen that there is no zeropoint discrepancy and that the rms scatter is about 0.1 mag, which is to be expected based on the known size of the random photographic errors of around 0.06-0.1 mag (see Chapter 3).

The reduction of the CCD frames of the cluster were performed in the same manner as the other regions, except that the dense, crowded core of the cluster was avoided. The DAOPHOT routine determines which groups of stars are to be reduced simultaneously and one very large group, numbering about 60 stars, was produced from detections (made by the FIND routine in DAOPHOT) in the core of the cluster. Since the cluster core was dominated by the integrated light of the cluster it was considered pointless to proceed with the reduction of this group of stars. However, outside the cluster core there were no groups larger than four stars for simultaneous reduction and most of the stars were isolated images. It is common practice for reductions of the crowded fields of clusters to require several passes, involving on the nth pass the subtraction from the frame of the stars detected in the $(n-1)$th pass, then recovery of stars not detected in the $(n-1)$th pass and finally repetition of the reductions on the revised stellar list (see e.g. Hesser *et al.* 1987). This was found not to be neces-

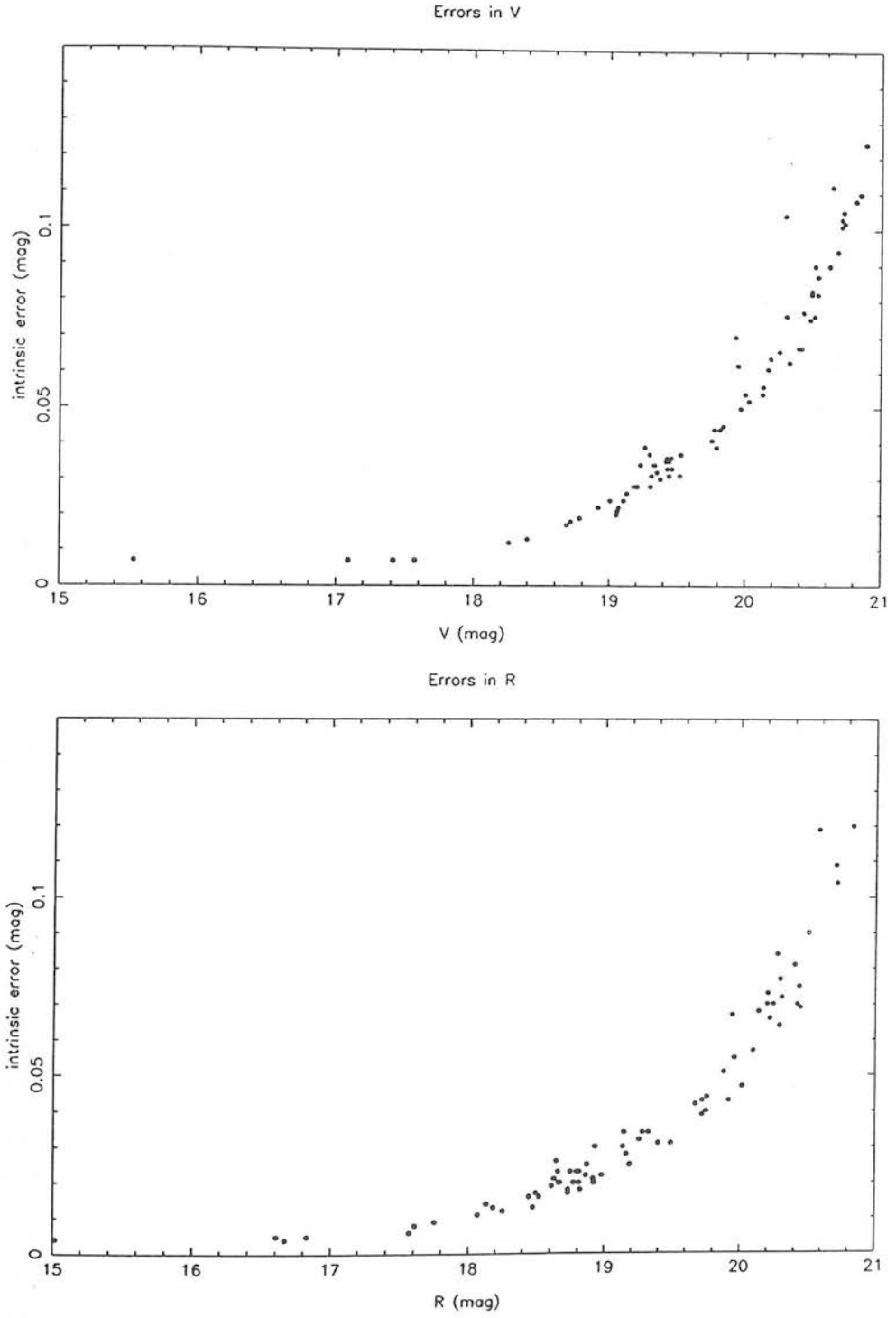

Figure 5.2: Intrinsic errors as a function of V and R magnitude for long exposure frames. Errors were estimated by the DAOPHOT PSF-fitting routine. Data from CCD region 1.

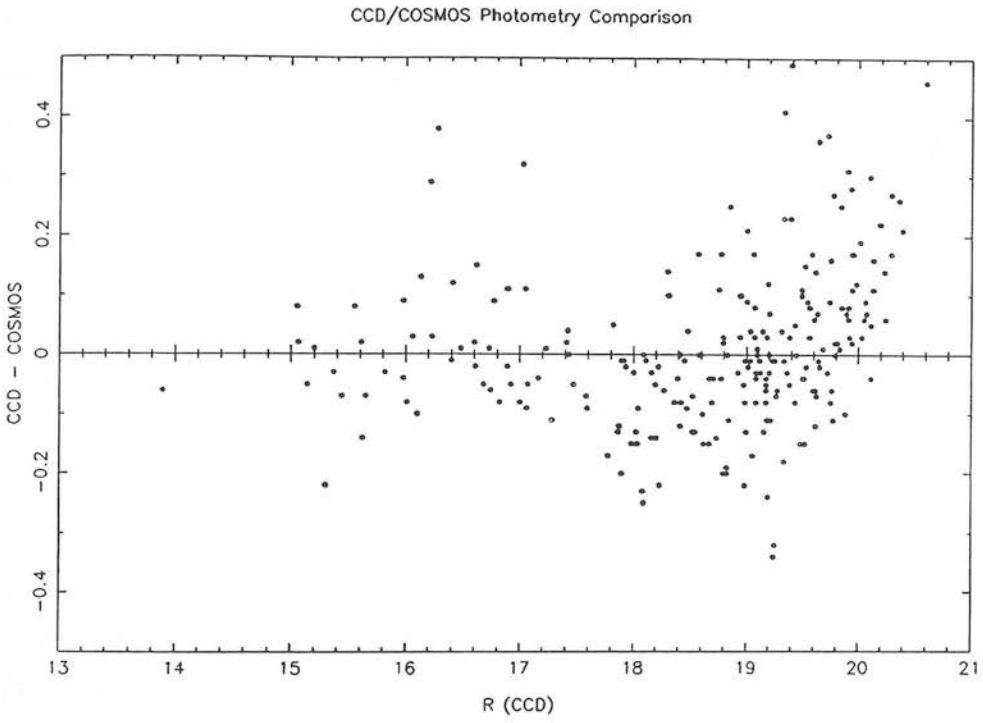

Figure 5.3: Comparison between R-band calibrated photographic photometry and SAAO CCD photometry. CCD−COSMOS magnitude is plotted as a function of CCD magnitude for 243 stars measured on both photographic plates and CCD frames.

sary for our observations of the cluster since outside the core of the cluster the image density was not very high. If the exposures had gone much deeper the greater density of stellar images would have required such reduction procedures to be employed.

In Appendix E, R-band contour image plots of the 16 CCD regions are presented with stars brighter than $R = 20$ numbered. The CCD image plots have the same orientation as the COSMOS map (Fig.5.1). In Appendix F the magnitude lists, including the standard errors derived from the zeropoint and intrinsic random errors added in quadrature, of all the stars paired on both V and R frames in the 16 CCD regions are given with the same ID numbers depicted on the contour image plots.

2 The Colour-Magnitude Diagrams

2.1 The Cluster Colour-Magnitude Diagram

The colour-magnitude diagram (CMD) in $R, V - R$ constructed from the magnitude list for CCD region 1 in Appendix F, is shown in Fig. 5.4 with selected isochrones overlaid to enable an age and metallicity analysis (see below). The CMD contains only 74 stars and does not reach significantly below the main sequence turnoff area, hampering the overall interpretation. Nevertheless, several of the features of the CMD are unambiguous, in contrast to the situation of the field CMD to be analysed afterwards. The HB/clump, centred on $R = 18.7, V - R = 0.5$ is prominent and a few stars can be seen defining the red giant branch. The $V - R$ colour of the HB/clump agrees well with that of the intermediate age LMC cluster, Hodge 4, studied by Mateo & Hodge (1986) using $UBVR$ photometry. There is no clearly defined subgiant branch, which would be expected below the HB/clump at roughly the same colour. There appears to be a main sequence turnoff between $R = 20$ and $R = 21$; its interpretation is, however, subject to the presence of field main sequence stars and the increasing size of photometric errors fainter than $R = 20$.

Before performing the age and metallicity analysis of the CMD of the cluster it is

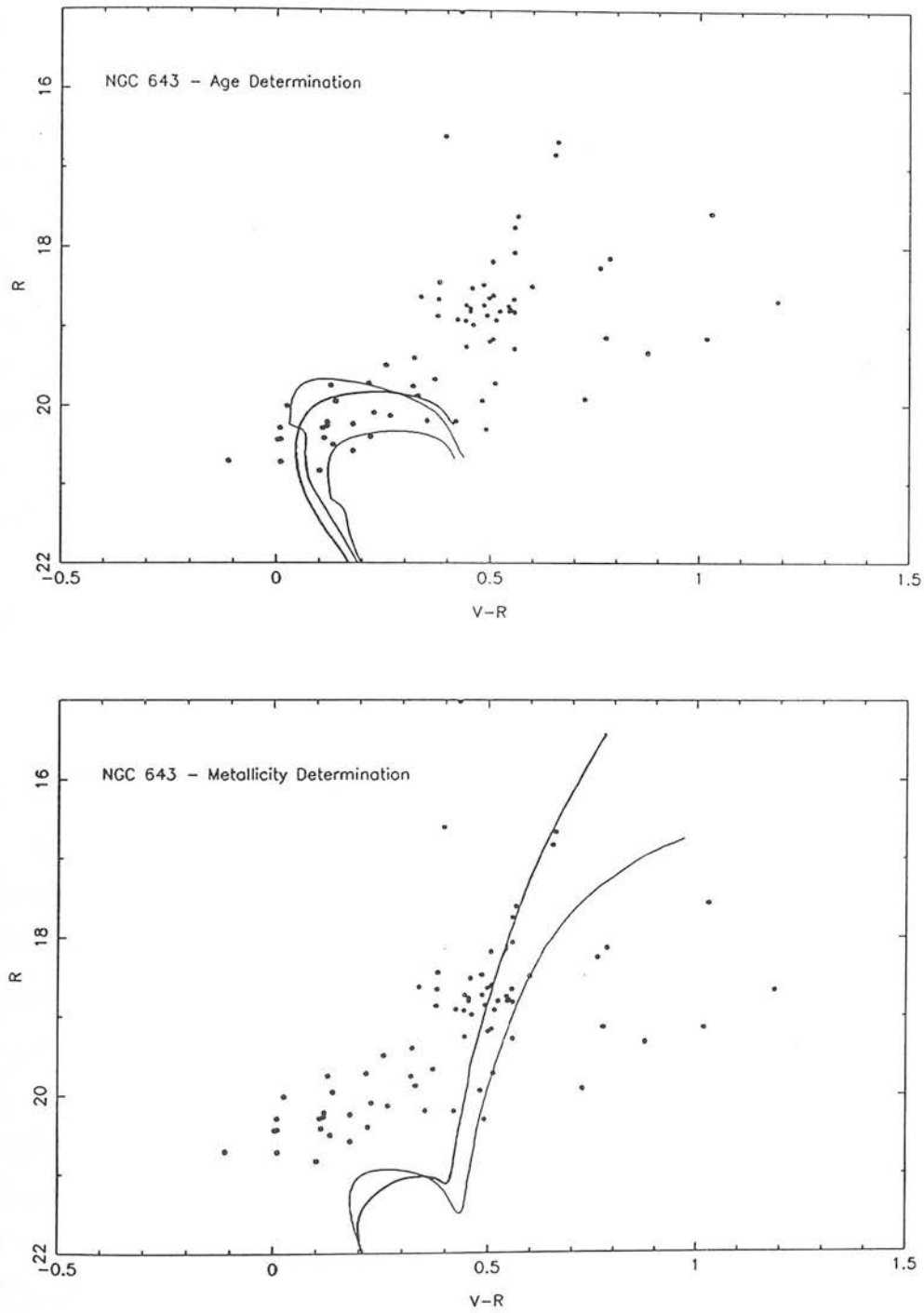

Figure 5.4: The $R, V-R$ colour-magnitude diagram for CCD region 1, including the cluster NGC 643, with superimposed isochrones. Reddening corrections, $E_{V-R} = 0.015$, $A_R = 0.07$, and SMC short distance modulus (18.8) have been adopted. *Top:* CMD with 1 and 2 Gyr isochrones ($Z = 0.004, Y = 0.2$), and 2 Gyr isochrone ($Z = 0.001, Y = 0.2$) (thicker curve) overlaid for age determination of the cluster. *Bottom:* CMD with 6 Gyr ($Z = 0.001, Y = 0.2$) and 3 Gyr ($Z = 0.004, Y = 0.2$) isochrones overlaid for metal abundance determination of the cluster.

necessary to discuss to what extent the features of the cluster CMD are due to the superimposed field population which just happens to lie along the line-of-sight of the cluster. From total counts of stars in the 15 field CCD regions and correcting for the area covered by the cluster core (which was excluded from the analysis) the field contribution was calculated to be about 25 per cent. If we construct a CMD for the cluster using only stars lying within 150 pixels of the cluster centre ($x = 160, y = 260$) the corresponding field star contribution is only 15% or 7 ± 3 stars out of 47 stars remaining in the CMD. In Fig. 5.5 we show the two CMDs for stars in CCD region 1 lying within this radius and outside this radius. It can be seen that the features of the CMD inside the 150 pixel radius do not differ significantly from the CMD constructed for all the stars in CCD region 1 in Fig. 5.4, so our analysis will be based mainly on the latter CMD, which has more stars. It is clear that, since there are 28 stars in the outer area CMD, compared to an expected number of about 11 stars due to the field population, the cluster extends beyond a radius of 150 pixels (1 arcmin).

We now discuss the age and metallicity of the cluster from isochrone analysis.

(i) Age

The cluster apparently contains main sequence stars which are brighter than the R limit at $R = 21$. However, the stars appear to be rather smeared out along the colour axis in the turnoff area, which may be due to large internal photometric errors which exceed 0.1 mag at $R = 20$. From the CMD of the inner cluster area in Fig. 5.5, it can be seen that there are 11 stars bluer than $V - R = 0.4$ which are too many to be accounted for purely by stars in the general field, whose *total* numbers are probably less than 10 in this area, as stated in the previous paragraph. In Fig. 5.4 (top figure) we have superimposed isochrones (derived from the Revised Yale Isochrones of Green, Demarque & King 1987) for 1 and 2 Gyr ($Z = 0.004, Y = 0.2$), and 2 Gyr ($Z = 0.001, Y = 0.2$) (thicker curve) with reddening corrections, $E_{V-R} = 0.015$, and $A_R = 0.07$ (see Chapter 4). The short distance modulus (18.8) has been assumed. The metallicities correspond to [Fe/H]$= -0.7$ and [Fe/H]$= -1.3$ (given $Z_\odot = 0.02$), which are appropriate for SMC clusters in the age range 1 to a few Gyr (see bibliography

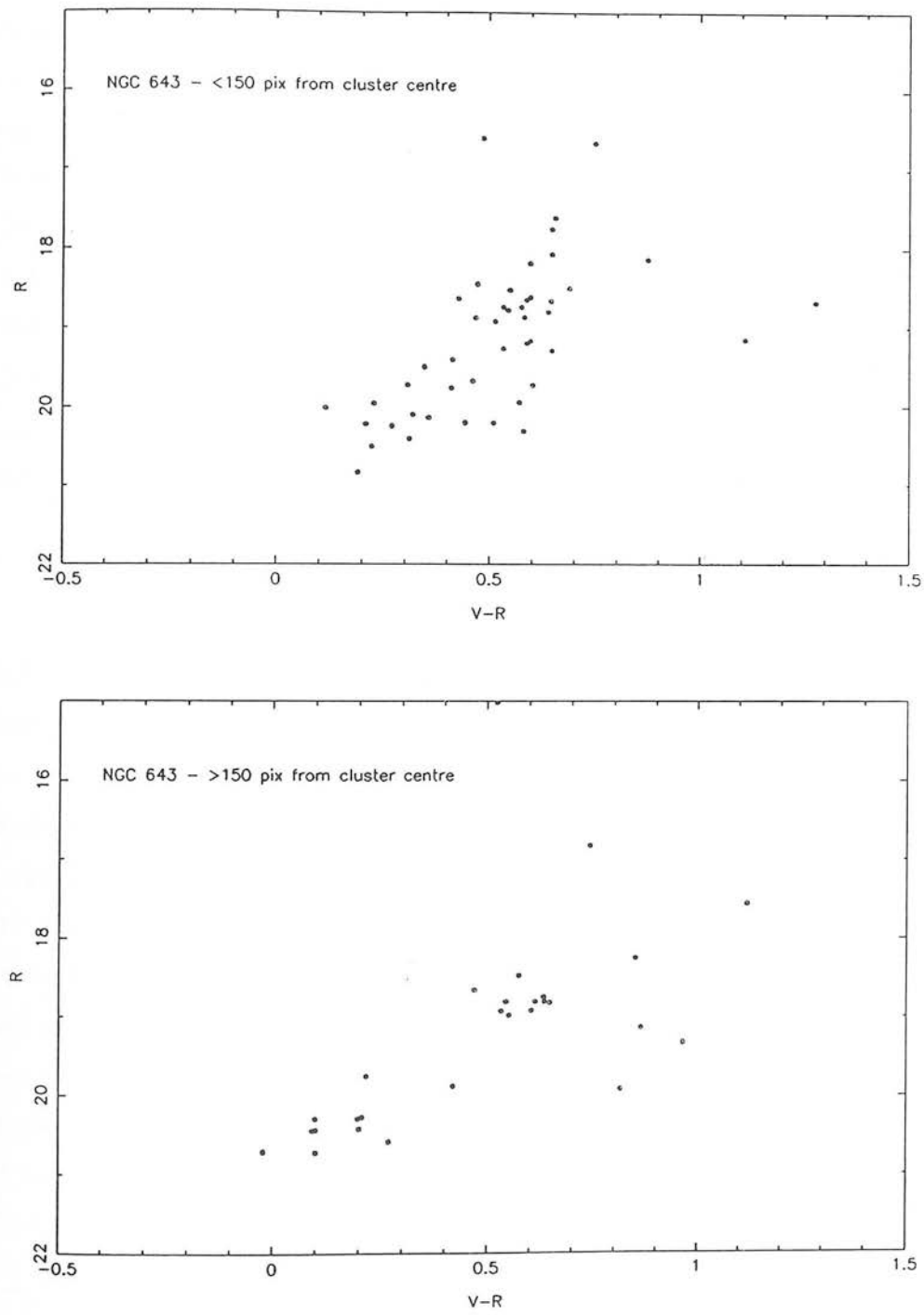

Figure 5.5: Colour-magnitude diagrams $(R, V-R)$ for CCD region 1:— *Top:* Stars within 150 pixels of cluster (NGC 643) centre. *Bottom:* Stars outside radius of 150 pixels from cluster centre.

of deep CCD-based studies of SMC clusters, Table 1.1). The colours of the bluest stars in the CMD agree well with the colour of the isochrones in the turnoff area. The age is not very well determined because of the large errors in the data near the faint limit and the fact that the photometry only just reaches the top of the main sequence. Nevertheless we can tentatively assign an age of around 2 Gyr from the isochrone fits. This estimate should be regarded with caution as examples of substantial revision of cluster ages resulting from determinations involving deeper magnitude limits abound. There are no published CMDs of NGC 643 (see the bibliography of Sagar & Pandey 1989). However, Hodge (1984) does make reference to a determination by Hesser and collaborators indicating that NGC 643 is of intermediate age, and our own estimate agrees with this age classification.

(ii) Metallicity

It is well known that the red giant branches of comparatively metal poor populations are taller and steeper than those of more metal rich ones. Unfortunately, no isochrones incorporating the red giant phase of evolution are available for populations younger than 3 Gyr for metallicities appropriate for SMC clusters. Inspection of the Revised Yale Isochrones of a given composition, for ages for which red giant branch evolutionary tracks exist, indicates that the RGB locus changes little with the age of the stellar population. Therefore, to obtain some reasonable estimate of the metallicity we have superimposed the Revised Yale Isochrones for 6 Gyr ($Z = 0.001, Y = 0.2$) and 3 Gyr ($Z = 0.004, Y = 0.2$) on the cluster CMD in Fig. 5.4 (bottom figure). It is readily apparent that the $Z = 0.001$ isochrone fits the data extremely well, while the slope of the $Z = 0.004$ isochrone is not steep enough to fit the RGB. Our estimate of the abundance of NGC 643 is thus $Z = 0.001$, corresponding to [Fe/H]$= -1.3$. This metallicity is similar to values derived for the outlying clusters L 113, Kron 3, L 1 and NGC 121 (see Table 1.1 for references), although these clusters are at least several Gyr older than NGC 643 according to our age determination. Clusters which lie closer to the SMC centre than NGC 643 including NGC 411 (GC1), NGC 416 and NGC 419 (Hardy & Durand 1984) but are in the same age range (1-3 Gyr) apparently

have higher metallicities exceeding [Fe/H]= -1.

Finally, we discuss the characteristics of the HB/clump in the cluster CMD. The clump is quite densely populated with a mean R magnitude of 18.73 mag and a narrow dispersion (1σ) of 0.15 mag. The dispersion is comparable to the dispersion of 0.10 mag found from analysis of the CMD of Kron 3 (see Chapter 4) and is slightly smaller than the intrinsic dispersion of 0.18 mag for the field populations of the SMC derived in Chapter 4. The mean clump magnitude is similar to that of the eastern outlying cluster L 113, which has a value of $R = 18.7$. Most of the other outlying clusters have a mean clump magnitude at least 0.1 mag fainter than this value and Seidel, Da Costa & Demarque (1987) concluded that L 113 actually has a shorter distance modulus by 0.2 mag compared with the SMC short distance modulus. NGC 643, which also lies on the eastern side of the SMC, might therefore also lie closer to us than the SMC main body.

2.2 The Colour-Magnitude Diagram of the Field Region

The CMD for the field region near NGC 643 was constructed from the magnitude lists for CCD regions 2-16 in Appendix F and is shown in Fig. 5.6. It was originally hoped to cover 40 CCD regions in the observing run but adverse weather conditions resulted in data for only 15 regions being obtained. The CMD consists of data from 280 stars, an insufficient number to define all the major features in the CMD due to stellar populations in the SMC. The only clearly defined feature is the HB/clump, with the red giant branch and subgiant branch rather difficult to identify owing to the presence of features due to the galactic foreground. There are, however, a few main sequence stars identifiable fainter than $R = 19$ and bluer than about $V - R = 0.3$.

The main emphasis of our study of the CMD of the field region is the HB/clump, which is relatively well-populated. An examination of the CMD shows that the clump feature has a broader range in luminosity compared to the clump in the cluster CMD (Fig. 5.4). Two concentrations can be identified at around $R = 18.5$ and

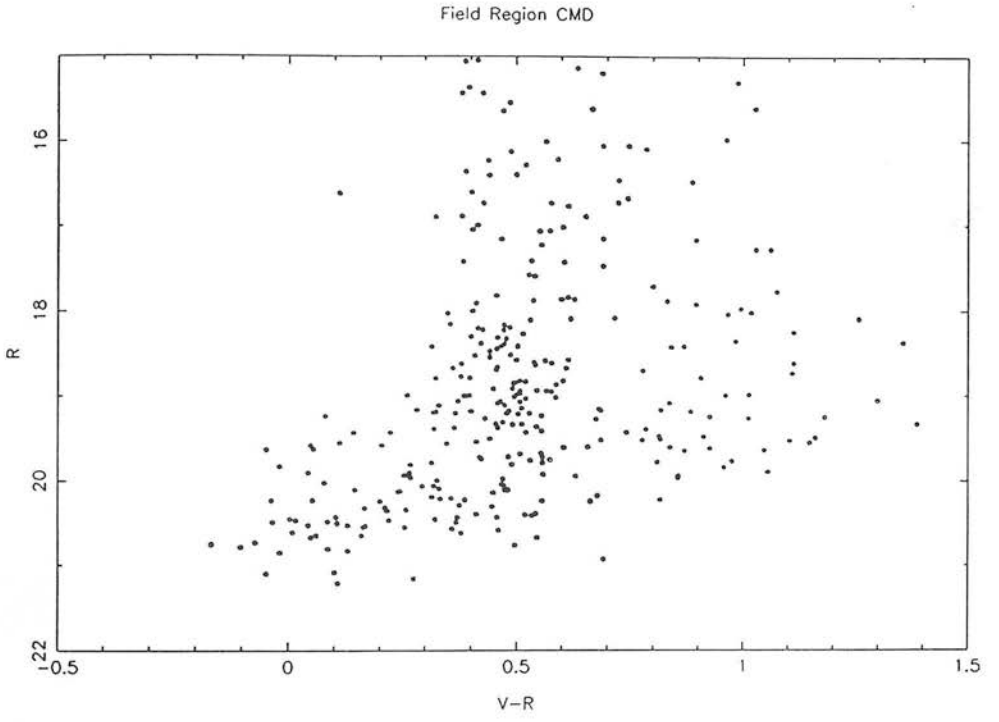

Figure 5.6: Colour-magnitude diagram $(R, V-R)$ for the field region (CCD regions 2-16).

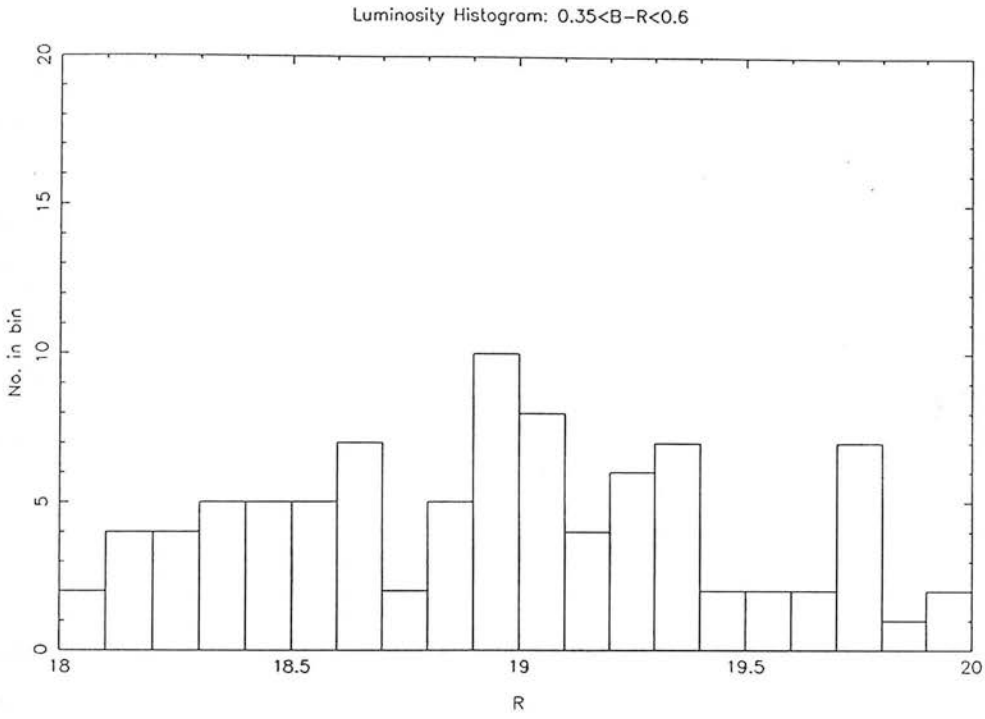

Figure 5.7: HB/clump number-magnitude histogram for the field region (CCD regions 2-16). The luminosity and colour ranges are $18 < R < 20$, $0.35 < V - R < 0.60$.

$R = 19.1$, with a conspicuous gap at about $R = 18.8$. Fig. 5.7 shows a number-magnitude histogram constructed for the luminosity range, $18 < R < 20$, for stars with $0.35 < V - R < 0.60$, which is the region of the CMD occupied by the clump stars. Although the statistics are poor and contaminated by the galactic foreground contribution, the histogram supports the existence of the two concentrations described here. The distribution can be compared with the foreground corrected clump luminosity histogram for grid region 29:21 (Appendix D), in which the region of the CCD study is located, which has a very broad luminosity distribution with a peak at $R = 19.0 - 19.1$. The peak in the CCD histogram at around $R = 19$ appears to be the stronger one and seems to coincide with the peak in the photographic data. The histograms for the neighbouring grid regions 29:22 and 29:31 (Appendix D) show a dip in the number counts in the magnitude range $R = 18.8 - 18.9$, suggesting a double-peaked distribution with peaks at $R = 18.7$ and $R = 19.1$, approximately corresponding to the two

concentrations in the clump observed in the CCD data.

From both the CCD data and the photographic data it appears that there is evidence for two separate components along the line-of-sight which contribute to a bimodal clump feature. The separation of these two peaks in the CMD is about 0.4-0.6 mag or 10-15 kpc along the line-of-sight. The two-component model described in Chapter 4 to account for the observational results determined for grid regions covering a large part of the SMC outer area is thus strengthened by the addition of the SAAO CCD data. It is interesting to note that the mean clump magnitude of the cluster NGC 643, given by $R = 18.73$ (see previous subsection), is apparently located in the 'gap' between the two concentrations in the CCD data. Its location within the nearer or farther component is thus uncertain, and it may indeed lie in a relatively depopulated zone between the two components. It would be interesting to survey other clusters in this area (e.g. L 109, L 112 and several rather inconspicuous HW clusters) in order to determine the distribution in distance of these clusters in relation to the two proposed components.

PART II: *THE 3D STRUCTURE*

CHAPTER

— 6 —

THE INTERACTING MILKY WAY — MAGELLANIC CLOUDS SYSTEM

As pointed out by Wayte (1991) the presence of a pair of Magellanic galaxies so close to a spiral galaxy such as the Milky Way means that there will be features produced as a result of the three-body interaction not seen in isolated Magellanic pairs. The global dynamics of the Milky Way-Magellanic Clouds system are a key factor in understanding the structural evolution, kinematics, star formation history and chemical evolution of the LMC and the SMC, and by a feedback process, these features may also help to define the parameters of the interactions involving the members of this system. This chapter deals primarily with the structural and dynamical prod-

ucts of the interacting system, while Chapter 10 presents a full discussion of the star formation history of the SMC including its interrelation with tidal interactions of the system. In this chapter we describe the main observational features of the interactions of the LMC-SMC-Galaxy system (Section 1) and then discuss the various models of the system that have been developed to reproduce these features (Section 2). Lastly, in Section 3, we discuss the geometrical picture of the SMC outer regions obtained by the analyses of Chapters 4 and 5 in the context of the SMC's membership of the Milky Way-Magellanic Clouds system.

1 Observational Characteristics of the Interacting System

The primary observational evidence that the Magellanic Clouds are interacting with each other comes from the existence of a common H I envelope connecting the LMC and the SMC. The strongest part of the H I envelope is the H I Bridge between the Clouds which also contains a number of young stellar associations (Irwin, Demers & Kunkel 1990). The gas in the inter-Cloud region covers some 600 square degrees and contains as much gas as the SMC itself (Wayte 1991). The Wing of the SMC, comprising numerous young stellar associations in an asymmetric prominence pointing towards the LMC, is another sign of the interaction of the Magellanic Clouds. The morphology, age distribution and origin of the Wing are considered in detail in Chapter 9. The interstellar gas belonging to the Magellanic System has been shown by polarisation measurements of stars and H II regions to be embedded in a 'pan-Magellanic' magnetic field oriented predominantly parallel to the LMC-SMC line (Mathewson & Ford 1970; Schmidt 1970). Based upon these observations, Schmidt (1970) has suggested that the Magellanic Clouds originated from the same cloud of gas.

Evidence for the interaction of the Galaxy with the Magellanic Clouds is provided by the existence of the Magellanic Stream. The Magellanic Stream is a narrow band of neutral hydrogen extending in a great circle for about 100° past the South Galactic

Pole from the Magellanic Clouds to $l = 90°, b = -30°$ (Wannier & Wrixon 1972; Mathewson, Cleary & Murray 1974). Its nature is essentially continuous but there are six main concentrations MS I—MS VI (Mathewson & Ford 1984) whose H I surface density decreases along the length of the Stream away from the Magellanic Clouds. The radial velocity decreases systematically with angular distance along the Magellanic Stream measured from its origin near the Magellanic Clouds ($l = 298°, b = -69°$), reaching a velocity of around -200 km s^{-1} at the tip of the Stream. The Magellanic Stream appears to be linked to the inter-Cloud region by the long 'spurs' extending northwards from the H I Bridge (Mathewson & Ford 1984). However, there is a sharp drop in velocity from the inter-Cloud gas to the Magellanic Stream at the beginning of the Stream which suggests that the Stream is not a simple extension of the gas in the inter-Cloud region (Wayte 1991). Despite extensive searches for stars in the Magellanic Stream (Brück & Hawkins 1983; Mathewson 1985; Irwin 1991), none have been found. The morphology and velocity profile of the Magellanic Stream have been a major spur to the construction of tidal models of the interacting Milky Way-Magellanic system (see next section).

There are a number of other observations which also may be interpreted as showing evidence for interactions between the LMC and the SMC. Mathewson & Ford (1984) have developed the hypothesis that the SMC is in a state of irreversible disintegration as a result of a relatively recent (a few 10^8 yr ago) close encounter between the Magellanic Clouds. They postulate the existence of two bodies, called by them the 'Mini-Magellanic Cloud' and the 'SMC Remnant', which are separating from each other at about 30 km s^{-1}, citing the velocity splitting in the SMC H I profiles obtained by Hindman (1967), McGee & Newton (1981) and Bajaja & Loiseau (1982) and a similar dichotomy shown by stars, H II regions and planetary nebulae in their radial velocities. This popular picture has been challenged by Martin, Maurice & Lequeux (1989), who find that there are *four* distinct H I velocity components in the SMC and state that there is no evidence for a division of the SMC into two bodies along the line-of-sight direction. In Section 3 we will compare the two-component model for the structure of the SMC outer regions described in Chapter 4 with the Mathewson &

Ford (1984) model. The whole area of research concerning the structure of the central areas of the SMC has been beset by controversy with earlier observations generally claiming the existence of very large depths of order 20-40 kpc for the SMC central regions, but many later observations indicating that the depth may be considerably smaller (see the review by Feast 1989 and references therein). Here, it suffices to say that the splitting of the SMC into two components as envisaged by Mathewson & Ford (1984) is by no means a generally accepted scenario.

The bursts of recent star formation in the LMC and SMC may also be due to the interactions of the LMC-SMC-Galaxy system. We have already mentioned the example of the SMC Wing region, whose stellar population is younger than 10^8 yr, but evidence of enhanced recent star-formation activity is provided by the existence of massive star forming regions (e.g. 30 Doradus), supergiant shells, very young clusters and OB associations in the Magellanic Clouds (Westerlund 1989; 1990). The fact that the globular clusters of the Magellanic Clouds span an age range from older than 10 Gyr to younger than 10^7 yr as opposed to exclusively older than 10 Gyr for the Galaxy has been used by Fujimoto & Kumai (1991) to argue that the Magellanic globular clusters were formed from colliding gas clouds resulting from tidal forces induced during close encounters between the Magellanic Clouds. The detailed role of tidal interactions in stimulating star formation in the SMC will be discussed in Chapter 10.

2 Models of the Interacting System

As already mentioned, most models of the Milky Way-Magellanic Clouds system were motivated by the quest to achieve a satisfactory representation of the observational features of the Magellanic Stream. As a by-product of these investigations the global dynamics of the LMC-SMC-Galaxy system could be examined and other key features of the interacting system could also be modelled to some extent. Early models of the interacting system involving particle simulations by several workers (Fujimoto &

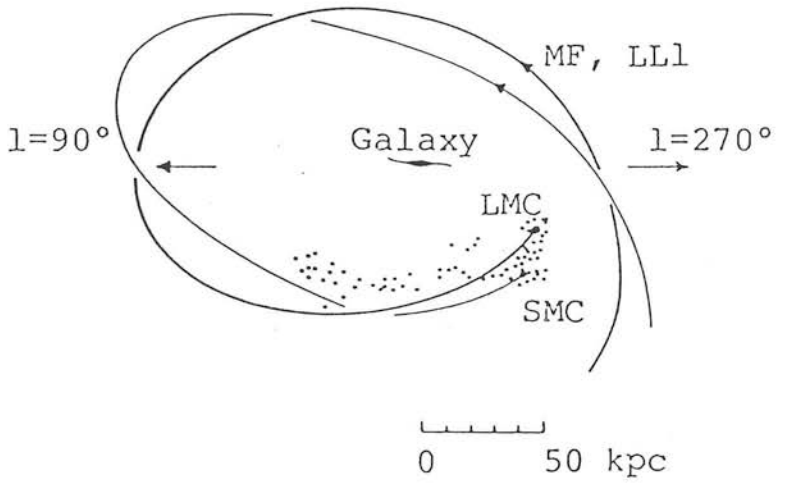

Figure 6.1: Tidal models of the Magellanic Stream showing orbits of the Magellanic Clouds around the Galaxy, reproduced from Fig. 2b of Fujimoto & Murai (1984). The orbits shown are the ones favoured by both Murai & Fujimoto (1980 - MF) and Lin & Lynden-Bell (1982 - LL1). The orbits of the Magellanic Clouds are approximately perpendicular to the galactic plane and are shown here as seen from the direction of $l = 180°, b = 0°$. The Magellanic Stream has been simulated by a few hundred test particles.

Sofue 1976; 1977; Lin & Lynden-Bell 1977 and Davies & Wright 1977) either could not successfully reproduce the high-negative radial velocities of the Magellanic Stream or satisfactorily model its observed geometry. However, these early models established that the orbit of the Magellanic Clouds around the Galaxy is approximately perpendicular to the galactic plane. Murai & Fujimoto (1980) and Lin & Lynden-Bell (1982) subsequently confirmed the sense of the orbit, i.e. counter-clockwise around the galactic centre as seen from the present position of the sun with the Magellanic Stream trailing behind the Magellanic Clouds. In Fig. 6.1 the orbits derived by these latter models are shown (the figure is reproduced from Fig. 2b of Fujimoto & Murai 1984). The more sophisticated model of Murai & Fujimoto (1980) (hereafter MF) (see also Fujimoto & Murai 1984; Murai & Fujimoto 1986) incorporated a massive galactic halo which produces a constant rotation velocity of 250 km s^{-1}, and succeeded in reproducing both the velocity profile of the Magellanic Stream and its overall geometrical appearance. Based on the success of this model in reproducing the key features of

the Magellanic Stream, some major aspects of the global dynamics of the interacting system which are favoured by this model have become generally accepted. The most important of these is the recent LMC-SMC close encounter about 2×10^8 yr ago proposed by the MF model, in which the centres of the the SMC and the LMC approached each other to within a few kpc.

Mathewson *et al.* (1987) (hereafter MWFR) (see also Wayte 1991) favour a different model for the origin of the Magellanic Stream. Their major objections to the proposition that the Stream is a *tidal* feature are the absence of stars in the Stream and the predominantly radial motion of the Magellanic Stream, whereas the tidal model requires a significant transverse motion. These authors favour a model (the ram pressure model) in which the Magellanic Stream was produced by interaction of the galactic halo environment (including high velocity clouds) with the gas in the inter-Cloud region. Nevertheless, they do not dispute the existence of the recent encounter between the Magellanic Clouds, which gave rise to the gas in the inter-Cloud region. Both the orbital computations of MF and MWFR involved 'integrating back' the equations of motion for the Magellanic Clouds and the Galaxy for a range of input parameters. The MF models included three bodies — the Galaxy, LMC and SMC and involved searching for bound orbits for the LMC-SMC binary system lasting over the whole of the past 10 Gyr. MWFR, on the other hand, used four bodies in their computations — the Galaxy, LMC, 'Mini-Magellanic Cloud' and 'SMC Remnant' (see Mathewson & Ford 1984). Both sets of workers find that a close encounter between the LMC and the SMC happened a few 10^8 yr ago. The precise timing of the event — MF propose 2×10^8 yr ago while MWFR propose 4×10^8 yr ago — was found by MWFR to depend on the adopted mass for the LMC. Wayte (1991) lists a number of signs that a relatively recent encounter event occurred. Among them are the existence of young stars in the inter-Cloud region, the unbound nature of much of the gas in the inter-Cloud region, the velocity dispersion of the Magellanic Stream and the velocity splitting between the 'Mini-Magellanic Cloud' and the 'SMC Remnant'. To this evidence should also be added the findings of the kinematical study of Hatzidimitriou *et al.* (1991) (see also Hatzidimitriou, Cannon & Hawkins 1991) of

the north-eastern outlying areas of the SMC which indicate a radial velocity-distance correlation suggesting that a tidal disturbance occurred a few 10^8 yr ago. Therefore it can be considered that the existence of the recent encounter event is well established both from an observational and a theoretical point of view.

In the later version of the MF model (see Murai & Fujimoto 1986) the assumption that the Magellanic Clouds have been bound to each other for 10 Gyr was relaxed and a more satisfactory representation of the Magellanic Stream was found if the SMC, previously orbiting independently around the Galaxy, was captured by the LMC about 1.7×10^9 yr ago. This later version of the MF model retains the prediction that a close encounter between the LMC and the SMC occurred about 2×10^8 yr ago. Given that there are still uncertainties in whether the Magellanic Stream is indeed a tidal feature, the most secure result emerging from the models of the interacting Galaxy-LMC-SMC system is the existence of the recent encounter event between the Magellanic Clouds. Even if it were accepted that the Magellanic Clouds have a common origin and were bound to each other for the past 10 Gyr, the epochs of earlier close encounters between the Magellanic Clouds are rather uncertain. A comparison of Figs 3a and 3b from MF showing the variation of the distance between the LMC and the SMC for different sets of input parameters indicates that the timing of such encounters is sensitive to the precise values of these parameters. The range of possible input parameters may be greatly reduced in future if the transverse velocities of the LMC and the SMC could be accurately determined by proper motion studies (see Tucholke & Hiesgen 1991).

Other results of the MF models pertain to the dynamical interaction between the Magellanic Clouds and the Galaxy. The implicit assumption of the MF models is that the Magellanic Clouds have been satellites of our Galaxy for the past 10 Gyr. MWFR, however, support the view that the Magellanic Clouds came under the control of the Galaxy only recently, being in hyperbolic orbits which accidentally pass near the Galaxy (see also Mathewson & Ford 1984). The MF models find that the binary state of the Magellanic Clouds could only be preserved if the perigalactic distance of the LMC is at least 40 kpc. Furthermore, they show that the distance between the

Magellanic Clouds and the Galaxy decreases in an oscillatory manner due to dynamical friction on the LMC (Tremaine 1976). Therefore, at the present epoch the Magellanic Clouds are closer to the Galaxy than at any previous time in their history, having experienced a very recent perigalacticon about 4×10^7 yr ago.

Concluding this section, orbital computations and particle simulations modelling the tidal interactions of the Milky Way-Magellanic Clouds system have made a valuable contribution to the understanding of its global dynamics. In particular, the relatively recent close encounter between the Magellanic Clouds about 2×10^8 yr ago is a well established result of these computations. Uncertainty remains, however, on the past duration of the existence of the Magellanic Clouds as satellites of the Galaxy and that of the binary state of the Magellanic Clouds themselves.

3 The Interacting System and the Geometry of the SMC

In this section we consider the geometry of the SMC, as revealed by the study of the 3D structure of the outer regions based on the luminosity and surface distribution of HB/clump stars in Chapter 4, in relation to the global dynamics of the Galaxy-LMC-SMC system. Previous studies of the geometry of the SMC have concentrated almost entirely on the young populations in the central regions of the SMC, and as already discussed, the picture presented by these studies is far from clear at present. The stellar populations represented by the HB/clump stars are mostly older than about 2 Gyr (as will be shown in more detail in Chapter 8) and therefore the structure of the SMC outer regions delineated by these populations is a record of the tidal perturbations experienced by the old stellar component of the SMC. With the exception of the Wing feature, these older populations extend several degrees in the plane of the sky further out than the young stellar populations concentrated towards the SMC centre. Therefore, the older populations are also likely to delineate the outer reaches of the SMC in the line-of-sight direction, and may therefore present a more reliable picture of the total extent of the SMC in all directions than can be obtained with younger

populations.

Firstly, we compare the 2D projected distribution of the old stellar component of the SMC, represented by the HB/clump stars, shown in Fig. 4.3, to the H I distribution in and around the SMC shown by the H I map of Mathewson & Ford (1984). To first order, the gaseous and stellar distributions should exhibit a similar response to tidal disturbances, and may thus help us to understand the nature of these disturbances. It is possible that the closeness of the recent collision between the LMC and the SMC (see previous section) may have resulted in hydrodynamical interaction between the gaseous envelopes of the LMC and the SMC and therefore the observed distribution of H I may not be due to tidal perturbations alone. The H I distribution in the SMC is extended towards the north, where it links up with the Magellanic Stream, and also towards the north-west, this extension perhaps representing the 'tail' produced in the LMC-SMC two-body interaction (Wayte 1991). There is also the bridge of gas connecting the Magellanic Clouds which extends from the eastern side of the SMC, with the strongest concentration in the Wing region. The extent of the H I gas in the west and south-west is smaller than in other areas with the H I contours bunching up particularly at the south-western edge.

The larger radial extent of the stellar distribution in the northern outer area of the SMC compared to the eastern and western directions was noted in Chapter 4 and may perhaps be linked to the extended H I distribution towards the northern direction. According to the MF models the Magellanic Stream is due to gas predominantly originating in the SMC being extended by the tidal field of the Galaxy. The influence of the galactic tidal field may perhaps also be invoked to account for the more extended stellar distribution in the northern direction. Interestingly, Lynden-Bell (1982) has suggested that for two dwarf spheroidal satellites of our Galaxy, Ursa Minor and Draco, for which the position angles of their major axes lie close to the plane defined by the Magellanic Stream, the tidal field of the Galaxy has resulted in elongation along this direction. The N-S elongation of the SMC suggested by Fig. 4.3 in a direction roughly parallel to the Magellanic Stream may also be connected to the phenomenon

of the alignment of the major axes of the Galaxy's satellites with the direction of the Magellanic Stream.

The stellar distribution appears to follow the H I distribution in the west and south-west, possessing a smaller radial extent in these directions than elsewhere. It is therefore probable that the south-western area was not significantly influenced by tidal disturbances as the small depths in the line-of-sight in these areas confirm (see Chapter 4). There is no indication of the existence of a stellar counterpart to the NW extension in the H I distribution, which is perhaps not surprising in view of the rather tenuous nature of the H I gas in this feature. In the east/south-eastern area, the old stellar distribution does not show any concentration in the Wing region, but in the outermost areas the HB/clump contours start to become perpendicular to the LMC-SMC line. It can be concluded that although the older stellar distribution projected on the plane of the sky does not clearly show the existence of optical counterparts to the H I features created by tidal interactions of the Galaxy-LMC-SMC system, there are some indications that the projected morphology of the SMC has been affected by these disturbances.

We next consider the question of whether the SMC exceeds its tidal radius and whether it is currently in the process of disintegration or at least losing some of its mass. Welch *et al.* (1987) suggested values of 4 and 9 kpc for the tidal radius of the SMC based on two different estimates for the mass of the Galaxy, but we will attempt to derive a more accurate value based on revised estimates of the mass of the Galaxy within 60 kpc of the galactic centre, using the formula from Binney & Tremaine (1987) (p.452). We employ the estimates of the mass of the Galaxy within 60 kpc of the galactic centre given by Norris & Hawkins (1991) of between 6.3 and $10.2 \times 10^{11} M_{\odot}$ together with a mass of $1.5 \times 10^{9} M_{\odot}$ for the SMC lying at a distance of 60 kpc from the Galaxy. The resulting tidal radius lies between 5.6 and 4.7 kpc. These figures would appear to be compatible with the projected radial extent of the SMC in the western outer regions which is between 5 and 6 kpc (see Chapter 4). Based on this estimate it appears possible that in the more extended northern outer areas the

SMC may exceed the tidal radius by a small fraction and is perhaps losing some stars.

We now consider whether the dimensions of the SMC measured along the line-of-sight direction are greater than the tidal diameter (about 12 kpc). We are limited to some extent in that the depths derived in Chapter 4 on the basis of the luminosity distribution of HB/clump stars are essentially dispersion quantities, and therefore our definition of the depth of the SMC is somewhat arbitrary. For a purely Gaussian distribution of distance moduli for stars in given grid region, the 2σ depth is the depth within which 68 per cent of the stars lie and the 4σ depth is that within which 95 per cent of the stars lie. In the western outer area of the SMC the average depth is below the tidal diameter even if the 4σ depth is considered. The situation becomes more complicated, however, for the eastern regions, where the clump luminosity distributions appear to be non-Gaussian. Apart from the south-eastern regions near the boundary between Fields 29 and 30, nearly all the other 2σ depth determinations are less than or below 13 kpc. Therefore, in about 80 per cent of the outer area of the SMC the *bulk*, i.e. about 70 per cent, of the stellar population lies within a range of distances less than or equal to that given by the tidal diameter. However, if the 4σ depth is a realistic estimate of the total range of distances enclosing the stellar population, then the tidal diameter is exceeded in the whole of the eastern outer area. In the south-eastern areas where the 2σ depths are greater than 20 kpc, the fact that the tidal diameter is exceeded is not in doubt, and it is clear that some stars are being lost from the SMC.

It is instructive to compare the depths determined for the outer regions of the SMC with those predicted by the MF particle simulations. MF optimised the choice of the initial velocities of the SMC and the LMC in order to ensure the best representation of the Magellanic Stream. Fig. 6.2, which has been reproduced from Fig. 7 of MF, shows the distribution of the radial distribution of test particles at the present time in the SMC and the Magellanic Stream. A close examination of this figure reveals that the test particles of the SMC are stretched out along the line-of-sight direction with an overall extension of 30 kpc, a figure which would seem to be compatible

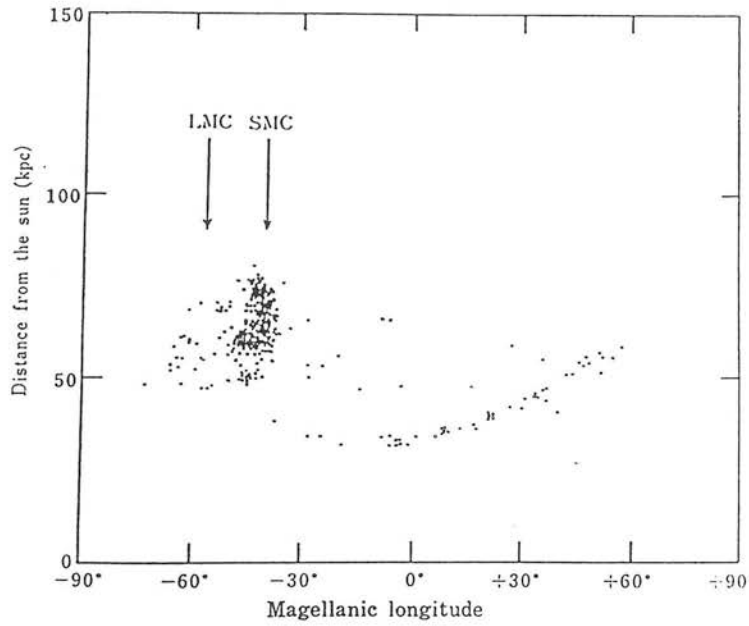

Figure 6.2: The radial distribution of test particles in the Magellanic system according to the particle simulations of Murai & Fujimoto (1980). The figure has been reproduced from Fig. 7 of that paper. The distances of the particles are shown as a function of Magellanic longitude, as defined by Wannier & Wrixon (1972).

with the large depths occurring in the south-eastern outer regions. This simulation shows that extensive disruption of the SMC occurring predominantly along the line-of-sight direction is to be expected as a result of the relatively recent close encounter between the Magellanic Clouds. Murai & Fujimoto (1986) confirm that as a result of this encounter: "...the SMC was severely disturbed, resulting in the formation of the Magellanic Stream. The outer part of the SMC is now being disrupted." Returning to MF's Fig. 7, both a detached portion in front and a tail-like extension behind the main body (defined by the densest particle concentration) can be seen. These features qualitatively resemble, respectively, the near component of the two-component model described in Chapter 4, and the possible 'tail' extending behind the rest of the SMC which is responsible for the very large depths found in the south-eastern outer regions. There are therefore grounds for optimism that the observed structure of the SMC may be modelled in some detail by such particle simulation experiments.

We consider now the relation of the two-component model described in Chapter 4 to the model of Mathewson & Ford (1984) proposing the existence of two entities in the SMC — the 'Mini-Magellanic Cloud' (MMC) and the 'SMC Remnant' (SMCR). According to Mathewson & Ford: "...the low velocity component must be in front of the high velocity component (Hindman 1964). It is assumed that the lower velocity component is the SMCR as it is the more intense. The SMCR is more compact than the MMC which extends further to the north-east." In the two-component model described in Chapter 4, the far component extends over most of the outer area of the SMC, whereas the near component extends over the eastern part only. Since the far component is the more extensive of the two, it may perhaps be associated with the SMCR, but according to the above description, the SMCR lies *in front* of the MMC. However, in two further papers by Mathewson, Ford & Visvanathan (1986;1988) these authors established that the Cepheids in the north-eastern part of the Bar are on average 10-15 kpc *closer* than those in the south-west and that the H I velocity structure is more complicated than originally believed. Furthermore, in their 1986 paper, they presented evidence for a possible bifurcation along the line-of-sight in their so-called 'Bridge' region (near the luminous inner Wing) on the eastern side of the 'Bar'. The

two concentrations of Cepheids found in the 'Bridge' area are separated by 8 kpc and appear to be consistent with the two-component model of Chapter 4 in which the proposed structures are separated by 7-11 kpc along the line-of-sight in the outlying area further to the east of the 'Bridge' region. At the present stage it appears that the structure and kinematics of the central areas of the SMC are too complex to support a simple two-component model, but there is some indication that there are two separate structures to the east of the SMC Bar, which fits well with the two-component picture formulated in Chapter 4.

In this chapter we have reviewed the major structural and dynamical products of the interactions of the interacting Milky Way-Magellanic Clouds system, and examined some of the tidal models that have been developed to account for them. A major result of these models is that a relatively recent close encounter between the LMC and the SMC occurred about 2×10^8 yr ago, but there remains considerable uncertainty as to the origin of the Magellanic Clouds binary system in the environment of our Galaxy. The large depths found in the eastern outer regions (Chapter 4) show that the SMC exceeds the tidal radius imposed by the gravitational field of the Galaxy, and is therefore likely to be splitting apart. A comparison of the observed geometry of the SMC outer regions with the results of the particle simulations of MF confirms that the relatively recent encounter between the Magellanic Clouds has caused extensive tidal disruption in the SMC giving rise to a very large overall line-of-sight extension. Major progress on understanding the global dynamics of the Galaxy-LMC-SMC system should occur when reliable proper motions are obtained for the Magellanic Clouds.

PART III: *THE AGE DISTRIBUTION*

CHAPTER

— 7 —

THE MAIN SEQUENCE AND YOUNGER POPULATIONS

The Magellanic Clouds are believed to have experienced a markedly different star formation history from the Galaxy, with the LMC and SMC considered to be less evolved galaxies compared to our own. The SMC in particular is characterised by a low metal content, high gas-to-total mass fraction and bluer integrated colours (Lequeux 1984) compared to normal spiral galaxies and in this respect is typical of dwarf irregular systems. As a dwarf irregular galaxy distinguished by its membership of an interacting system of galaxies, the SMC is able to provide us with insights into the evolutionary development of dwarf irregular galaxies as well as the role of external

dynamical interactions in stimulating star formation events. The relative importance of the role of local star formation processes internal to the SMC with respect to that of external disturbances is one of the key questions which has yet to be properly answered.

The ultimate aim of studies of the stellar content of the outer regions of the SMC is to achieve a complete description of its star formation history from the age spectrum and spatial distribution of its stellar population. Most of our knowledge of the age distribution of the outer parts of the SMC comes from colour-magnitude diagram studies of star clusters and adjacent regions in the SMC general field as well as from a small number of larger area studies of the SMC field population at several locations in the outer regions (see Table 1.1 for a bibliography of deep, CCD-based studies). In general, because of the small areas covered by these studies, and the fact that the observations were usually obtained with some purpose other than the detailed study of the stellar population structure, we do not yet have a clear idea of the large-scale distribution of various stellar populations belonging to different ages from which we can begin to reconstruct a coherent picture of the past star formation history of the SMC.

Based on our extensive observational data, which covers most of the outer area of the SMC, we are able to investigate in a systematic way the distributions of different stellar populations over the surface of the SMC. We begin, in this chapter, by reviewing the properties of the main sequence to uncover the relatively recent star formation history of the outer regions of the SMC up to about 2 Gyr ago. In the following chapter, older populations are considered and in Chapter 9, we pursue in more detail the nature of stellar populations in the Wing region before embarking on a full discussion of the star formation history of the SMC in Chapter 10.

In this chapter, firstly we consider the use of main sequence populations as age calibrators (Section 1); secondly, we examine the surface distribution of main sequence populations at various magnitude cuts (Section 2); and finally, in Section 3; we consider the main sequence luminosity functions of various parts of the SMC outlying regions.

1 The Age-Dating of Main Sequence Populations

The main sequence (MS) chronology is one of the main tools for investigating the ages of stellar populations in star clusters and field populations. In particular the location of the MS turnoff point (i.e. the region in the Hertzsprung–Russell diagram where the stars deviate from their core-hydrogen-burning locus) is a direct measure of the age. The age-dating procedure involves the comparison of theoretical isochrones with the observed colour-magnitude diagram of the stellar population. From consideration of the luminosity functions associated with such isochrones, Da Costa, Mould & Crawford (1985) suggested that the best feature to use to date clusters (or coeval populations) in the age range of a few Gyr is the 'tip' of the MS, i.e. the point on the isochrone where rapid evolution to the red begins. The reason for this is that the blueward jump predicted by the isochrones at the point of core-H-exhaustion is not actually observed, making the definition of the turnoff difficult for these ages.

The age calibration which we will employ is the revised calibration of Hodge (1987a), based on observational data for a large number of Magellanic Cloud clusters. The ages of 29 calibrating clusters, ranging in age from 50 million to 10 Gyr, were derived using main sequence fitting of the isochrones of vandenBerg (1985) and other models used in Hodge's first attempt at an age calibration (Hodge 1983). The relation between the B magnitude of the MS 'tip', given by the magnitude of the brightest blue star, and log (cluster age) was found to be well represented by a least-squares linear relation. For the SMC, the calibration gives

$$\log_{10} \tau(yr) = 2.58 + 0.335B.$$

Inspection of the CMDs in Appendix C shows that the MS locus has a roughly constant colour of $B - R = -0.1$ above the effective magnitude limit, therefore the relation for the R magnitude of the MS 'tip' becomes

$$\log_{10} \tau(yr) = 2.55 + 0.335R. \qquad (1)$$

According to eqn.(1) the age of the oldest MS population that can be detected above our effective magnitude limit at $R = 20$ is 1.8 Gyr. We present in Table 7.1 the

Age (Gyr)	MS tip (R mag.)
0.05	15.4
0.1	16.3
0.2	17.2
0.3	17.7
0.4	18.1
0.5	18.4
0.6	18.6
0.7	18.8
0.8	19.0
0.9	19.1
1.0	19.3
1.2	19.5
1.4	19.7
1.6	19.9
1.8	20.0
2.0	20.2
2.2	20.3
2.4	20.4
2.6	20.5

Table 7.1: The age versus MS 'tip' relation for SMC populations derived from the age calibration of Hodge (1987a).

apparent R magnitudes for the MS 'tips' for different stellar ages for populations located at the SMC short distance modulus, tabulated for convenient reference.

Hodge's calibration incorporates the effects of reddening towards the SMC, which is generally considered to be small. The value derived for the outer regions of the SMC in Chapter 3 was $A_R = 0.07$ mag and although higher reddening values may exist for the Wing region where the H I surface density is greater, the size of the differential reddening was considered small enough to be neglected. Regarding the distance modulus of the SMC, Hodge's calibration has made use of the short distance modulus scale for the Magellanic Clouds which has come to be favoured recently and has been adopted throughout this project (see Chapter 3). However, non-uniform distance moduli for different areas of the SMC can result in significant adjustments to the age calibration. Caldwell & Coulson (1986) derived distance moduli about 0.3 mag less than that of the main body of the SMC for Cepheids in the Wing region,

while Seidel, Da Costa & Demarque (1987) have argued that the distance modulus of the eastern outlying cluster L 113 is about 0.2 mag less than that of several other outlying clusters. Results from the investigation of the 3D structure of the SMC in Chapter 4 indicate the existence of large depths of at least 20 kpc in the south-eastern outer regions and depths exceeding 10 kpc over the whole of the eastern area. Fig. 4.9 shows that the front section of the NE area may extend to distances as small as 11 kpc less than the standard distance of the SMC given by the short distance modulus. This corresponds to dm=18.34, i.e. more than 0.4 mag less than the short distance modulus (18.8) of the SMC (main body). For MS populations with a distance modulus of 18.34 the corresponding ages are about 40 per cent higher than those given by eqn.(1) for a given apparent magnitude. This results in an upper age limit of 2.5 Gyr for such populations to be detected above the magnitude limit.

An additional problem not included in conventional evolutionary models employed by the Hodge calibration is the effect of convective overshooting. Stars with masses in excess of about 1.5 solar masses have convective cores. The MS lifetime of such stars and the luminosity they reach before evolving to the red depend on the extent to which the MS evolution is prolonged by the internal mixing that arises from overshooting outside the convective core. The implications of convective overshooting for age determinations of Magellanic Cloud clusters are discussed by Bertelli, Bressan, & Chiosi (1985). Their Fig. 18 gives the relationship between the main sequence termination luminosity and age for models incorporating convective overshoot. Using this figure, the ages of stars younger than 1 Gyr determined using our derived age calibration may be underestimated by around 50 per cent. For older ages the two methods give rapidly converging results. Although we shall adopt an age calibration based on classical evolutionary models we should be aware that ages under 1 Gyr quoted below may be subject to revision if models incorporating convective overshooting were to gain wider acceptance.

2 The Surface Distribution of Main Sequence Stars

Blue main sequence stars visible above the plate limit provide us with the possibility of mapping the surface distribution of fairly young stars representing different age groups up to a maximum of 2 Gyr by applying different limiting magnitudes to the data. Using the full database from all six survey fields we selected main sequence (MS) populations on the basis of their locations in colour-magnitude space using limits of $R < 20, B - R < 0.1$. For these populations, there is essentially no contribution from the galactic foreground to the MS counts as the MS stars lie blueward of the 'yellow ridge' due to spheroidal component subgiants in the Galaxy. For different magnitude limits, $R < 20.0, < 19.5, < 19.0, < 18.5, < 17.5$ and < 16.5, number counts for the MS population were performed in small sized pixels and processed as described in Chapter 3 (Section 3) in order to produce a series of surface contour plots, shown in Figs 7.1 (a–f). According to eqn.(1) and Table 7.1 the age groups represented in each of these plots are $\tau < 1.8$ Gyr ($R < 20.0$), $\tau < 1.2$ Gyr ($R < 19.5$), $\tau < 0.8$ Gyr ($R < 19.0$), $\tau < 0.6$ Gyr ($R < 18.5$), $\tau < 0.25$ Gyr ($R < 17.5$), and $\tau < 0.1$ Gyr ($R < 16.5$). Fig. 7.1 (a) may be affected by incompleteness towards faint magnitudes but the continuity of the contours between adjacent fields indicates that differences in the levels of completeness between different fields fainter than $R = 19.5$ is not a serious problem.

We move now to a brief discussion of the main features of the MS distribution corresponding to the distribution of stars younger than about 2 Gyr (Fig. 7.1 (a)) before discussing how these features change at successively brighter magnitude cuts. The complete absence of MS stars above the detection limit in the north-west is striking, while there is a considerable MS population over a large part of the eastern and southern area. Very prominent in the east is the SMC Wing feature, which is known to consist of extreme Population I objects such as blue and yellow supergiants, OB associations and H II regions (Westerlund 1970). Also conspicuous are a 'bulge' in the surface distribution in the SSE direction, and the extended distribution in the north-east out to about 5° from the SMC centre. Along the NE-SW line on either side

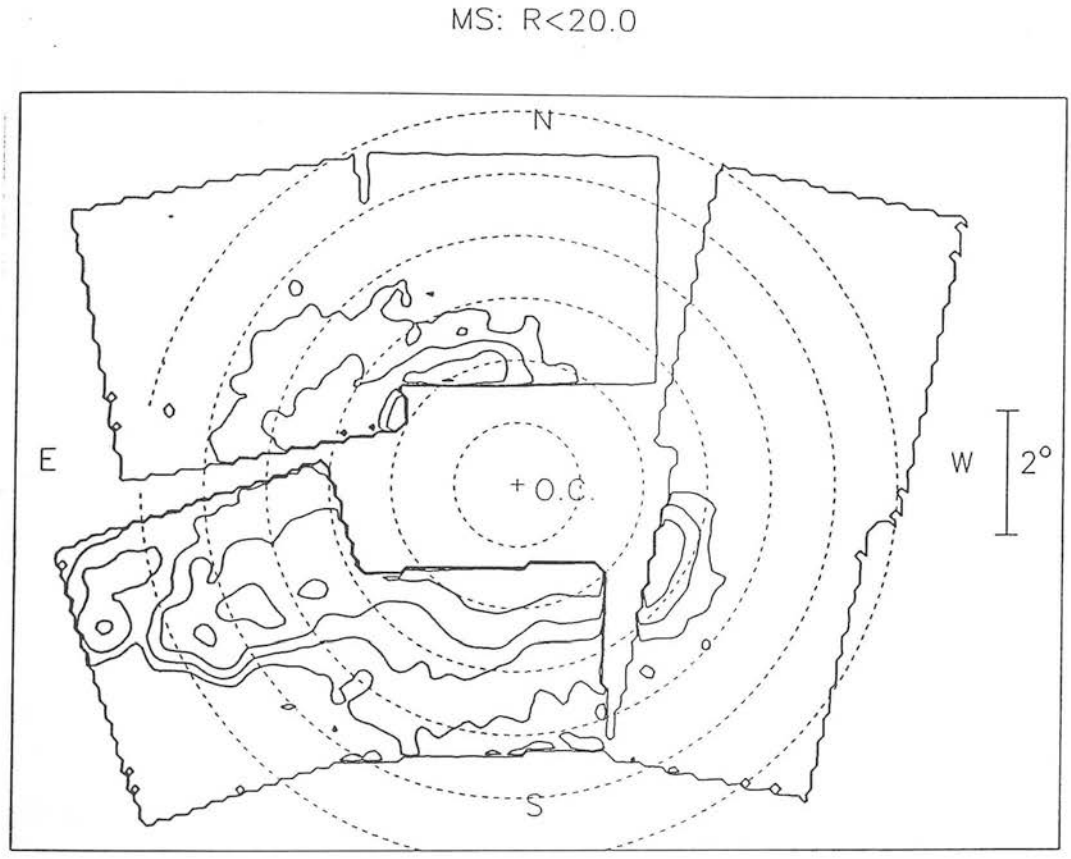

Figure 7.1: (a). Contour plot of the surface distribution of main sequence stars with $B - R < 0.1$, $R < 20.0$ for all six survey fields. The contour levels generally increase towards the SMC centre, with successive levels a multiple of three times the level below. The upper age limit represented by these populations is $\tau < 1.8$ Gyr and the lowest contour level is 1.0 stars per pixel. Concentric radii at 1,2,3,4,5,6 degrees from the SMC optical centre are shown. To obtain the number of stars per square degree multiply counts per pixel by 115.

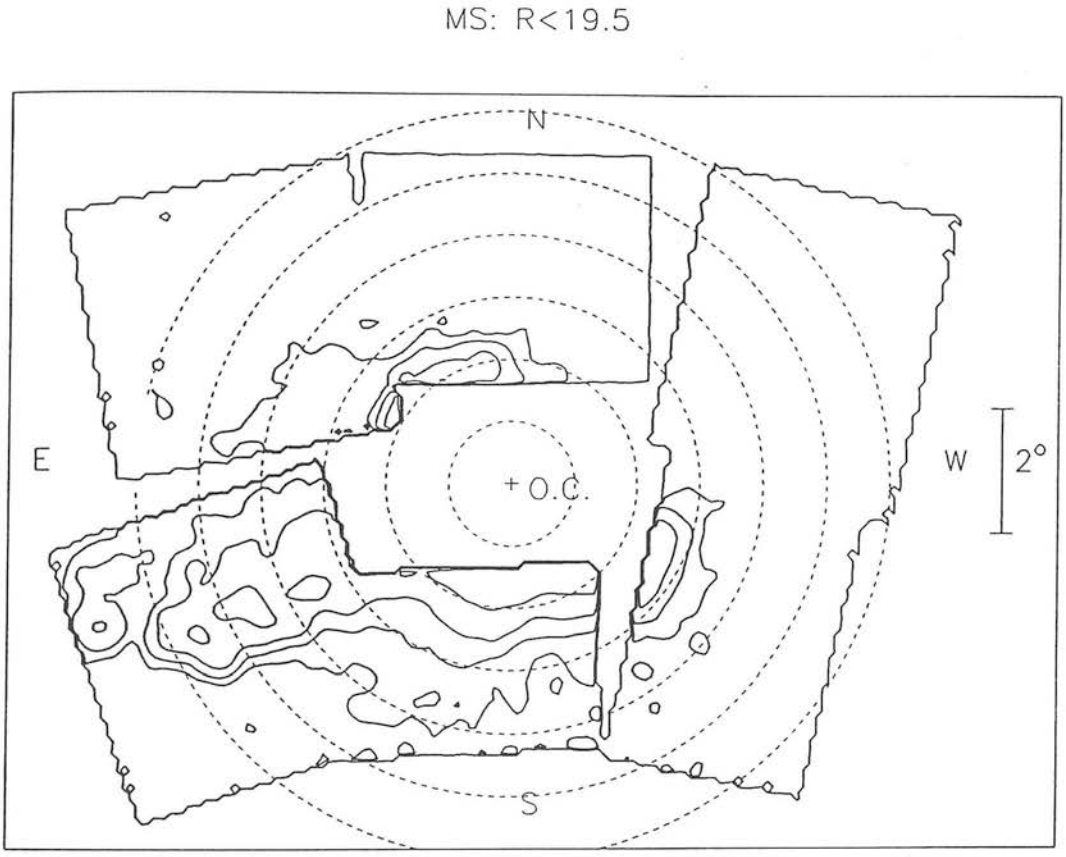

Figure 7.1: (b). Contour plot of the surface distribution of main sequence stars with $B - R < 0.1$, $R < 19.5$ for all six survey fields. The contour levels generally increase towards the SMC centre, with successive levels a multiple of three times the level below. The upper age limit represented by these populations is $\tau < 1.2$ Gyr and the lowest contour level is 0.8 stars per pixel.

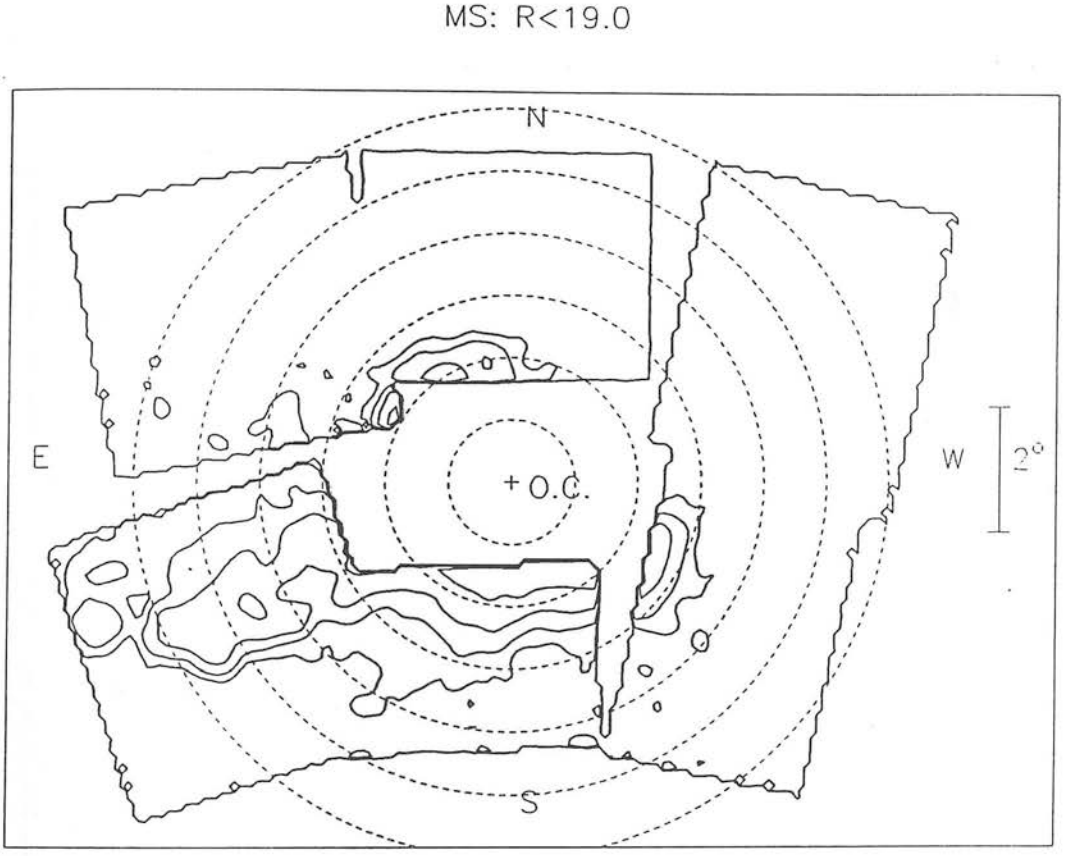

Figure 7.1: (c). Contour plot of the surface distribution of main sequence stars with $B - R < 0.1$, $R < 19.0$ for all six survey fields. The contour levels generally increase towards the SMC centre, with successive levels a multiple of three times the level below. The upper age limit represented by these populations is $\tau < 0.8$ Gyr and the lowest contour level is 0.7 stars per pixel.

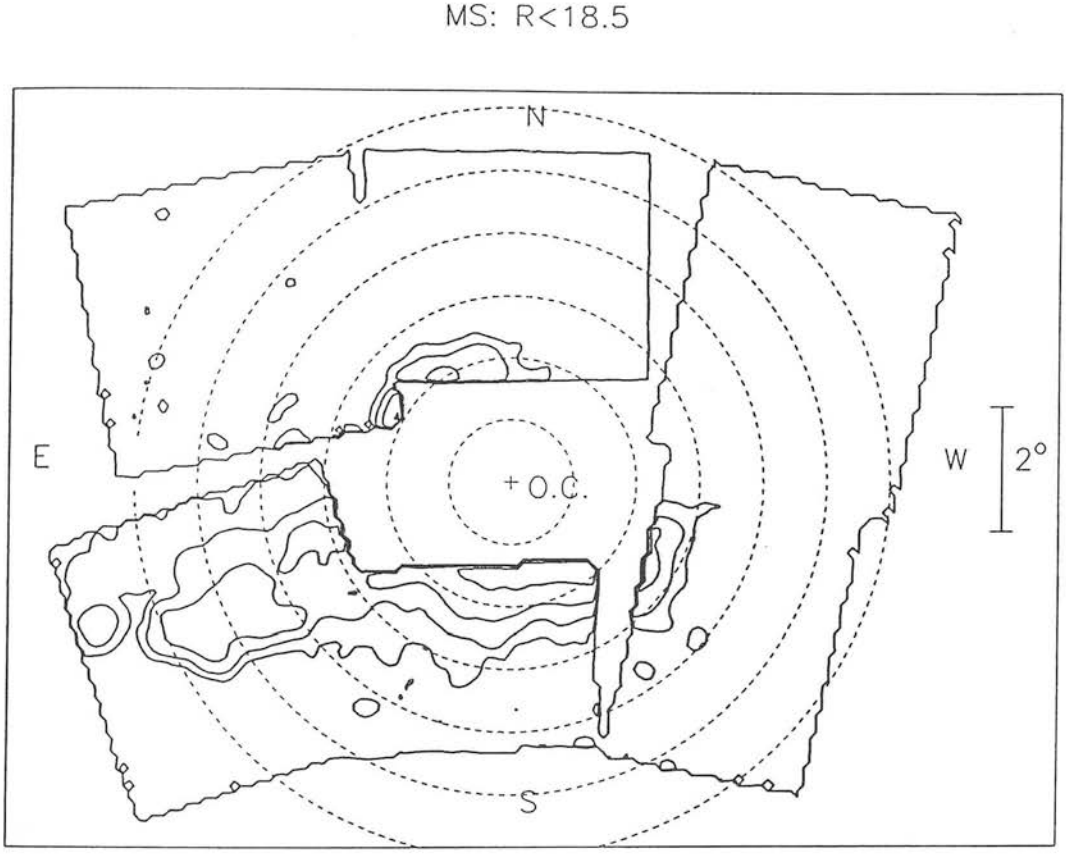

Figure 7.1: (d). Contour plot of the surface distribution of main sequence stars with $B - R < 0.1$, $R < 18.5$ for all six survey fields. The contour levels generally increase towards the SMC centre, with successive levels a multiple of three times the level below. The upper age limit represented by these populations is $\tau < 0.6$ Gyr and the lowest contour level is 0.6 stars per pixel.

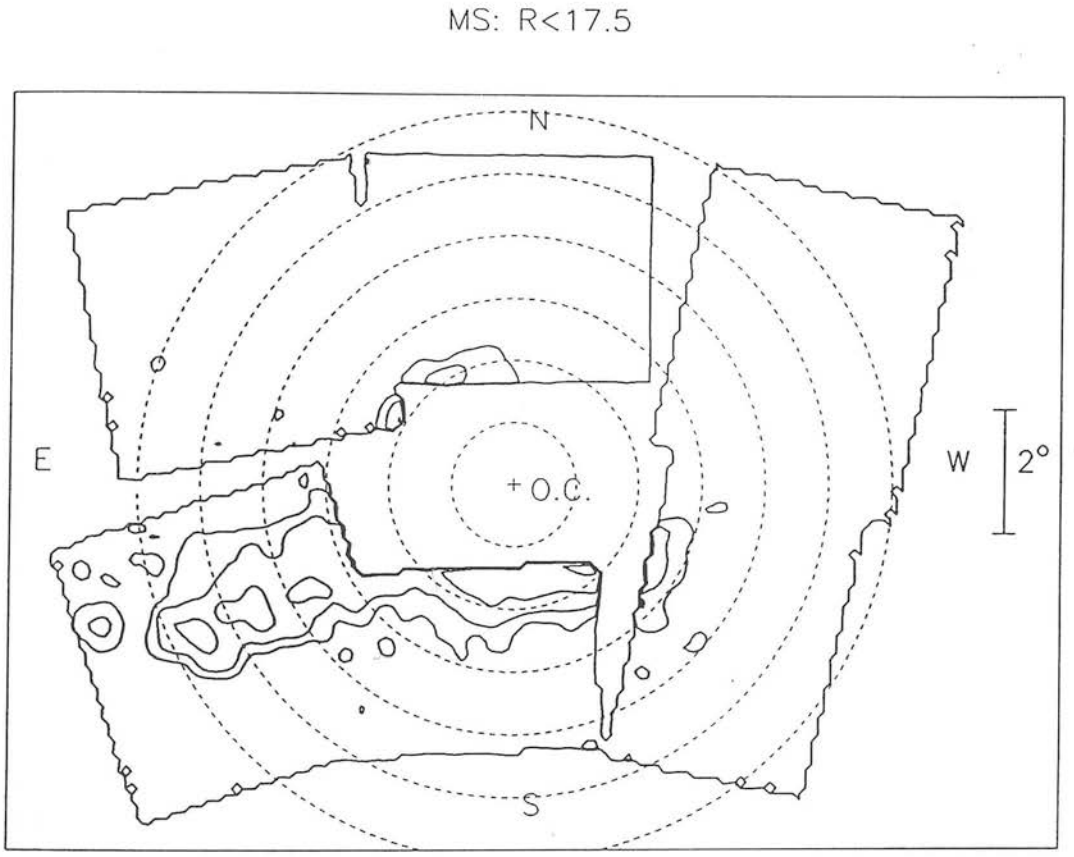

Figure 7.1: (e). Contour plot of the surface distribution of main sequence stars with $B - R < 0.1$, $R < 17.5$ for all six survey fields. The contour levels generally increase towards the SMC centre, with successive levels a multiple of three times the level below. The upper age limit represented by these populations is $\tau < 0.25$ Gyr and the lowest contour level is 0.5 stars per pixel.

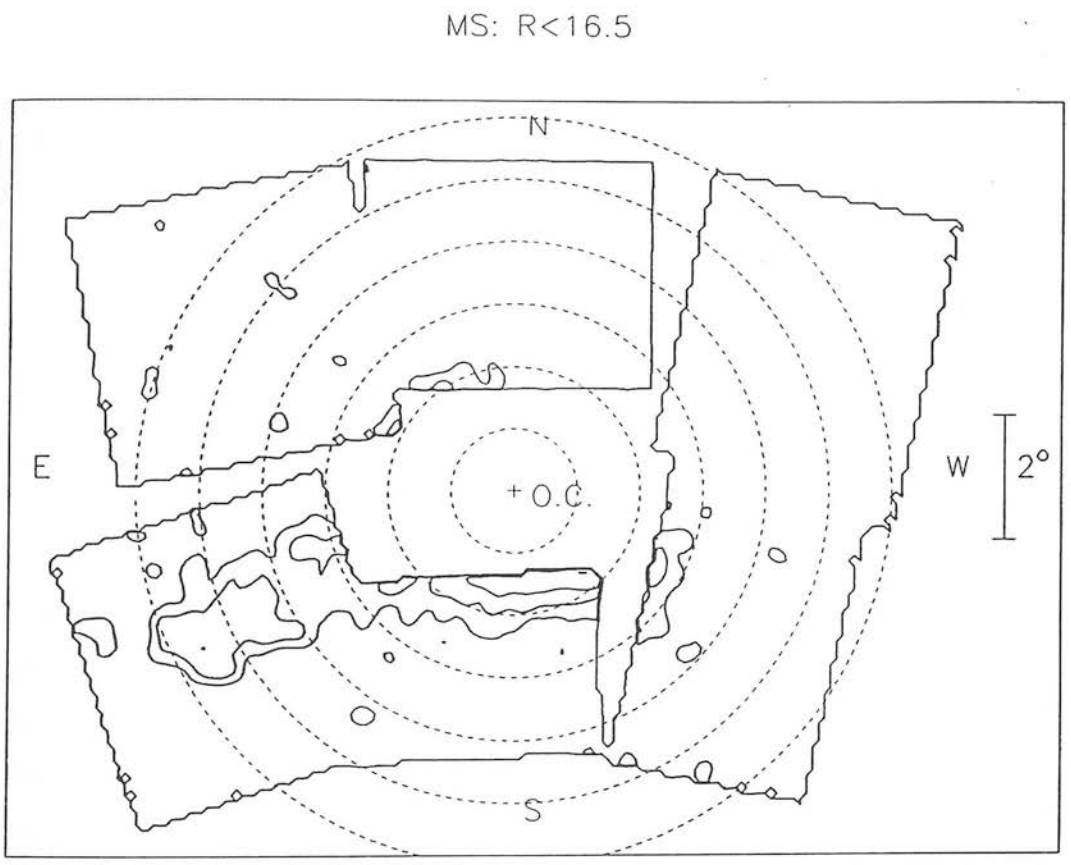

Figure 7.1: (f). Contour plot of the surface distribution of main sequence stars with $B - R < 0.1$, $R < 16.5$ for all six survey fields. The contour levels generally increase towards the SMC centre, with successive levels a multiple of three times the level below. The upper age limit represented by these populations is $\tau < 0.1$ Gyr and the lowest contour level is 0.3 stars per pixel.

of the optical centre there appear to be MS stars comprising extensions of the SMC main 'Bar'. These areas are characterised by steeply rising numbers with decreasing distance from the optical centre.

We now examine, in turn, how the main MS features, namely the Wing, the SE 'bulge' feature, the extended NE feature, and the central 'Bar' features, are altered at successive magnitude cuts, to determine the characteristic ages associated with these features.

(1) The Wing feature, which comprises very young populations, maintains its appearance at successively brighter magnitude cuts without significant alteration except for the apparent disappearance of MS stars in the northernmost parts of Field 30 brighter than $R = 17.5$ which may be partly due to low signal-to-noise and contouring effects. We conclude from the presence of MS stars in the Wing brighter than $R = 16.5$ that the Wing feature is younger than 0.1 Gyr.

(2) The central 'Bar' features in the north-east and south-west do not change significantly until $R < 17.5$, where a contraction of these features occurs. It appears that there may be a significant age component between 0.25 and 0.6 Gyr whose omission from the $R < 17.5$ plot may have caused the apparent contraction of the MS distribution in these areas. Although reduced in extent, these central features are still present at $R < 16.5$ exhibiting a bar-like morphology, indicating that very young (< 0.1 Gyr) populations are also represented in these features.

(3) The SE 'bulge' feature extends as far as 4° from the SMC centre in the plot for $R < 19.0$, indicating that populations as young as 0.8 Gyr are present, but contracts more rapidly at successive magnitude cuts, until it is barely discernible as a separate feature at $R < 16.5$. Qualitatively, it appears that this feature contains a range of ages whose representation diminishes with decreasing age quite rapidly for ages younger than about 0.8 Gyr.

(4) Regarding the extended NE feature, a major change occurs at $R < 19.0$, with the feature all but disappearing apart from some MS stars at the bottom edge of Field 52 at a distance of about 3.7° from the SMC centre. Evidently, the great majority of MS stars in the NE feature are older than about 0.8 Gyr. At the next brightest magnitude

cut, $R < 18.5$, the NE feature has vanished, whereas, by way of comparison, the SE 'bulge' is still prominent, extending to over 3° from the SMC centre.

The MS contour plots in Fig. 7.1 give us an overview of the distribution and age constitution of fairly young populations (less than 1.8-2.5 Gyr depending on the distance modulus) but in order to obtain a more refined picture of the age distribution we have to perform an analysis of the MS luminosity functions, which is the purpose of the next section.

3 Main Sequence Luminosity Functions

With the aid of the contour plot for the MS distribution as a guide to likely changes in the population structure, we have constructed main sequence luminosity functions (LF) for stars lying between circular annuli centred on the SMC optical centre. We have used bins of size 0.5 mag from $R = 13$ to $R = 20$ to obtain the number of stars per bin, N, and then calculated the logarithmic luminosity function, $\log N(R)$, which allows a simple shift along the y-axis when intercomparing various LFs. The faintest magnitude bin, $R = 19.5 - 20.0$, suffers from incompleteness due to proximity to the plate limit, so will largely be ignored in the following analysis. Table 7.2 lists the regions for which the LFs have been constructed, the radial limits within which the stars lie for each region (referred to the optical centre), the logarithmic offset added to the actual $\log N$ statistics to give $\log \phi$ (the scaled luminosity function) in the plots of the various LFs shown in Fig. 7.2, and the symbol used for the LF data in these plots. For Field 29, we have derived two sets of LF, one for the central or middle section and one for the western section. The LF of the central section represents the SE 'bulge' feature, while the other LF is due to the western part of Field 29 away from the 'bulge'. The extreme eastern part of Field 29 contains a contribution from the SMC Wing and has not been plotted.

The interpretation of the LF of a superposition of populations of different ages is a non-trivial task, since identification of distinct age components is hampered by

Region	Inner/Outer Radii (deg.)	Plot Offset	Plot Symbol
Wing (IDK)	–	0.3	Filled square
F30 (Inner)	3/4	0.3	Triangle
F30 (Middle)	4/5	0.1	Circle
F30 (Outer)	5/8	0.0	Curve
F29 Centre (Inner)	2/2.5	0.0	Filled square
F29 Centre (Outer)	2.5/4	0.3	Triangle
F29 West	2.3/3	0.0	Filled square
F52 (Inner)	2/2.5	0.0	Filled square
F52 (Outer)	2.5/4	0.0	Triangle
F51 (Inner)	2/2.5	0.0	Filled square
F51 (Outer)	2.5/3	0.7	Triangle
F28	2/3	0.0	Filled Square

Table 7.2: Data for the circular grid regions used for the main sequence LF study. *Column* 1 gives the region name (including the Field no.; IDK represents the LF derived in the study by Irwin, Demers & Kunkel 1990), *Column* 2 gives the inner and outer distances from the SMC centre in degrees enclosing each region, *Column* 3 gives the logarithmic offset added to log(Number counts per bin) for the LF plots in Fig. 7.2, and *Column 4* gives the symbols used in Fig. 7.2 to denote the LF for each region.

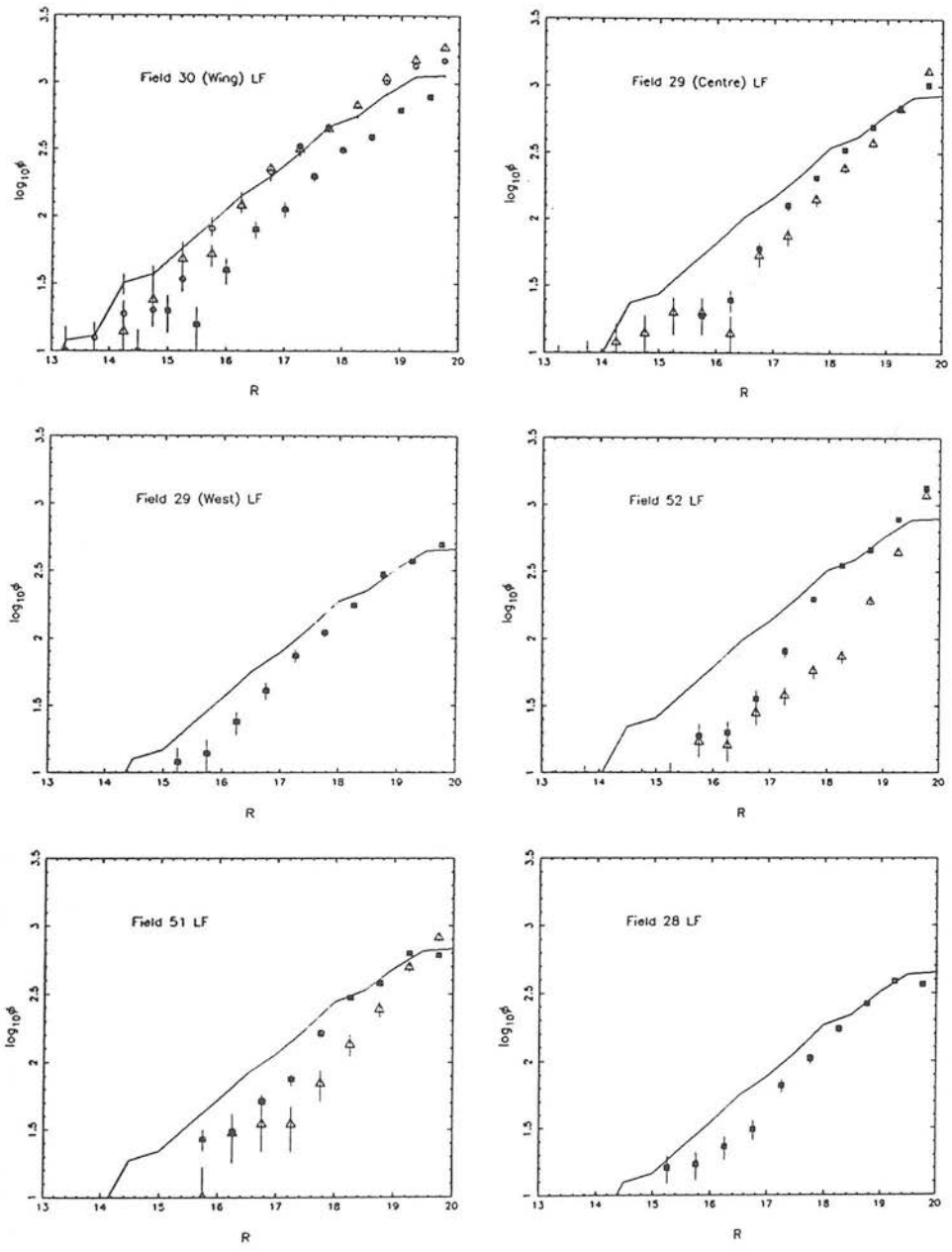

Figure 7.2: Main sequence differential luminosity functions for several circular grid regions compared with a superposed luminosity function from the Wing region representing an 'initial luminosity function'. The faintest magnitude bin, 19.5-20.0 mag suffers from significant incompleteness as can be seen from the turnover in the number counts in some luminosity functions. See Table 7.2 for details of symbols.

reduced contrast in the turnoff area. We can, however, make some progress using a technique involving the comparison of the LF slopes with some 'initial LF' given the assumption that this ILF has remained constant within the SMC over the past 2 Gyr. We have to hand the LF of the SMC Wing region which we shall show is due to an essentially coeval stellar population whose slope represents an ILF over the range $-5 < M_R < 1$. In what follows we analyse the luminosity functions of Fig. 7.2 with the aid of the approximate turnoff luminosities for different ages given in Table 7.1, taking into account the effect of the large depth of some areas of the SMC.

3.1 The SMC Wing Region (Field 30)

We consider first the main sequence luminosity functions (LF) of the SMC Wing in order to explore the possibility that the stellar populations of the Wing can provide us with a general 'initial luminosity function' for a coeval stellar population in the SMC. The work of Irwin, Demers & Kunkel (1990) (hereafter IDK) on the outer Wing of the SMC and the inter-Cloud region showed that the composite LF for several blue stellar aggregates in the outer Wing (east of $RA = 2^h15^m$, $DEC = -74°$) was virtually identical to the LF determined for several Magellanic Cloud clusters by Mateo (1988). The area covered by the IDK study overlaps the easternmost area of Field 30, so it is not surprising that our LFs for the Wing region are similar to theirs. In Fig. 7.2 (Field 30 Wing) their LF has been shown together with three other LFs representing the inner, middle and outer areas in Field 30. Agreement between the four LFs is very good for $R < 18$, whereas fainter than this the LFs of the inner and middle areas are slightly steeper than that of the outer area. This is almost certainly due to the presence of an older stellar population superimposed on the inner part of the Wing. The difference in $\log \phi$ is about 0.1 indicating that this population comprises about one-fifth of the numbers of MS stars in this section of the LF. Thus only the LF for the outer area can be considered to be the true Wing LF. From visual inspection of CMDs in Field 30 (see Appendix C) it appears that the brightest main sequence stars reach $R = 15.5$, making the age of the SMC Wing about 50 million years old according

to Table 7.1.

The resemblance of the Wing LF to the LF of the Magellanic clusters observed by Mateo (1988) noted by IDK not only supports the existence of a global initial mass function for the Magellanic Clouds but also confirms that the SMC Wing was created by a single star formation event. Based on good agreement with the initial mass function of the solar neighbourhood derived by Scalo (1986), Mateo argued that his data supported the hypothesis of a universal initial mass function given by a single power law, IMF$\sim M^{-(1+x)}$ with $x \sim 2.5$. Regardless of the existence of a universal IMF, since Mateo's study included clusters up to 2.5 Gyr in age, we are justified in using the assumption that the LF of the SMC Wing region represents a uniform 'ILF' for the SMC over the past 2 Gyr to infer the age distribution in other parts of the SMC outer area. To do this correctly we also need to know whether the distance modulus for the SMC Wing differs from the short distance modulus of the SMC. The study of SMC structure using Cepheids by Caldwell & Coulson (1986) (see their Fig. 7) showed that Cepheids in the Wing (the'near arm') have a distance modulus 0.3 mag closer (nearly 8 kpc) than that of the centroid of the main bar. Therefore, we have to shift the LF of the Wing fainter by 0.3 mag in order to derive the 'initial LF' applicable to our adopted distance modulus. In the LF plots in Fig. 7.2 the luminosity-shifted LF of the outer Wing region (i.e. the 'ILF') has been superposed on the the LF of the other regions.

3.2 The Remaining Outer Areas

Examination of the plots of the luminosity functions in Fig. 7.2 reveals that for the inner studied areas lying within 2.5° of the SMC centre plus the LFs for Fields 28 and 29(west), for which most of the MS stars lie within 3° of the SMC centre, the slopes of the logarithmic luminosity functions are shallower than those for the outlying regions for the section fainter than $R = 18$. The inner areas have higher image densities than the outer areas so one may ask whether the turnover in the LFs in the inner areas is due to incompleteness affecting fainter magnitudes. As discussed fully in Chapter

3 (Section 2.4), the incompleteness in the data set, although increasing towards the more crowded inner regions, is largely independent of magnitude for magnitudes well above the effective magnitude limit. In any case, an excess incompleteness of over 100 per cent at $R = 19$ compared to that at $R = 18$ is required to make the slope of the LF of the inner region in Field 52 identical to that of the outer region, so the difference in the shapes of the LFs for this field do appear to demonstrate a true difference in the age composition of the inner and outer areas.

The inner areas of the northern Fields 51 and 52 both have a fairly well defined 'break' or 'knee' in their LFs at $R = 18$ after which the LF follows the 'ILF' quite closely. We can thus infer the presence of a population component aged about 0.4-0.6 Gyr depending on the distance modulus applicable to the MS populations. The uncertainty in this age determination is due to the uncertainty in the distance modulus, since these areas possess smaller mean distance moduli than most other areas (see Chapter 4). In the western and southern inner areas (Fields 28 and 29(west)) a strong break in the LFs is not seen, but the slopes of the LFs follow the shape of the 'ILF' in the section fainter than $R = 18.5$. This indicates the existence of a component of similar age to the inner areas in Fields 51 and 52, about 0.6 Gyr, but younger populations at least down to 0.2 Gyr old (MS 'tip' luminosity, $R = 17.2$) are also present in significant numbers. These results are consistent with the results from the surface distributions of MS stars for different magnitude limits, from which a significant component aged 0.25-0.6 Gyr was suggested based on the decreased extent of the central 'Bar' regions in the plot for $R < 17.5$ compared to $R < 18.5$.

The LFs for the outlying areas in Fields 51, 52, and 29(central 'bulge' region) all have fairly steep slopes exceeding the 'ILF' slope along all sections of the LF. This can be ascribed to the presence of a series of MS 'turnoffs' along the LF, with the increasing deficit in star numbers with respect to the superposed 'ILF' with decreasing magnitude indicating that the contribution of younger populations is declining with decreasing age. Therefore, for populations aged up to about 1.2 Gyr, which is the limit defined by the completeness limit at $R = 19.5$, the age spectrum is to a greater

extent biased towards older ages in the outer area. The slope of the LF is steeper for the outlying regions in Field 52 than for the SE 'bulge' region (Field 29), which reflects an older composition for the north-eastern outlying areas, as was suggested by the observation that the extent of the NE MS feature declined much more noticeably than the SE 'bulge' feature in the contour maps for $R < 19.0$ and $R < 18.5$.

4 Surface Age Distribution Maps

As an aid to visualising the surface distribution of stellar populations of different ages, we have constructed surface distribution plots which show the ratios of the numbers of MS stars in different magnitude ranges. We have split up the main sequence stars into three groups on the basis of their R magnitudes; the first group defined by $16.5 < R < 17.5$ comprises stars including all ages younger than 0.25 Gyr (we call this the 'very young' group), the second group defined by $17.5 < R < 18.5$ comprises stars younger than 0.6 Gyr (we call this the 'young' group), and the third group defined by $18.5 < R < 19.5$ comprises stars younger than 1.2 Gyr (we call this the 'older' group). For simplicity we have assumed that all stars lie at the same distance modulus. In Fig. 7.3 we have plotted the ratio of number of stars per pixel in the 'very young' group to that in the 'older' group, and likewise in Fig. 7.4 the ratio of number of stars in the 'young' group to that in the 'older' group has been plotted. Thus, Fig. 7.3 gives us an idea of the relative contribution of populations younger than about 0.25 Gyr to the total population younger than about 1.2 Gyr with the areas with the largest contribution shaded darkest and Fig. 7.4 tells us the relative contribution of populations aged younger than about 0.6 Gyr to the total population younger than about 1.2 Gyr.

There is a considerable amount of noise in the plots due to poor statistics in the outermost areas populated by MS stars. Nevertheless, these maps essentially reinforce the findings of the LF analysis above, showing that younger populations (< 0.6 Gyr in age) are concentrated towards the centre of the SMC and in the Wing region. Other

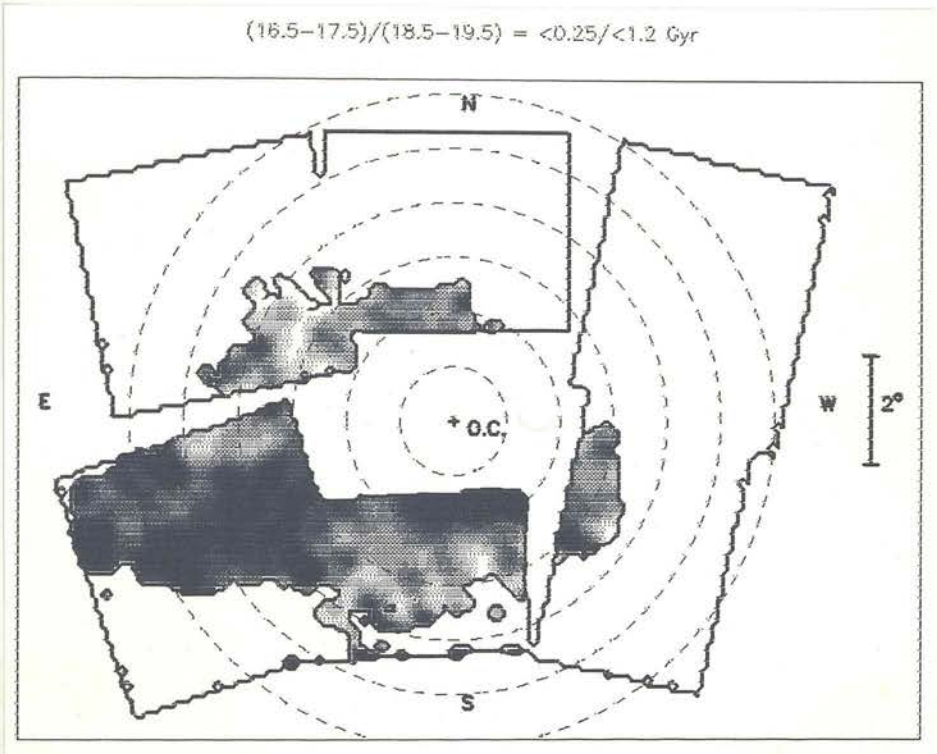

Figure 7.3: Surface age distribution map for main sequence populations showing relative ratios of very young to older MS populations. The ratio of the number of MS stars with $16.5 < R < 17.5$ to that with $18.5 < R < 19.5$ is plotted using greyscale representation. This ratio is related to the relative contribution of very young (< 0.25 Gyr) main sequence populations defined by $16.5 < R < 17.5$ to the total population younger than about 1.2 Gyr. The areas shaded darkest correspond to areas dominated by very young stars.

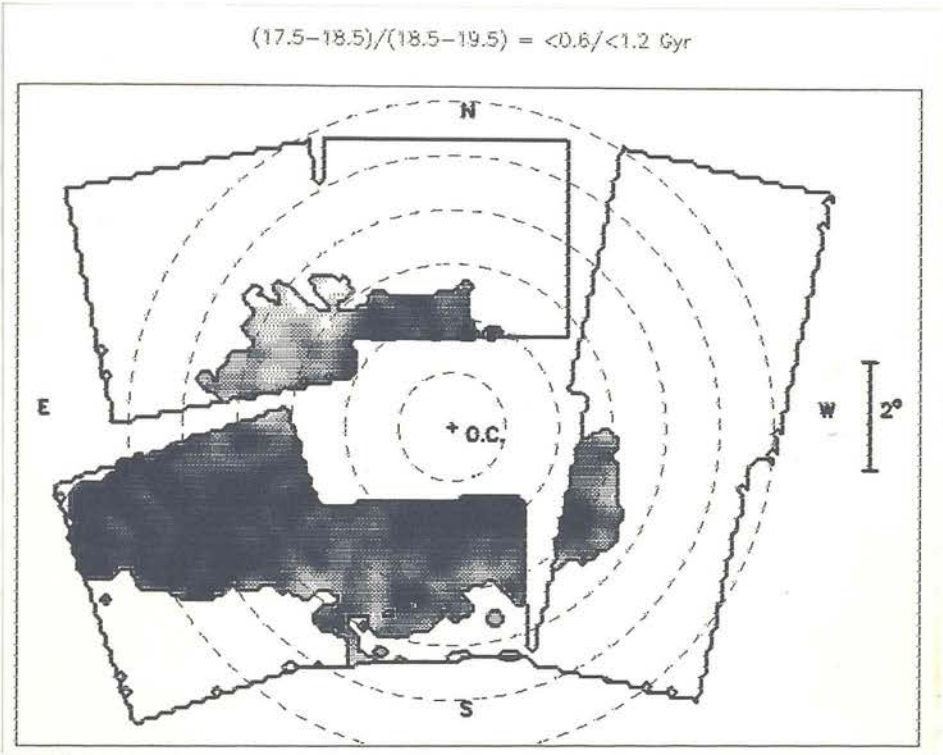

Figure 7.4: Surface age distribution map for main sequence populations showing relative ratios of younger to older MS populations. The ratio of the number of MS stars with $17.5 < R < 18.5$ to that with $18.5 < R < 19.5$ is plotted using greyscale representation. This ratio is related to the relative contribution of young (< 0.6 Gyr) main sequence populations defined by $17.5 < R < 18.5$ to the total population younger than about 1.2 Gyr. The areas shaded darkest correspond to areas dominated by younger stars.

areas populated by MS stars display an older age constitution, notably the north-eastern outer area which has low numbers of 'young' and 'very young' stars and parts of the southern and south-western area which have small numbers of 'very young' stars.

The appearance of these maps in the Wing region (Field 30) can tell us also about the distribution of MS populations other than those directly associated with the Wing feature but which happen to lie on the same line-of-sight. These maps show a fall-off in the contribution of younger populations in the western section of the area near the northern edge of Field 30 (the Wing area). We noted earlier that a contribution from an older underlying population has affected the LFs for the inner part of the Wing. Since this older population is more centrally concentrated than the younger 'Wing' population this is reflected in the proportionally reduced contribution of 'very young' and 'young' stars within 5° of the SMC centre. The easternmost area in Field 52 populated by MS stars shows signs that it is populated by brighter MS stars than neighbouring outer areas in Field 52, and Fig. 7.1 (c) (surface contour plot for $R < 19.0$) indicates an excess of MS stars brighter than $R = 19.0$ in this area. This may indicate that younger stars from the Wing region have streamed northwards into this region.

The greyscale representation in Figs 7.3 and 7.4 is also able to convey information on radial age gradients, which may help to establish whether there is a continuous aging of populations towards the periphery of the SMC. We have already established an aging towards the periphery in the sense that the younger MS populations are concentrated towards the central $2 - 3°$, while older populations are detected in the outlying regions, but this also includes the possibility of abrupt (rather than continuous) changes in the age composition as a function of distance from the SMC centre. Within the central 'Bar' regions lying roughly along the SMC major axis, there is no clear pattern of darkening towards the SMC centre, suggesting that the same mixture of ages is present throughout the more central areas ($2 - 3°$ from the SMC centre) observed here. For the SE 'bulge' region, there is a clear lightening towards the pe-

riphery, indicating continuous aging with increasing distance from the SMC centre for the MS populations considered here. The situation is less clear in the north-eastern outer area. In Fig. 7.4 the shading becomes much lighter very abruptly at around 2.5° from the SMC centre in the north-east which implies that the younger populations towards the SMC centre vanish at this distance, but in the more remote areas the aging trend appears to be from south to north. This indicates further support for the idea that younger populations associated with the Wing to the south are mixed in with older MS populations in the southern part of Field 52.

Concluding this chapter on the age distribution of the SMC outer regions inferred from relatively young stars belonging to the main sequence, the following major results were obtained:—

• The distribution of MS populations is very irregular, being biased towards the eastern side of the SMC, with the north-west devoid of MS populations.

• The Wing contains very young stars about 0.05 Gyr old, while populations with a mixture of ages up to about 0.6 Gyr are found in the north-eastern and south-western 'extensions' of the SMC main 'Bar'. There is evidence that there is a significant age component between 0.4-0.6 Gyr in these more central areas.

• Extended distributions of MS stars brighter than $R = 20$ out to $4 - 5°$ from the SMC centre are found in the north-eastern and south-eastern outer regions. Both these areas are characterised by steep MS luminosity functions, but the north-eastern outlying areas are dominated by stars older than about 0.8 Gyr, whereas the south-eastern outlying areas show a continuous aging towards the periphery.

The detailed study of the MS populations, undertaken by means of surface distribution and luminosity function analysis, has provided important data for the understanding of the fairly recent (from ~ 2 Gyr ago to the present) star formation history of the SMC, which forms an integral part of the discussion of the overall evolutionary development of the SMC, presented in Chapter 10.

PART III: *THE AGE DISTRIBUTION*

CHAPTER

— 8 —

THE CLUMP/HB AND THE OLDER POPULATIONS

Note: Sections 1 and 2 of this chapter were initially drafted by D. Hatzidimitriou for inclusion in the fourth paper reporting the findings of this project (Gardiner & Hatzidimitriou 1991). The draft versions of these sections were subsequently revised by myself and the paper was submitted to *MNRAS* in July 1991.

This chapter investigates the age distribution of the outer regions of the SMC based on the morphology of the horizontal branch, which we will see represents the predominantly older stellar population of the outlying regions. The appearance of the horizontal branch can display considerable variety, from the 'clump' characteristic of

galactic open clusters and intermediate-age Magellanic Cloud clusters, to the more horizontal appearance exhibited by the oldest known stellar aggregates, the globular clusters of the Galaxy. Despite this great variation in morphology, stars on the horizontal branch are all core-helium burning, and the lifetime of this evolutionary phase is almost independent of stellar mass according to stellar evolutionary models (e.g. Seidel, Demarque & Weinberg 1987; Lee & Demarque 1990). Populations older than a few 10^8 yr generally have prominent horizontal branch features, and thus HB morphology plays an important role in understanding the formation history of the Galaxy from studies of globular clusters and field populations (e.g Preston, Schectman & Beers 1991) as well as the evolutionary history of Local Group galaxies (see Hatzidimitriou 1991).

The clump/red-horizontal-branch is the most conspicuous feature of the CMD in the SMC general field, with the exception of the Wing region (Field 30), where young stars populating the main sequence dominate. Stellar populations belonging to a wide range of ages display purely red horizontal branches, the youngest being a few 10^8 yr old such as open clusters in our own Galaxy, while the oldest can be as old as the galactic globular clusters 47 Tuc, Palomar 4 and Eridanus, i.e. around 15 Gyr old. The 'clump' describes the RHB of younger populations, while a more 'horizontal' morphology seems to be appropriate for older populations. Populations older than about 12 Gyr are known to possess horizontal branches which extend into the instability strip, which may be populated by RR-Lyrae variables. This chapter deals with populations represented by the HB/clump, red horizontal branch and RR-Lyraes based upon the observational data from the six project fields.

Firstly, in this chapter we analyse the morphology of the observed HB to derive some information about the major age contributors in the SMC general field (Section 1); secondly, we investigate the oldest populations in relation to the morphology of the HB and discuss the absence of a blue HB in our CMDs (section 2); and finally we conduct some studies of RR-Lyrae variable stars in Field 51, which has enough blue plates to enable a sample to be selected from variability in conjunction with colour

information (Section 3).

1 Age Estimates for the Bulk of the SMC Field Population

1.1 Contribution to the Clump/RHB from Populations Younger than about 2 Gyr

A comparison between the plot of the surface distribution of HB/clump stars (Fig. 4.3) and that of the surface distribution of main sequence stars brighter than $R = 20$ (Fig. 7.1 (a)) shows that the projected distribution of the HB/clump population is more symmetrical with respect to the SMC centre and extends over a larger area (except for the Wing region) than the main sequence populations younger than about 2 Gyr. The north-western outer regions, which possess no MS populations, must therefore be populated entirely by stars older than 2 Gyr, and it is very probable that in other regions the clump contains a large proportion of stars older than the 2 Gyr limit defined by the MS populations. As mentioned in Chapter 7, the MS stars located in the outer regions span an age range from a few 10^8 yr (or younger in the Wing region) to probably $\simeq$2 Gyr. We now investigate the extent to which the observed numbers of clump/RHB stars can be interpreted as originating in these younger populations for regions populated by significant numbers of MS stars.

Firstly, we consider whether any contribution to the clump would be expected from the very young (< 0.1 Gyr) stars of the SMC Wing. Cannon (1970) (hereafter C70) and Mateo & Hodge (1985) find that, for galactic open clusters younger than $3 - 5 \times 10^8$yr, the 'clump' due to core-helium burning stars becomes rapidly brighter with decreasing age in agreement with theoretical models (e.g. Faulkner & Cannon 1973). Inspection of the colour-magnitude diagrams of galactic open clusters compiled by Mermilliod (1981a) in conjunction with the ages determined by Mermilliod (1981b) shows that the 'clump' of red giants is fairly well-defined between ages of 0.6 Gyr and

0.2 Gyr, but at about 0.1 Gyr it becomes less concentrated until its existence is very doubtful at an age of 0.05 Gyr. If the stellar population of the Wing is about the same age as the Pleiades open cluster with an age of about 0.08 Gyr, a loosely defined 'clump' feature would be expected at around $M_R = -3$ or $R = 16$. The fact that no such feature could be identified in the CMDs in the Wing region (see Appendix C) seems to confirm our age assignment of 0.05 Gyr for the Wing feature made in Chapter 7 (Section 3).

As discussed by Mateo & Hodge (1985) (see also Chapter 4), populations aged between a few 10^8 yr and 10 Gyr possess a clump of core-helium burning red giants whose mean magnitude is largely independent of age and metallicity, and hence for areas possessing MS populations outside the Wing region, clump stars coeval with the detected MS populations would be expected at the same luminosity level as populations older than 2 Gyr. In order to investigate the contribution of populations aged less than 2 Gyr but older than about 0.3 Gyr to the total population present in areas with significant MS populations, we use, as an approximation, the equation derived by C70 for obtaining the lifetimes of stars in different evolutionary phases except that we will assume that the lifetimes are known and use the equation to predict the numbers of clump stars due to populations coeval with the young MS populations. The equation is

$$\frac{\Delta t}{t} = 0.74 \frac{N}{N_0} \tag{1}$$

where Δt is the HB/clump lifetime, t is the age of the stellar population, N is the number of clump stars and N_0 is the number of stars per unit magnitude range in the section of the zero-age main sequence from which the progenitors of the clump stars were derived. This equation was obtained by assuming that the stars observed in an advanced stage of evolution have a spread of masses such that they have come from a section of the zero-age main sequence possessing a finite range in luminosity, given by δm mag. It is therefore argued that the lifetime in the advanced evolutionary phase is given by the difference in main sequence lifetimes between stars on the initial main sequence with luminosities differing by δm. Simple homologous arguments were used in order to relate the main sequence lifetimes to the magnitude range δm, hence

producing eqn.(1) using the relation $N = N_o \delta m$. The latter relation simply states the number of stars in the advanced evolutionary phase is given by the product of the magnitude range, δm, of the section of the main sequence from which they were derived and the number of stars per unit magnitude range, N_o, in this section of the main sequence.

Following C70 we assume that the progenitors of the clump stars came from the section of the MS 0.5 mag above the MS turnoff and that the LF of the ZAMS is flat in this region, a reasonable approximation given the shape of the Wing LF used to derive an 'initial LF' in Chapter 7. We adopt the HB/clump lifetime found by C70 of about 2×10^8 yr, which agrees roughly with the lifetimes obtained from the theoretical models of Seidel, Demarque & Weinberg (1987) whose evolutionary tracks for the HB/clump phase cover about 1×10^8 yr. We have evaluated the contribution to the clump, from populations coeval with the observed main sequence, for two areas, namely the 'inner' region of Field 52 within $2° < r_{oc} < 2.5°$, and the 'outer' region of Field 52 within $2.5° < r_{oc} < 4°$. The results given by eqn.(1) are sensitive to the assumed age of the stellar population. For the inner region the age of the dominant MS population is fairly well defined (0.4-0.6 Gyr), and we have counted the numbers of MS stars in the section between $R = 18.0 - 18.5$ which presumably represents the half-magnitude below the MS turnoff. Since we have assumed a flat LF this is also the number of stars on the unevolved MS 0.5 mag above the top of the MS from which the clump stars originated. For the outer region, we have assumed an age of around 1 Gyr (R (turnoff) ~ 19) but as stated earlier there is no dominant age contribution. Since older stars contribute to a steep observed LF, the MS counts for a populations aged less than 1 Gyr will have been overestimated giving an upper estimate of the < 1 Gyr contribution to the clump.

Table 8.1 shows the relevant data for the calculation of the contribution of fairly young populations to the clump. Since we are dealing with ratios of number counts, the increasing level of incompleteness towards the more crowded inner regions, reaching up to about 40 per cent, does not affect the final result in a significant manner. It

	F52:Inner	F52:Outer
Inner/Outer radii (deg.)	2/2.5	2.5/4
Assumed age (Gyr)	0.4	1.0
Count range (R mag)	18.0 – 18.5	19.0 – 19.5
Number per unit mag, N_o	266	548
Calculated contribution to clump, N	180	148
Observed number in clump	1322	6272
Percentage contribution	14	3

Table 8.1: Data for the study of the contribution of < 2 Gyr populations to the HB/clump in two circular grid regions in Field 52. See text for details.

can be seen that for the outer region the contribution of the young populations is exceedingly small, of the order of a few per cent, and even in the inner regions this contribution only rises to about 14 per cent of the total clump numbers. For the outer region, if we were to assume a dominant age of 1.5 Gyr rather than 1 Gyr and count the numbers of MS stars in the range $R = 19.5 - 20.0$ the result would still be only 4 per cent for the contribution to the observed clump numbers, although this number is affected more by incompleteness towards faint magnitudes. These figures give some indication of the absolute contribution of these younger populations to the total stellar population beyond 2° from the SMC centre and shows quite conclusively that it consists largely of populations older than about 2 Gyr.

1.2 Contribution to the Clump/RHB from Populations Older than 2 Gyr

As was demonstrated in the previous paragraph, less than 15 per cent of the clump population can be ascribed to stars younger than 2 Gyr, hence the bulk of the underlying population is older than $\simeq$2 Gyr. We shall attempt now to use the clump/RHB morphology to further analyse its age constitution.

The methodology that will be used for this purpose was recently discussed by Hatzidimitriou (1991) (hereafter H91), and involves a new age index, d_{B-R}, defined as the difference between the median colour (in $B-R$) of the clump/RHB and the colour of the red giant branch at the level of the HB. The age dependence of this index was investigated both empirically (using several well-studied open and globular clusters in our own Galaxy and in the Magellanic Clouds) and theoretically using the Seidel, Demarque & Weinberg (1987) (hereafter SDW) clump/RHB models in conjunction with the Revised Yale Isochrones (Green, Demarque & King 1987). Empirically, there is a well-defined linear correlation between d_{B-R} and age that is given by the equation (see H91):

$$d_{B-R} = 0.08 \pm 0.01 + (0.015 \pm 0.001) \times \tau(\ Gyr). \qquad (2)$$

This age calibration scheme is applicable to populations with purely red HBs, older than 1-2 Gyr and with metal abundances ranging from [Fe/H]$= -1.7$ to solar. It is independent of reddening, distance modulus and systematic errors in the photometry (since d_{B-R} is a difference of two quantities affected identically by systematic errors), and it is largely insensitive to metallicity within the age and metallicity ranges mentioned above.

It should be emphasized here that the age estimates derived for mixed populations using the d_{B-R} index correspond to the median age of the mixture, which may be strongly biased by the age of the dominant population, if such a dominant population exists. In the following, the index d_{B-R} will be used to estimate the ages of the dominant populations in the SMC general field.

The method has been applied to all existing good quality CCD CMDs of SMC field regions, all located near well-studied clusters, for which the index d_{B-R} can be defined. Table 8.2 lists the regions, their distance from the optical centre of the SMC, the derived value of d_{B-R} and the corresponding median age from the application of eqn.(2). Fig. 8.1 indicates the location of the regions on the contour plot of the clump stars and in Fig. 8.2 we have plotted the derived median age against distance from the SMC optical centre. An inspection of Table 8.2 shows that except for the innermost

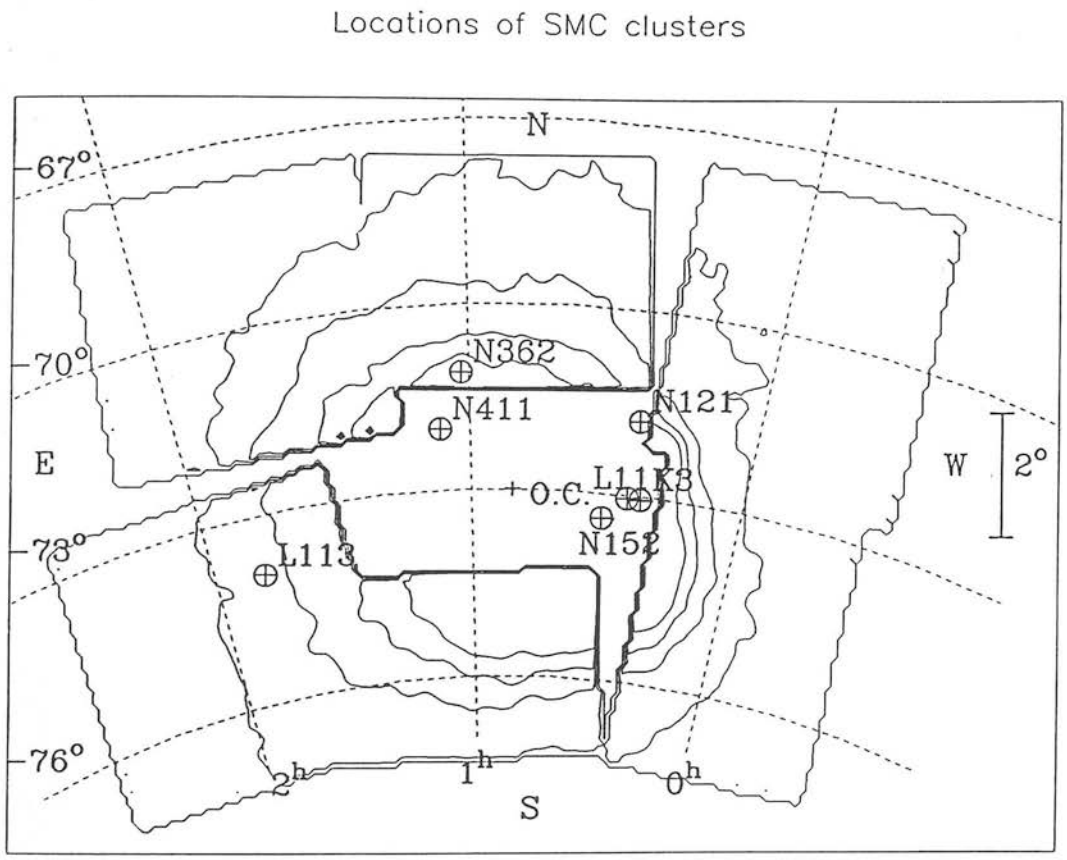

Figure 8.1: Locations of clusters and field regions used for studying the median age of stellar populations in the SMC, superimposed on the contour plot of the surface distribution of HB/clump stars. The contour levels increase towards the SMC centre and consist of levels of 12,24,36,48 stars per pixel with a Galactic foreground contribution of 7.5 stars per pixel.

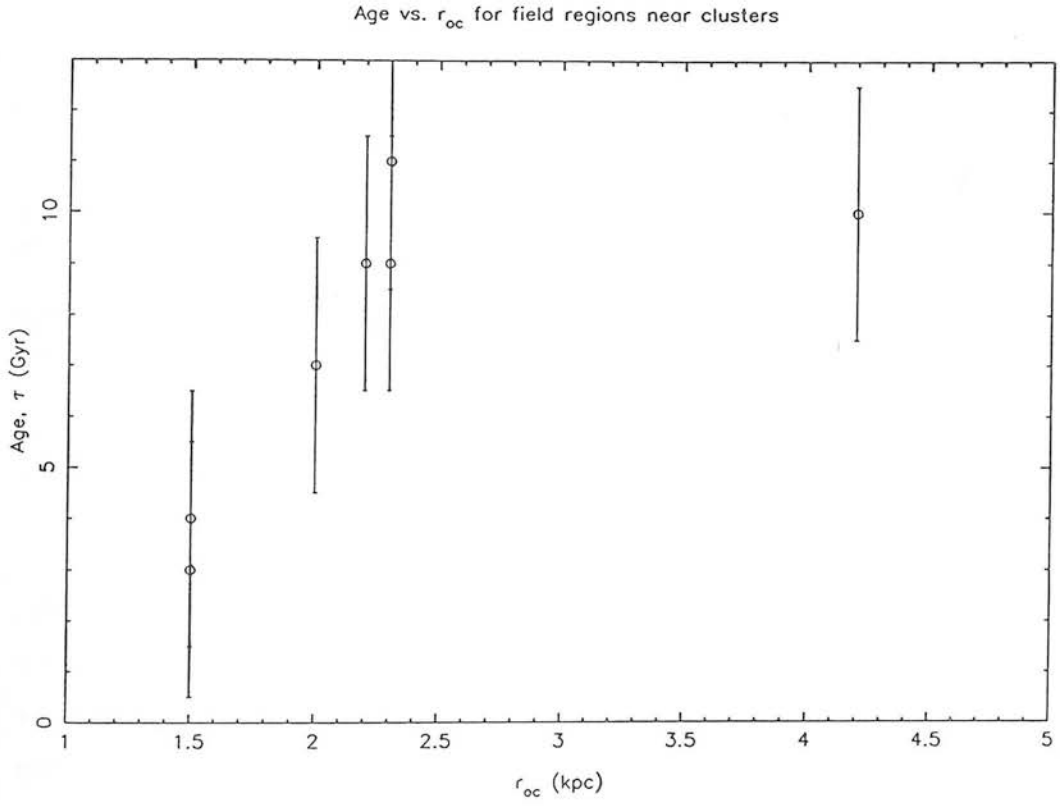

Figure 8.2: Median age vs. distance from SMC optical centre for field regions located near clusters studied with CCD photometry (see Table 8.2 for data). The median age was derived using the d_{B-R} indicator as described in text.

Region	r_{oc}(kpc)	d_{B-R}	$<\tau>$(Gyr)
NGC121	2.3	0.25	11
NGC152	1.5	0.12	3
NGC362	2.2	0.22	9
NGC411	1.5	0.14	4
L11	2.3	0.22	9
L113	4.2	0.23	10
K3	2.0	0.19	7

Table 8.2: Median ages of SMC field populations near clusters. The ages were derived by applying the d_{B-R} indicator of Hatzidimitriou (1991) to CCD observations of field regions near well-studied clusters. *Column* 1 gives the name of the cluster near which the SMC field region lies, *Column* 2 gives the projected radial distance in kpc of the region from the optical centre, *Column* 3 gives the estimated value of d_{B-R}, and finally *Column* 4 gives the estimated median age of the field derived from eqn.(2). The typical estimated error for d_{B-R} is ± 0.04, which corresponds to an uncertainty in the estimated median age of the order of ± 2.5 Gyr. *Note*: The references for the field CMDs can be found in Table 1.1.

areas near clusters NGC 411 and NGC 152 which have a median clump age around 4 Gyr, most other areas have median ages between 9-11 Gyr. The region near Kron 3 has an intermediate value of 8-9 Gyr. This rapid increase of the median clump age within the central 2.5° (see also Fig. 8.2) is consistent with a faster decrease of the younger populations with respect to the older ones with distance from the centre.

Next, we consider our own photographic database, for which the photometric errors are larger than for the good quality CCD CMDs discussed above. Although the definition of the index d_{B-R} does not require deep CMDs, it does require CMDs with a clump feature possessing a narrow luminosity range and a well-delineated RGB in order to accurately define the colour difference between the median colour of the clump and the RGB at the level of the HB. As can be seen from the CMDs in Appendix C, these requirements are not always satisfied. However, in most cases where d_{B-R} could be defined in our CMDs, values comparable –within the errors– to those found near NGC 121 and L 113 (i.e. $d_{B-R} \sim 0.20 - 0.25$ giving $\tau \sim 10$ Gyr) were found.

These areas do not reach the outermost contour of Fig. 8.1, where d_{B-R} could not be reliably defined.

2 The Oldest Populations

2.1 Red Horizontal Branch Morphology

It is well known that the morphology of the HB of older populations (possessing ages similar to the ages of globular clusters), i.e. whether it is purely red, or whether it extends to the instability strip and beyond, depends on metallicity as well as on several other possible parameters (candidates for the so-called 'second parameter'). Metallicity is the dominant 'first parameter' since in general metal-poor galactic globular clusters exhibit blue HBs while metal-rich ones are observed to possess red HBs. However, the HB morphology of globular clusters beyond 12 kpc from the galactic centre is not particularly well correlated with metallicity (Searle & Zinn 1978), hence the necessity for the second parameter to explain the HB morphology. Nevertheless, no *extremely* metal-poor ([Fe/H]~ -2.0) globular clusters are seen to have a purely red HB. For the present analysis we note that old galactic globular clusters with purely red HBs have metallicities between [Fe/H]$= -0.7$ (47 Tuc) and -1.7 (Palomar 4), and that old giants in the SMC halo have metallicities around [Fe/H]$= -1.6 \pm 0.3$ (Suntzeff *et al.* 1986). Therefore, unless a 'second' parameter is at play, SMC populations as old as 15 Gyr —if present— may exhibit red HBs.

We now analyse in detail the red horizontal branch in one of the grid region CMDs in our database Region F51:24 (see Appendix C). This CMD was chosen on the basis of the existence of a well delineated RGB and a small clump magnitude range indicating a relatively small line-of-sight depth in the region.

A close inspection of the CMD F51:24 shows that there is an apparent asymmetric extension of the main clump to hotter temperatures. For a convincing analysis of the clump/HB region we need to remove the contribution of the RGB (which mostly affects

$B-R$	$< R >$	n
0.7-0.8	19.14	23
0.8-0.9	19.23	32
0.9-1.0	19.04	61
1.0-1.1	19.01	91
1.1-1.2	18.96	293
1.2-1.3	18.97	344
1.3-1.4	18.97	232
1.4-1.5	19.00	152
1.5-1.6	19.00	50
1.6-1.7	18.98	12

Table 8.3: The mean R-magnitude of clump/RHB stars (*Column 2*) in the indicated (*Column 1*) colour intervals, for the region F51:24. The mean R-magnitude was calculated after removing the foreground and RGB contributions using the luminosity histograms in Fig. 8.3 as explained in the text. *Column 3* gives the number of clump/HB stars in each colour bin.

the main clump) and foreground stars (which affects the asymmetric blue extension) as best as possible. The method chosen to deal with the problem can be described as follows: a series of magnitude histograms between $18 < R < 20$ were constructed in 0.1 mag colour strips covering the range from $B - R = 0.6$ to $B - R = 1.8$ (Fig. 8.3). In each of these histograms the foreground plus RGB contribution was defined and the adopted number subtracted from the each bin. The remaining stars are treated as 'real' clump/HB stars. Table 8.3 shows the total number of clump/HB stars in each colour bin along with the corresponding mean magnitude of the stars.

First, we notice that even after the removal of the foreground plus RGB contributions, there are still some HB stars reaching colours as low as $B - R = 0.7$. Second, the mean magnitude of the clump/HB stars becomes brighter with increasing colour by roughly 0.15 mag. This change does not happen in a continuous fashion, but rather in a step, with the first 2 colour bins having a systematically fainter mean magnitude

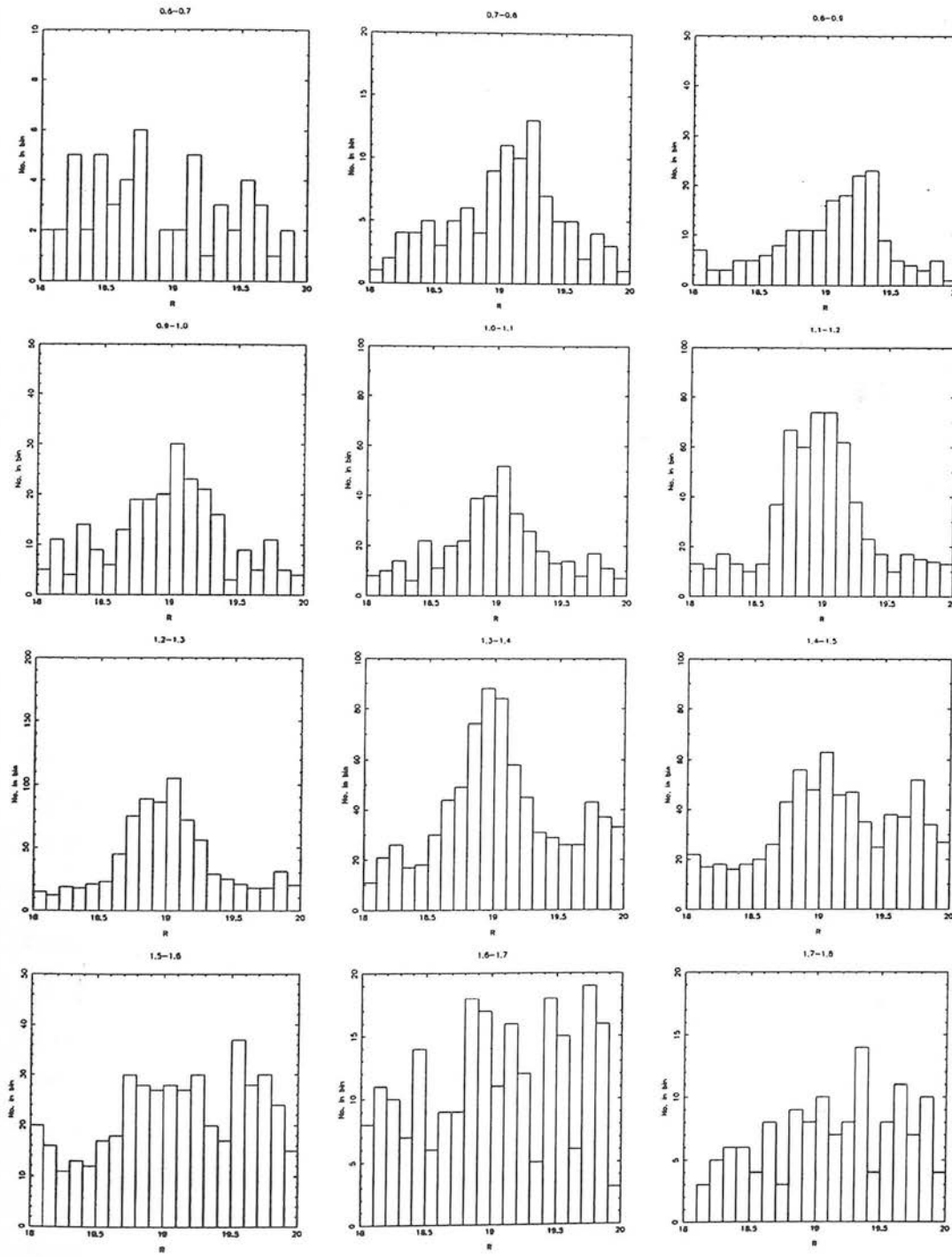

Figure 8.3: Luminosity histograms for the study of the clump/HB in region F51:24. Each histogram represents the number magnitude relation in 0.1 mag bins between $18 < R < 20$ lying within the $B - R$ colour range indicated at the top of each plot. See text for details of analysis.

than the last 8 bins. We know from the clump/RHB models of SDW that the mean magnitude of the RHB becomes fainter with increasing age, the rate of decrease in the luminosity being significantly greater for clump masses approaching 0.74 $M_{\odot}$, or ages larger than $\simeq$10-13 Gyr. Therefore the above observation may indicate the presence of a population older than the dominant ones represented by the well populated 'main' clump.

Turning to the colour distribution of the clump/HB stars as derived from Table 8.3 (Fig. 8.3), we note the asymmetric tail towards bluer colours. All of the stars in the colour bin 1.0-1.1 and a large proportion of the stars in the 0.9-1.0 bin can be interpreted as higher error points from the main clump peak. Most of the stars in the 0.7-0.8 and 0.8-0.9 bins however are genuinely bluer RHB stars. The total number of these bluer RHB stars in this area, after accounting for the contribution from high error points from the main clump, is of the order of 100, while the number of stars belonging to the main clump is about 1100. The mean colour of the 'bluer' RHB stars is $B-R \simeq 0.9$, while the main clump has a mean colour of $B-R \simeq 1.25$. The mean colour of the RGB at the level of the HB is around 1.5. This value is interpreted as representing the RGB of the dominant populations. The blue edge of the RGB is used for the 'older' populations (in order to derive a lower limit for d_{B-R}), giving a value of 1.25 for $(B-R)_g$. Thus we derive a value of 0.25 for the index d_{B-R} for the main clump/HB, and a value of $\simeq 0.35$ for the 'bluer' HB. The first value is comparable to the value derived from CCD CMDs near NGC 121 described above, and corresponds to an age of 10-12 Gyr (from eqn.(2)). The second value is comparable to the values derived for the old galactic globular clusters with purely red HBs (like 47 Tuc, Pal 4 and Eridanus).

From the previous discussion it can be concluded that these older stars are an order of magnitude ($\simeq$ 9 per cent from the numbers given above) less frequent than the dominant population with a median age of 10-12 Gyr. Interestingly, Frogel (1984) has concluded that the old population which is responsible for the field RR-Lyrae stars near NGC 121 amounts to approximately 6 per cent of the total mass in that area.

This number is not incompatible with our estimate for the 15-16 Gyr old population. To convert the percentage 9 per cent mentioned above to relative mass involved in the two groups, we need to take into account the relative lifetimes in the RHB as a function of age as well as the difference in the mass of the stars. From the models of SDW we conclude that the first of these factors is very near unity. The second factor is around 0.8 (from e.g. Revised Yale Isochrones), bringing down the estimated relative contribution to total mass of the two systems to $\simeq$7 per cent.

The small numbers of stars belonging to this old population, plus the fact that higher error points from the main clump contribute to the number counts of stars belonging to the asymmetric blue extension, make the investigation of the detailed surface distribution of this population difficult to perform. However, by constructing luminosity histogram plots similar to Fig. 8.3 for other CMDs in Field 51 it was found that, to first order, the number of stars belonging to this old population remained a fixed proportion of the number of stars in the main clump independent of distance from the SMC centre. The detailed distribution may perhaps best be investigated by employing large-format CCDs which would give sufficient areal coverage as well as better photometric accuracy to enable an unambiguous identification of stars belonging to the asymmetric blue extension.

The presence of a population at least as old as 12 Gyr is of course also indicated by the presence of RR-Lyrae stars in the SMC general field. This lower age limit for RR-Lyrae variables is defined by the age of the cluster NGC 121 which is the youngest known cluster which possesses RR-Lyrae variables (see GC5). What we have achieved here is to push the lower age limit for the SMC general field to higher values by suggesting that stars as old as 15-16 Gyr are very likely to be present. This analysis has assumed that the d_{B-R} age indicator is applicable to SMC field populations, which has been confirmed by checking its relationship with other indicators of relative age (see H91).

2.2 Blue Horizontal Branch Stars

The general field in both the SMC and the LMC is not known to contain blue horizontal branch stars. Although in the LMC there are a few star clusters with a blue HB (like Hodge 11 and NGC 2257), there are no such clusters in the SMC. Because of the still unknown factor of the 'second parameter' which affects the horizontal branch morphology, it is not yet clear whether this apparent absence of blue HB stars in the SMC is due to higher metallicity (first parameter) or lower age (one of the second parameter candidates) or some other parameter. Metal enrichment may have happened quite fast in the Magellanic Clouds (as in our own galaxy), in which case the numbers of very metal poor old stars that would contribute to a BHB population may be very low. The present study, because it covers large areas of the SMC field region, can be used to set statistically some upper limits on the possible numbers of such stars.

A blue HB similar to the one found in the CMD of the LMC cluster Hodge 11 (Stryker *et al.* 1984; Andersen, Blecha & Walker 1984), would occupy a region in a SMC field CMD roughly within the limits $19 < R < 20$ and $B - R < 0.1$. Although there is not much foreground contamination in this part of the CMD, there are varying numbers of main sequence stars. An additional problem is the increasing incompleteness of our survey beyond $R = 19.5$ (see Chapter 3).

A first inspection of the CMDs of Appendix C shows that there is definitely no conspicuous BHB in the general field population. In the higher star number density areas (nearer the central parts of the SMC) the BHB would appear as a bump in the MS LF around $R = 19.5$ mag, if sufficiently well populated; the apparent peak of some LFs around 19.5 mag (Fig. 7.2) is easily explained as a result of incompleteness towards faint magnitudes. In the lower star number density regions, the statistics are poor, albeit the contribution of MS stars becomes less important. In these regions we combined CMDs from several grid regions (Field 50 CMDs with virtually no observable MS population were used) to improve the statistics, but were still unable to find any definable BHB. An upper limit of 10 BHB stars per square degree, subject to

increasing incompleteness towards faint magnitudes, is obtained using the colour-magnitude limits defined above on the combined CMDs, indicating that BHB stars, if they exist at all, are an order of magnitude less frequent than the old ($\sim$ 15 Gyr) RHB stars.

3 RR-Lyrae Variables

The detection of RR-Lyraes in the old SMC cluster NGC 121 and confirmation of the existence of RR-Lyraes in the SMC general field (Graham 1975) suggest the presence of populations in the SMC at least as old as 12 Gyr. A systematic search for RR-Lyrae variables involving a large number of B_J plates in two of the survey fields included in this project, Fields 28 and 52, is currently being undertaken by D. Hatzidimitriou at the Anglo-Australian Observatory (private communication). This search will doubtless provide results of fundamental importance on the spatial distribution of the older populations represented by the population of RR-Lyrae variables, and may also enable an independent check on the results of the study of the 3D structure of the SMC using clump stars (Chapter 4). A less complete search for RR-Lyraes can be undertaken in fields possessing more than three B_J plates, i.e. in Fields 51 and 50 using our database, since the data sets for both these fields include four blue plates. However, owing to the fact that two of the plates in the B_J data set for Field 50 (J3670 and J12700) had unacceptably high overall random errors, a sample of RR-Lyrae candidates could be obtained only for Field 51.

The technique used to search for variable candidates is the standard one employed to detect variables from individual measurements based on several plates (see e.g. Reid & Freedman 1991, Hawkins 1984). The method involves calculating the rms error of the multiple magnitude measurements for each image and taking as variable candidates those objects whose deviation exceeds some cutoff value. Objects whose apparent variability is due to one measurement only are rejected since emulsion flaws, satellite trails etc. may result in a single discrepant measurement not repeated on

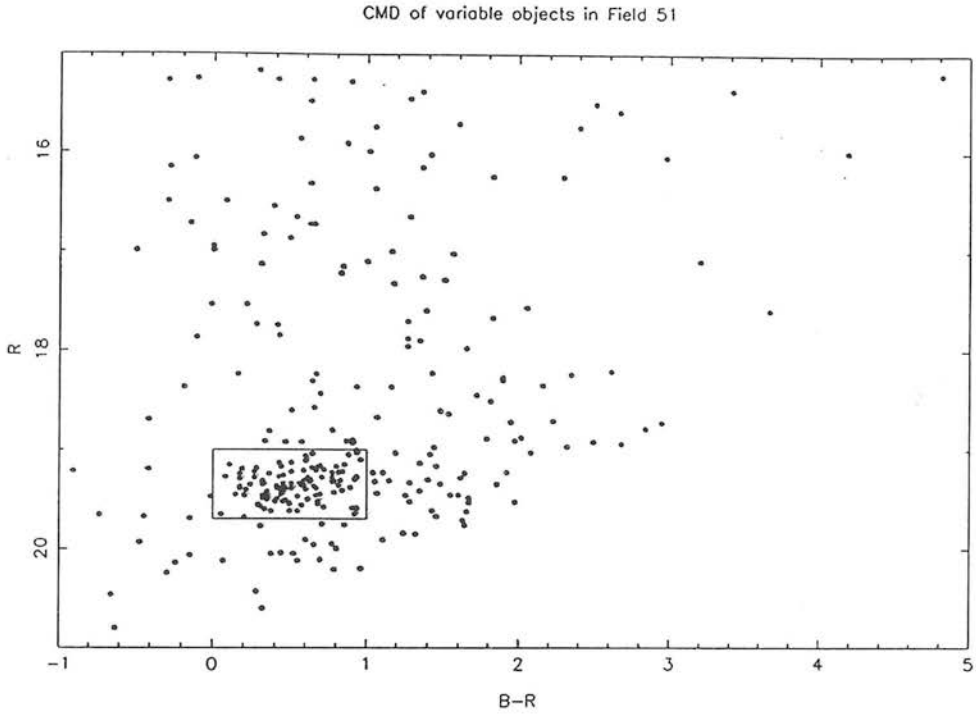

Figure 8.4: $R, B-R$ colour-magnitude diagram for 300 variable objects in Field 51 selected by an rms error criterion as described in text. The box defined by $19.0 < R < 19.7$, $0.0 < B - R < 1.0$ has been used to select candidate RR-Lyrae stars.

other plates. The criterion used to select variable objects in Field 51 was the following: the rms variation for the remaining three measurements after the highest and lowest measurements were omitted in turn both had to exceed 0.20 mag. This was found empirically to be the best selection criterion on the basis of the appearance of a well-defined group of RR-Lyraes in the CMD of the selected variable objects, and is effectively the same criterion as that used by Hawkins (1984) (hereafter H84) to identify a sample of galactic halo RR-Lyrae stars from a larger number (14) of UKST plates. The rms distribution of magnitude errors of the four B_J plates in Field 51 has been shown in Fig. 3.5, and indicates that objects with an rms variation greater than 0.2 mag lie in the non-Gaussian tail of the error distribution.

The colour-magnitude diagram for all selected variable objects in Field 51 is shown in Fig. 8.4. There is a conspicuous grouping of stars at around $R = 19.4$, $B - R = 0.5$.

It is evident that this grouping is due to RR-Lyraes in the SMC since their colours and luminosities are appropriate for such stars lying at the distance of the SMC. Firstly, their colours are similar to those of the galactic halo RR-Lyraes detected by H84, which possess $B-R$ colours of between 0.3 and 1.0. Secondly, the luminosities of these variable objects are consistent with them being RR-Lyraes located at the distance of the SMC, given $< M_B >= 0.9$ (from H84) or $< M_R >= 0.4$ for RR-Lyraes together with the SMC short distance modulus, dm=18.8. In all exactly 300 variable objects were found, of which 105 lay within the colour-magnitude limits $19.0 < R < 19.7$, $0.0 < B - R < 1.0$ and are thus possible RR-Lyrae stars. A visual inspection of this sample on one of the plates was carried out to confirm if each of these candidates was a genuine isolated star-like object with no nearby contaminating nebulosity, bright star haloes and the like. Ten objects, mostly possessing a diffuse, non-stellar appearance, were subsequently removed from the candidate list, reducing the list of candidates to 95 stars. The RA, DEC coordinates for the remaining RR-Lyrae candidates are listed in Appendix G.

Graham's (1975) survey for RR-Lyrae in a $1° \times 1.3°$ area near the galactic globular cluster 47 Tuc resulted in the discovery of 81 RR-Lyrae variables with an estimated completeness of 93 per cent for type *ab* variables and a 50 per cent rate for type *c* variables, giving an overall discovery completeness of around 78 per cent. The area of our search in Field 51 is 19.5 $\deg^2$ or 15 times the area of the Graham study. Our own discovery rate is therefore probably less than 10 per cent, which is not surprising given the small number of plates used to detect the variability. The mean B magnitude of the RR-Lyraes in our sample is 19.85 which is very similar to the value $< B >= 19.88$ for the RR-Lyraes lying in the central plate area of the Graham study. Using the value $< M_B >= 0.9$ for the mean absolute magnitude of RR-Lyraes quoted by H84, and an extinction, $A_B = 0.11$, for the SMC outer regions (from $A_R = 0.07$ and $E_{B-R} = 0.04$ — Chapter 3), the mean distance modulus of the RR-Lyrae population in Field 51 is calculated to be 18.84, a value which favours the the SMC short distance modulus (18.8) as opposed to the long distance modulus (19.3).

We can use our sample of RR-Lyrae candidate stars to conduct some investigations of the radial distribution of the old stellar population of the SMC. Previous investigation of this question (Graham 1975) concluded that the RR-Lyrae population showed little concentration towards the SMC centre but could not give any quantitative information on the form of any variation. Our sample of RR-Lyraes is likely to be affected by differential incompleteness between the more crowded areas towards the SMC centre and the more remote areas. The area of this study avoids the densest regions in Field 51, and most of the field, with the exception of the area within the central 2.5° of the SMC centre, has a total surface density of less than 3 images arcmin^{-2} implying less than 20 per cent incompleteness according to the discussion in Chapter 3 (Section 2.4). Thus, outside the central 2.5°, the logarithm of the number counts, which is the important quantity for the study of the radial distribution of RR-Lyraes, is different from the quantity which would be given by complete data by less than 0.1 dex. Fig. 8.5 shows the X, Y positions of the RR-Lyrae candidates in Field 51. This plot shows the division of the area of the field to allow the surface density of RR-Lyraes to be calculated as a function of distance from the SMC centre. Number counts were obtained in annuli between radii 2° – 2.5°, 2.5° – 3.5°, 3.5° – 4.5°, and 4.5° – 5.5° and converted to a surface number density by dividing by the area. Examination of Fig. 8.5 confirms Graham's earlier suggestion of a weak central concentration for the RR-Lyrae population, but there is nevertheless a falloff in the surface density with increasing distance from the SMC centre. If we assume that the *space* distribution of RR-Lyraes is given by a power law, $\rho \sim r^{-\alpha}$, then the corresponding *surface* distribution is given by $N \sim r^{1-\alpha}$ (see Hughes, Wood & Reid 1991). By fitting a power law to the observed radial surface distribution we can derive the power law exponent, α. This has been done by plotting the logarithm of the surface number counts per deg^2 in the annuli described above against the logarithm of the distance from the SMC centre (see Fig. 8.6), and fitting a straight line. We have omitted the innermost point from the fit because of the higher incompleteness in the data. The remaining three points define a good straight line with a gradient of -1.52, implying a power law exponent, $\alpha = +2.52$. The paucity of points and the large size of the error bars derived from

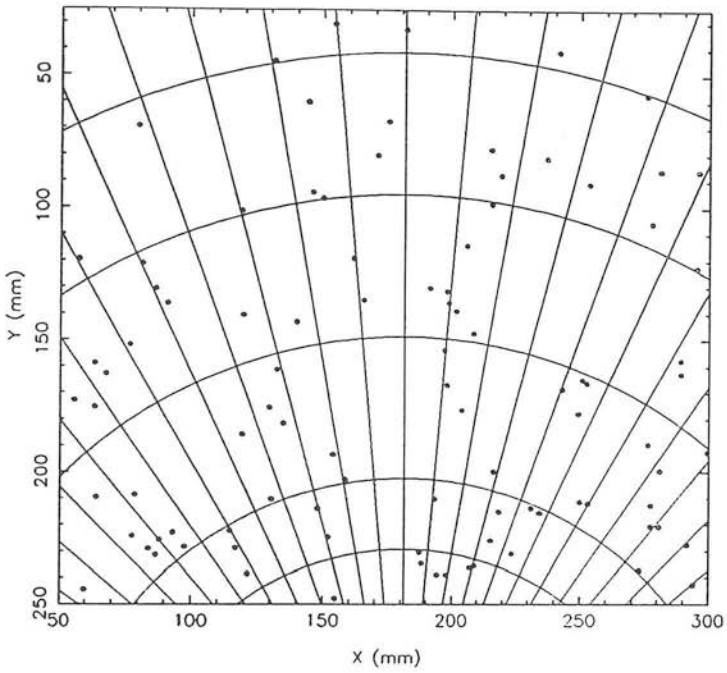

Figure 8.5: X, Y positions of visually inspected RR-Lyrae candidates in Field 51. The arcs are concentric with respect to the SMC optical centre at distances of 2°, 2.5°, 3.5°, 4.5° and 5.5° from the SMC centre. The straight lines are radii emanating from the SMC centre assisting the calculation of the surface density of RR-Lyraes as a function of distance from the SMC centre.

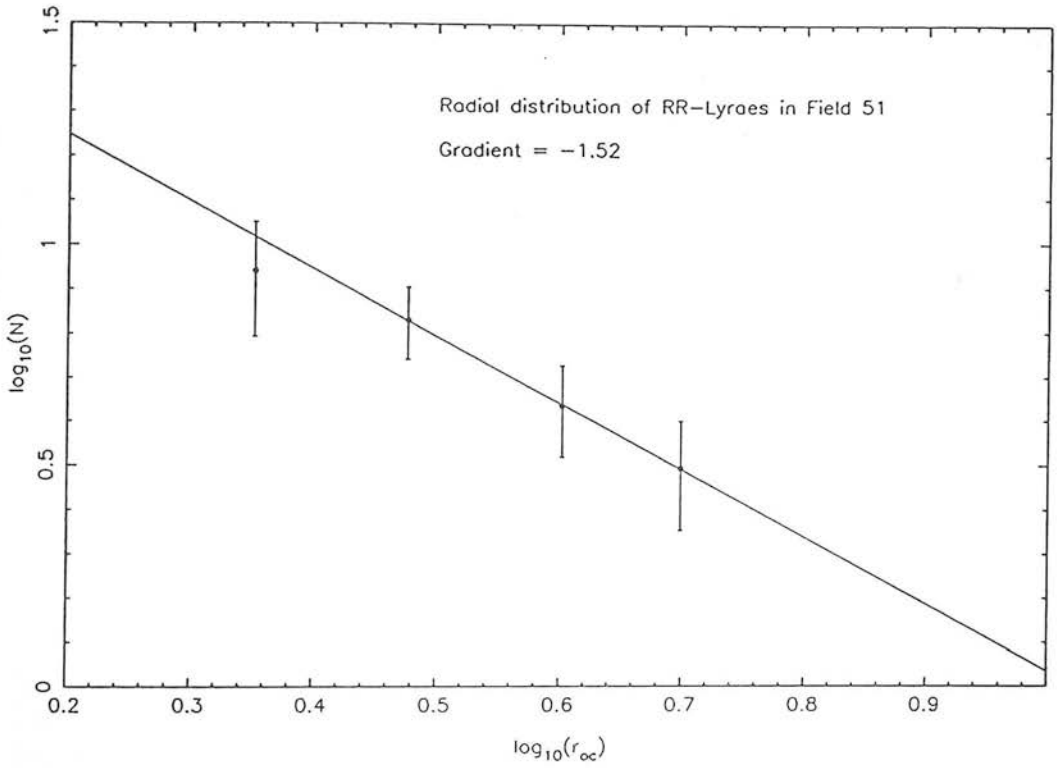

Figure 8.6: The radial distribution of the projected surface density of candidate RR-Lyraes with respect to the SMC centre. $\log_{10}(N(deg^{-2}))$ is plotted against $\log_{10}(r_{oc}(deg))$ with the (Poissonian) error bars based on the actual number counts. The straight line is a least squares fit to the outermost three data points, with the innermost data point considered to be unreliable because of greater incompleteness towards the crowded central regions of the SMC. The gradient of the line is -1.52, giving a space density power law of form $\rho \sim r^{-2.5}$ for the RR-Lyrae population.

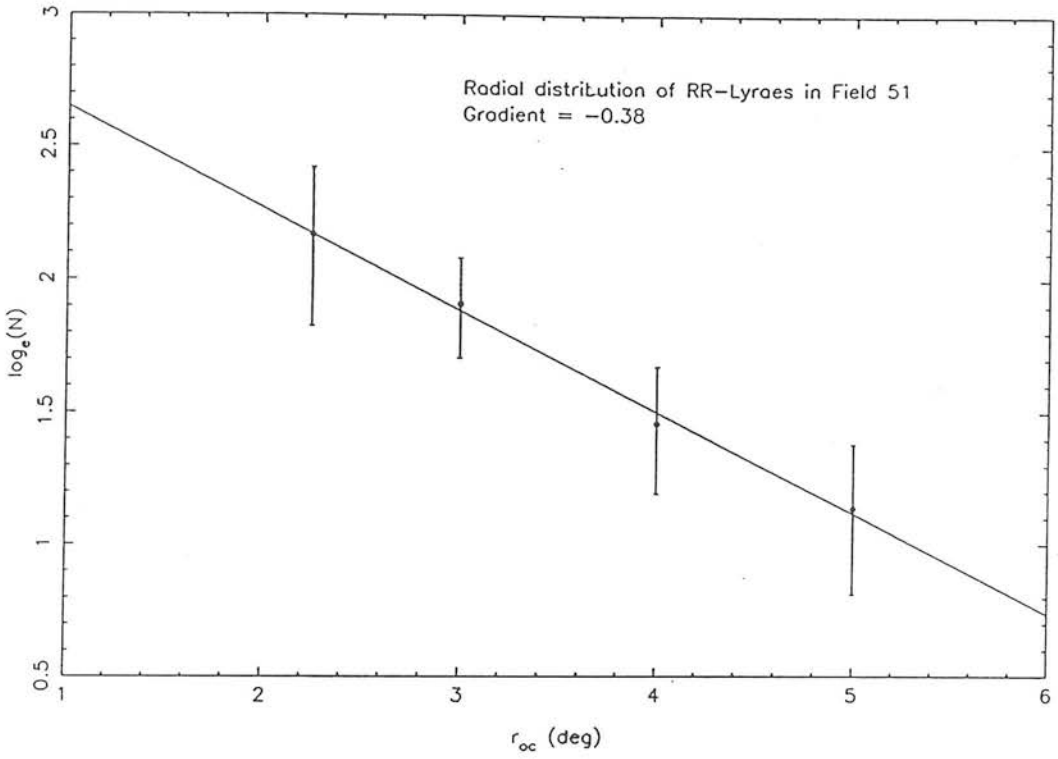

Figure 8.7: The radial distribution of the projected surface density of candidate RR-Lyraes with respect to the SMC centre with $\log_e(N(deg^{-2}))$ plotted against r_{oc}. The straight line is a least squares fit to the data. The gradient of the line is -0.38, implying an exponential decay of the surface density of RR-Lyraes given by $N \sim exp(-r/2.6°)$.

the number counts point to a fairly large uncertainty in this determination.

Although we have assumed a power law distribution, an exponential falloff in the surface density with distance from the SMC centre also fits the data given the size of the error bars on the data. In Fig. 8.7 we have plotted the natural logarithm of the surface number counts against distance (not the logarithm of the distance) from the SMC centre. The fitted straight line has a slope of -0.38. The exponential scale length is given by the reciprocal of this gradient, and hence the surface density varies roughly as $exp(-r/2.6°)$. The scale length is greater than that found for the HB/clump population, where a value of 2° was determined for the radial profile in the northern direction. This result confirms the weaker central concentration of the

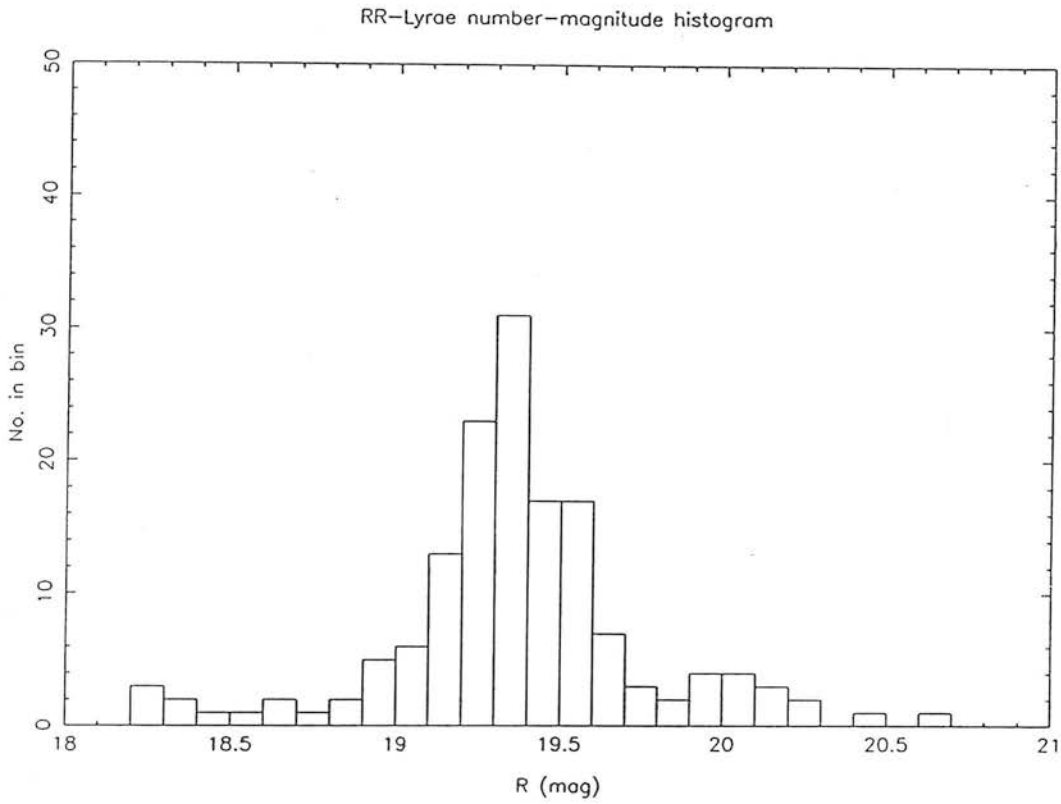

Figure 8.8: $R-$magnitude luminosity histogram of variable objects in Field 51 with $0.0 < B - R < 1.0$. Most of the RR-Lyraes lie between $19.1 < R < 19.6$ implying a depth of less than 13 kpc for RR-Lyraes within Field 51.

RR-Lyrae population with respect to the dominant populations of the outer regions of the SMC.

Finally, we consider the luminosity range of the RR-Lyraes in our sample as an indicator of the depth a long the line of sight direction. In Fig. 8.8 a histogram of the $R-$magnitude distribution for all variables with $0.0 < B - R < 1.0$, $18 < R < 21$ has been plotted. It is evident that most of the variable objects are concentrated between $R = 19.1$ and $R = 19.6$, putting an upper limit of 13 kpc on the depth containing the RR-Lyrae population. This figure is approximately the same as the overall projected diameter of the SMC, and confirms that the depth in most of Field 51 is fairly small, consistent with the narrow luminosity range of the HB/clump stars found in most

areas of Field 51 (see Chapter 4). The actual depth containing the RR-Lyraes may in fact be smaller than 13 kpc owing to variability producing an increased luminosity dispersion.

To conclude this chapter, we summarise the findings of the study of the age distribution in the outer regions of the SMC based on stars belonging to the horizontal branch evolutionary phase. The major results obtained were:—

• Populations aged less than about 2 Gyr coeval with the main sequence populations detected above the effective magnitude limit make up a very small fraction of the total stellar population in the outer regions, their contribution rising to 14 per cent in the innermost studied areas.

• The bulk of the stellar population of the outer regions was found to be aged about 9-11 Gyr old based on the application of the d_{B-R} age calibrator (Hatzidimitriou 1991) to the morphology of the HB/clump in CCD CMDs of field regions near well-studied clusters and also to the photographic CMDs of this project.

• An asymmetric blue HB extension, distinct from the main clump feature, has been identified on some CMDs. By applying the d_{B-R} indicator to this population, an age of at least 15 Gyr was determined, suggesting that objects as old as galactic globular clusters may well be present in the SMC. The contribution of this population was calculated to be about 7 per cent by mass to the total mass contained in the outer area of the SMC.

• No conspicuous blue horizontal branch was found on any of the colour-magnitude diagrams.

• 95 likely RR-Lyrae variables in Field 51 have been identified from variability on four B_J plates in conjunction with colour-magnitude data. Their surface distribution is less centrally concentrated than the HB/clump population. If it is assumed that their space distribution has a power law form, the space density of RR-Lyraes is given by $\rho \sim r^{-2.5}$.

PART III: *THE AGE DISTRIBUTION*

CHAPTER

— 9 —

THE WING OF THE SMC

As mentioned in Chapter 6, the Wing is a notable feature of the interaction between the Magellanic Clouds. Its existence has been known since 1940, when it was discovered by Shapley (1940) who described it as a "large cloud of faint stars" which "extends eastward in the general direction toward the Large [Magellanic] Cloud". According to Westerlund (1970) the Wing consists of stellar associations and emission nebulae stretching from $RA = 1^h10^m, DEC = -73°24'$ to $RA = 2^h15^m, DEC = -74°30'$. Other Population I objects discovered in the Wing include blue and yellow supergiants and Cepheids (Westerlund 1970) and a number of embedded clusters (Westerlund & Glaspey 1971). A distinction is sometimes made between an inner, more luminous Wing lying west of $RA = 1^h30^m(1950)$ (the 'tidal arm' of Lindsay & McFarland 1970) and an outer Wing, which shows up only on deep photographs, but star count data (Westerlund & Glaspey 1971) have shown that the two parts are directly connected.

The eastern tip of the Wing and the inter-Cloud region has been the subject of a continuing research program conducted by the Cambridge-Montreal group who have identified a stellar link comprising young blue stars between the Magellanic Clouds as a result of a photographic survey. They have also obtained CCD photometry of some young stellar associations and spectroscopy of individual stars in these regions (Irwin, Demers & Kunkel 1990 (IDK); Grondin *et al.* 1990; Demers *et al.* 1991a; Demers *et al.* 1991b). One of our project fields, Field 30, includes the easternmost tip of the Wing and thus contains part of the area of the IDK study. Other surveys of the Wing region based on photographic material were carried out by Westerlund & Glaspey (1971) and Brück (1978), and between these studies and that of IDK a fairly comprehensive picture of the distribution of the young stellar populations of the Wing has emerged. Based upon our data, in Section 1 we review the surface distribution of young stars in the SMC Wing, and using our magnitude data we discuss its age composition. In Section 2 we investigate the correlation between stellar and H I density, which has not been extensively discussed in previous studies, and in Section 3 we consider the origin of the Wing in the context of past interactions between the Magellanic Clouds and the Galaxy.

1 The Stellar Distribution

The prominent features of the stellar distribution of blue main sequence stars in the Wing are visible in the main sequence contour plots for all the project fields shown in Fig. 7.1. The main features are identical to those revealed by the isodensitogram produced by Westerlund & Glaspey (1971) from counts of blue stars in the Wing region, excluding, however, the eastern tip beyond $RA = 2^h20^m$. In order to further delineate the detailed surface distribution of Wing stars, in Fig. 9.1 we have plotted the positions of 12700 blue stars surveyed in the Wing region in Field 30 with $B-R < 0.1$ and $R < 20$. In Figs 9.2 and 9.3 we have also constructed similar plots showing the positions of blue stars with $R < 17$ and $R < 15.5$ respectively to aid the discussion of the stellar distribution and age composition of the Wing. We describe the detailed

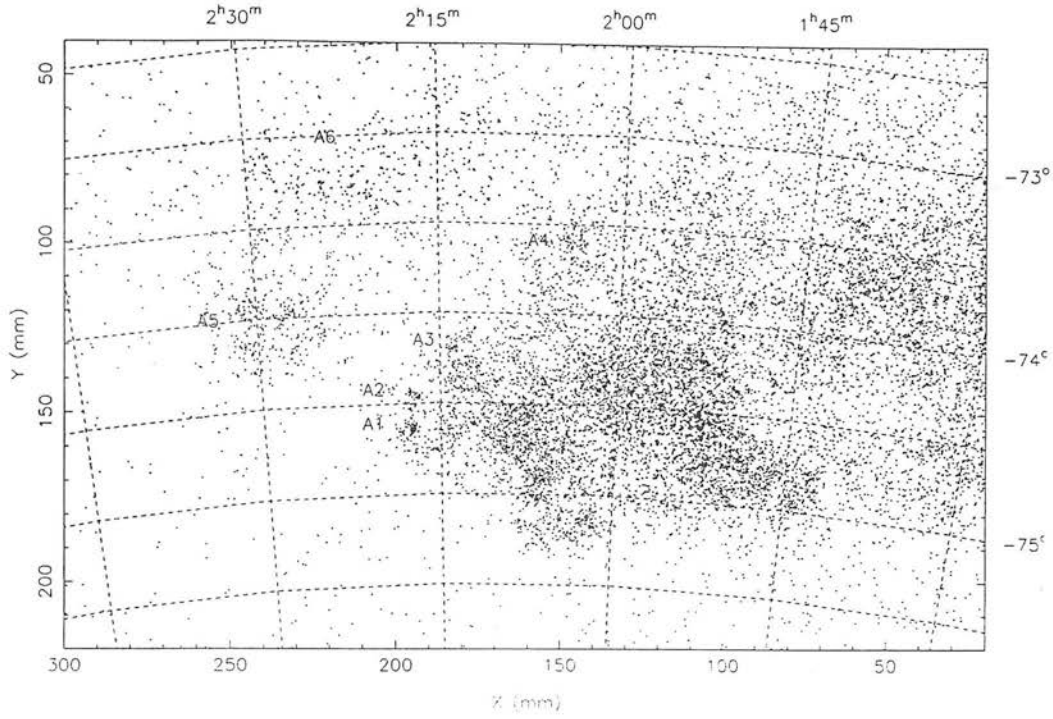

Figure 9.1: Plot of X, Y positions of stars with $B - R < 0.1$, $R < 20$ in Field 30. The colour-magnitude limits have been selected to include blue main sequence stars belonging mainly to the SMC Wing. Prominent stellar aggregates, A1-A6, are indicated. The coordinates are for 1950.

distribution of blue stars in the Wing below, making reference to previous studies of the Wing region.

Some prominent stellar aggregates (A1-A6) are labelled on Fig. 9.1. As noted by Westerlund (1970) numerous individual collections of blue stars or stellar associations are seen to make up the overall distribution, contributing to a very clumpy, disordered structure. There are two major concentrations containing the largest surface densities of blue stars, which we will call C1 and C2, centred on $RA = 2^h07^m$, $DEC = -74°45'$ (C1) and $RA = 1^h53^m$, $DEC = -74°30'$ (C2). In between, and to the north and to the west of these major concentrations there are more thinly populated distributions of blue stars. The 'neck' connecting the inner and outer Wing referred to by Brück (1978) at $RA = 1^h45^m, DEC = -74°$ can also be seen as a region possessing an

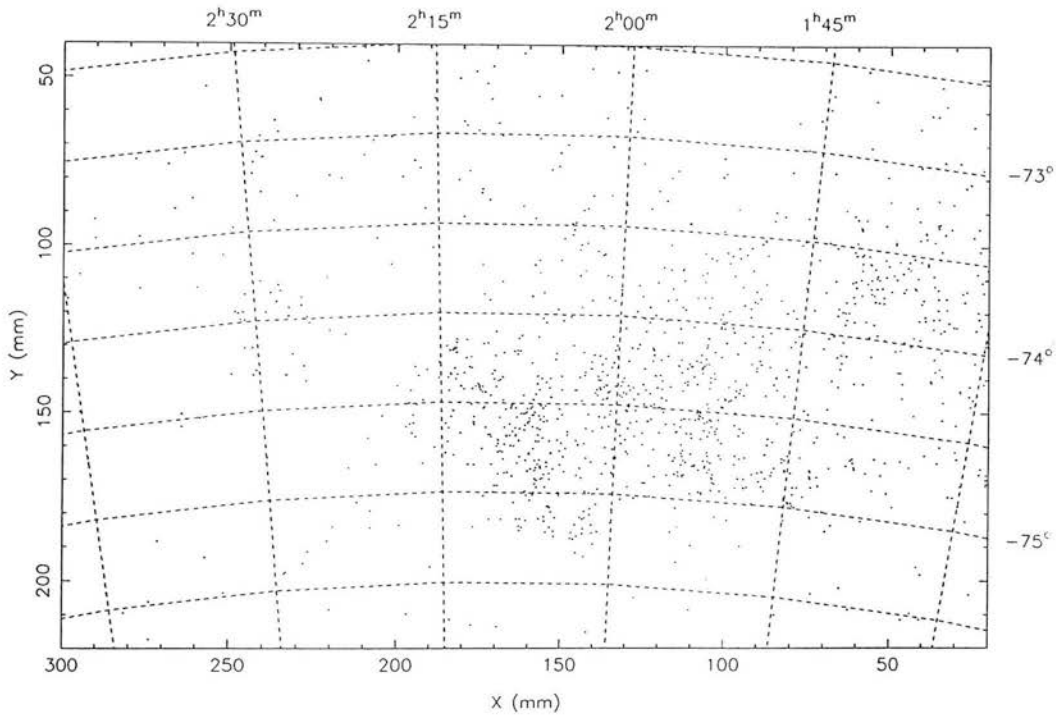

Figure 9.2: Plot of X, Y positions of stars with $B - R < 0.1$, $R < 17$ in Field 30. The coordinates are for 1950.

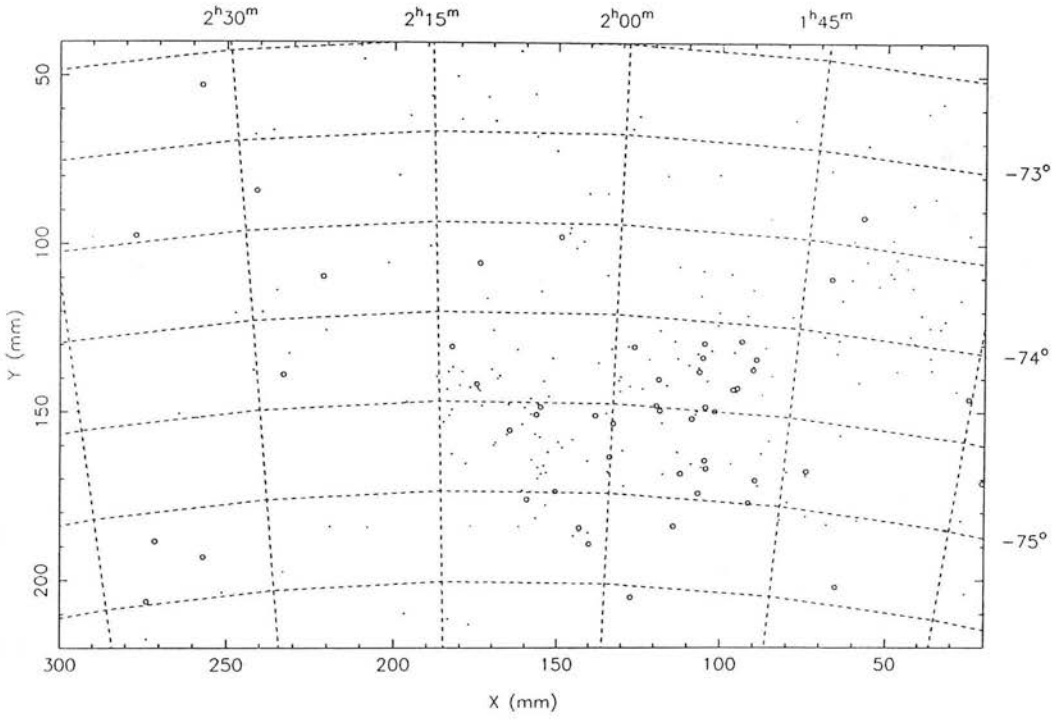

Figure 9.3: Plot of X, Y positions of stars with $B - R < 0.1$, $R < 15.5$ in Field 30. Stars with $R < 14$ are shown by open circles. The coordinates are for 1950.

overdensity of blue stars near the western edge of Field 30. The concentrations C1 and C2 have a sharp southern boundary with very few blue stars present southward of $DEC = -75°$. Lying off the eastern edge of the C1 concentration an isolated group of stellar aggregates (A1, A2, A3 — see Fig. 9.1) can be found. These collections of blue stars define the eastern 'tip' of the Wing. The aggregates A5 and A6 are not considered part of the conventional Wing since they are separated from the Wing's main body, lying at distances of nearly 7° from the SMC centre. These aggregates are discussed in the study by IDK, where they are referred to in their Table III as aggregate number 3 (our aggregate A5) and numbers 1 and 2 (our aggregate A6). A5 is an extended group of blue stars discovered by Kunkel (1980), while A6 comprises a 'sheet' of blue stars stretching west of $RA = 2^h30^m$ occupying an area of about one square degree according to IDK. The discovery of these aggregates had to wait until blue stars could be selected using both blue and red plates, since Brück (1978), using plate material of only one colour, did not detect these groups as an excess density region. The aggregate A4 is a prominent patch of blue stars about 10 arcmin in diameter lying to the north of the concentrations C1 and C2. It lies within the envelope of blue stars defining the main body of the Wing, as distinct from the other aggregates described here which are isolated 'islands' of blue stars.

We next deal with the question of the northern and southern boundaries defining the extent of the Wing region. The presence of an underlying older main sequence population in the Wing region was discussed in Chapter 7, and may contribute significantly to the blue stellar population in the more thinly populated areas away from the major concentrations and stellar aggregates. In the less densely populated area west of the C2 concentration, there is a sharp southern boundary which would not be expected if all the MS stars in this area belong to the older main sequence population. The northern extent of the Wing is a less clear cut issue, however, since the neighbouring Field 52 to the north possesses an older underlying population (stars mostly older than 0.8 Gyr — see Chapter 7) which almost certainly extends into Field 30. The plot of the positions of blue stars in Field 30 but including only stars brighter than $R < 17.0$ (Fig. 9.2) shows some decrease in the surface density of stars in the

areas north of $DEC = -73°$ with respect to other parts of the Wing. According to the isodensitogram of Westerlund & Glaspey (1971) the northern boundary of the Wing lies at $DEC = -73°$. Their star counts were based on blue stars brighter than $V = 18.5$ and would thus mostly exclude the contribution of the older underlying population. However, although the overall surface density is reduced, Figs 9.2 and 9.3 indicates that there are a significant number of bright blue stars lying north of this declination and that it seems likely that the Wing extends at least as far north as $DEC = -72°30'$. As discussed in Chapter 7, small numbers of bright MS stars from the Wing appear to be responsible for a south-north aging of MS populations in Field 52. Therefore, unlike the southern boundary, the northern boundary of the Wing is not clearly delineated.

We consider next whether there is any evidence that different parts of the Wing possess stars of different ages. In Chapter 7, we considered the luminosity functions of the main sequence stars in the Wing in three regions between different radii centred on the SMC centre. From their apparent similarity to each other we concluded that the Wing was produced by a single star formation event and that the stellar populations contained in it are effectively the same age. The grid region CMDs of Field 30 (Appendix C) show a well-defined and bright main sequence in all regions possessing stars belonging to the Wing. The tendency for CMDs with very well-populated main sequences to appear to reach brighter magnitudes than less well populated ones (e.g. CMDs F30:41, 51 which include the aggregates A5 and A6) is due simply to statistical effects as Fig. 9.4 shows. In this figure we have plotted the logarithmic luminosity functions, $\log N(R)$ in 0.5 mag bins, for the main sequence stars in the aggregate A5 and that for the whole area in Field 30 enclosed within $4° < r_{oc} < 5°$, an area which includes the concentration C2. Within the statistical errors there is very little difference between the form of the two luminosity functions. The Hodge (1987a) age calibration, based on the luminosity of the MS 'tip', was used in Chapter 7 to establish an age of around 50 million years for the age of the stellar populations of the Wing. The distribution of bright ($R < 15.5$) blue stars in the Wing shown in Fig. 9.3 confirms that stars as young as 50 million years old can be found in the

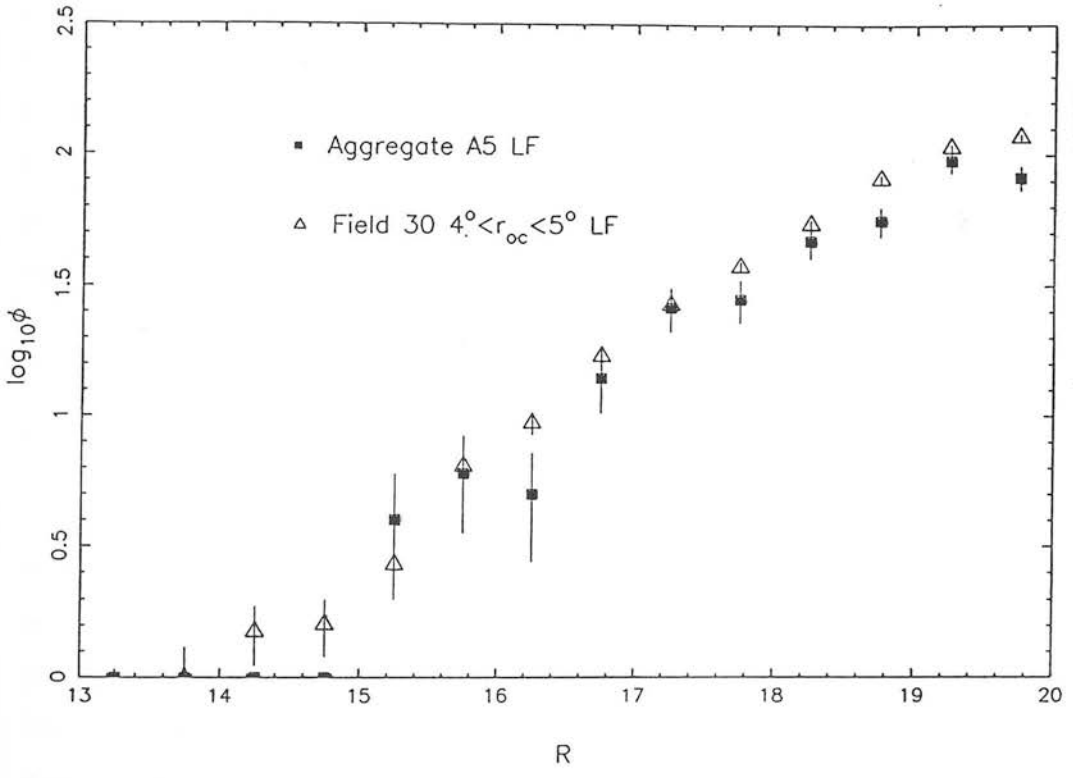

Figure 9.4: Main sequence differential luminosity functions for the aggregate A5 (square symbols) and for the region within $4° < r_{oc} < 5°$ (triangles) in Field 30, which includes the major stellar concentration C2. The logarithm of the number of blue stars per 0.5 mag bin is plotted with an arbitrary offset of -1.0 dex added to the latter of the two luminosity functions for comparison purposes.

main concentrations and aggregates of the Wing. On this plot the positions of blue stars brighter than $R = 14$ have been marked with open circles and there appears to be some indication that the brightest blue supergiants are found preferentially in the concentration C2. If we define the areas belonging to the concentrations C1 and C2 as bounded in right ascension by $2^h00^m < RA < 2^h15^m$ and $1^h45^m < RA < 2^h00^m$ respectively and by $-75°$ and $-74°$ in declination, the total numbers of blue stars brighter than $R = 15.5$ in the two concentrations are virtually identical but C2 has three times as many stars as C1 brighter than $R = 14$. It therefore appears that the C2 concentration is younger than the C1 concentration. It is impossible to tell whether the C2 concentration is younger than the other areas of the Wing because of the poor statistics in the less densely populated regions. Therefore, although it appears that the stellar populations of the Wing consist universally of very young stars, some areas may be slightly younger than others.

Lastly in this section we assess the scale of the star formation burst in the Wing in order to determine its contribution to the total stellar population of the SMC. This result will be useful in the discussion of the relative importance of externally stimulated star formation compared with that resulting from processes internal to the SMC in the following chapter. We may perform a calculation based on the numbers of HB/clump stars that would be observed in the SMC in about 1 Gyr time and comparing this number to the number of clump stars observed at present, which we assume will not have altered significantly 1 Gyr later. We adopt the technique described in Chapter 8 (Section 1), using eqn.(1) derived by Cannon (1970), which enables the determination of the numbers of evolved stars coeval with the main sequence of any stellar population based on the population statistics of the main sequence. The MS 'tip' luminosity for a 1 Gyr population for the Wing is $R = 19$, taking into account that the Wing appears to be located closer than the SMC main body with a difference in the distance modulus of 0.3 mag from the Cepheid distance determinations of Caldwell & Coulson (1986). Then, the clump stars in 1 Gyr time will have originally come from the section of the MS between $R = 18.5 - 19.0$. There are presently 2261 MS stars in this half-magnitude range in Field 30, and application of eqn.(1) of Chapter 8 with an HB/clump lifetime

of 0.2 Gyr gives the result that a total of 1220 clump stars will exist due to the Wing feature beyond about 3° from the SMC centre in 1 Gyr time. It can probably be assumed that the Wing 'feature' itself will be smeared out uniformly over the surface of the SMC as a result of orbital or dynamical mixing processes which operate on a timescale of a few 10^8 yr. This can be compared with a present number of about 65000 true clump stars in all six survey fields located beyond 3° from the SMC centre after having corrected for the galactic foreground and RGB contributions. Therefore, the contribution of the Wing population to the present stellar content in the SMC outer area is about 2 per cent. Thus, although the Wing is a very prominent localised optical feature, it can be concluded that it has not contributed very significantly to the overall stellar content of the SMC.

2 The H I Distribution in the Wing

McGee & Newton (1986) (hereafter MN) mapped the SMC Wing region and the inter-Cloud region in H I and also produced maps of the Gaussian components corresponding to different H I velocity groups. It is instructive to compare the features of the stellar distribution in the Wing region with these maps in order to identify correlations which may help us to understand the formation history of the Wing.

MN comment that the $N_H = 10^{21}$ cm^{-2} contour coincides approximately with the boundary of the Wing defined by the star counts of Westerlund & Glaspey (1971), and this is confirmed by comparing Fig. 9.1 with MN's Fig. 4 showing the N_H contours in the inter-Cloud region. The eastern tip of the Wing at around $RA = 2^h20^m, DEC = -74°30'$ is delineated by the 10^{21} cm^{-2} contour and the aggregate A5 coincides with an 'island' centred on $RA = 2^h30^m, DEC = -74°$ where the H I column density exceeds 10^{21} cm^{-2}. The major stellar concentrations C1 and C2, however, are not particularly well correlated with the high H I column density region with $N_H > 12 \times 10^{20}$ cm^{-2}. It will be seen that these features are correlated better with features of the maps corresponding to different velocity groups produced by MN.

The contour maps of the three groups with mean radial velocities $+155, +177$ and $+195$ km s^{-1} associated with the H I distribution show that in the SMC Wing region the two lower velocity components are stronger than the $+195$ km s^{-1} component, which is more tenuous and extends further into the inter-Cloud region. The best agreement of the stellar distribution of the Wing region is seen to occur for the $+177$ km s^{-1} map. This map shows that the 2×10^{20} cm^{-2} contour level encompasses the region between declinations 74° and 75° where the bulk of the stellar population of the Wing is found. In addition, the aggregate A5 and concentration C1 coincide with major peaks in the H I distribution at this velocity. Curiously however, the peak in the H I distribution bounded approximately by 1^h45^m and 1^h30^m in RA and $-74°$ and $-75°$ in DEC coincides with a thinly populated region of the Wing to the west of the concentration C2. Furthermore, IDK remark that no strong correlation exists between regions with enhanced H I density and the blue stellar aggregates found in the inter-Cloud region. The implications of these observations are considered in the following section. Finally, the concentration C2 is best matched by a region of higher H I density in the 195 km s^{-1} map.

Various workers have obtained radial velocities of blue stars belonging to the Wing, but in general the determinations are not accurate enough to confirm whether a detailed correlation exists with H I masses associated with different velocity components. The radial velocity study of Carrozzi, Peyrin & Robin (1971) of 49 early-type stars in the Wing region was based mainly on determinations from objective prism plates giving quite coarse results, and even their higher accuracy velocities based on medium dispersion spectra showed systematic discrepancies from earlier velocity determinations quoted in their paper. More recent velocity determinations in the Wing region have been reported by IDK and Demers *et al.* (1991b) with a nominal accuracy of 10 km s^{-1}. For stars lying to the west of $RA = 2^h30^m$ the radial velocities were found to lie between 170 and 220 km s^{-1}. The velocities under 200 km s^{-1} are consistent with the mean heliocentric velocity of the H I for the Wing region (see Fig. 4 of MN), but the higher velocities do not fit easily into the pattern of the major H I velocity groups seen in this region. However, Demers *et al.* (1991b) state that the small overall

west to east velocity gradient found for stars lying in the Wing and in stellar associations in the inter-Cloud region is consistent with these associations being connected with the SMC Wing rather than being directly associated with the higher velocity component of the inter-Cloud gas. In conclusion, more comprehensive and accurate data are required to establish the detailed radial velocity pattern in the Wing and inter-Cloud region.

3 The Origin of the Wing

Although it is accepted that the Wing is a product of the interactions of the LMC-SMC-Galaxy System, its precise origin is uncertain; IDK consider that it resulted from a burst of star formation triggered by the near collision between the LMC and SMC about 200 million years ago predicted by the models of Murai & Fujimoto (1980) (MF); Westerlund (1990), however, considers it to be part of the very young stellar generation seen in the Magellanic Clouds whose formation was triggered by the perigalactic approach of the Magellanic Clouds about 40 million years ago also suggested by the MF models. The approximate coevality of the Wing and the blue stellar aggregates in the inter-Cloud region point to a common origin for these features, with the Wing being merely the strongest part of the stellar link between the Magellanic Clouds. Although the young age of the Wing ($< 10^8$ yr) and the stellar aggregates in the inter-Cloud region suggest that the perigalactic approach may have been the actual trigger for star formation to proceed, the formation of the H I mass between the Magellanic Clouds, in which the stellar structures formed, appears to be linked to the last close encounter between the Magellanic Clouds themselves.

We first consider the origin of the gas complex in the Wing and the H I Bridge in the inter-Cloud region, out of which the stars subsequently condensed. Toomre & Toomre (1972) have investigated the formation of bridges and tails as a result of tidal interactions between galaxies involved in a near encounter, confirming that such features are a common product of galaxy-galaxy interactions. A tidal origin

for the Magellanic H I Bridge is favoured by the models of Murai & Fujimoto (1980) (MF). Their test particle simulation of the triple interacting LMC-SMC-Galaxy system results in a distribution of particles in the neighbourhood of the Magellanic Clouds which shows a bridge connecting the LMC and the SMC and a possible Wing of the SMC. The H I Bridge between the Magellanic Clouds represents the inter-galaxy 'bridge' formed as a result of their tidal interaction, while the Magellanic Stream represents the 'tail' which has been subsequently extended by the tidal field of the Galaxy.

One problem with the interpretation of the Wing and H I Bridge as a tidal feature is that already formed stars, distinct from the young stars forming later in the inter-Cloud region, would be expected in the inter-Cloud region. However, the existence of an older counterpart to the young stars forming the stellar link between the Magellanic Clouds has not been proven, and the distribution of older populations seen in projection against the Wing region is very different from that of the young stars and H I gas. This can be readily seen by comparing the surface distribution of the HB/clump stars (see Fig. 4.3), representing the older populations to the younger populations directly associated with the Wing. The distribution of older populations shows neither the finger-like extension towards the east nor the clumpy distribution exhibited by the stars of the Wing, which are also seen to extend well beyond the outer HB/clump contours. As mentioned by Wayte (1991) the recent close encounter between the Magellanic Clouds could have involved hydrodynamical effects if the encounter between the Clouds was close enough, i.e. was really a collision. Murai & Fujimoto (1980) advocate a close (and hence hydrodynamical) collision between the LMC and the SMC 2×10^8 yr ago, in contrast to Wayte (1991), who favours a separation between the two galaxies at closest approach of at least 5 kpc. If we consider that the encounter event was close enough for the gaseous haloes of the two Clouds to interact directly, it seems possible that the gas concentrations in the Wing and the H I Bridge were created by the action of ram pressure forces between the the gas envelopes of the SMC and LMC, leading to the formation of dense compressions in the region between the Magellanic Clouds. The maps of different H I velocity components pro-

duced by MN show the existence of no fewer than eight different velocity components for the gas in the inter-Cloud region. Two of these components have no counterparts to the velocity components seen in the LMC or the SMC and appear to form a distinct inter-Cloud gas mass, which perhaps indicates that at least part of the inter-Cloud gas was not simply tidally removed from the Magellanic Clouds. According to the MF tidal models the gas in the inter-Cloud region originated mainly from the SMC. Therefore, an abundance analysis of young stellar associations located on the LMC side of the inter-Cloud region would constitute the best test for the tidal origin theory of the gas in the H I Bridge, as such an analysis would confirm its origin in the SMC in accordance with this theory or alternatively provide evidence that it is derived from the more metal-rich LMC. Detailed modelling of the velocity structure of the gas in the inter-Cloud region would also help to clarify the origin of the inter-Cloud gas.

In Section 1 we examined the age composition of the Wing and concluded that all parts of the Wing are aged 50 million years or less, with the C2 concentration apparently slightly younger than the C1 concentration. There is also some evidence for an age gradient in the general inter-Cloud/Wing region from the main sequence photometry of two very young stellar associations, one located within the halo of the LMC and the other within the A5 aggregate near the Wing (see Fig. 9.1), reported by Grondin *et al.* (1991). The presence of evolutionary deviations from the theoretical main sequence for the latter association was taken to imply an older age for this association and a possible east-west (positive) age gradient for stellar aggregates in the inter-Cloud region. This observation appears to be consistent with the possibility that star formation begun in the Wing region where the H I density is greatest according to the H I maps of MN.

The study of the correlation between stellar and H I density in the Wing region in the previous section showed that although some areas of high stellar density correspond to peaks in the H I distribution associated with individual velocity components, this was not always the case. In particular a low density area in the stellar distribution lying to the west of the concentration C2 was seen to coincide with a major peak

in the +177 km s^{-1} H I map. This presumably indicates that high density of H I gas is a necessary but not sufficient condition for star formation to proceed, with additional energy required to lead to precipitation of stars from the existing gas clouds. This observation is consistent with the apparent time-lag between the close encounter between the Magellanic Clouds, believed to have occurred 2×10^8 yr ago, and the more recent formation of stars in the Wing, which indicates that self-gravitational collapse of gas clouds to form stars did not spontaneously occur.

The main results from this chapter can be summarised as follows:—

• The Wing is an approximately coeval feature younger than 50 million years old. It is also coeval with the blue stellar aggregates in the inter-Cloud region discovered by IDK.

• One of the major concentrations of stars in the Wing, located at around $RA = 1^h53^m$, $DEC = -74°30'$, appears to possess more bright blue supergiant stars with $R < 14$ ($M_R < -5$) than other regions of the Wing, and is presumably slightly younger.

• Based upon star counts in the Wing and comparison with the numbers of the older HB/clump stars in the six project fields, the contribution of the stellar population associated with the Wing to the total stellar population of the SMC beyond 3° from the SMC centre was found to be only about 2 per cent.

• The main distributions of young stars in the Wing correspond fairly well to the H I density map for the 177 km s^{-1} velocity component produced by McGee & Newton (1986).

• The recent (about 2×10^8 yr ago) close encounter between the LMC and the SMC probably accounts for the formation of the H I Bridge between the Magellanic Clouds. The Wing is the strongest part of the stellar link between the Magellanic Clouds which formed subsequently from the inter-Cloud gas.

PART III: *THE AGE DISTRIBUTION*

CHAPTER
— 10 —

THE STAR FORMATION HISTORY OF THE SMC

In this chapter we review the star formation (SF) history of the SMC based on the detailed findings of the Chapters 7, 8 and 9. We begin in Section 1 by comparing the results derived in these chapters with the age distribution indicated by other studies of different population groups in the SMC. In Section 2 we briefly review the age distribution of the LMC, focussing on the similarities and differences between the two Magellanic Clouds. In Section 3 we discuss the chemical evolution of the SMC which in principle provides a record of its star formation history. Finally, in Section 4 we present a discussion of the star formation processes which may account for the

observed evolutionary development of the outer regions of the SMC.

1 Population Group Studies in the SMC

Studies of different population groups have aided the tracing of the age distribution in the SMC, but have generally lacked the large areal coverage of the present study. Here, we augment our understanding of the age distribution by means of comparison with these studies.

Azzopardi & Rebeirot (1991) have summarised the properties of the distributions of several population groups including young populations (less than a few 10^8 yr) such as late- and early-type supergiants, Hα emission line stars and small nebulae, and intermediate-age population groups such as carbon stars and planetary nebulae. It is evident that the younger populations are concentrated in the Bar of the SMC and in the Wing with the older age groups apparently less centrally concentrated but still possessing an elongation along the axis of the Bar in the NE-SW direction. This general pattern can be compared with the elongated and highly centrally concentrated distribution of the younger (0.3-0.6 Gyr) MS populations along the SMC major axis and the less centrally concentrated distribution of the older HB/clump population. A more detailed comparison of the HB/clump surface distribution with that of the carbon stars, whose ages range from about 0.8 to 8 Gyr (see e.g. Iben 1984) and therefore overlap with the ages of HB/clump stars, is instructive. As noted in Chapter 4 (see Fig. 4.3), the HB/clump distribution in the inner parts appears to be elliptical in projection with its major axis aligned in a NE-SW direction. On closer inspection the centre of this distribution appears to be located about half a degree to the south-west of the optical centre. The corresponding carbon star distribution based on continuous star counts is also elongated along the SMC major axis and its centroid is displaced to the south of the optical centre. Although it is not clear that the two distributions are due to coeval populations, the similarities between the distributions suggest that they may share a common structural interpretation. The kinematical study of Hardy,

Suntzeff & Azzopardi (1989) of a sample of carbon stars is consistent with the conclusion that the carbon stars belong to a kinematical spheroidal population. Johnson (1961) has also suggested the existence of a dwarf elliptical Fornax-type component for the old stellar component in the SMC from the projected elliptical outline on an infrared photograph. The outermost HB/clump contours are more circular than the inner contours and therefore this elliptically shaped component appears to be confined to the more central areas not beyond 4° from the optical centre.

The properties of the SMC cluster distribution should also be mentioned here. Van den Bergh (1991) has noted the concentration of young clusters in the SMC Bar and the more dispersed distribution of the older clusters, again following the general pattern described in the previous paragraph. Brück (1975), however, based on a larger cluster sample but using more subjective age-dating criteria, locates the centroid of the oldest clusters somewhat to the south-west of the optical centre, an observation which coincides with the displacement of the inner elliptical HB/clump component, representing the older stellar populations, to the south-west. Da Costa (1991) (hereafter DC) has described the age distribution and age-metallicity relation for Magellanic Cloud clusters which have been studied down to the MS-turnoff. For the SMC, it is clear that production of clusters has been more or less continuous over the last 10-12 Gyr with no favoured epoch. Although the star formation history in the general field may differ from the history of cluster formation, the uniform age distribution of SMC clusters indicates that star formation has been occurring at significant levels in parts of the SMC outer regions throughout the past 10 Gyr. The age composition in the general field in the outer areas has been shown by deep CCD colour-magnitude diagram studies near clusters (see Table 1.1) to be dominated by populations aged around 10 Gyr, often in contrast to the embedded (in projection) clusters, which are generally younger (e.g. GC2, GC3). This result on the age of the bulk of the field populations in the outer regions is in agreement with our conclusions on the median age of populations derived using the d_{B-R} indicator in Chapter 8.

The projected distributions of old stellar populations ($\geq$ 10 Gyr) such as old

long-period variables and RR-Lyrae stars in the SMC have not been comprehensively studied. The study of a sample of RR-Lyraes in Field 51 (see Chapter 8) is the only wide area search in the SMC at the present time. The degree of incompleteness of the study makes the conclusions somewhat tentative but the results apparently indicate a weaker central condensation than for the HB/clump population, representing the bulk of the stellar population aged younger than about 10 Gyr. This result is consistent with the observations by Graham (1975), who observed no significant radial falloff of the RR-Lyrae distribution in his more complete study covering a smaller area near the galactic globular cluster 47 Tuc.

2 Comparison with the LMC Age Distribution

In the LMC, although a number of globular clusters similar in ages to galactic globular clusters, possessing RR-Lyraes and/or blue horizontal branches, exist, the general field in the LMC is believed to be younger in the mean than that of the SMC. Studies by Stryker (1984a), Stryker & Butcher (1981), and more recently by Hodge (1987b) have shown that out to 9° from the LMC Bar the dominant population is of intermediate age. The latter two studies investigated fields within 5° of the LMC Bar and found evidence for a dominant population component aged 2-4 Gyr which may indicate that a burst of star formation occurred in this epoch. The more remote area lying 9° NE of the LMC Bar studied by Stryker (1984a) indicated the presence of a 7 Gyr field population at least several Gyr younger than the nearby old LMC globular cluster NGC 2257. A median age of 7-9 Gyr was also derived by H91 for the field population near the cluster Hodge 11, in good agreement with Stryker's result. There is thus a strong possibility that the dominant populations in the general field in the LMC are at least 2-3 Gyr younger in the mean than the dominant field populations in the SMC, however towards the remote outlying areas of the LMC the ages of the dominant field populations may converge to that of the SMC outer regions.

The cluster formation history of (at least the more massive) clusters in the two

Clouds also seems to be quite diverse. The age distribution of LMC clusters (see DC) shows a conspicuous gap between 4 and 15 Gyr, populated by only one cluster. In contrast, the SMC has a few clusters in this age range. There are a large number of LMC clusters aged between 1 and 3 Gyr, whereas this does not appear to be a favoured epoch for cluster formation in the SMC. In this respect the cluster formation history in the Magellanic Clouds from about 3 Gyr ago appears to parallel the star formation history in the general field. The major star formation epoch in the LMC field seems to have begun about 2-4 Gyr ago as discussed above, while the results of the age distribution study of main sequence stars younger than about 2 Gyr ago in the outer regions of the SMC (Chapter 7) indicate that the major period of relatively recent star formation began about 0.6 Gyr ago in the regions associated with the Bar of the SMC. It is evident that the disparate nature of the age distributions between the Magellanic Clouds of both cluster and field populations is not easily explained if they are assumed to be bound to each other over most of their history.

In all studied field areas in the LMC no trace of a horizontal branch lying on the blue side of the instability strip has been found, despite the fact that LMC globular clusters with blue HBs exist. As stated in Chapter 8, no BHB population was found in the SMC either. The implications of the absence of BHB populations in the field populations of the Magellanic Clouds for their early evolutionary history will be discussed in the Section 4.

3 The Chemical Evolution of the SMC

The chemical evolution of a galaxy should provide a record of its star formation history, since heavy elements are produced inside massive stars and subsequently dispersed into the interstellar medium. The metallicity-age relation is the main tool for the study of the chemical enrichment history of a galaxy. The metallicity-age relation for the SMC was extensively discussed in H-thesis (pp.171-180) and various attempts were also made to model the relation.

According to H-thesis, the form of the metallicity-age relation, as defined by well-studied SMC clusters (see the cluster metallicity-age relation produced by DC), and abundance determinations of individual stellar objects such as RR-Lyraes and supergiant stars, shows a swift enrichment in the early epoch before 10 Gyr ago and a nearly constant value of around [Fe/H]= −1.3 between 10-12 and 3 Gyr ago followed by a steep increase from 3 Gyr ago to the present-day value of about −0.6 dex. Dopita (1991), in his review of the chemical evolution of the Magellanic Clouds, confirms the qualitative form of the metallicity-age relation described above and proposes three explanations for the relative constancy of the metal abundance until about 3 Gyr ago. The first of the possible explanations, that the star formation rate was very low during this period, was discounted by Dopita on the grounds that clusters were still being formed throughout this period. The bulk of the stellar population in the outer parts of the SMC was also formed near the beginning of this period according to the discussion in Section 1. Dopita considers that either infall of relatively unprocessed material is required to keep the metallicity at low levels for several Gyr or galactic winds carried away newly processed material from star-forming regions. Similar conclusions were derived from the detailed modelling of the metallicity-age relation in H-thesis, as summarised below.

Both the closed-box model of chemical evolution (Searle & Sargent 1972; Pagel & Patchett 1975) and the simple model with stochastic SF bursts (Matteucci & Chiosi 1983) were found to give an inadequate representation of the observed metallicity-age relation for the SMC. It was found that the qualitative features of the metallicity-age relation could be reproduced by the gas infall or accretion model (Larson 1972; Twarog 1980) by which relatively unprocessed gas is allowed to enter the disk at some rate which is abruptly lowered at around 3 Gyr ago. Alternatively, instead of a decrease in the infall rate, an enhanced rate of star formation beginning 3 Gyr ago may explain the increase in the rate of chemical enrichment starting at this epoch. Both a reduction in the infall rate and an increase in the star formation rate seem to require an external perturbation, possibly provided by the close encounter between the LMC and the SMC which occurred about 3 Gyr ago according to the Murai & Fujimoto

(1980) tidal models (see their Fig. 3b). The start of a *major* epoch of star formation in the SMC about 2-3 Gyr ago lasting until the present is not supported by the age distribution study (see Chapter 7) of the outer regions based on main sequence populations aged younger than about 2 Gyr ago, so a decrease in the infall rate is favoured. However, given that our study is confined to the outer areas, we cannot be certain that an enhanced period of star formation did not occur from about 3 Gyr ago in the Bar of the SMC. Hunter & Gallagher (1986) note that there is no clear physical evidence for gas infall occurring in Magellanic irregulars, but observations showing that star-forming regions in irregular galaxies are confined to the inner 60 per cent of their optical dimensions by Hunter (1982) suggest that the relative depletion of gas in the outer regions and the low metallicities of such systems may be explained by such a mechanism.

In conclusion, the form of the metallicity-age relation does not accurately reflect the star formation history of the SMC, requiring processes such as gas infall or galactic winds to be invoked in order to properly account for it. Therefore, in order to achieve a complete understanding of the star formation history of the SMC, its chemical evolution must be considered in conjunction with these processes as well as the role of the Bar of the SMC (Dopita 1991).

4 Discussion of the Star Formation History of the SMC

In this section we consider the processes responsible for star formation (SF) in the outer parts of the SMC on the basis of our current picture of the age distribution in the SMC. As an irregular galaxy it may be expected to display a rather disordered pattern of star formation, but the role of interactions with the Galaxy and the LMC might also be important. We begin by considering the early star formation history of the SMC (subsection 4.1) and then examine the effect of interactions with the Galaxy and the LMC on the star formation history of the SMC (subsection 4.2). Finally we discuss the internal processes believed to be responsible for star formation in irregular

galaxies (subsection 4.3).

4.1 The Early Star Formation History

The discovery of an asymmetric blue extension from the main horizontal branch/clump feature on several CMDs in the outer regions (see Chapter 8) suggests that populations as old as globular clusters in the Galaxy may well be present in the SMC. The very old stellar component was found to constitute only 7 per cent of the total mass in the area surveyed, a proportion which is comparable to the ratio of spheroidal to disk mass in our Galaxy within the solar circle. Analogous to the disk-halo dichotomy in the Galaxy, it is possible that this very old stellar component was formed in the initial collapse of the SMC protogalaxy, and that the bulk of star formation occurred at about 10 Gyr ago in the disk component of the SMC which formed subsequently. Stryker (1984b) comments that the age of the background sheet in the SMC is similar to that found in the galactic disk, and a disk-halo scenario was also suggested for the LMC by Stryker & Butcher (1981) to explain the apparent time-lag between the formation of the old globular cluster system in the LMC and the bulk of the population, which is of intermediate age. However, the work of Freeman, Illingworth & Oemler (1983), has cast some doubt on this hypothesis by showing that the oldest clusters in the LMC constitute a separate rotating disk from that of younger populations in the LMC. The existence of distinct kinematical disk and spheroid components in the outer regions of the SMC is at present completely unknown since radial velocity data for the outer regions of the SMC is very sparse.

The absence of any populations with a blue horizontal branch in the field populations of both the SMC and the LMC points to differences between the early evolutionary phases of the Galaxy and the Magellanic Clouds. The nature of the 'second parameter' controlling horizontal branch morphology is not well understood and therefore the implications of the absence of blue HB populations are not completely clear. The study of Sarajedini & King (1989), which presents evidence for a 5 Gyr age spread among galactic globular clusters, favours age as the second parameter, with the oldest

galactic globular clusters exhibiting the bluest HBs. Therefore, the absence of BHB stars in the SMC may simply indicate that the SMC is a few Gyr younger than the Galaxy but this interpretation seems to conflict with the ages determined using the d_{B-R} calibrator for the oldest populations in the SMC in Chapter 8. Alternatively, if we assume that metallicity is the main parameter controlling the morphology of the horizontal branch for very old populations, we may consider that rapid chemical enrichment followed a very brief initial burst of star formation or perhaps that the Magellanic Clouds were not formed from primordial gas. A few BHB stars would still be expected according to the former scenario which maybe argues against its validity. Nevertheless, several clusters with BHBs *were* produced in the LMC and these can perhaps be attributed to this initial burst. The lack of such clusters in the SMC is in itself not surprising on statistical grounds if the numbers of these clusters were to be proportional to the galaxy mass. Only 1-2 such clusters in the SMC would be expected given LMC and SMC masses of 6 and 1.5×10^9 $M_\odot$ respectively. A non-primordial origin for the gas which formed the Magellanic Clouds can be understood if the Magellanic Clouds were formed from already processed gas ejected from the Galaxy possibly as a result of a close encounter with another massive galaxy. Such an encounter may also help to explain the distribution of several galactic globular clusters and dwarf spheroidal galaxies in a polar ring around the Galaxy (see Mathewson 1985). In this connection, it is worth noting that of the eight dwarf elliptical satellites of the Galaxy only Ursa Minor has a predominantly blue horizontal branch (Mateo *et al.* 1991), whereas the other satellites have horizontal branches more closely resembling the extended red horizontal branch morphology which we have found for the oldest populations in the SMC.

4.2 The SMC Age Distribution and the Interacting Magellanic System

The phenomenon of active star formation in interacting galaxies began to be noticed in the late 1970s. Strong evidence for star formation induced by tidal interaction

between galaxies was provided by Larson & Tinsley's (1978) study confirming a large colour scatter for the interacting galaxies from *the Atlas of Peculiar Galaxies* (Arp 1966), and this has prompted numerical modelling of tidal encounters between galaxies including the response of both the stellar and gaseous components. In particular, Noguchi & Ishibashi (1986) (see also Noguchi 1990) have shown that for a galaxy having undergone a tidal encounter (involving gravitational interaction only between the "colliding" galaxies) cloud-cloud collisions (represented by test-particle collisions in their simulations) are about ten times more frequent than their pre-encounter values. Assuming stars form from these collisions, a comparable enhancement of star formation occurs in the outer disk region of the galaxy where the tidal deformation is the most remarkable. Subsequent models developed by Noguchi (1987, 1988) have also investigated the formation of bar structures, which are sites of greatly enhanced star formation activity, as a result of tidal encounters between galaxies. From these simulations it is clear that there is an adequate theoretical basis for the idea that star formation can be stimulated by galaxy-galaxy encounters.

Past interactions of the Milky Way-Magellanic System may be presumed to have stimulated star formation in its constituent galaxies. In the following we discuss the evidence for the effects of external interactions with the LMC and the Galaxy on the age distribution of the SMC by considering the results we have obtained from the studies of the field populations of the outer regions as well as aspects of the age distributions in the Magellanic Clouds highlighted in the previous sections in this chapter. We begin by considering the hypothesis that the major stellar generations were produced as a result of tidal interactions between the members of the LMC-SMC-Galaxy system, and then discuss the evidence for bursts of star formation based upon the age distribution studies of the previous chapters. Finally, we discuss the origin of the extended distributions of relatively young (less than about 2 Gyr old) main sequence populations in the eastern outer areas of the SMC in the context of the interactions of the LMC-SMC-Galaxy system.

(i) The Interacting Magellanic System and Comparative Age Distributions of the Magellanic Clouds

The case for externally induced global bursts of star formation in the Magellanic Clouds has been described by Westerlund (1989) (see also Westerlund 1991; Westerlund & Danziger 1985). The formation of the different stellar generations in the Magellanic Clouds is supposed to begin with epochs which agree with the time of close encounters between the Magellanic Clouds themselves and with the Galaxy according to the models of Murai & Fujimoto (1980) (MF) (see also Fujimoto & Murai 1984). Although broadly speaking, old, intermediate-age and young populations are seen to exist in both Clouds it is by no means certain that they define distinct and synchronous star formation episodes. These broad categories possess a large age range, e.g. intermediate-age objects are considered to have ages between 2 and 8 Gyr, and therefore the argument that the different star-forming episodes are synchronous depends on the duration of each episode and hence on the mechanisms responsible for propagation of star formation within the Magellanic Clouds.

Although young, intermediate-age and old stellar populations are all represented in the Magellanic Clouds, the detailed age distribution appears to justify rejection of the above hypothesis. As discussed in Section 2, the ages of the major generations of stars in the outlying general field and the age distribution of clusters in the two Magellanic Clouds exhibit considerable differences. The MF tidal models suggest that the distance between the Magellanic Clouds and the Galaxy has been decreasing in an oscillatory manner over the past 10^{10} yr, which may indicate that only the comparatively more recent tidal encounters with the Galaxy have had a major influence on the star formation histories of the Magellanic Clouds. Another explanation is that the Magellanic Clouds have not existed in a binary state for most of their history. This possibility is supported by the particle simulation experiments of Murai & Fujimoto (1986) who found that the best representation of the Magellanic Stream could be obtained if the SMC was independently orbiting the Galaxy and captured by the LMC about 1.7×10^9 yr ago. In short, the poor correlation between the detailed

star formation histories of the two Magellanic Clouds does *not* support the view that interactions of the Galaxy-LMC-SMC system are responsible in a major way for the production of the various stellar generations present in the Magellanic Clouds.

Indirect evidence, from the existence of globular-like clusters in the Magellanic Clouds, may indicate that we cannot altogether dismiss an important role for interactions between the Magellanic Clouds in stimulating star formation. Fujimoto & Kumai (1991) and Ashman & Zepf (1992) provide evidence that globular clusters are formed preferentially in interacting systems such as the Magellanic Clouds and galaxies at the centres of galaxy clusters. The formation of massive colliding gas clouds is favoured during galaxy-galaxy interactions, producing conditions similar to those prevailing in the initial collapse of the Galaxy during which the galactic globular clusters formed. However, the production of globular clusters may not be accompanied by vigorous production of field stars. In Section 1 we noted that for some SMC clusters the adjacent field population is much older than that of the cluster. Furthermore, the different age distributions for well-studied LMC and SMC clusters (see DC) provide grounds for scepticism that Magellanic globular clusters were formed only during tidal encounters. However, we cannot rule out the presence of arbitrary selection effects as well as disruption of less massive globular clusters giving rise to cluster samples which do not truly reflect the cluster formation history of the Magellanic Clouds.

(ii) Evidence for Bursts of Star Formation in the SMC

We now examine the evidence for the existence of star formation bursts in the outer regions of the SMC, based upon the observational results described in Chapters 7, 8 and 9. Such bursts may not necessarily preclude internal processes as their cause, since many isolated irregular galaxies are believed to be undergoing bursts of star formation (Gallagher & Hunter 1984). However, if such bursts coincide with the epochs of close encounter events, a more compelling case may be made for their origin in terms of such external interactions.

The Wing region, which was extensively discussed in the previous Chapter, is a

clear example of a burst of star formation triggered by the interactions of the Milky Way-Magellanic Clouds system. The close encounter between the Magellanic Clouds about 2×10^8 yr ago is believed to have produced the distributions of gas seen in the Wing and the inter-Cloud region, but the formation of stars may have been triggered by tidal shocks as a result of the perigalactic passage of the Magellanic Clouds about 40 million years ago according to the MF models. The contribution of the stellar population of the Wing to the total stellar population in the outer regions of the SMC was estimated to be only about 2 per cent. If this is the typical strength of a tidally induced star formation burst it is hard to see how the major stellar generations could have been produced as a result of interaction events as Westerlund (1989) hypothesises. However, there are many variable factors in determining the strength of a star formation burst, such as the quantity of gas available for star formation (which would be higher in the past) and the strength of the tidal forces which would be a function of the impact parameter of the encounter, and therefore a conclusive statement cannot be made to this effect.

Aside from the SMC Wing, our direct observational evidence for bursts of star formation in the SMC outer regions is not conclusive, being hampered by the fact that we only have good time resolution up to about 2 Gyr ago. As discussed in the previous subsection, the majority of stars in the outer regions of the SMC appear to have been formed in one major burst or enhanced SF phase of unknown duration around 10 Gyr ago and further progress on this question will depend on more extensive deep observational data. The best supporting evidence we have for an enhancement in the SF rate in any region over the past 2 Gyr is the well defined break in the main sequence LF at about $R = 18$ in the LFs for the inner regions within 2.5° of the SMC centre in Fields 51 and 52, implying the existence of a population component aged about 0.4-0.6 Gyr, depending on the distance modulus. This result also indicates that the SF rate was comparatively low for at least 1 Gyr prior this time in agreement with statement by Westerlund (1990) that: "Star production has been low between 2 Gyr and 0.7 Gyr [ago]". These areas are located near the edge of the northern outer arm and Brück (1980) also suggests that star formation in these areas was due

to a bursting SF mode. This burst of star formation may perhaps coincide with the epoch of the most recent encounter between the Magellanic Clouds; the models of the Magellanic system developed by Mathewson *et al.* (1987) place the recent close encounter between the LMC and the SMC at 0.4 Gyr ago (instead of 0.2 Gyr ago according to the MF models), compatible with our lower estimate for this population component.

No distinct period of SF could be identified from the MS LFs of the outer studied regions (see Chapter 7). The steep LFs in the outer regions of Fields 52, 51 and 29 indicate that the SF rate has been decreasing with time over the past 2 Gyr or so and is currently at insignificant levels. It is possible that we are observing the tail end of an SF episode begun sometime not long before 2 Gyr ago or that star formation has been decreasing continuously over a much longer period of time. Observations to fainter magnitudes are required to determine whether there is a 'break' in the LF corresponding to the start of a definite epoch of star formation.

(iii) Origin of the Extended Distribution of Relatively Young Main Sequence Populations in the Eastern Outer Areas

Observations from Chapter 7 show an asymmetrical distribution of MS populations brighter than $R = 20$, corresponding to ages younger than about 2 Gyr, with respect to both the SMC centre and the distribution of the older stellar component represented by the HB/clump population. The fact that these extended distributions of MS stars, reaching up to $4 - 5°$ from the SMC centre, are found in the eastern part of the SMC on the same side of the SMC as the Wing region suggests that their origin is linked with the interactions of the LMC-SMC binary system. As we shall see, however, the precise origin of these distributions cannot be easily explained.

The non-uniformity of the MS distributions for populations younger than about 2 Gyr suggests a relatively recent origin for these features since orbital and dynamical mixing processes have not had time to smooth them out over the whole projected area of the SMC. The rotational period for the H I gas lying within 2.6 kpc of the

SMC centre is about 4×10^8 yr from data given by Hindman (1967), and therefore one would expect localised features to be dispersed on a timescale comparable to one or two rotation periods. Since the MS LFs indicate that the age distributions of these areas are biased towards older ages up to the 2 Gyr limit defined by the effective magnitude limit, it appears likely that the extended MS distributions are a tidal feature produced possibly as a result of the most recent (2×10^8 yr ago) encounter between the SMC and the LMC.

Two alternative explanations are then available to us. We discuss these possibilities in turn.

(1) Stars were dislocated by tidal forces from the central regions of the SMC which possess a younger age distribution than the outer regions. The age distribution of these extended distributions of MS stars is different for the north-eastern outlying area and the area of the SE 'bulge' feature described in Chapter 7, but both areas show an older age constitution with respect to the more central areas. In Chapter 7 it was noted that the average age of the MS populations decreases towards the SMC centre in the SE 'bulge' feature and it may be possible to understand the age distribution in this area as a combination of an older component (mostly aged greater than about 0.8 Gyr) similar to that observed in the north-east plus a separate younger component, with the apparent aging towards the periphery being due to the different radial distributions of the two populations. If so, the younger component can be understood as representing a tidal distortion caused by young stars being pulled out from the central SMC areas as suggested by the bulge-like morphology of the south-eastern feature. The older component discussed here, which possesses a weak central concentration and extends over a large part of the eastern outer area, is rather more difficult to explain, since the age distribution does not seem to reflect the younger age distribution found in the more central regions. One can conjecture that the tidal disturbance occurred *before* the formation of the younger populations in the central areas, which are less than 0.4-0.6 Gyr old (Chapter 7). This argument relies on the stellar and gaseous components responding differently to the tidal disturbance.

(2) The second explanation is that a differential distance modulus between the eastern

areas and western areas may account for older MS populations being seen above the magnitude limit in the east but not in the west. The good agreement between the extended distribution of the MS stars and the area over which the near component of the two-component model of SMC structure extends (see Chapter 4), suggests that this may provide a plausible explanation. The radial velocity-distance correlation in the north-eastern outer area found by Hatzidimitriou, Cannon & Hawkins (1991) gives an expansion timescale which agrees with the time of the recent (2×10^8 yr) LMC-SMC encounter according to the MF models, thus providing a consistent explanation for both the large depths and the presence of extended distributions of MS stars in these areas. The main problem with this explanation is that the distribution of MS stars brighter than $R = 19.5$ (Fig. 7.1 (b)) still shows an extended distribution of MS stars in the north-east with respect to other outer areas. This would not be the case if a differential distance modulus of around 0.5 mag (corresponding to about 12 kpc) were solely responsible for a uniformly distributed population aged greater than 2 Gyr being observed above the magnitude limit only in the eastern areas. Despite the attractiveness of this explanation, this major objection appears to be insurmountable. Therefore, apart from the SE 'bulge' feature, which appears to be a genuine tidal feature comprising fairly young (mostly less than 0.8 Gyr old) stars, there are a number of difficulties which render the 'tidal' interpretation of the extended distributions of observed main sequence stars problematic.

One further possibility is that the extended distribution of older MS populations in the eastern area forms part of a quasi-stable structure which has survived for at least 2 Gyr. Recent observations of irregular galaxies and low surface brightness galaxies show that non-uniform distributions of old stellar populations apparently can exist in relatively stable configurations. James (1991) found that several dwarf irregular galaxies in the Virgo Cluster possessed significantly asymmetrical infrared light distributions and Bothun, Impey & Malin (1991) observed numerous random surface brightness enhancements (i.e. 'blobs') embedded in the envelope of low surface brightness galaxies belonging to the Fornax Cluster. They point out that these blobs have identical colours to the rest of the galaxy and are presumably composed of the

same stellar populations. These authors attributed the blobs to stochastic orbits which may have been produced by interactions with other galaxies in the Fornax cluster. Therefore we cannot dismiss the possibility that the asymmetric distribution of younger populations in the SMC outlying areas is a long-lived feature. If so, these relatively young populations may have been produced as a result of a period of renewed star formation beginning sometime before 2 Gyr ago in regions remote from the SMC centre. The star formation process in this case perhaps followed the scenario predicted by the Noguchi & Ishibashi (1986) simulations showing star formation in the tidally disrupted outer disk produced by galaxy-galaxy interactions.

To conclude this discussion on the effect of previous interactions with neighbouring galaxies on the age distribution of the SMC outer areas, we state that on the whole, there is insubstantial evidence for the hypothesis that the major generations of stars were produced as a result of interaction events. However, there is evidence that tidally induced bursts of star formation, seen in the Wing region and possibly also in the northern 'outer arm' of the SMC, can contribute relatively small numbers of stars to the overall stellar population. There is evidence from the unusual distributions of main sequence stars in the outer regions of the SMC that tidal interactions have affected the observed population structure, leading to the detection of relatively young stars at remote distances from the SMC centre.

4.3 Star Formation Processes in Irregular Galaxies

Finally, we discuss the internal processes which seem to be required to account for the bulk of the star formation in the Magellanic Clouds. As in the case of the Galaxy, the initial collapse of the protogalactic cloud leading to possible disk and halo structures may have produced the oldest stellar populations, but subsequent SF processes may be similar to those thought to have operated in other irregular galaxies. Gallagher & Hunter (1984) provide evidence that isolated irregulars can be just as vigorous in star production as the disk of the Milky Way. In this regard, we note the existence of several isolated Magellanic irregulars e.g. NGC 4449 (Bothun 1986), possessing

clumpy distributions of sites of star formation and overall disordered optical appearance. Such galaxies are believed to have undergone star formation via a chaotic, free-wheeling mode unrestricted by dynamical forcing due to differential disk rotation (Gallagher & Hunter 1984). Gas mobility is probably an important factor in inducing star formation, either in the creation of local density fluctuations due to large non-circular motions in the gas component (Hunter 1982) or the propagation of star formation between neighbouring areas via expansion of H II regions, stellar winds and supernovae (stochastic self-propagating star formation). Models of stochastic self-propagating star formation have been developed by several workers and applied with some degree of success to irregular galaxies including the case of the Magellanic Clouds (see Gerola, Seiden & Schulman 1980).

Hunter (1982) has observed that the outer parts of irregular galaxies have ceased to be active sites of star formation. In her study of the sizes and spatial distribution of H II regions (which she identified as the sites of active star formation) she found that these regions were confined to within the central 60 per cent of the optical dimensions. She concluded that a gas density threshold effect was operating in such a way that the outer parts did not possess high enough gas densities to support star formation. Further support for the concept of a gas density threshold for star formation comes from the work on the star formation law in normal disk galaxies by Kennicutt (1989), who established the reality of a critical threshold gas density for star formation, varying between galaxies and within individual galaxies depending on the rotation properties of the disk. For densities below the critical threshold the gas is stable to cloud-forming large-scale gravitational perturbations, whereas above the threshold gravitational instabilities can result in a star formation rate which increases rapidly with increasing density. The aging towards the periphery of the SMC indicated by Fig. 8.2 suggests that after successive generations of stars were created, star formation became progressively more concentrated towards the central regions of the SMC as the gas content of the outer zones became exhausted.

To conclude this chapter we state that we have extended our picture of the age distribution of the SMC outer regions obtained in Chapters 7, 8 and 9 by reference to previous studies of field populations and other age tracers in the SMC. Various aspects of the star formation history revealed by our work and existing studies were discussed in order to evaluate the relative importance of externally versus internally stimulated star formation in the SMC. The current evidence reviewed here suggests, at first sight, that external interactions involving the SMC and its neighbours play a relatively minor role in the *overall* star formation history of the outer regions of the SMC, but have possibly had a more significant impact on this history in the more recent past.

CHAPTER

— 11 —

CONCLUSIONS

The study of the 3D structure and stellar age distribution of the outer regions of the SMC was conducted using photographic photometry of 1.1 million objects covering an area of about 130 deg^2. This database (Part I) has been compiled from COSMOS scans of 38 blue and red photographic plates in six standard ESO/SERC survey fields, Fields 28, 29, 30 ,50, 51 and 52. CCD observations obtained at the Danish 1.5-m telescope were used to calibrate the photographic photometry. The quality of the data set is defined by the following results on the accuracy and completeness of the colour-magnitude information:—

(1) The random errors in the $B-$ and R-band photometry are less than 0.1 mag down to the effective magnitude limits at $R \sim 20$, $B_J \sim 21$.

(2) Systematic errors in the photometry, estimated from the field overlaps, are below 0.2 mag, but are generally smaller for *fainter* magnitudes due to the smaller impact of field effects on unsaturated stellar images. At the magnitude level of the HB/clump

stars ($R \sim 19$), the maximum discrepancy in the R magnitudes in the field overlap areas was 0.13 mag.

(3) In relatively uncrowded areas with image densities less than 2 images arcmin^{-2}, the overall completeness is greater than 90 per cent down to $R \sim 19.5, B_J \sim 20.5$, and starts to increase at fainter magnitudes.

(4) The level of incompleteness in more crowded areas, i.e. in much of the area within about 3° of the SMC centre, was found to be about 20 per cent (for magnitudes well above the effective magnitude limit), rising to 40 per cent in the densest regions.

(5) Differential loss of faint images with respect to bright images in fairly crowded regions was found to be very small since most multiple images are removed altogether from the data set as a result of the plate-pairing procedure.

The methods used to examine the 3D structure of the SMC using the surface and luminosity distribution of HB/clump stars were described and clearly justified. The main results of the investigation of the 3D structure of the SMC outer regions (Part II) are summarised below:—

(1) The 2D projected distribution of the HB/clump stars shows an asymmetrical structure indicating a tidally disturbed system. There appears to be an inner elliptical distribution offset to the south-west of the SMC centre embedded in a more circular —in projection— 'halo'. This 'halo' appears to be more extended in the northern outer regions towards the direction defined by the Magellanic Stream.

(2) In the western part of the SMC, covering roughly half of the projected outer area of the SMC, the HB/clump feature on the areal grid of colour-magnitude diagrams has a compact visual appearance. 2σ 'dispersion' average depths of less than 6 kpc were derived for Fields 28, 50 and the western area of Field 51. These depths are compatible with the projected dimensions of the SMC of around 12 kpc.

(3) In the eastern part of the SMC outer regions the appearance of the HB/clump is much broader in luminosity. 2σ depths of 10-15 kpc were derived for most of this area, with very large depths, of size 20-26 kpc occurring in the remote south-eastern area.

(4) The information on the depth of the SMC outer regions as a function of position

was combined with data on the mean distance modulus of each grid region to derive a two-component model for the structure of the SMC. The far component is believed to cover most of the projected outer area of the SMC, while the near component lies some 7-11 kpc in front of the far component in the eastern area.

(5) Follow-up CCD observations of the area near the south-eastern SMC cluster NGC 643 were obtained with the SAAO 1-m telescope. These observations confirmed the broad nature of the HB/clump feature in these regions and strengthened the evidence for the two-component hypothesis of SMC structure. From the study of the colour-magnitude diagram of the NGC 643, an age of about 2 Gyr and metallicity of [Fe/H]= -1.3 for the cluster are estimated.

(6) The bulk (about 70 per cent) of the stellar population in all areas except the south-eastern area are contained within a range of distances along the line-of-sight that is compatible with the estimated tidal diameter of around 12 kpc for the SMC. However, the total extension of the eastern areas along the line of sight is greater than this diameter, and combined with the very large depths found in the south-east and the proposed splitting of the SMC outer area into two components, this does suggest that the SMC is irreversibly fragmenting.

(7) The orbital computations of Murai & Fujimoto (1984) and Mathewson *et al.* (1987) predict that a close encounter between the LMC and the SMC occurred a few 10^8 yr ago. Particle simulations by the former authors successfully modelled the features of the Magellanic Stream and showed that as a result of this relatively recent encounter, the SMC has been extended along the line-of-sight direction. There is some qualitative agreement between the predictions of this model and the observed 3D structure of the SMC outer regions.

The stellar age distribution in the outer regions of the SMC was studied predominantly on the basis of main sequence and horizontal branch populations (Part III). The main observational results are summarised below:—

(1) The surface distribution of the younger (less than 2 Gyr old) populations, exemplified by the main sequence stars detected above the effective magnitude limit, was shown to be highly non-uniform with respect to that of the older stellar content of the

SMC represented by the HB/clump. The main sequence distribution was found to be biassed towards the eastern side of the SMC facing the LMC with no populations younger than 2 Gyr old being observed in the north-western outer area.

(2) Analysis of main sequence luminosity functions shows the existence of very young (less than 0.1 Gyr) populations in the Wing and a population component aged 0.4-0.6 Gyr in the north-eastern and south-western extensions of the central 'Bar' of the SMC. The more remote main sequence populations beyond 2.5° from the SMC centre in the north-eastern and south-eastern outlying area exhibit steeper luminosity functions indicating older age compositions.

(3) A detailed study of the morphology and age distribution of the Wing region using blue main sequence stars showed that it is an essentially coeval feature younger than 50 million years old with a very different distribution from the older stellar component. There is evidence that one of the major stellar concentrations located at around $RA = 1^h53^m$, $DEC = -74°30'$ possesses more blue supergiants brighter than $R = 14$ than other regions of the Wing and may thus be slightly younger.

(4) The bulk of the stellar population of the outer areas was found to be about 9-11 Gyr old from application of the d_{B-R} indicator of Hatzidimitriou (1991) to the horizontal branch morphology of existing deep CCD colour-magnitude diagrams near well-studied clusters. This result was also confirmed by the photographic data of the present study. The application of this indicator showed that the median age of the stellar population increases from about 3-4 Gyr at 1.5 kpc from the SMC centre to 9-11 Gyr at about 2.5 kpc from the SMC centre.

(5) A weak 'horizontal extension' from the main 'clump' towards bluer colours (but to the red of the instability strip) has been identified on some colour-magnitude diagrams. This can be interpreted as belonging to a population a few Gyr older than the dominant population of the 'main' clump, and may thus represent a population with age similar to that of globular clusters in the Galaxy. This population was found to account for about 7 per cent of the mass of the total population in this area.

(6) 95 RR-Lyrae variable candidates in Field 51 have been identified from variability on four B_J plates in conjunction with colour-magnitude data. Their surface distribu-

tion is less centrally concentrated than the HB/clump population, in agreement with earlier studies (see Graham 1975) which suggested a very flat radial distribution for this older population.

Based on the results of the study of the stellar age distribution of the outer regions of the SMC together with other population studies, several insights were gained into the organisation of star formation in the SMC (Chapter 10). Among these were:—

(1) The detailed age distributions of the field populations and clusters of the LMC and SMC show sufficient diversity to seriously contest the hypothesis that synchronous star formation events triggered by periodic close encounters between the Magellanic Clouds led to the formation of the bulk of the stellar generations of the Magellanic Clouds.

(2) There are signs, however, that relatively recent star formation activity has been triggered by this tidal interaction. The Wing feature is clearly due to an externally induced burst of star formation, which may be identified with the close encounter between the LMC and the SMC according to the Murai & Fujimoto (1980) models or the more recent perigalactic passage of the Magellanic Clouds. Star count analysis, however, shows that the contribution of the stellar content of the Wing amounts to about only 2 per cent of the stellar content of the SMC outer area. The main sequence luminosity functions of areas near the northern 'outer arm' also indicate the existence of a star formation burst a few 10^8 yr ago.

(3) The main sequence luminosity functions of the inner studied regions seem to indicate that star formation rates were comparatively low for several 10^8 yr before about 0.6 Gyr ago, providing evidence for large fluctuations in past star formation rates.

(4) The progressive aging of stellar populations towards the periphery of the SMC appears to be connected to the depletion of gas as a function of time in the outer regions which may halt further star formation once the gas density falls below a certain critical density (see Kennicutt 1989).

(5) The irregular distribution of main sequence populations mostly older than 0.8 Gyr raises the possibility that non-uniform structures in irregular galaxies can be fairly

long-lived as suggested by the infrared observations of dwarf irregular galaxies by James (1991).

As a result of the investigations in Parts II and III the questions posed in the introduction have been tackled with some success, notably those concerning the present structure and possible disintegration of the SMC. Kinematical data on the stellar populations of the outer regions of the SMC will ultimately complete the picture concerning its dynamical state and the nature of the influence of the gravitational fields of the LMC and the Galaxy on the SMC. The study of the detailed star formation history of the outer regions of the SMC has been restricted by the fact that the photographic data does not go deep enough to directly analyse the star formation history prior to about 2 Gyr ago with the use of main sequence luminosity functions. Nevertheless, fundamental data on the overall pattern of star formation in the SMC outer regions have been gathered which may stimulate deep photometric studies of the older stellar populations in the general field and in faint outlying clusters. This present work and other studies have shown that the SMC possesses a remarkably complex structure and stellar population synthesis, befitting its 'irregular' galaxy designation. The search for final solutions to these problems will continue to provide a profound challenge to the analytical powers and dedication of workers engaged in this field of astronomical research.

Appendix A: — The CCD Sequences

The CCD sequences used for calibration of photographic photometry in ESO/SERC Fields 50, 51, 30 and 29 are presented here. The sequences are grouped according to their location (see Fig. 2.6) and the first digit of the star ID corresponds to these location codes. The suffix on the star ID indicates whether the stars belong to bright(B) or faint(F) sequences.

ID no.	*RA* (1950)	*DEC* (1950)	*B* (mag)	*R* (mag)
1001F	00 51 15	-70 04 36	16.73	15.60
1002F	00 51 30	-70 04 06	18.22	16.13
1003F	00 51 24	-70 03 03	18.96	17.59
1004F	00 51 28	-70 06 49	19.16	17.64
1005F	00 51 19	-70 03 26	19.22	17.84
1006F	00 51 30	-70 05 33	19.46	17.91
1007F	00 51 16	-70 05 25	19.91	18.66
1008F	00 51 27	-70 04 51	19.97	18.79
1009F	00 51 30	-70 03 47	20.03	18.70
1010F	00 51 23	-70 06 48	20.04	18.54
1011F	00 51 24	-70 05 18	20.06	18.83
1012F	00 51 07	-70 03 13	20.09	18.69
1013F	00 51 29	-70 05 06	20.19	18.99
1014F	00 51 29	-70 04 47	20.30	18.86
1015F	00 51 07	-70 03 34	20.56	19.15
1016F	00 51 16	-70 03 07	20.57	19.37
1017F	00 51 18	-70 05 35	20.83	19.50
1018F	00 51 13	-70 06 22	21.08	–
1019F	00 51 06	-70 04 12	21.13	–
1020F	00 51 29	-70 06 25	21.18	–
1021F	00 51 16	-70 05 17	21.38	–
1022F	00 51 09	-70 03 46	21.39	20.46
1023F	00 51 24	-70 04 53	21.49	19.72
1024F	00 51 25	-70 04 39	21.62	18.85
1025F	00 51 30	-70 06 09	–	18.33
1001B	00 52 11	-70 00 05	13.86	12.74
1002B	00 52 03	-70 00 53	16.95	–
1003B	00 52 23	-70 02 06	17.57	15.92
1004B	00 52 15	-69 59 57	–	17.10
1005B	00 52 17	-70 01 09	–	17.79
2001F	01 14 27	-68 06 20	16.15	15.23
2002F	01 14 19	-68 03 20	18.26	–
2003F	01 14 15	-68 04 42	18.53	16.93
2004F	01 14 08	-68 06 24	18.98	17.78
2005F	01 14 21	-68 05 53	19.49	18.10
2006F	01 14 19	-68 04 03	19.81	17.23
2007F	01 14 26	-68 04 51	20.10	19.00
2008F	01 14 14	-68 03 27	20.26	18.92
2009F	01 14 25	-68 02 53	20.59	19.19
2010F	01 14 18	-68 02 51	20.66	19.79
2011F	01 14 16	-68 06 14	20.78	18.16
2012F	01 14 23	-68 04 50	21.15	18.92

ID no.	*RA* (1950)	*DEC* (1950)	*B* (mag)	*R* (mag)
2013F	01 14 26	-68 06 36	21.21	18.53
2014F	01 14 20	-68 06 18	21.55	–
2015F	01 14 08	-68 03 31	21.74	–
2016F	01 14 08	-68 04 20	21.78	–
2017F	01 14 07	-68 03 49	21.76	19.80
2018F	01 14 09	-68 03 13	22.04	19.54
2019F	01 14 11	-68 03 50	22.10	–
2020F	01 14 15	-68 02 51	–	19.42
2021F	01 14 06	-68 06 24	–	19.60
2022F	01 14 26	-68 06 04	–	20.24
2001B	01 13 13	-68 01 44	13.24	12.17
2002B	01 12 59	-68 01 13	13.39	12.55
2003B	01 13 03	-68 01 00	16.42	14.49
2004B	01 12 56	-68 03 11	16.87	15.61
2005B	01 13 15	-68 00 51	–	16.59
2006B	01 13 11	-68 03 01	–	17.67
3001F	00 30 02	-71 53 06	16.53	15.46
3002F	00 29 40	-71 53 05	16.83	15.73
3003F	00 29 57	-71 52 31	17.49	–
3004F	00 29 53	-71 51 57	17.92	16.39
3005F	00 29 50	-71 53 20	18.21	17.46
3006F	00 29 36	-71 53 23	18.39	16.19
3007F	00 29 41	-71 51 26	18.73	17.53
3008F	00 29 57	-71 55 12	19.29	17.77
3009F	00 29 44	-71 54 31	19.74	18.49
3010F	00 30 02	-71 51 54	20.11	18.66
3011F	00 30 03	-71 54 40	20.13	18.96
3012F	00 29 36	-71 52 16	20.15	18.99
3013F	00 29 37	-71 52 22	20.19	18.82
3014F	00 29 33	-71 52 54	20.22	19.05
3015F	00 29 51	-71 53 43	20.31	18.96
3016F	00 29 33	-71 53 30	20.32	18.90
3017F	00 29 47	-71 54 11	20.38	19.12
3018F	00 29 56	-71 52 56	20.46	19.27
3019F	00 30 01	-71 53 49	20.53	19.13
3020F	00 29 35	-71 54 29	21.28	–
3021F	00 29 45	-71 52 21	21.29	–
3022F	00 29 40	-71 54 39	21.36	–
3023F	00 30 00	-71 52 20	21.39	–
3024F	00 29 39	-71 51 31	21.39	–
3025F	00 29 47	-71 51 51	21.44	–
3026F	00 29 32	-71 53 08	21.45	–

ID no.	*RA* (1950)	*DEC* (1950)	*B* (mag)	*R* (mag)
3027F	00 29 40	-71 54 15	21.56	19.90
3028F	00 29 51	-71 53 20	21.62	–
3029F	00 29 48	-71 51 27	21.94	–
3030F	00 29 51	-71 53 00	–	16.94
3031F	00 29 43	-71 53 09	–	18.84
3032F	00 29 57	-71 54 53	–	18.88
3033F	00 29 51	-71 54 56	–	18.98
3034F	00 29 40	-71 53 20	–	19.62
3035F	00 29 35	-71 53 43	–	19.88
3001B	00 27 32	-72 07 43	14.84	13.72
3002B	00 27 34	-72 10 43	14.88	13.58
3003B	00 27 41	-72 07 26	17.19	15.86
3004B	00 27 24	-72 07 21	17.51	16.23
3005B	00 27 19	-72 10 43	–	16.37
3006B	00 27 46	-72 10 42	–	16.38
3007B	00 27 22	-72 07 43	–	16.82
3008B	00 27 33	-72 09 51	–	17.28
3009B	00 27 46	-72 07 31	–	17.72
3010B	00 27 39	-72 10 30	–	17.80
3011B	00 27 38	-72 07 59	–	18.31
3012B	00 27 48	-72 10 12	–	18.48
3013B	00 27 35	-72 08 44	–	18.70
4001F	00 01 39	-69 57 46	16.40	14.82
4002F	00 01 39	-69 58 39	16.48	15.31
4003F	00 01 37	-69 56 55	17.39	15.54
4004F	00 01 53	-70 00 02	17.41	16.30
4005F	00 01 54	-69 58 29	17.79	16.66
4006F	00 01 40	-69 59 17	18.03	16.61
4007F	00 01 49	-69 58 46	18.48	–
4008F	00 01 47	-69 59 51	19.05	17.79
4009F	00 01 40	-69 58 05	19.61	–
4010F	00 01 42	-69 57 12	19.81	18.34
4011F	00 01 52	-69 59 30	19.95	17.30
4012F	00 01 35	-69 59 37	20.01	18.78
4013F	00 01 33	-69 59 55	20.16	19.06
4014F	00 01 46	-69 57 31	20.28	19.30
4015F	00 01 58	-69 59 03	20.42	19.32
4016F	00 01 44	-69 59 26	20.47	18.49
4017F	00 01 55	-69 56 41	21.01	20.26
4018F	00 01 51	-69 59 39	21.22	20.23
4019F	00 01 35	-69 57 17	21.90	19.30
4020F	00 01 53	-69 59 37	–	20.56

ID no.	*RA* (1950)	*DEC* (1950)	*B* (mag)	*R* (mag)
4001B	00 01 12.0	-69 50 04	12.62	11.78
4002B	00 01 14.5	-69 51 27	13.42	12.22
4003B	00 00 57.4	-69 50 13	16.02	14.82
4004B	00 00 51.3	-69 52 59	16.89	15.39
5001F	23 39 43.2	-68 27 55	16.87	14.75
5002F	23 39 38.6	-68 28 09	17.54	15.54
5003F	23 39 39.5	-68 27 12	19.07	16.99
5004F	23 39 47.5	-68 27 12	19.86	17.41
5005F	23 39 48.3	-68 28 08	20.11	–
5006F	23 39 47.2	-68 26 50	20.56	–
5007F	23 39 42.1	-68 28 04	20.69	–
5008F	23 39 56.0	-68 25 45	20.85	19.78
5009F	23 39 50.3	-68 27 57	21.13	20.12
5010F	23 39 48.0	-68 26 16	21.13	–
5001B	23 38 42.5	-68 27 45	12.73	11.54
5002B	23 38 31.7	-68 29 51	14.09	12.97
5003B	23 38 39.7	-68 30 14	14.62	13.22
5004B	23 38 28.8	-68 28 28	15.99	14.93
5005B	23 38 33.6	-68 28 47	17.29	15.97
5006B	23 38 22.8	-68 27 34	18.14	16.69
5007B	23 38 22.1	-68 30 23	18.73	–
6001F	02 06 04	-74 58 28	15.91	16.19
6002F	02 06 11	-74 59 23	17.84	18.05
6003F	02 06 20	-75 01 41	18.43	18.61
6004F	02 06 27	-74 58 32	18.44	17.74
6005F	02 06 18	-75 00 02	18.50	18.74
6006F	02 06 16	-75 00 40	18.65	18.90
6007F	02 06 29	-74 59 09	19.36	19.53
6008F	02 06 12	-74 59 35	19.41	19.32
6009F	02 06 02	-75 00 49	19.78	–
6010F	02 06 16	-75 01 08	19.97	19.94
6011F	02 06 27	-75 00 04	20.03	19.34
6012F	02 06 13	-74 58 12	–	17.40
6013F	02 06 15	-74 59 44	–	17.80
6014F	02 06 16	-74 59 33	–	18.87
6001B	02 09 43	-75 07 54	11.84	11.06
6002B	02 09 54	-75 08 51	13.49	12.54
6003B	02 09 36	-75 10 07	16.58	15.63
6004B	02 09 34	-75 09 40	–	10.74
7001F	02 39 06	-76 18 04	16.71	15.09
7002F	02 38 56	-76 19 27	17.05	15.86
7003F	02 38 55	-76 20 26	17.38	15.07

ID no.	*RA* (1950)	*DEC* (1950)	*B* (mag)	*R* (mag)
7004F	02 38 49	-76 18 06	17.59	16.57
7005F	02 39 23	-76 19 07	17.73	16.57
7006F	02 38 45	-76 20 37	18.07	16.98
7007F	02 38 52	-76 18 40	18.68	17.57
7008F	02 39 08	-76 18 20	19.76	18.67
7009F	02 39 01	-76 20 29	19.99	19.13
7010F	02 39 05	-76 20 12	20.90	18.34
7011F	02 39 00	-76 19 50	21.25	–
7012F	02 39 02	-76 20 00	21.38	19.58
7013F	02 39 23	-76 18 30	–	19.62
7001B	02 40 45	-76 23 30	12.31	11.64
7002B	02 41 06	-76 24 17	13.62	11.95
7003B	02 41 09	-76 23 16	17.06	15.58
8001F	02 36 06	-73 18 37	16.41	15.27
8002F	02 36 03	-73 19 32	17.25	16.14
8003F	02 36 34	-73 19 13	18.00	17.29
8004F	02 36 04	-73 21 19	18.53	18.67
8005F	02 36 08	-73 19 15	19.45	18.16
8006F	02 36 23	-73 19 35	19.51	18.94
8007F	02 36 18	-73 19 00	20.19	17.52
8008F	02 36 23	-73 20 07	20.34	18.87
8009F	02 36 21	-73 19 28	20.85	19.41
8010F	02 36 06	-73 20 09	21.03	–
8011F	02 36 05	-73 17 53	21.21	18.90
8012F	02 36 17	-73 19 56	–	16.22
8013F	02 36 18	-73 20 09	–	18.46
8014F	02 36 19	-73 20 01	–	19.07
8015F	02 36 25	-73 20 58	–	19.34
8016F	02 36 19	-73 17 50	–	20.24
8001B	02 36 10	-73 11 58	12.64	11.61
8002B	02 36 20	-73 14 26	12.72	11.86
8003B	02 36 10	-73 13 37	13.33	12.51
8004B	02 36 19	-73 11 39	15.12	13.55
8005B	02 35 59	-73 11 14	16.08	14.01
8006B	02 36 02	-73 13 58	17.22	16.19
9001F	01 35 25	-76 20 43	15.65	14.53
9002F	01 35 34	-76 23 02	15.70	14.52
9003F	01 35 21	-76 22 12	15.90	15.09
9004F	01 35 26	-76 22 27	16.61	13.98
9005F	01 35 44	-76 21 53	17.39	16.24
9006F	01 35 36	-76 19 38	17.67	16.81
9007F	01 35 29	-76 19 53	18.01	15.76

ID no.	*RA* (1950)	*DEC* (1950)	*B* (mag)	*R* (mag)
9008F	01 35 17	-76 20 04	18.92	17.09
9009F	01 35 20	-76 19 59	18.97	17.25
9010F	01 35 42	-76 19 49	19.11	17.55
9011F	01 35 42	-76 21 24	19.69	–
9012F	01 35 21	-76 21 15	19.83	18.85
9013F	01 35 41	-76 21 37	20.09	19.00
9014F	01 35 12	-76 20 25	20.15	19.14
9015F	01 35 38	-76 19 57	20.24	17.84
9016F	01 35 50	-76 21 22	20.27	18.86
9017F	01 35 46	-76 21 41	20.40	18.99
9018F	01 35 46	-76 22 08	20.49	19.02
9019F	01 35 26	-76 20 30	20.56	–
9020F	01 35 12	-76 20 49	20.69	–
9021F	01 35 29	-76 20 08	21.00	–
9022F	01 35 16	-76 22 43	21.10	18.50
9023F	01 35 30	-76 21 51	21.21	–
9024F	01 35 33	-76 21 14	–	19.36
9022F	01 35 37	-76 19 56	–	17.84
9023F	01 35 29	-76 22 56	–	19.34
9001B	01 38 06	-76 06 32	13.08	12.18
9002B	01 38 34	-76 08 23	15.99	14.59
9003B	01 38 16	-76 06 38	16.37	14.43
9011B	01 38 40	-76 06 56	–	17.32
9013B	01 38 09	-76 09 47	–	18.25
0001F	01 14 36	-74 51 02	17.68	15.82
0002F	01 14 45	-74 51 03	18.31	15.86
0003F	01 14 50	-74 51 31	18.86	18.15
0004F	01 14 57	-74 52 09	18.93	17.77
0005F	01 14 44	-74 49 23	19.16	19.19
0006F	01 14 43	-74 51 56	19.55	17.92
0007F	01 14 43	-74 51 06	19.74	18.25
0008F	01 14 51	-74 51 02	19.76	18.53
0009F	01 14 56	-74 51 58	19.84	–
0010F	01 14 55	-74 51 33	19.97	18.57
0011F	01 14 30	-74 52 05	20.06	18.76
0012F	01 14 34	-74 50 41	20.09	18.71
0013F	01 14 40	-74 53 11	20.29	18.92
0014F	01 14 53	-74 51 58	20.31	19.15
0015F	01 14 27	-74 52 20	20.33	19.01
0016F	01 14 26	-74 50 40	20.33	–
0017F	01 14 53	-74 49 29	20.46	19.20
0018F	01 14 44	-74 51 34	20.62	19.15

ID no.	*RA* (1950)	*DEC* (1950)	*B* (mag)	*R* (mag)
0019F	01 14 47	-74 49 29	20.88	–
0020F	01 14 35	-74 52 05	21.05	–
0021F	01 14 43	-74 51 19	21.16	–
0022F	01 14 50	-74 52 00	21.18	19.92
0023F	01 14 38	-74 52 39	21.22	18.78
0024F	01 14 48	-74 51 19	21.26	19.33
0025F	01 14 52	-74 52 15	21.28	–
0026F	01 14 57	-74 51 41	21.28	–
0027F	01 14 37	-74 52 26	21.28	–
0028F	01 14 47	-74 50 11	21.41	–
0029F	01 14 27	-74 51 05	21.46	–
0030F	01 14 26	-74 51 51	21.50	–
0031F	01 14 55	-74 51 11	21.52	–
0032F	01 14 56	-74 50 54	21.56	–
0033F	01 14 26	-74 53 05	21.56	–
0034F	01 14 59	-74 50 41	21.60	–
0035F	01 14 32	-74 52 07	21.67	–
0036F	01 14 41	-74 51 10	21.61	–
0037F	01 14 26	-74 51 14	21.62	–
0038F	01 14 35	-74 49 35	21.62	–
0039F	01 14 33	-74 50 27	21.65	–
0040F	01 14 48	-74 51 36	21.67	–
0041F	01 14 46	-74 52 14	21.74	–
0042F	01 14 27	-74 49 37	21.81	–
0043F	01 14 25	-74 52 49	21.81	–
0044F	01 14 29	-74 49 42	22.06	–
0045F	01 14 48	-74 50 48	22.07	–
0046F	01 14 36	-74 50 21	22.28	–
0047F	01 14 25	-74 50 38	–	16.22
0048F	01 14 35	-74 50 45	–	18.79
0049F	01 14 57	-74 50 27	–	19.01
0050F	01 14 55	-74 53 11	–	19.35
0051F	01 14 25	-74 52 07	–	19.80
0001B	01 12 31	-74 50 58	13.66	12.52
0002B	01 12 25	-74 51 26	15.72	14.81
0003B	01 12 28	-74 51 34	17.17	15.99
0004B	01 12 26	-74 50 12	18.09	16.33
0005B	01 12 29	-74 48 59	–	11.08
0006B	01 12 27	-74 49 33	–	12.18
0007B	01 12 20	-74 49 50	–	16.83
0008B	01 12 46	-74 50 04	–	17.78
0009B	01 12 42	-74 48 27	–	18.94

Appendix B:

— The Colour-Magnitude Diagrams / Compact Format

The grid region colour-magnitude diagrams (CMDs) from ESO/SERC Fields 28, 29, 30, 50, 51, 52 are presented here in a compact format. All the CMDs for each field are laid out on a single page, with the position of each CMD in the array indicating the spatial position of the grid region within a given field. (North is at the top and east is to the left). The grid regions are numbered according to Fig. 3.13. The division of the area of each field into 0.87 deg^2 (or half this size in a few cases) grid regions has been described in Chapter 3 (Section 3). In the following pages the field numbers are indicated on the header at the top of the page.

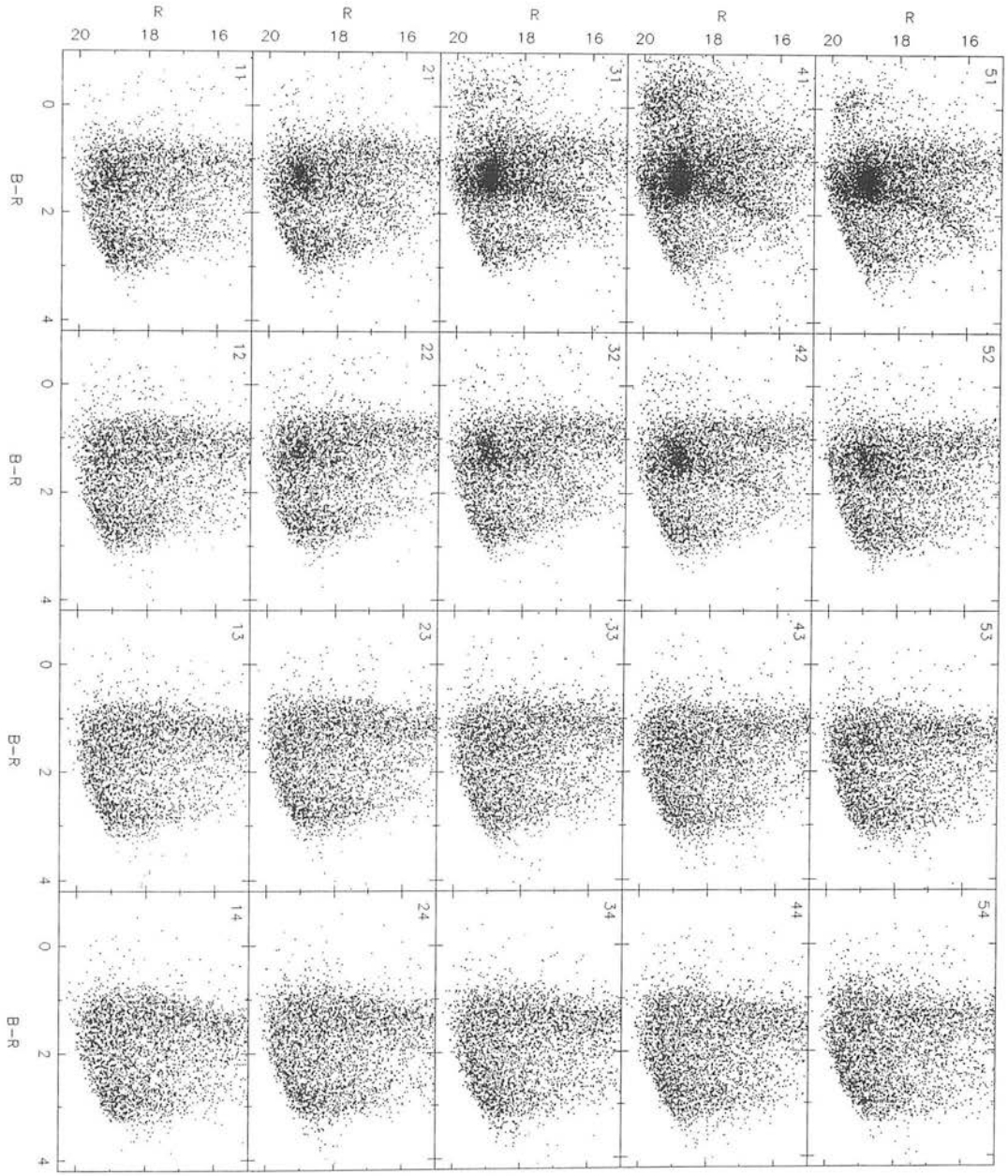
R
20
18
16
B-R
0
2
4
11
21
31
41
51
12
22
32
42
52
13
23
33
43
53
14
24
34
44
54

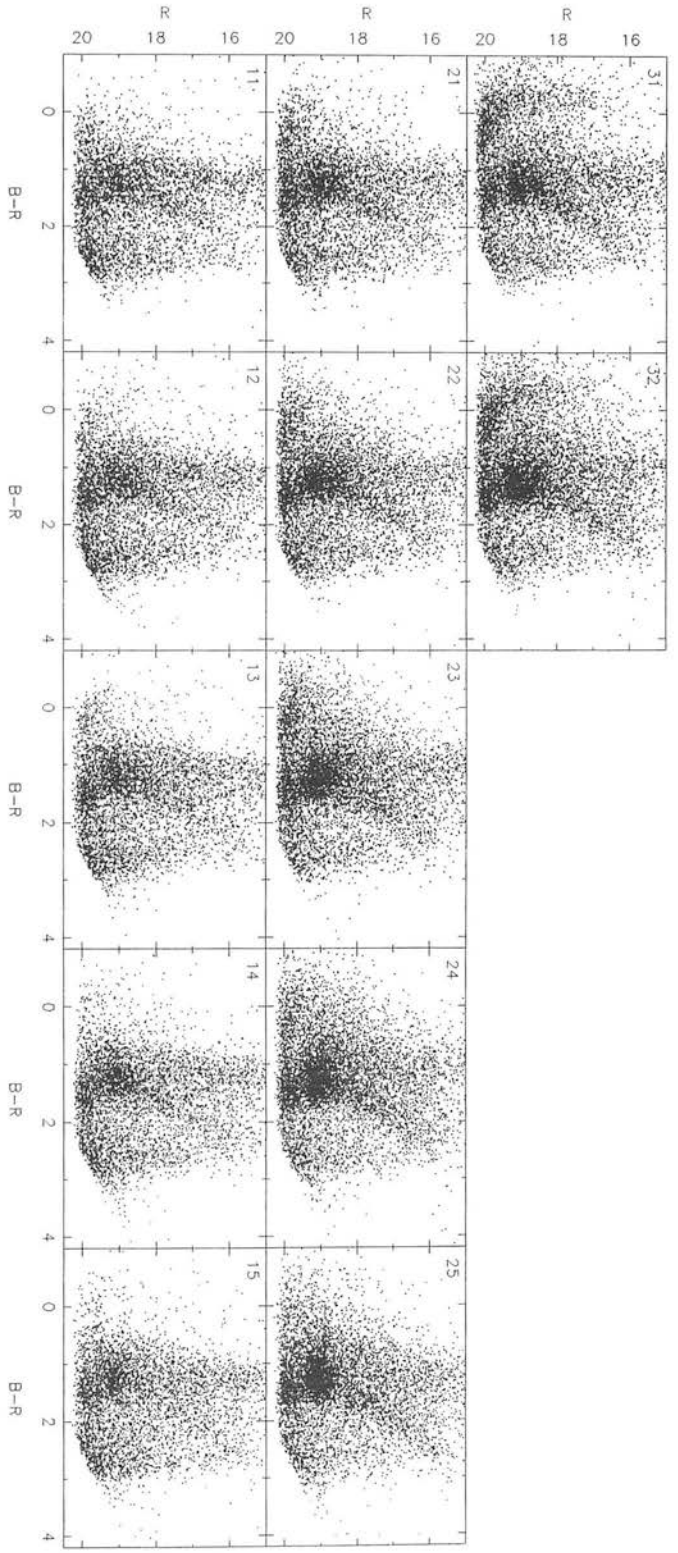
R
20
18
16
B−R
0
2
4
11
21
31
12
22
32
13
23
14
24
15
25

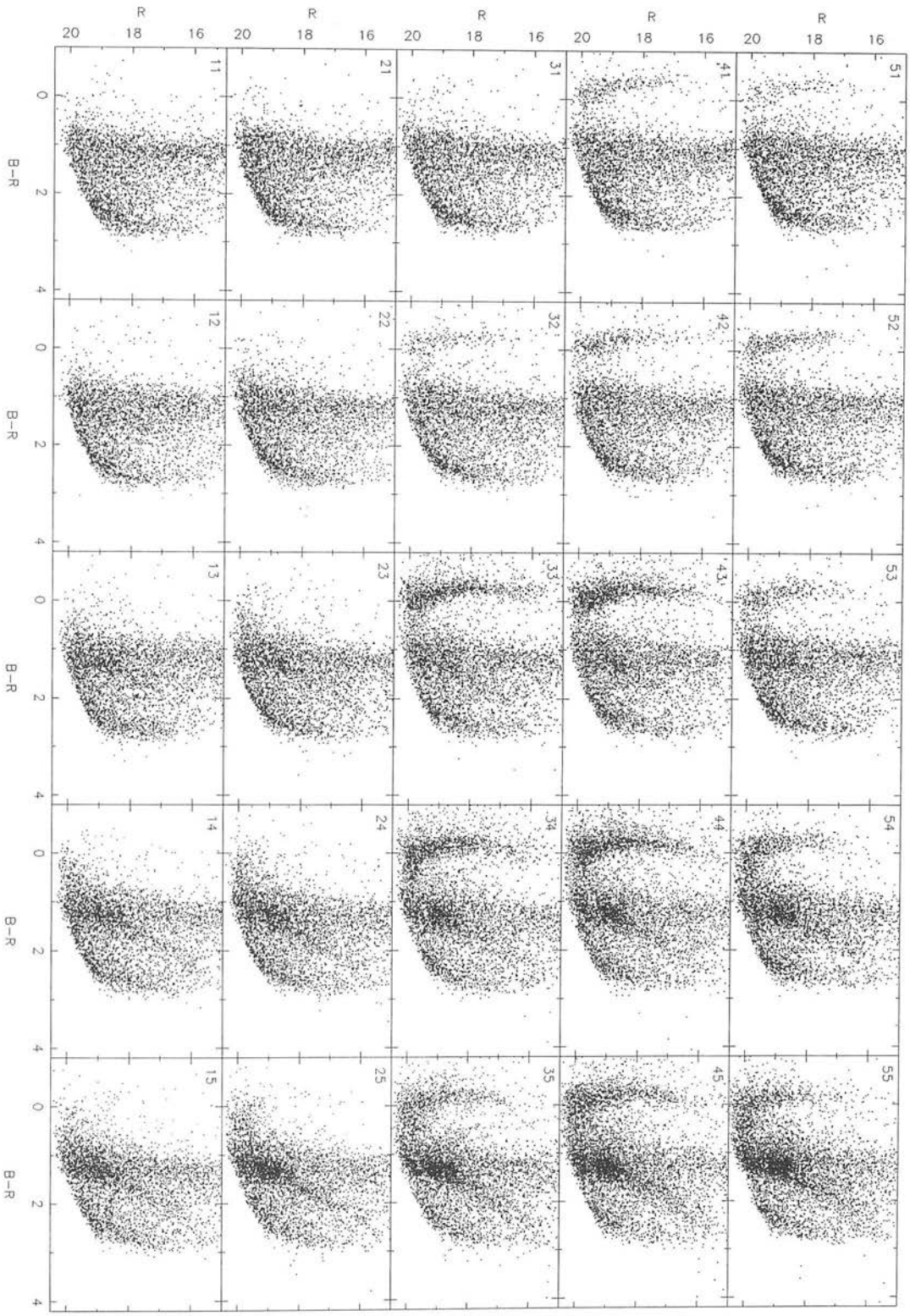
R
20
18
16
B-R
0
2
4
11
21
31
41
51
12
22
32
42
52
13
23
33
43
53
14
24
34
44
54
15
25
35
45
55

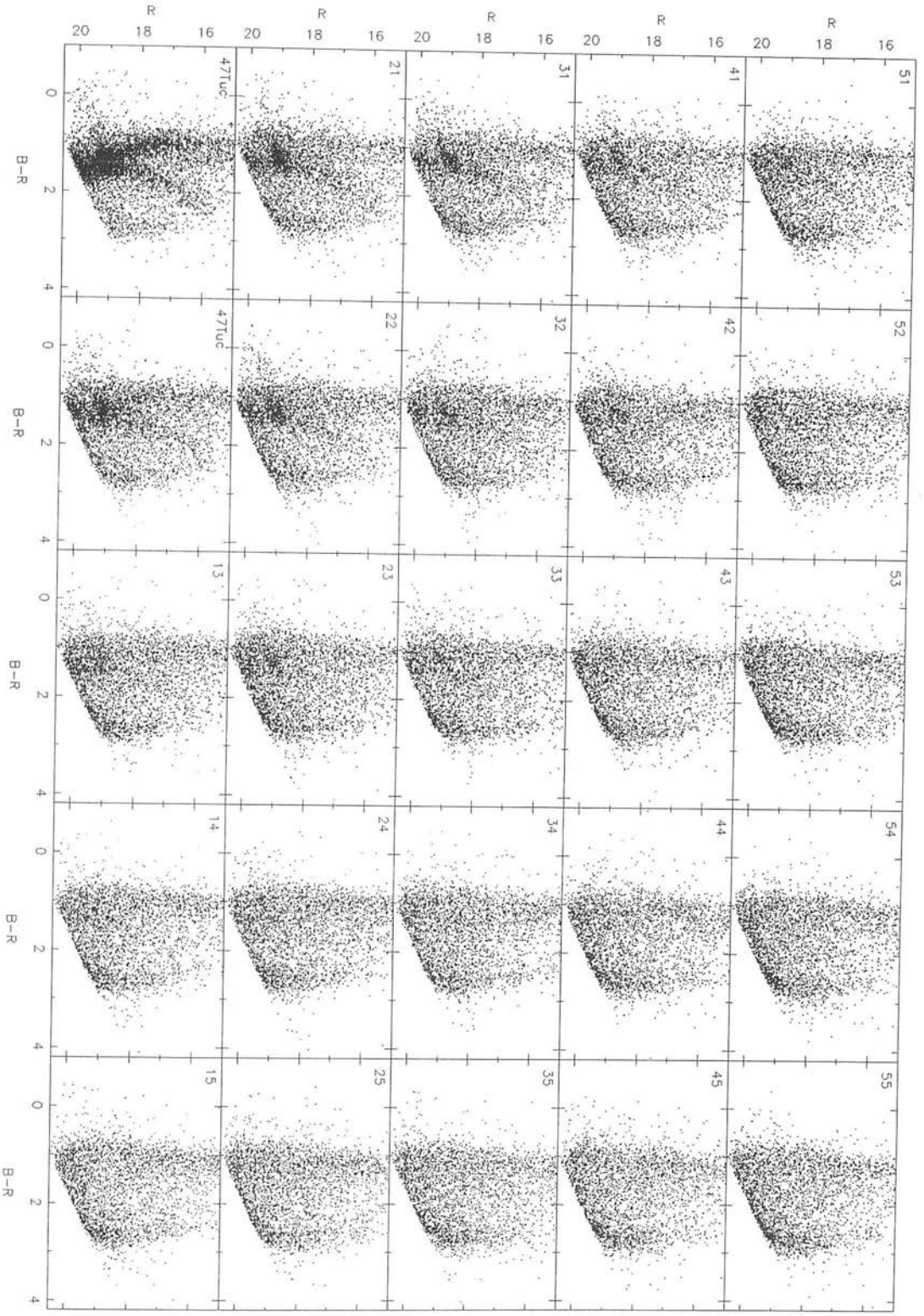
R
20
18
16
B−R
0
2
4
47Tuc
11
21
31
41
51
12
22
32
42
52
13
23
33
43
53
14
24
34
44
54
15
25
35
45
55

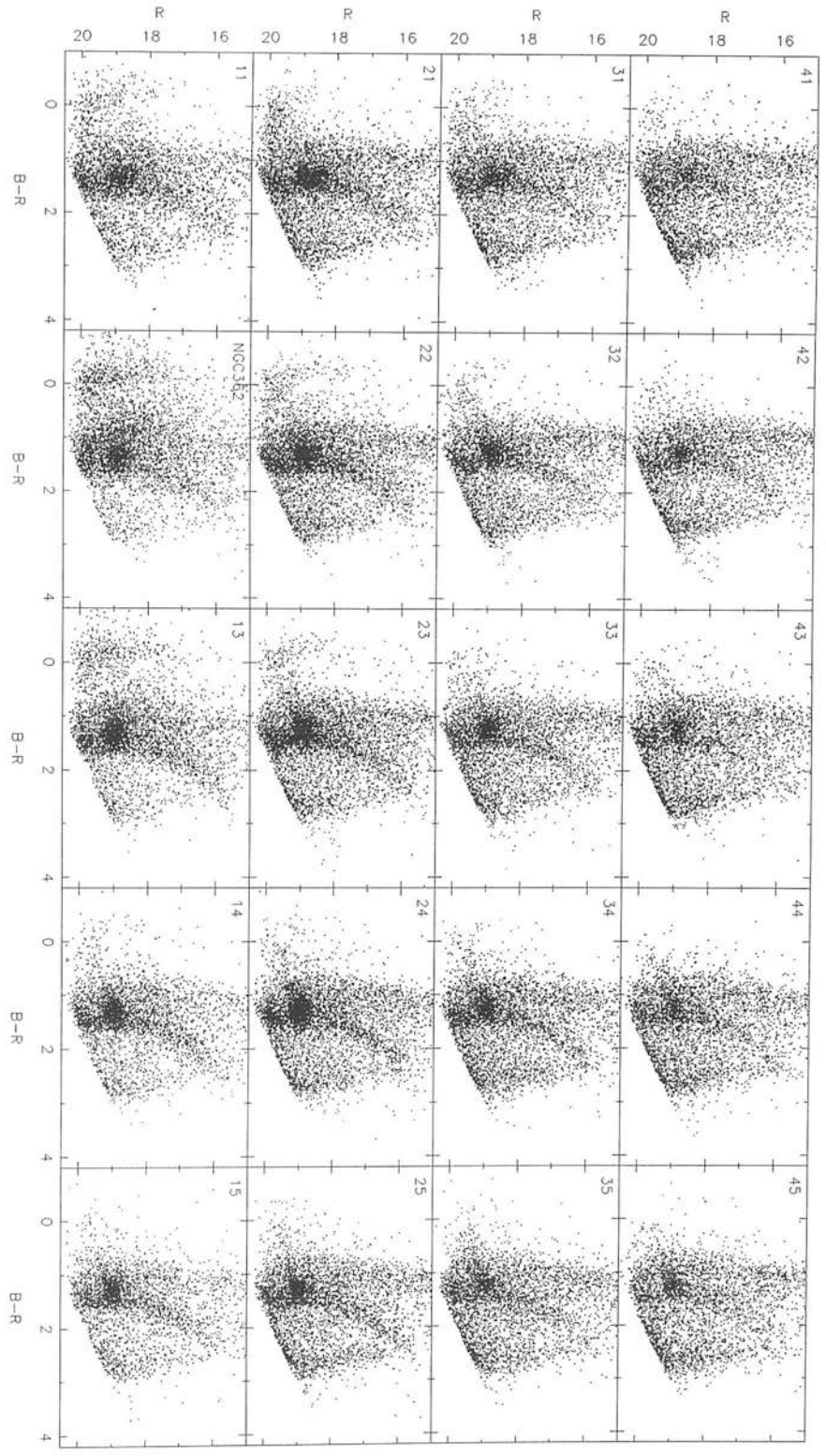
R
20
18
16
B−R
0
2
4
11
21
31
41
NGC362
22
32
42
13
23
33
43
14
24
34
44
15
25
35
45

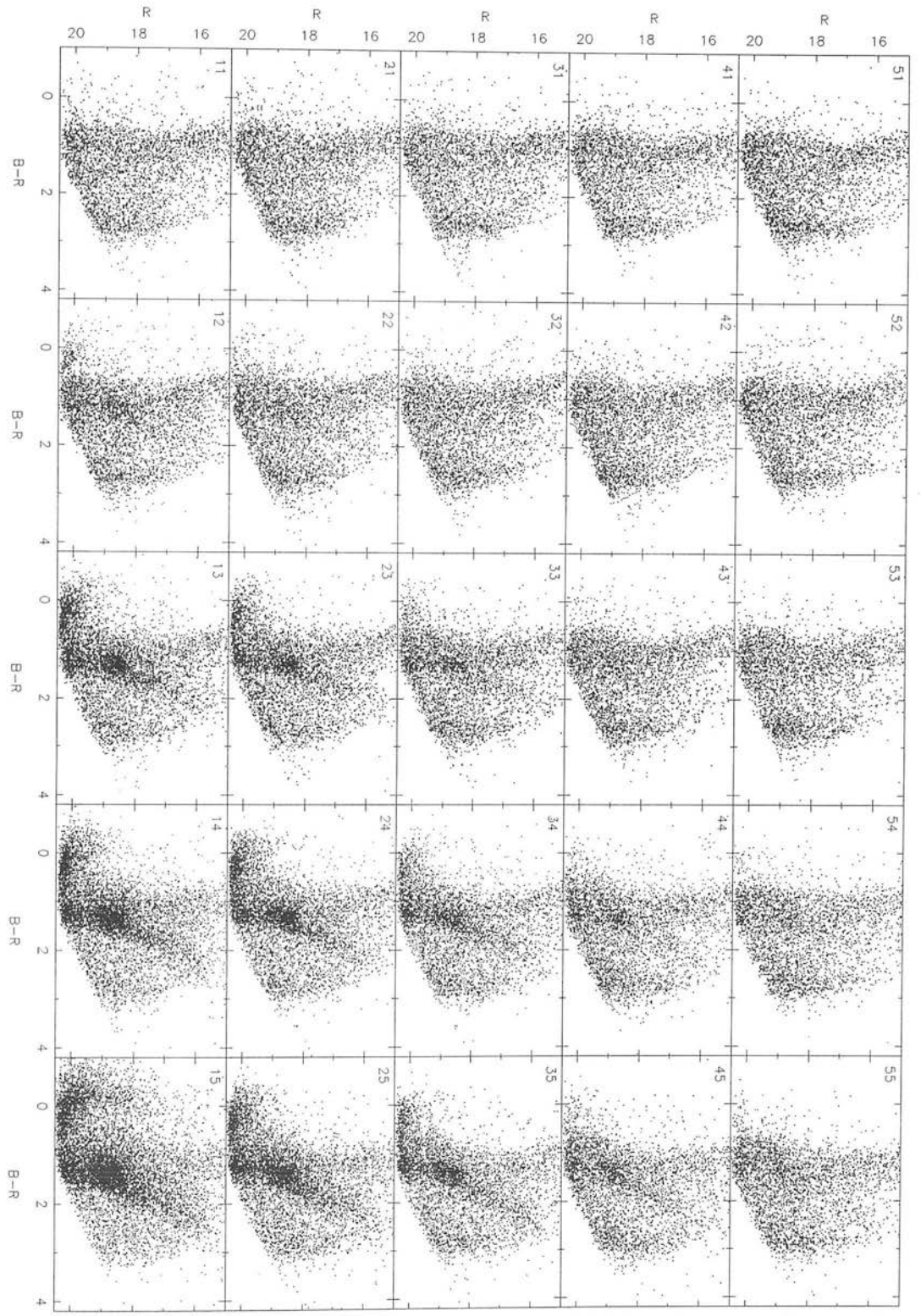
R
20
18
16
B–R
0
2
4
11
21
31
41
51
12
22
32
42
52
13
23
33
43
53
14
24
34
44
54
15
25
35
45
55

Appendix C:

— The Colour-Magnitude Diagrams / Large Format

Representative CMDs selected from Appendix B are presented here in a larger format allowing greater detail to be seen. Four CMDs from each of ESO/SERC Fields 28, 29, 30, 50, 51 and 52 are shown together on a single page. The grid regions CMDs are numbered according to Fig. 3.13.

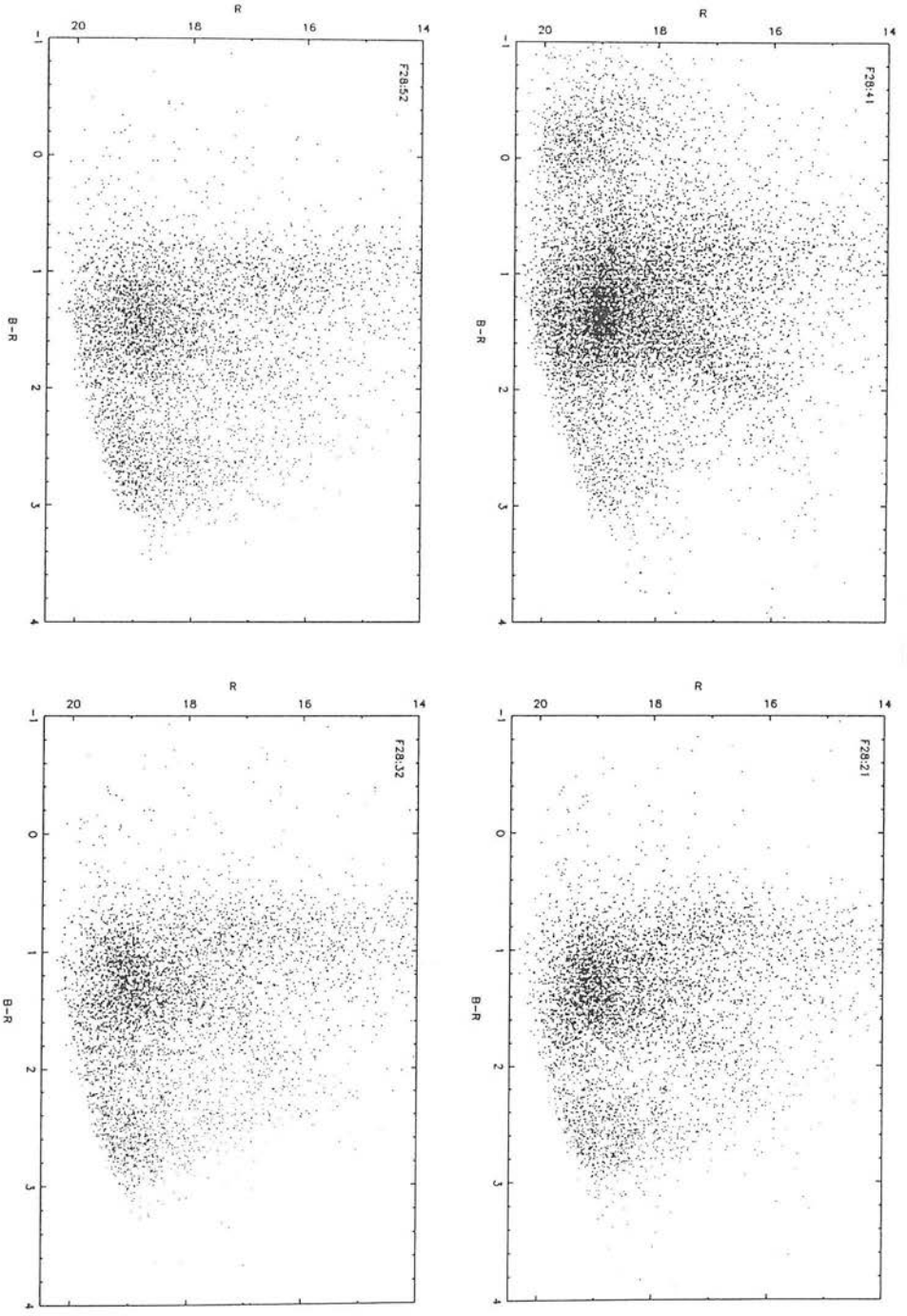
F28:52
F28:41
F28:32
F28:21
R
B-R
20
18
16
14
-1
0
1
2
3
4

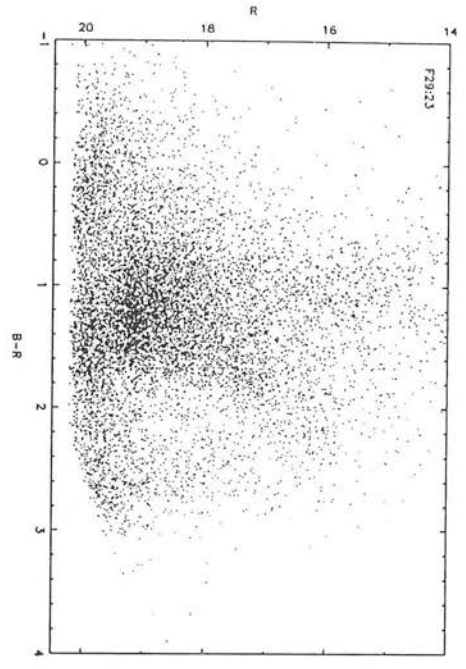
R
20
18
16
14
B-R
-1
0
1
2
3
4
F29:23

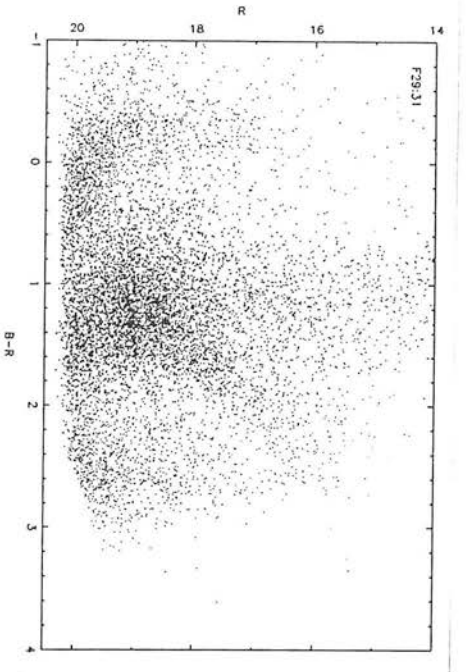
R
20
18
16
14
B-R
-1
0
1
2
3
4
F29:31

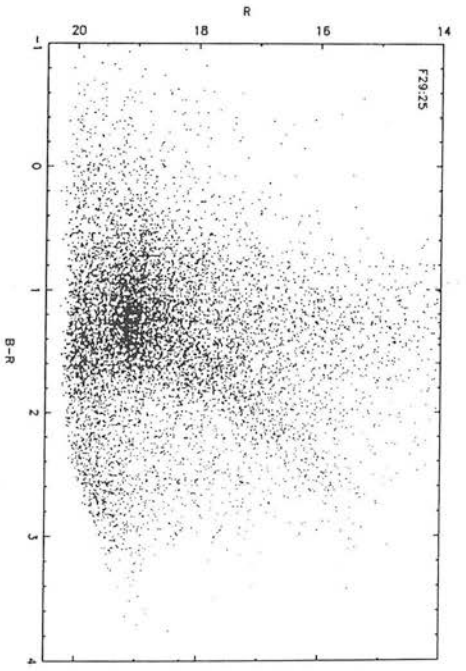
R
20
18
16
14
B-R
-1
0
1
2
3
4
F29:25

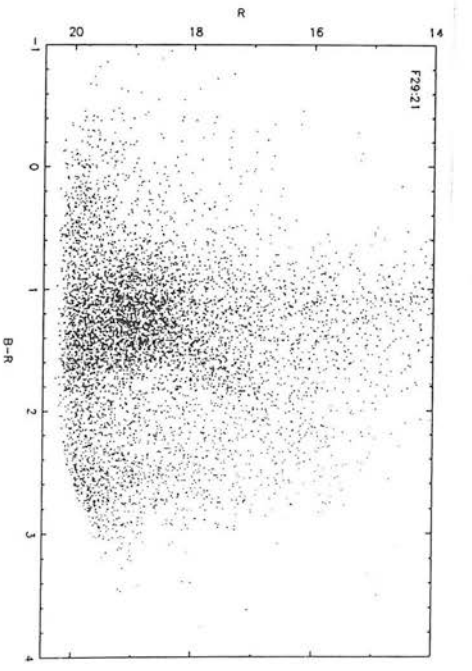
R
20
18
16
14
B-R
-1
0
1
2
3
4
F29:21

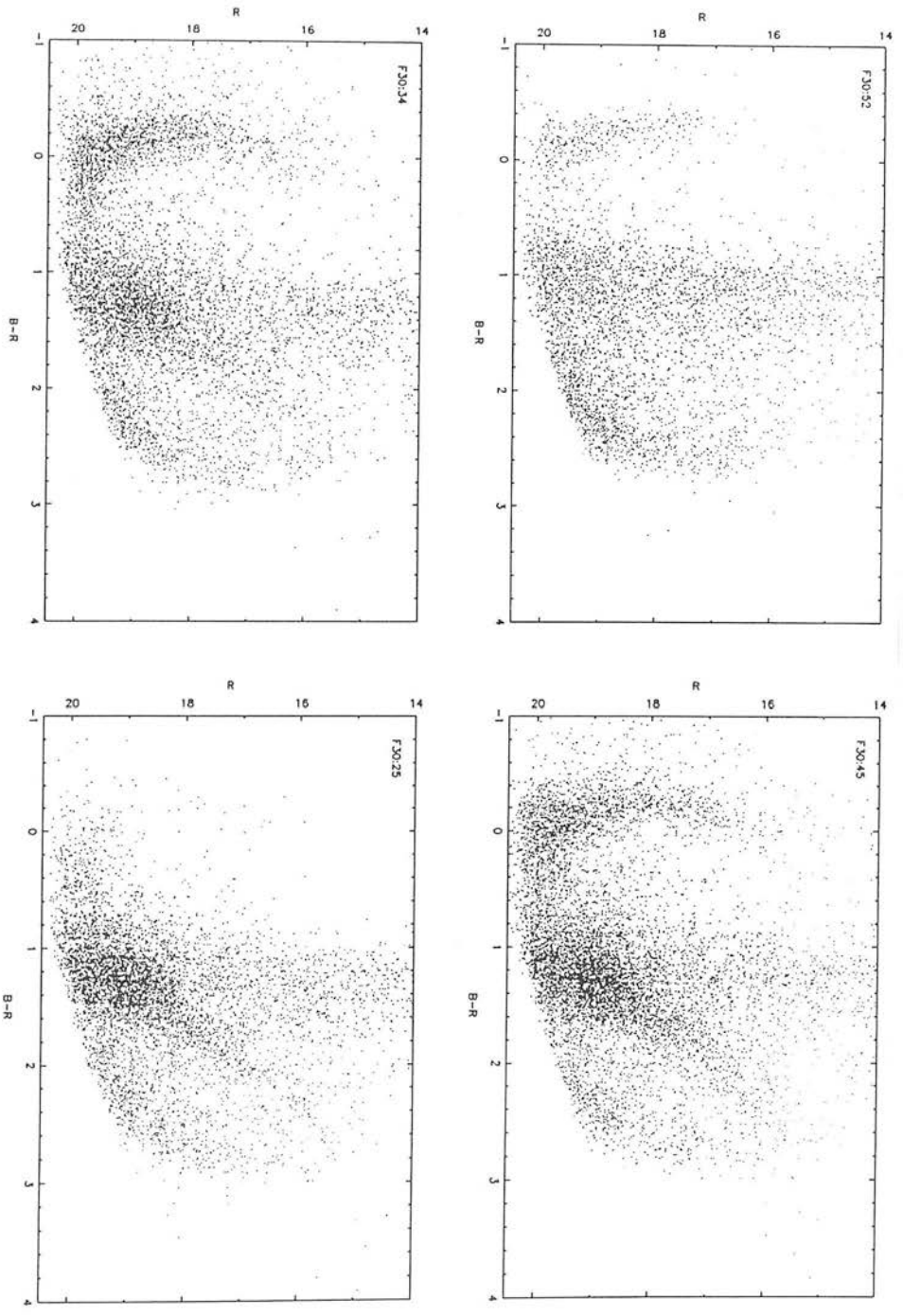
F30:34
F30:52
F30:25
F30:45
R
B-R
20
18
16
14
-1
0
1
2
3
4

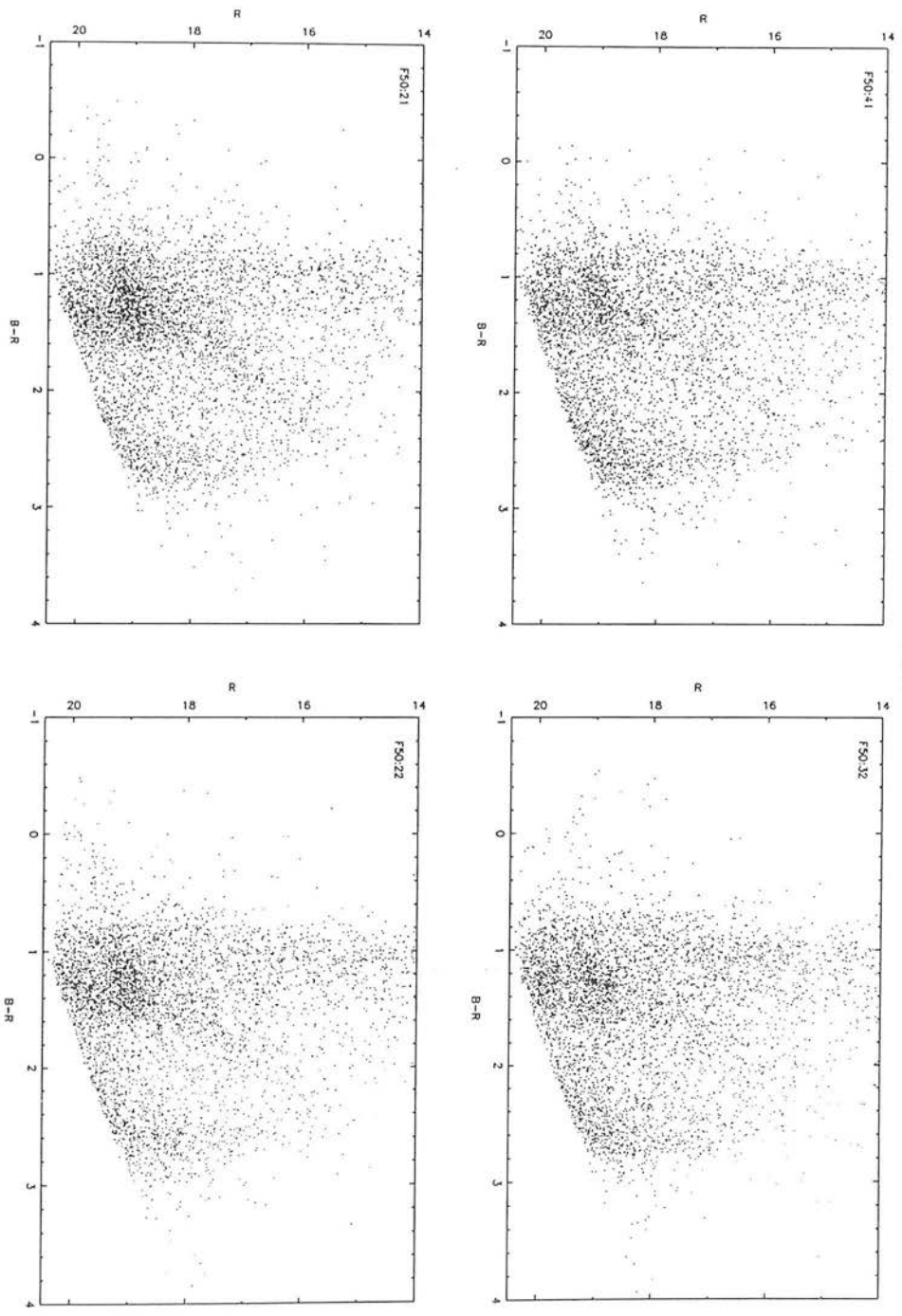
F50-21
F50-41
F50-22
F50-32
R
B-R
20
18
16
14
-1
0
1
2
3
4

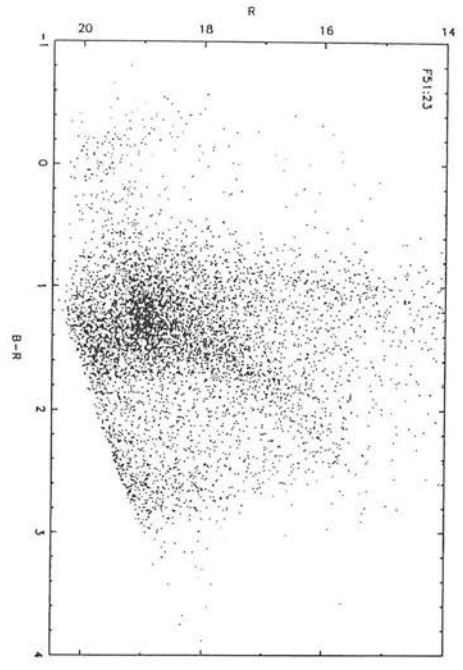
R
20
18
16
14
B-R
-1
0
1
2
3
4
F51:23

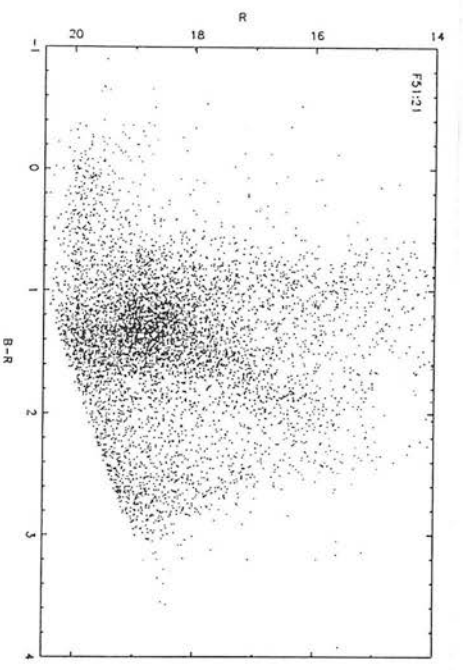
R
20
18
16
14
B-R
-1
0
1
2
3
4
F51:21

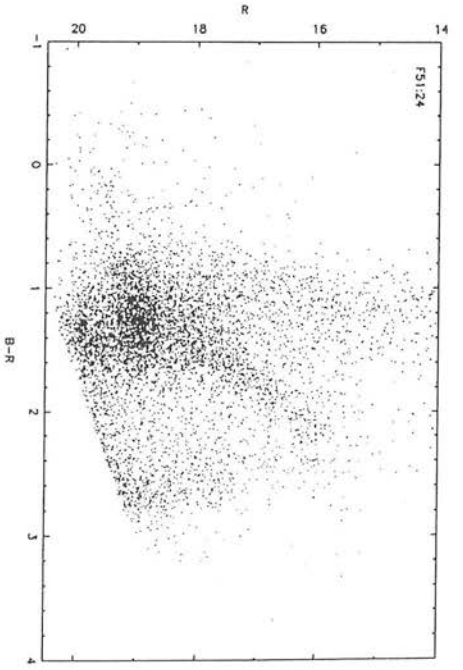
R
20
18
16
14
B-R
-1
0
1
2
3
4
F51:24

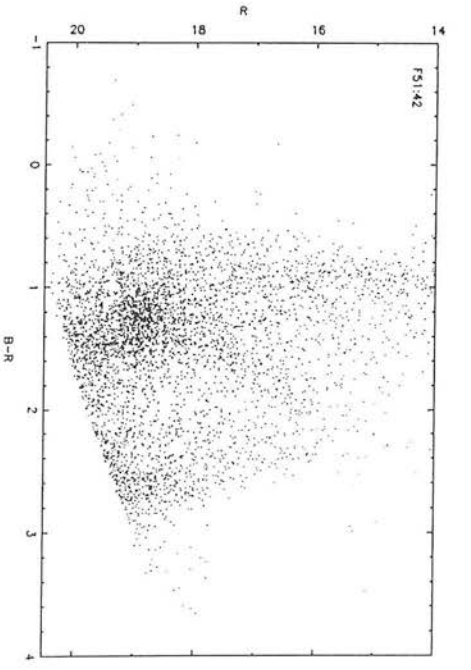
R
20
18
16
14
B-R
-1
0
1
2
3
4
F51:42

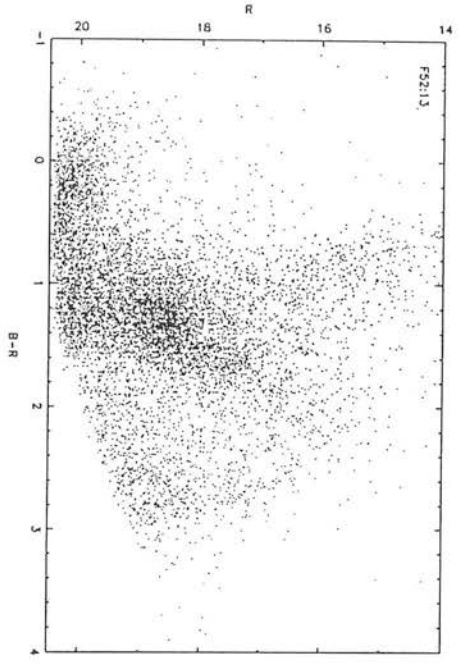
R
20
18
16
14
B-R
-1
0
1
2
3
4
F52:13

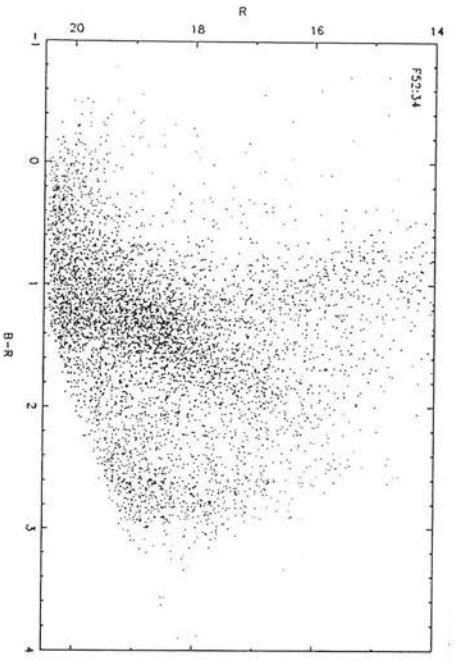
R
20
18
16
14
B-R
-1
0
1
2
3
4
F52:34

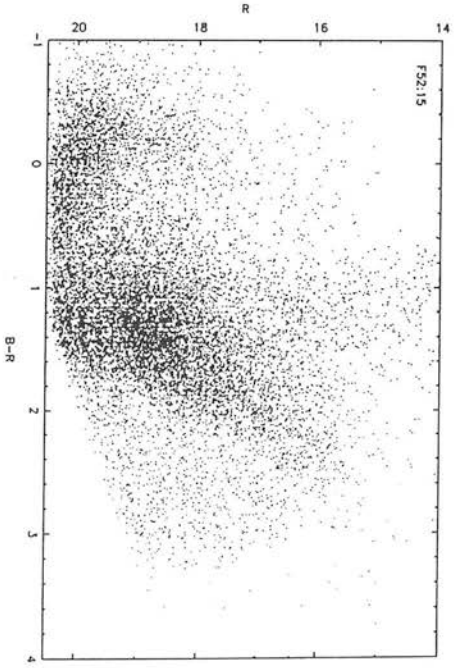
R
20
18
16
14
B-R
-1
0
1
2
3
4
F52:15

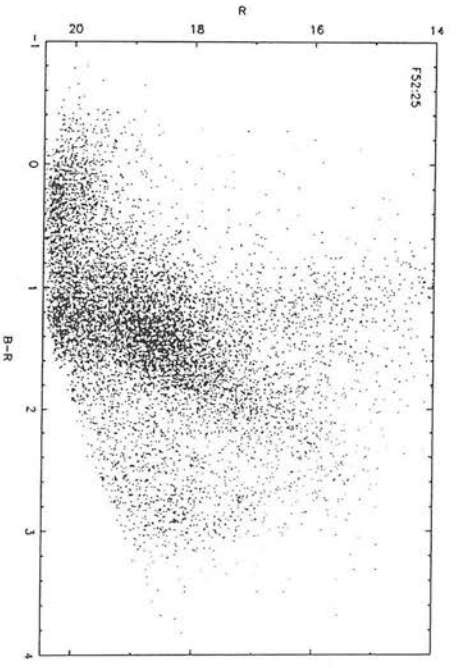
R
20
18
16
14
B-R
-1
0
1
2
3
4
F52:25

Appendix D: — The HB/Clump Luminosity Histograms

HB/clump luminosity histograms for the grid regions from ESO/SERC Fields 28, 29, 30, 50, 51, 52 are presented here. The histograms were constructed for stars with $0.6 < B - R < 1.8$ for the luminosity range $18 < R < 20$ and corrected for the contribution from the galactic foreground population. All the histograms for each field are laid out on a single page, with the position of each histogram in the array indicating the spatial position of the grid region within a given field. (North is at the top and east is to the left). The grid regions are numbered according to Fig. 3.13. In the following pages the field numbers are indicated on the header at the top of the page.

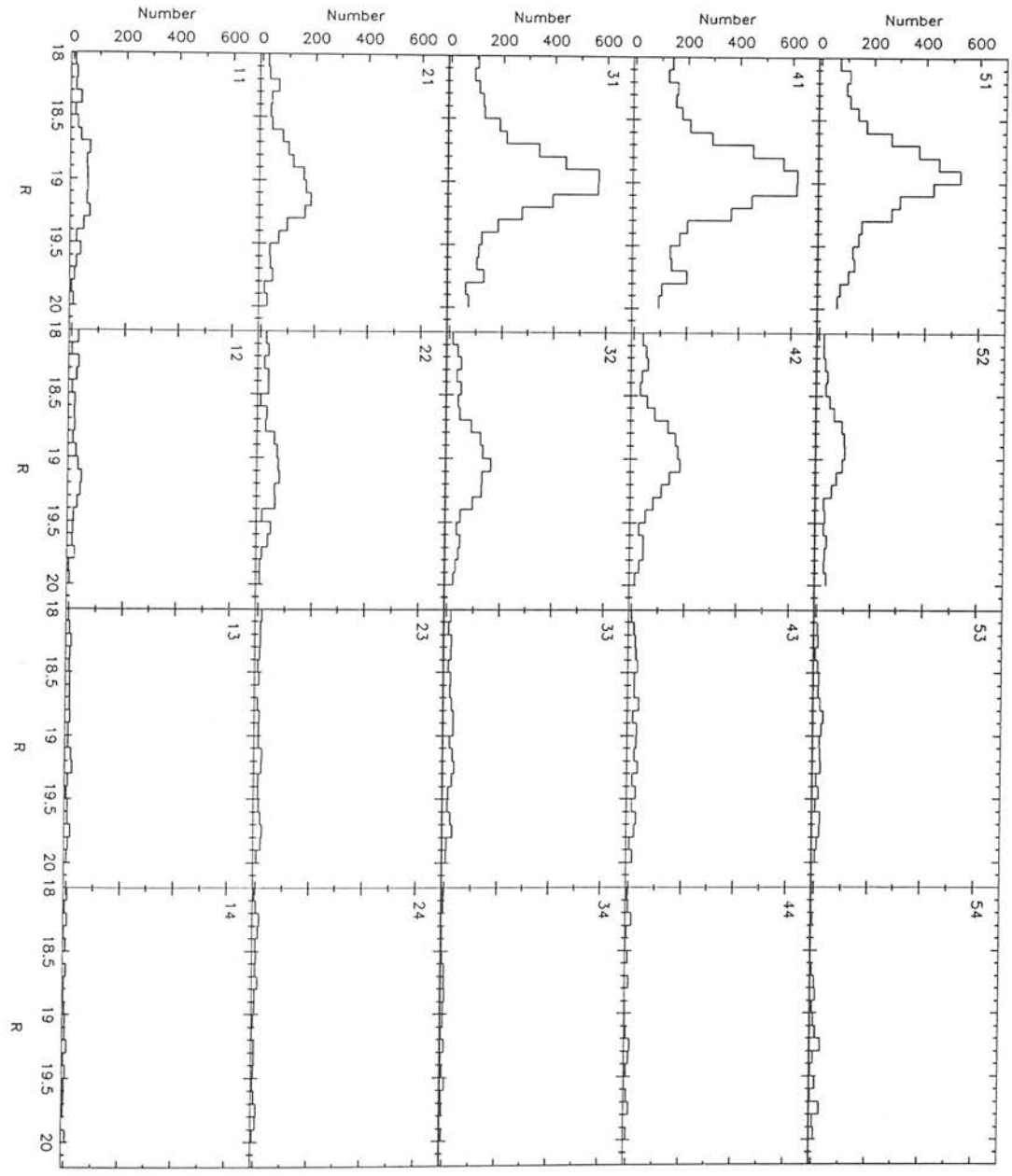
Number
0
200
400
600
R
18
18.5
19
19.5
20
11
12
13
14
21
22
23
24
31
32
33
34
41
42
43
44
51
52
53
54

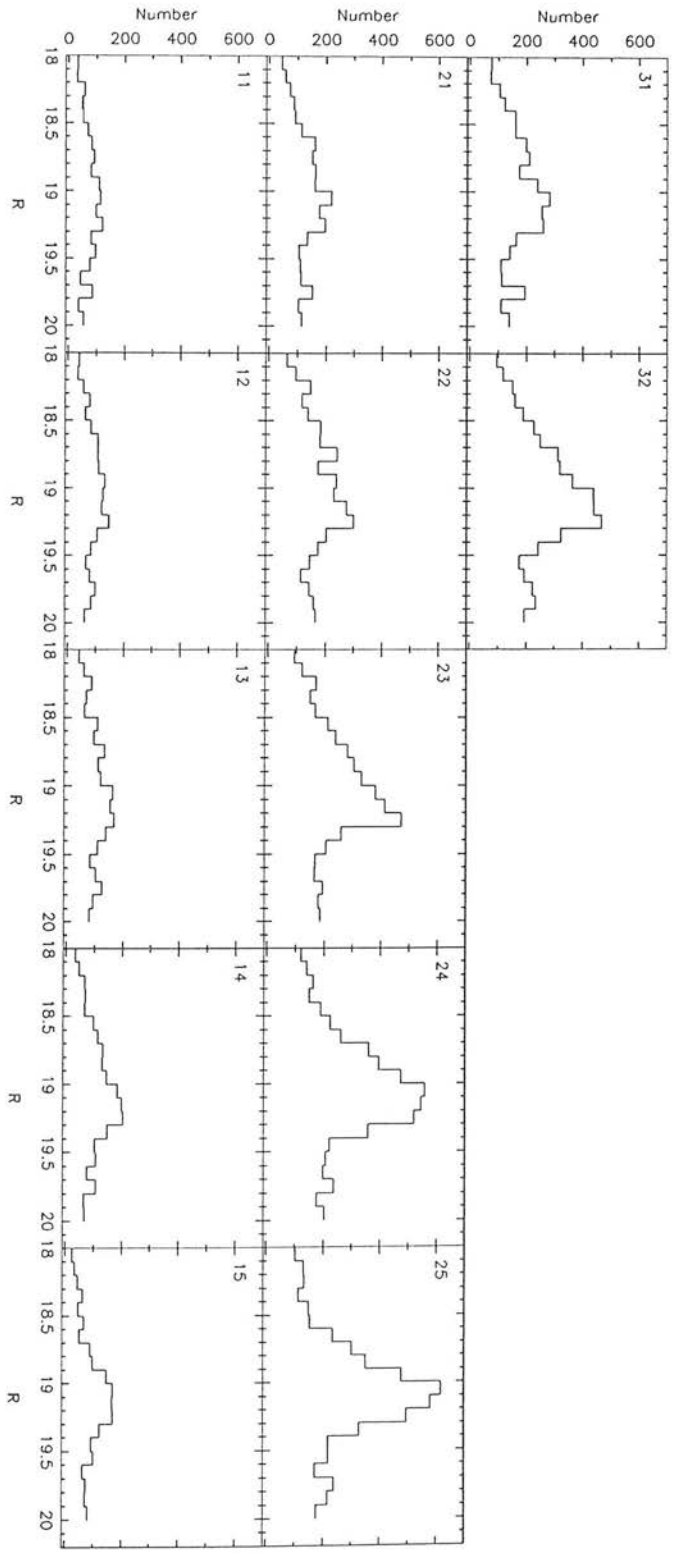
Number
0
200
400
600
R
18
18.5
19
19.5
20
11
12
13
14
15
21
22
23
24
25
31
32

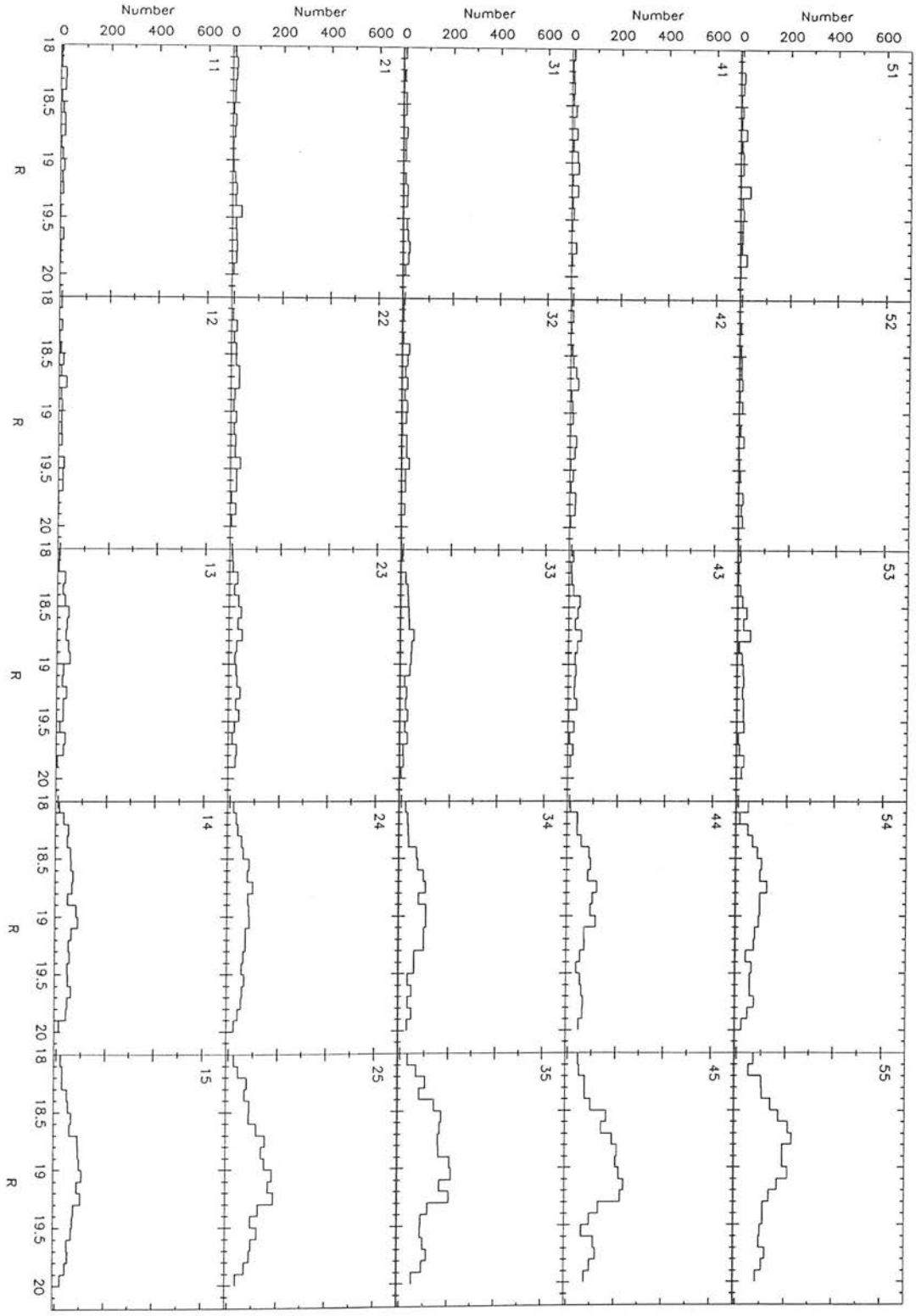
Number
0
200
400
600
R
18
18.5
19
19.5
20
11
12
13
14
15
21
22
23
24
25
31
32
33
34
35
41
42
43
44
45
51
52
53
54
55

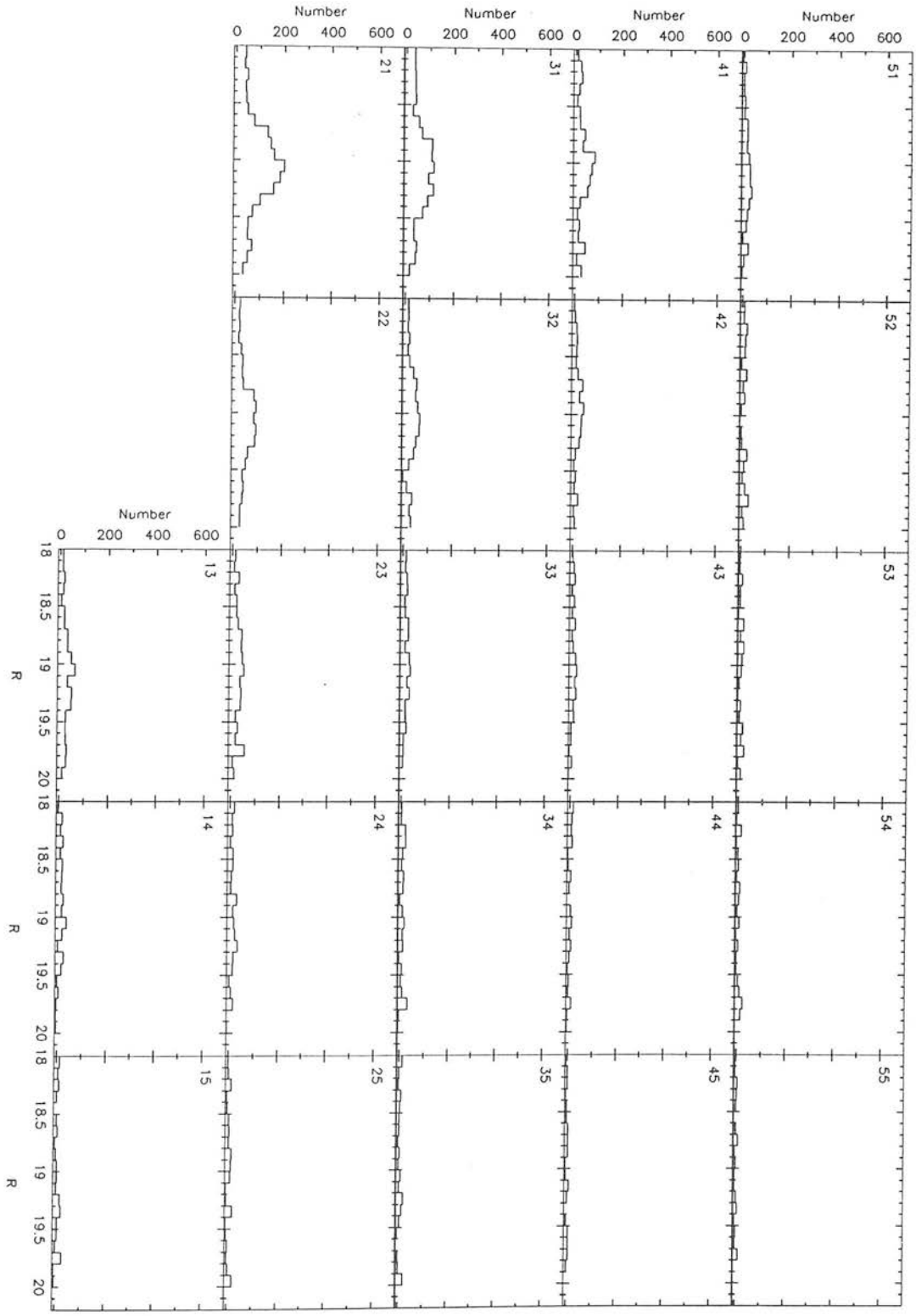
Number
0 200 400 600
R
18 18.5 19 19.5 20

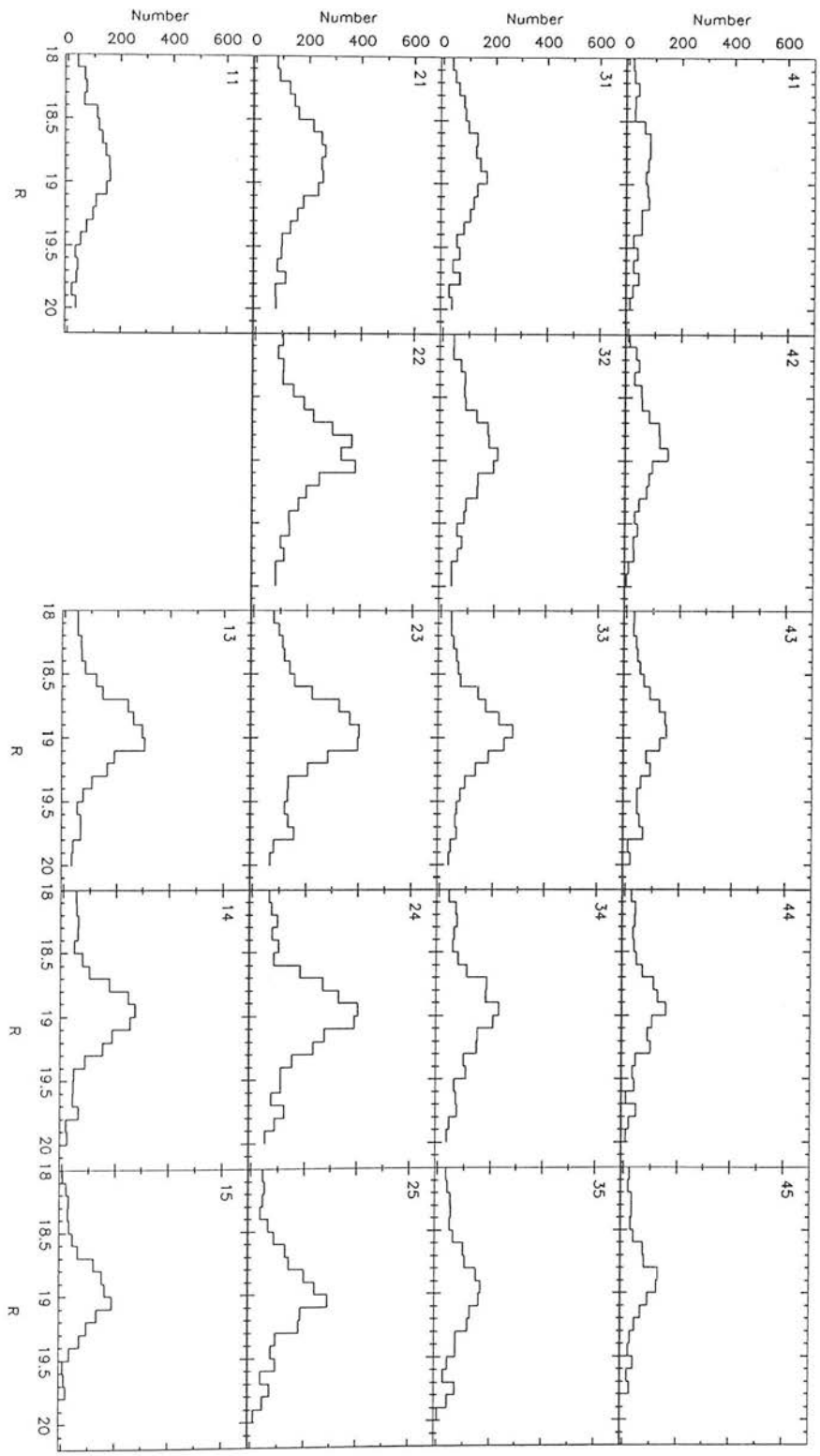
Number
0
200
400
600
R
18
18.5
19
19.5
20
11
21
31
41
12
22
32
42
13
23
33
43
14
24
34
44
15
25
35
45

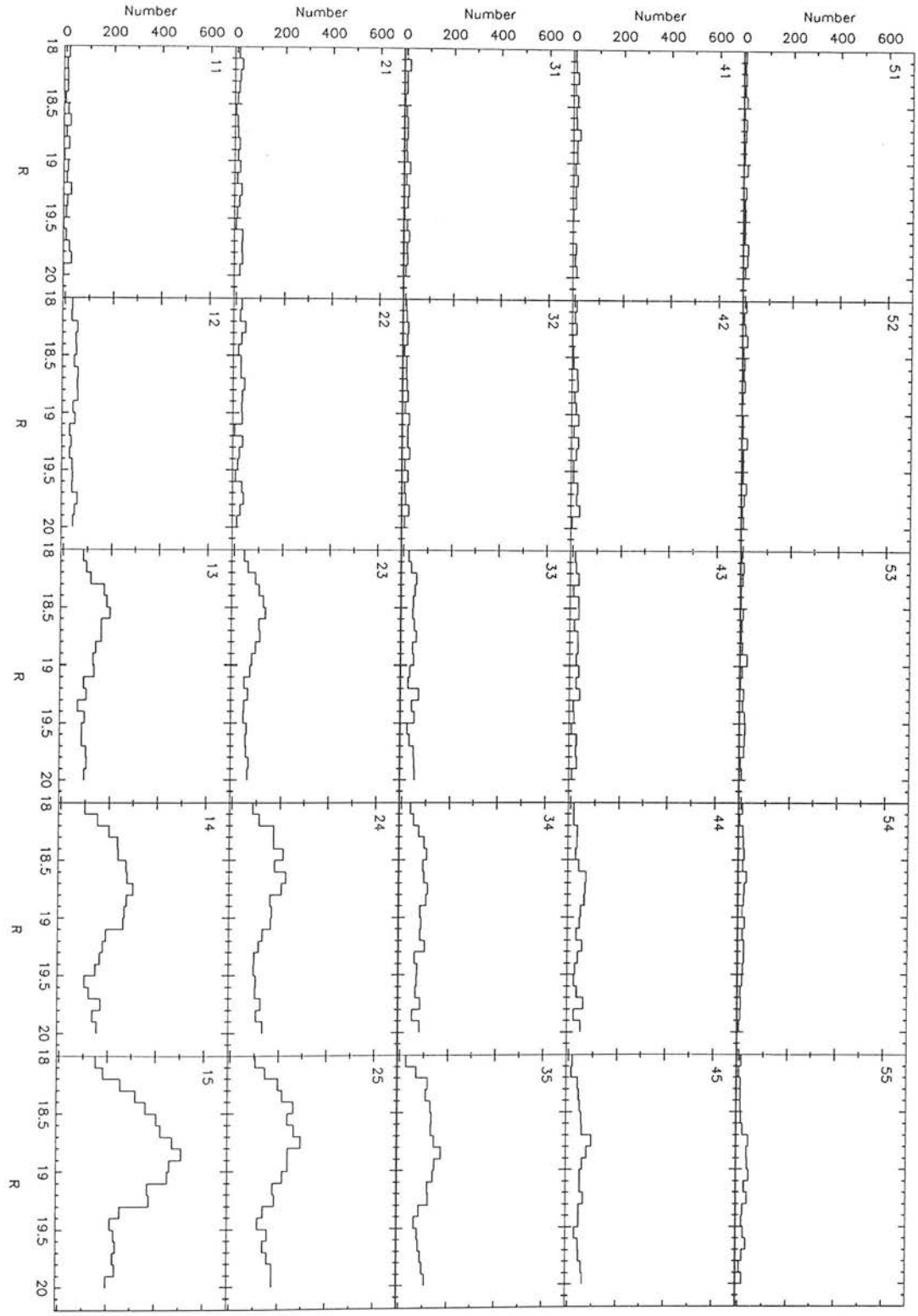
Number
0 200 400 600
R
18 18.5 19 19.5 20
11 12 13 14 15
21 22 23 24 25
31 32 33 34 35
41 42 43 44 45
51 52 53 54 55

Appendix E: — SAAO CCD Images

Contour plots of R-band SAAO CCD images (see Chapter 5) are presented here. Each image represents one of the sixteen CCD regions used in the study and are labelled 1-16. CCD region 1 is the region of the cluster NGC 643. ID numbers are indicated for all stellar images brighter than $R = 20$ and their magnitudes are given in the magnitude lists of Appendix F. The CCD image plots have the same orientation as the COSMOS map of the whole area of the study (Fig.5.1) with north at the top of the frame and east to the *right.*

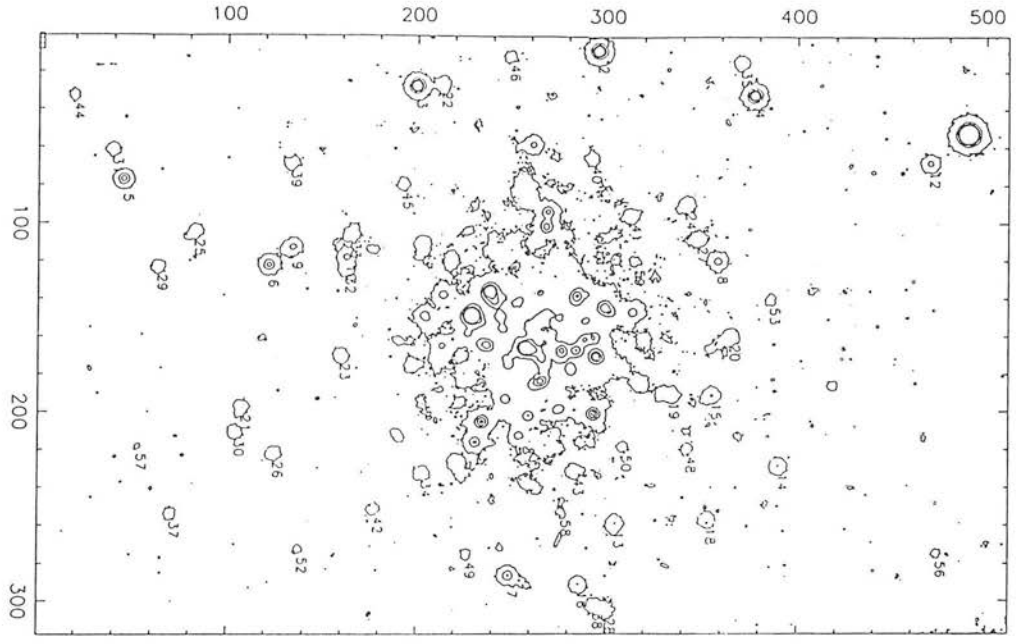
100
200
300
400
500
100
200
300
CCD 1

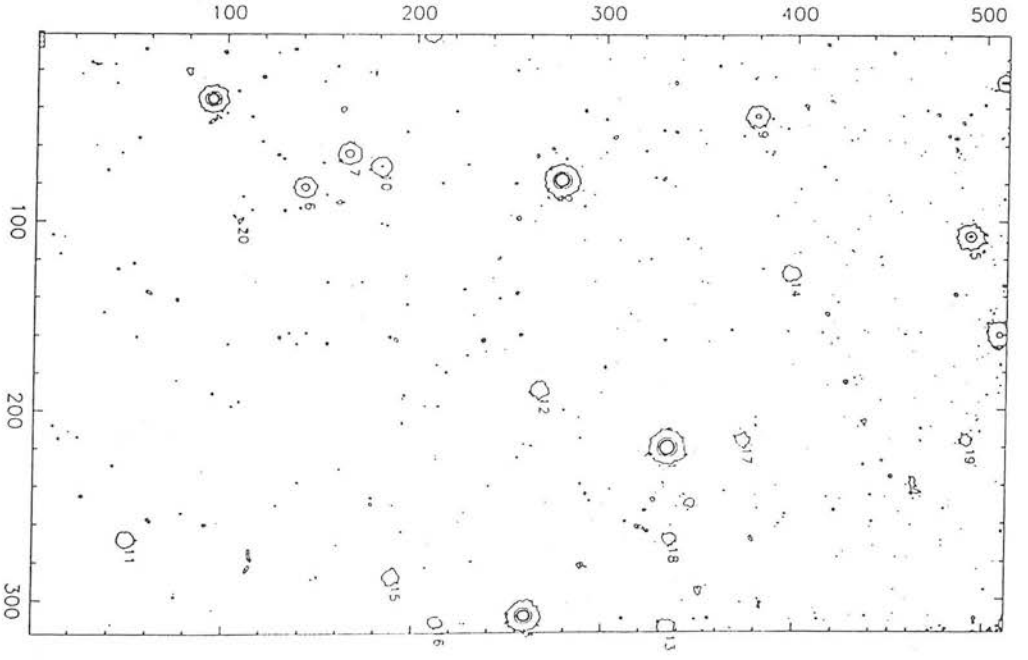
100
200
300
400
500
100
200
300
CCD 2

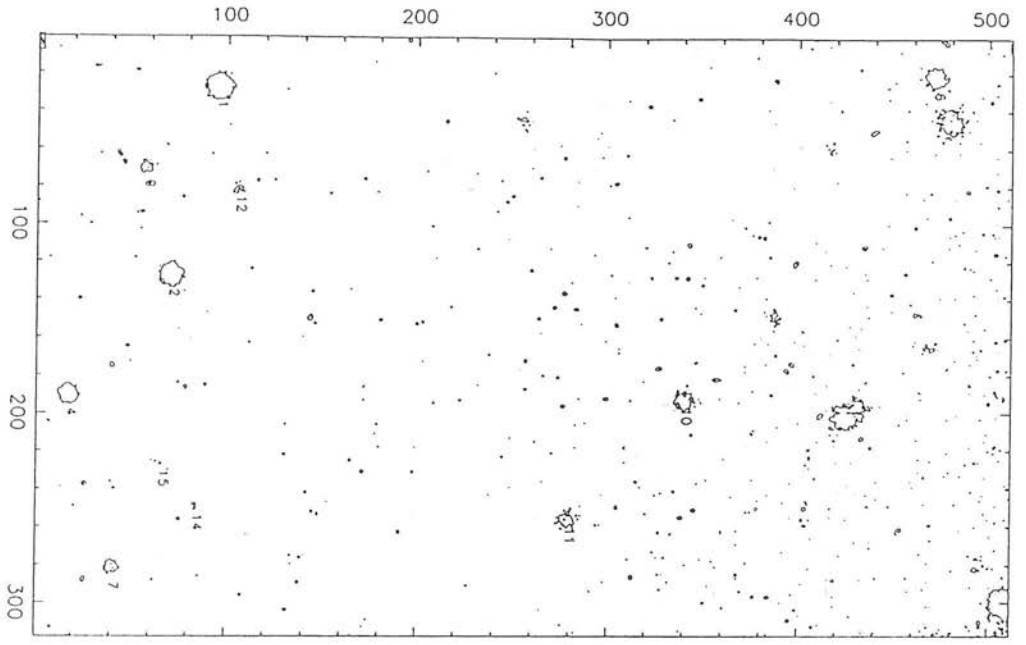
100
200
300
400
500
100
200
300
CCD 3

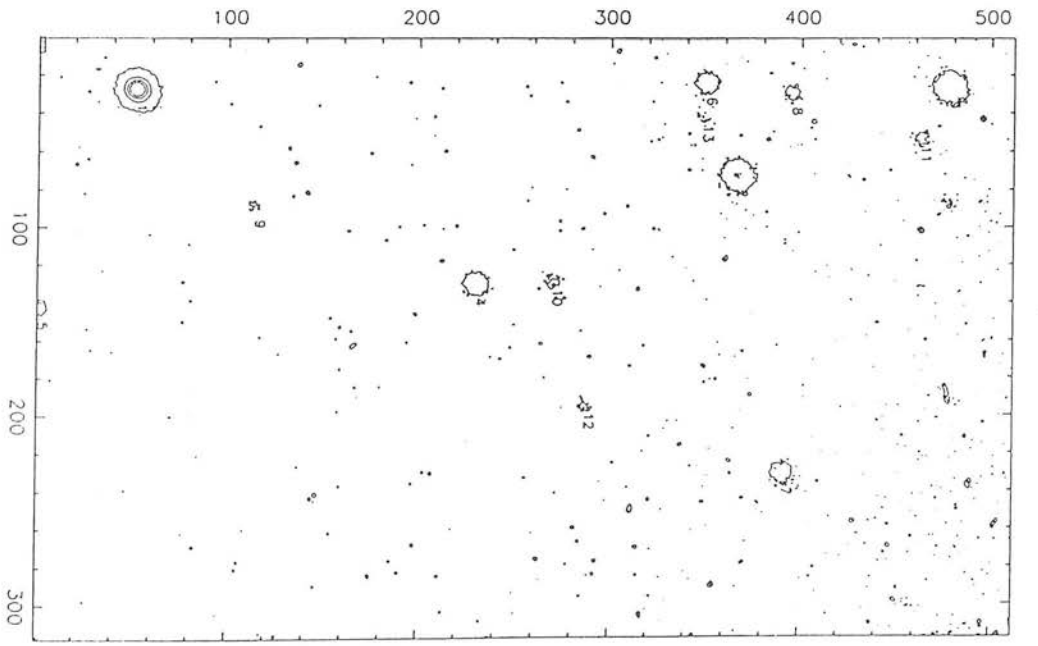
100
200
300
400
500
100
200
300
CCD 4

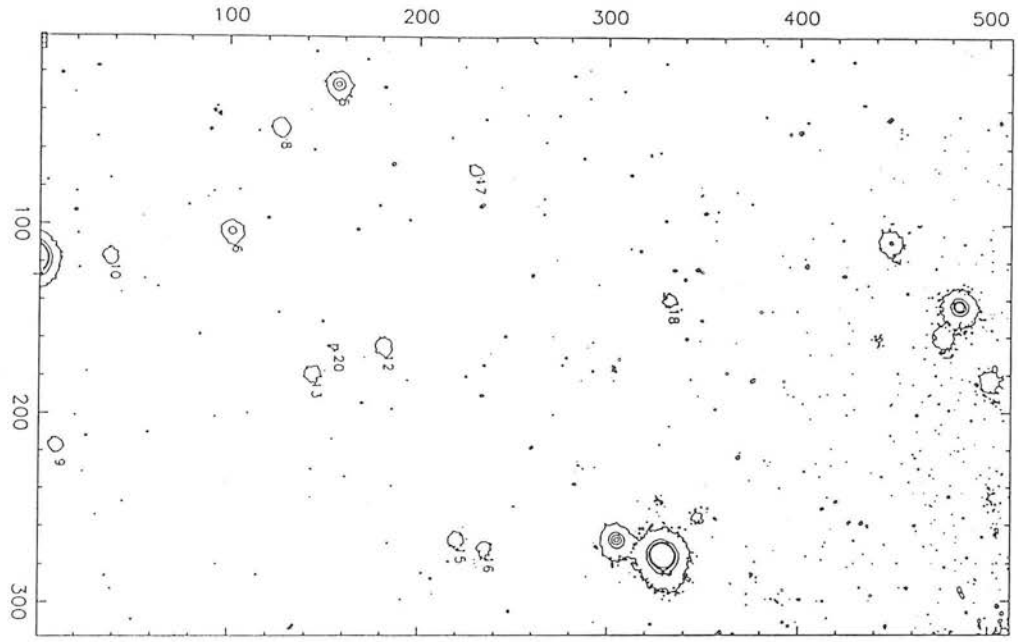

CCD 5

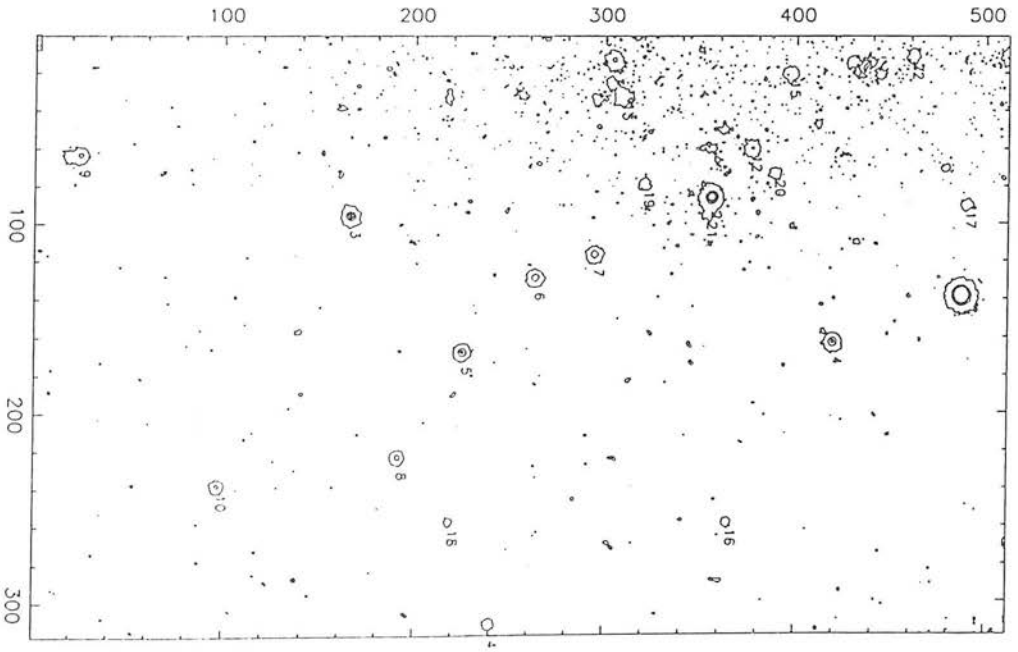

CCD 6

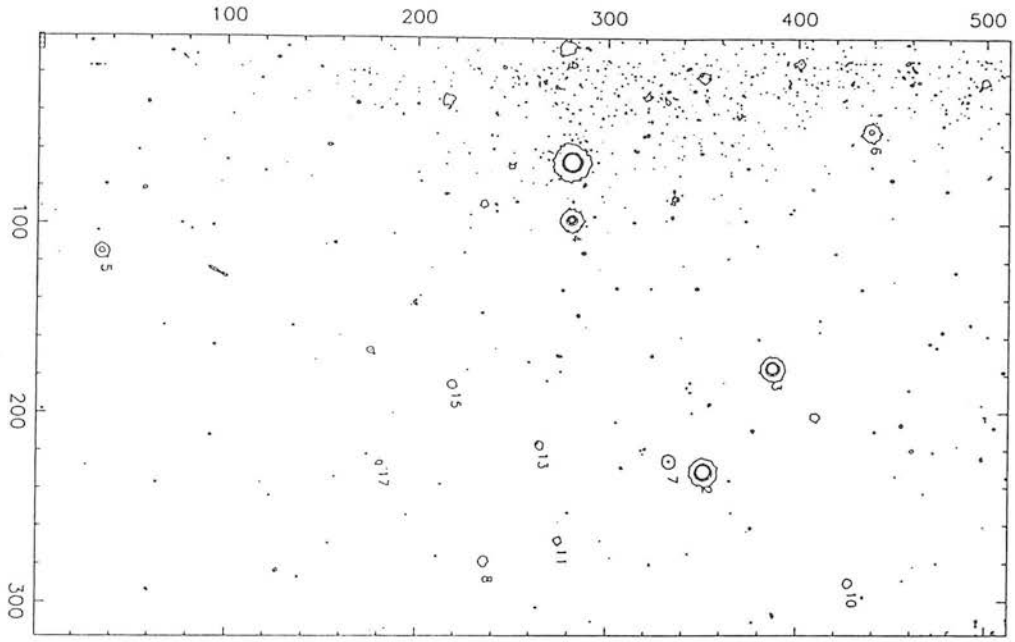
100
200
300
400
500
100
200
300
CCD 7

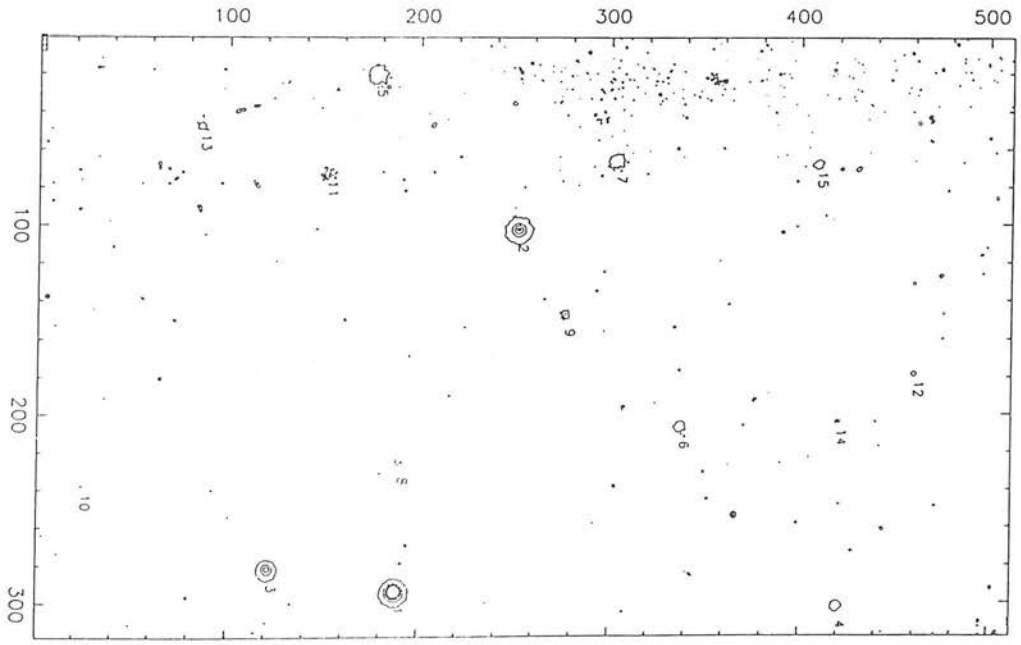
100
200
300
400
500
100
200
300
CCD 8

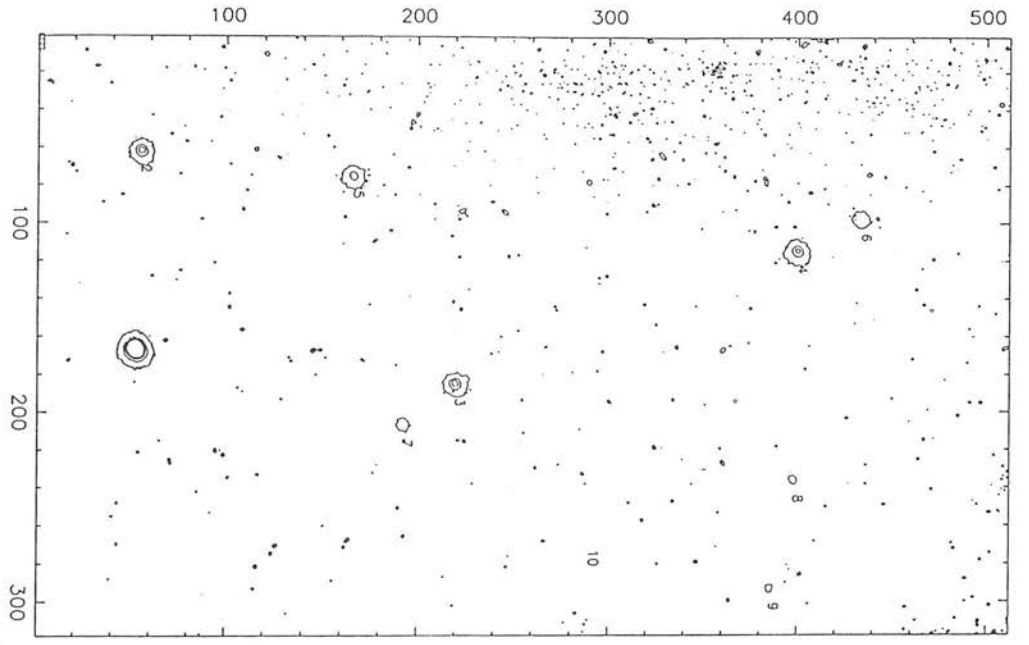
100
200
300
400
500
100
200
300
CCD 9

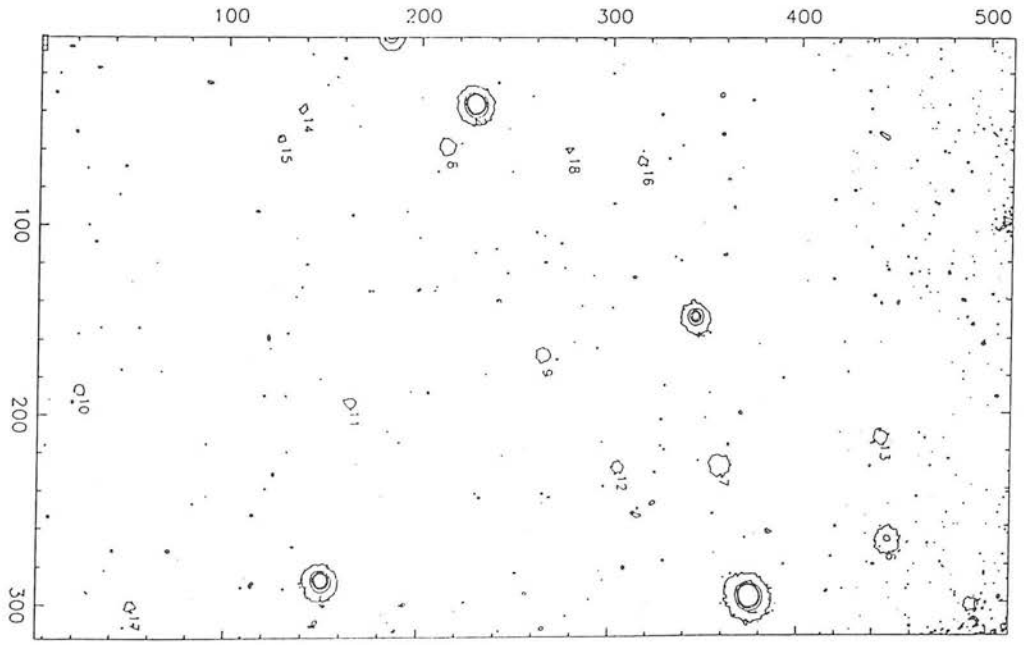
100
200
300
400
500
100
200
300
CCD 10

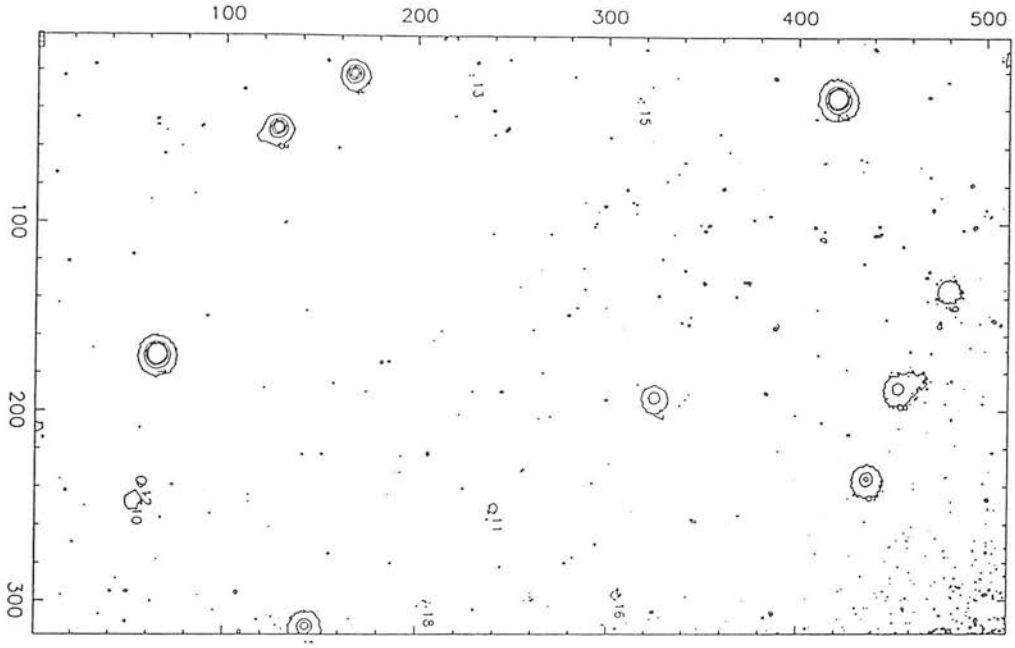
100
200
300
400
500
100
200
300
CCD 11

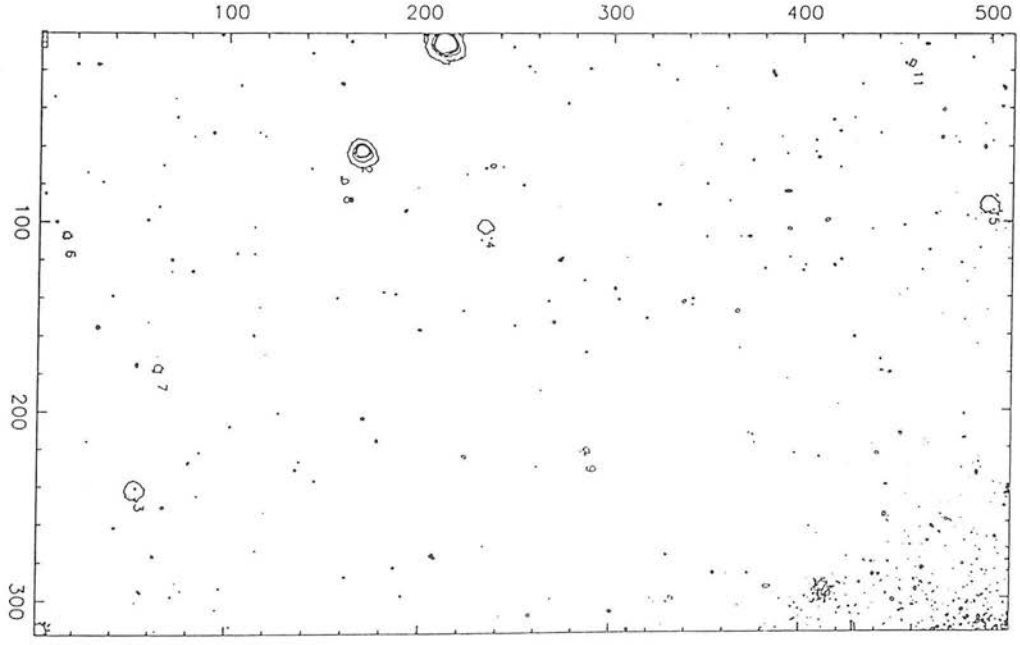
100
200
300
400
500
100
200
300
CCD 12

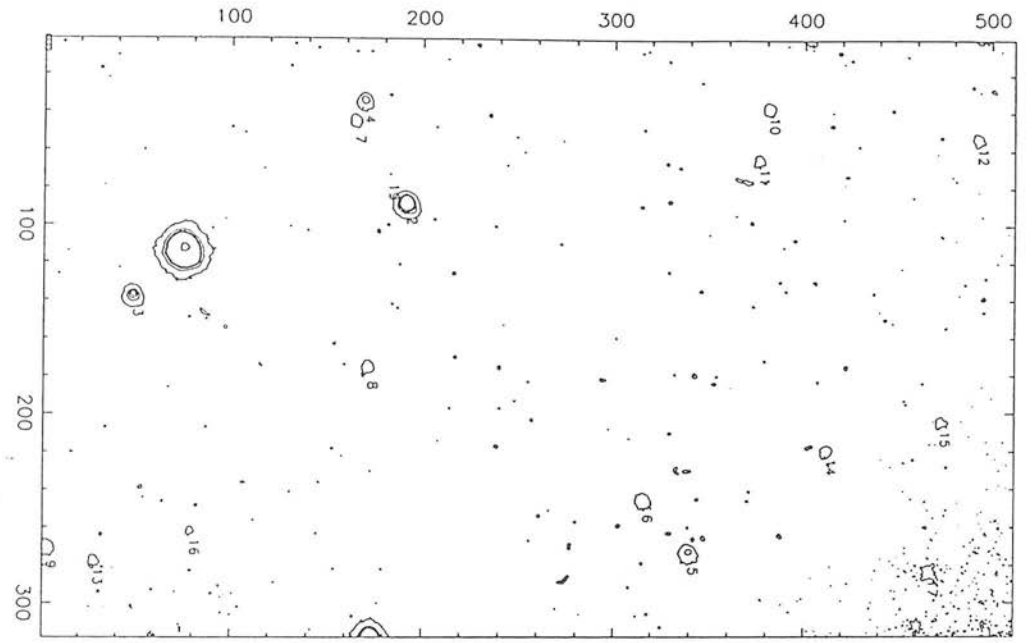
100
200
300
400
500
100
200
300
CCD 13

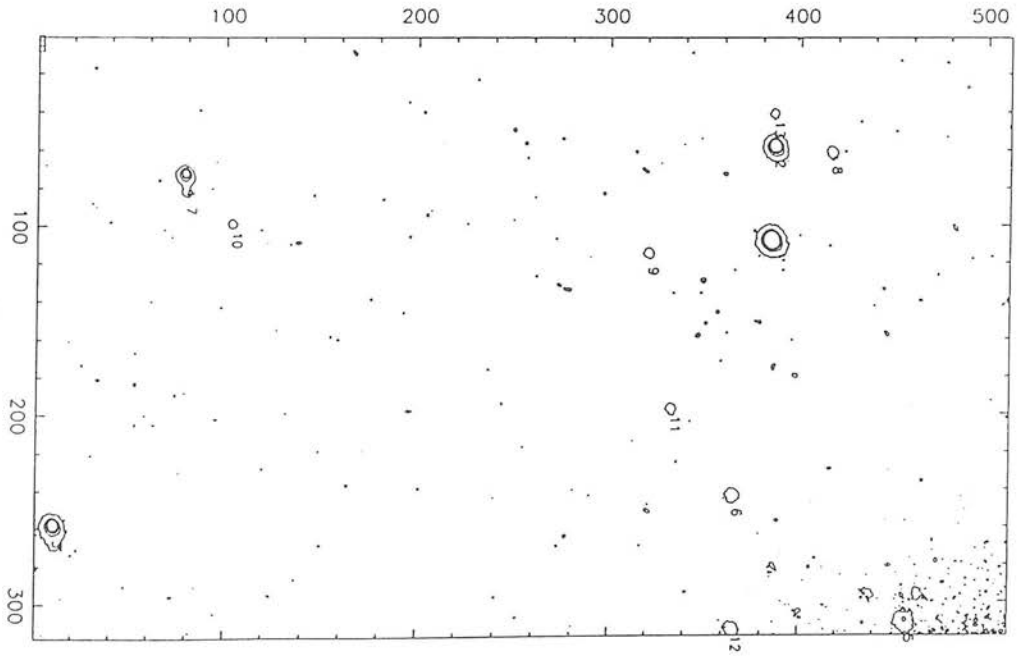
100
200
300
400
500
100
200
300
CCD 14

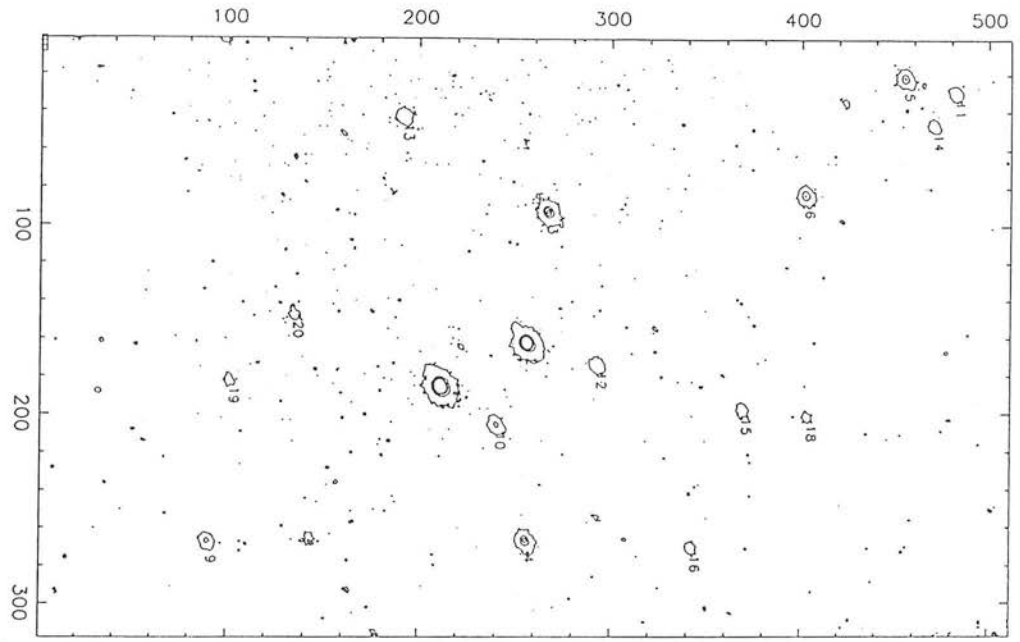
100
200
300
400
500
100
200
300
CCD 15

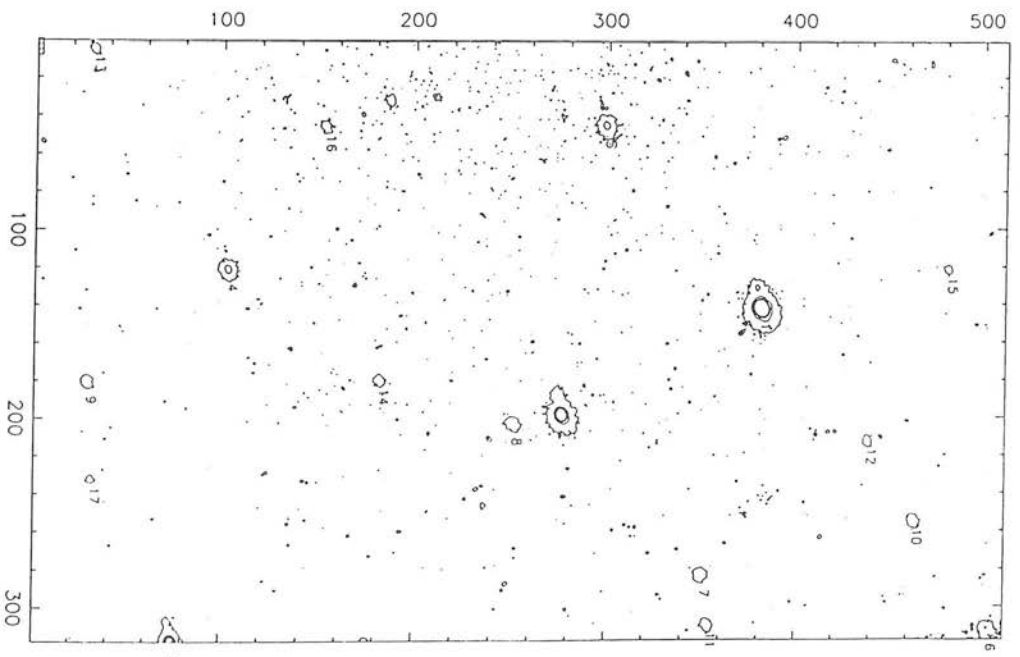
100
200
300
400
500
100
200
300
CCD 16

Appendix F: — SAAO CCD Magnitude Lists

Magnitude lists for SAAO CCD regions 1-16 (see Chapter 5) are presented here. The data listed include the star ID number (as in the CCD images produced in Appendix E) prefixed by the CCD region number, $x - y$ positions on the CCD frame, magnitudes and associated standard errors. The standard errors incorporate the errors due to the use of secondary standards to define zeropoints for the CCD regions.

ID No.	x (pix)	y (pix)	R / σ_R	$V-R$ / σ_{V-R}
1–01	52.66	490.21	15.018 0.042	0.432 0.054
1–02	8.62	295.48	16.604 0.042	0.396 0.054
1–03	27.84	199.32	16.665 0.042	0.659 0.054
1–04	32.38	377.34	16.827 0.042	0.652 0.054
1–05	77.33	44.96	17.565 0.042	1.029 0.056
1–06	122.55	121.76	17.607 0.042	0.565 0.055
1–07	286.65	248.78	17.750 0.043	0.557 0.056
1–08	119.95	358.27	18.067 0.043	0.557 0.057
1–09	113.02	134.27	18.132 0.044	0.783 0.060
1–10	118.23	162.42	18.182 0.044	0.506 0.058
1–12	68.33	469.90	18.253 0.043	0.760 0.060
1–13	259.23	304.60	18.445 0.045	0.382 0.060
1–14	228.71	390.08	18.475 0.044	0.485 0.059
1–15	191.47	355.16	18.496 0.045	0.598 0.063
1–16	291.33	285.50	18.519 0.045	0.458 0.060
1–17	111.64	202.77	18.609 0.046	0.507 0.063
1–18	257.47	352.60	18.629 0.047	0.338 0.061
1–19	191.17	333.20	18.643 0.049	0.498 0.068
1–20	160.37	365.09	18.657 0.048	0.555 0.069
1–21	198.01	107.55	18.659 0.046	0.380 0.063
1–22	26.81	212.90	18.671 0.046	1.187 0.084
1–23	170.68	159.62	18.731 0.045	0.486 0.063
1–24	90.28	341.55	18.731 0.045	0.444 0.069
1–25	104.86	82.85	18.745 0.048	0.543 0.065
1–26	222.39	124.58	18.771 0.046	0.454 0.065
1–27	108.07	347.74	18.793 0.048	0.549 0.067
1–28	305.49	300.35	18.810 0.048	0.454 0.066
1–29	123.48	63.07	18.810 0.046	0.545 0.065
1–30	211.08	103.94	18.810 0.046	0.523 0.067
1–31	61.62	39.39	18.819 0.045	0.557 0.065
1–32	124.80	162.18	18.860 0.047	0.493 0.068
1–33	106.11	164.78	18.868 0.049	0.378 0.068
1–34	232.69	202.83	18.914 0.047	0.424 0.068
1–35	14.91	370.46	18.920 0.046	0.514 0.065
1–36	120.29	218.03	18.929 0.051	0.443 0.071
1–37	254.03	69.97	18.978 0.047	0.461 0.069
1–38	302.61	293.80	19.137 0.051	0.774 0.082
1–39	69.03	133.49	19.143 0.054	1.018 0.091
1–40	66.28	292.00	19.162 0.050	0.507 0.073
1–41	96.51	313.09	19.187 0.049	0.499 0.074
1–42	251.55	177.44	19.258 0.053	0.444 0.074
1–43	231.50	283.21	19.283 0.054	0.557 0.094

ID No.	x (pix)	y (pix)	R / σ_R	$V-R$ / σ_{V-R}
1–44	33.09	19.35	19.328 0.054	0.875 0.122
1–45	80.11	192.30	19.401 0.052	0.323 0.076
1–46	12.04	248.75	19.493 0.052	0.256 0.076
1–48	219.77	341.97	19.671 0.059	0.371 0.088
1–49	275.36	226.43	19.721 0.057	0.512 0.091
1–50	218.90	308.48	19.722 0.060	0.216 0.086
1–52	272.64	137.55	19.751 0.058	0.127 0.083
1–53	140.47	385.82	19.757 0.061	0.320 0.092
1–56	274.93	473.38	19.881 0.066	0.330 0.106
1–57	218.20	52.42	19.919 0.060	0.724 0.123
1–58	253.14	276.69	19.942 0.079	0.481 0.124
1–59	120.40	314.83	19.957 0.069	0.137 0.100
1–60	161.16	118.25	20.014 0.063	0.025 0.089
1–61	213.14	369.39	20.096 0.071	0.228 0.103
1–63	257.07	334.65	20.134 0.080	0.266 0.120
1–66	47.75	231.60	20.197 0.081	0.353 0.142
1–67	271.81	244.47	20.200 0.084	0.420 0.137
1–68	51.30	197.74	20.219 0.078	0.118 0.115
1–69	210.72	342.14	20.242 0.081	0.179 0.116
1–70	249.21	383.18	20.271 0.094	0.117 0.125
1–71	213.68	466.26	20.289 0.076	0.108 0.117
1–72	135.89	407.48	20.292 0.088	0.009 0.115
1–74	32.84	270.32	20.305 0.083	0.491 0.153
1–78	62.10	148.88	20.400 0.091	0.220 0.140
1–83	69.86	427.49	20.420 0.081	0.111 0.126
1–84	239.92	427.86	20.434 0.086	0.010 0.123
1–87	135.77	424.43	20.443 0.081	0.003 0.123
1–89	86.54	326.66	20.503 0.099	0.132 0.148
1–92	17.71	488.33	20.580 0.126	0.179 0.171
1–94	263.96	14.71	20.706 0.117	-0.112 0.154
1–95	72.59	15.92	20.715 0.112	0.010 0.159
1–98	28.79	294.66	20.832 0.127	0.100 0.191
2–01	220.09	333.76	16.233 0.081	0.434 0.103
2–02	78.31	276.82	16.399 0.081	0.496 0.103
2–03	308.79	259.53	16.605 0.081	0.397 0.103
2–04	35.31	92.59	16.736 0.081	0.423 0.103
2–05	107.92	492.02	17.592 0.081	0.536 0.104
2–06	82.08	141.50	17.862 0.081	0.623 0.105
2–07	64.35	164.69	17.880 0.082	0.533 0.105
2–09	44.32	379.23	18.161 0.082	0.468 0.105
2–10	71.11	181.62	18.325 0.082	0.472 0.106
2–11	267.87	49.52	18.376 0.082	1.350 0.112

ID No.	x (pix)	y (pix)	R / σ_R	$V-R$ / σ_{V-R}
2–12	189.62	266.46	18.769 0.083	0.374 0.108
2–13	315.32	334.49	18.939 0.083	0.503 0.110
2–14	127.73	397.53	18.941 0.085	0.562 0.112
2–15	287.77	189.11	19.008 0.084	0.490 0.112
2–16	312.14	212.80	19.435 0.088	0.218 0.117
2–17	216.03	373.24	19.519 0.088	0.771 0.133
2–18	268.43	335.43	19.632 0.091	0.049 0.118
2–19	216.40	490.60	19.808 0.093	0.484 0.137
2–20	98.88	106.92	19.940 0.100	0.248 0.136
2–22	40.99	161.33	20.108 0.099	0.480 0.147
2–23	249.50	346.23	20.113 0.099	0.473 0.148
3–01	27.83	94.48	17.821 0.103	0.456 0.146
3–02	127.37	70.18	18.018 0.104	1.018 0.149
3–04	190.08	16.95	18.301 0.105	0.401 0.148
3–06	21.40	470.65	18.831 0.107	0.520 0.158
3–07	281.50	39.84	18.848 0.107	0.494 0.156
3–09	69.75	56.93	18.938 0.108	0.545 0.157
3–10	192.82	339.21	19.116 0.111	0.330 0.160
3–11	256.05	278.40	19.312 0.112	0.469 0.167
3–12	81.76	104.71	19.391 0.112	0.320 0.165
3–14	249.43	83.16	19.611 0.115	0.605 0.181
3–15	226.34	65.38	19.636 0.119	-0.047 0.176
4–01	27.27	51.76	15.612 0.054	1.026 0.076
4–02	72.53	366.60	17.276 0.054	1.028 0.077
4–03	26.03	478.06	17.414 0.054	0.534 0.077
4–04	130.10	230.18	17.975 0.055	0.995 0.082
4–05	142.11	1.27	18.107 0.061	0.531 0.084
4–06	24.04	350.22	18.379 0.057	0.422 0.082
4–07	230.83	391.15	18.671 0.060	0.361 0.087
4–08	29.50	395.07	19.063 0.065	0.372 0.093
4–09	88.39	114.31	19.065 0.066	0.464 0.099
4–10	129.34	270.35	19.190 0.074	0.324 0.103
4–11	53.50	463.04	19.363 0.073	0.544 0.113
4–12	194.91	287.19	19.379 0.078	0.364 0.118
4–13	42.63	348.43	19.718 0.094	0.481 0.138
4–16	133.32	462.77	20.359 0.136	0.215 0.189
5–01	116.98	-2.30	13.889 0.049	0.518 0.058
5–02	275.28	328.97	14.629 0.039	0.436 0.050
5–03	143.03	484.44	16.463 0.040	0.725 0.050
5–04	267.46	305.07	16.733 0.040	0.577 0.050
5–05	26.48	156.61	17.066 0.040	0.552 0.050
5–06	104.00	101.51	17.577 0.040	0.528 0.051

ID No.	x (pix)	y (pix)	R / σ_R	$V-R$ / σ_{V-R}
5–07	109.19	447.84	17.886 0.041	0.831 0.054
5–08	49.27	126.46	18.195 0.042	0.486 0.055
5–09	216.93	10.05	18.390 0.042	0.473 0.058
5–10	117.06	38.22	18.421 0.043	0.868 0.063
5–11	159.42	475.78	18.428 0.047	0.840 0.066
5–12	165.29	181.61	18.516 0.043	0.487 0.058
5–13	179.74	143.47	18.617 0.046	1.112 0.073
5–14	183.00	500.87	18.691 0.047	0.455 0.063
5–15	267.20	220.29	18.912 0.048	0.491 0.069
5–16	272.07	235.08	19.196 0.057	0.319 0.078
5–17	71.67	229.36	19.263 0.052	0.431 0.076
5–18	139.94	331.60	19.333 0.058	0.511 0.086
5–20	165.79	155.10	19.743 0.068	0.422 0.105
5–22	177.84	303.53	20.057 0.085	0.471 0.136
5–23	97.20	54.75	20.112 0.085	0.144 0.122
5–25	83.44	348.70	20.194 0.081	0.315 0.148
5–29	149.46	149.66	20.735 0.147	-0.071 0.190
6–01	138.17	487.24	15.621 0.050	0.667 0.073
6–02	86.10	355.62	17.166 0.050	0.895 0.073
6–03	95.71	165.77	17.717 0.051	0.800 0.074
6–04	162.89	419.40	18.001 0.051	0.404 0.074
6–05	167.64	224.93	18.028 0.051	0.350 0.074
6–06	128.76	263.46	18.202 0.051	0.416 0.075
6–07	116.59	294.63	18.227 0.051	0.472 0.075
6–08	223.19	191.35	18.411 0.051	0.466 0.076
6–09	63.33	24.76	18.441 0.056	0.457 0.081
6–10	238.11	97.02	18.542 0.052	0.442 0.077
6–11	13.10	304.18	18.632 0.052	0.542 0.079
6–12	59.95	376.72	18.866 0.053	0.588 0.081
6–13	32.33	308.62	18.995 0.055	0.396 0.083
6–14	312.00	239.85	19.019 0.054	0.587 0.081
6–15	20.56	396.33	19.427 0.067	0.520 0.094
6–16	258.26	364.57	19.552 0.059	1.148 0.128
6–17	90.21	489.52	19.679 0.062	0.554 0.111
6–18	257.38	218.44	19.683 0.062	0.508 0.100
6–19	78.97	320.49	19.724 0.062	0.557 0.104
6–20	73.16	389.06	19.780 0.064	0.809 0.115
6–21	95.46	353.53	19.815 0.077	0.267 0.109
6–22	10.86	461.02	19.940 0.068	0.258 0.104
6–23	273.15	114.99	20.134 0.096	0.240 0.144
6–25	34.16	295.31	20.236 0.079	-0.037 0.112
6–26	50.27	361.96	20.247 0.084	0.200 0.121

ID No.	x (pix)	y (pix)	R / σ_R	$V-R$ / σ_{V-R}
6–27	274.28	31.99	20.305 0.077	0.446 0.135
6–28	33.09	217.23	20.318 0.087	0.211 0.125
6–31	295.70	144.17	20.405 0.084	0.518 0.148
6–32	70.46	478.72	20.410 0.087	0.534 0.153
6–34	213.88	17.54	20.473 0.100	0.220 0.144
6–35	31.78	255.79	20.473 0.084	0.016 0.128
6–36	21.06	443.57	20.493 0.096	-0.034 0.141
6–37	182.99	312.83	20.505 0.087	0.106 0.133
6–40	109.70	431.40	20.586 0.096	0.460 0.164
6–41	109.79	198.70	20.619 0.106	0.379 0.181
6–42	38.33	160.84	20.649 0.105	0.159 0.171
6–43	101.62	398.06	20.787 0.104	-0.102 0.150
6–45	47.03	411.39	20.831 0.110	0.129 0.163
6–46	57.00	52.66	20.930 0.119	0.691 0.250
6–47	241.54	380.88	21.083 0.130	0.100 0.195
7–01	66.37	281.27	15.647 0.055	0.471 0.075
7–02	230.92	351.06	16.061 0.055	0.747 0.076
7–03	175.81	387.03	16.728 0.055	0.724 0.076
7–04	97.50	281.21	17.474 0.056	0.691 0.076
7–05	114.80	34.78	18.271 0.056	0.515 0.079
7–06	49.98	438.22	18.471 0.057	0.442 0.083
7–07	225.51	332.69	18.586 0.057	0.564 0.082
7–08	278.48	235.84	18.980 0.059	0.501 0.087
7–09	5.74	279.01	19.168 0.061	0.686 0.102
7–10	290.12	427.08	19.212 0.060	0.503 0.090
7–11	268.05	274.91	19.439 0.067	0.141 0.098
7–13	216.92	264.99	19.514 0.069	0.816 0.118
7–15	184.77	218.67	19.559 0.073	0.111 0.102
7–17	226.63	180.87	19.832 0.071	-0.019 0.100
7–18	34.00	215.85	20.063 0.077	0.319 0.123
7–19	141.60	198.79	20.143 0.087	0.448 0.134
7–20	228.69	307.96	20.175 0.080	0.677 0.162
7–21	89.13	235.28	20.211 0.088	0.357 0.134
7–24	222.56	123.85	20.456 0.092	0.003 0.140
7–26	278.06	77.69	20.550 0.099	0.163 0.165
7–41	96.54	448.12	21.162 0.160	0.275 0.276
8–01	293.89	188.16	16.096 0.064	0.785 0.107
8–02	102.59	252.06	16.997 0.064	0.415 0.107
8–03	281.87	121.58	17.155 0.064	0.691 0.108
8–04	302.29	420.03	18.612 0.067	0.578 0.111
8–05	20.18	176.86	18.673 0.068	0.610 0.113
8–06	206.86	337.28	18.842 0.069	0.498 0.116

ID No.	x (pix)	y (pix)	R / σ_R	$V-R$ / σ_{V-R}
8–07	66.14	303.09	19.154 0.071	0.681 0.120
8–08	225.32	189.57	19.250 0.072	1.180 0.134
8–09	147.18	276.91	19.334 0.078	1.386 0.163
8–10	237.69	24.25	19.394 0.075	0.784 0.128
8–11	72.49	151.44	19.517 0.087	0.686 0.143
8–12	178.41	460.21	19.528 0.078	1.103 0.152
8–13	48.06	85.40	19.609 0.083	0.604 0.136
8–14	204.19	419.76	19.639 0.081	1.047 0.163
8–15	67.76	408.62	19.761 0.085	0.529 0.137
8–17	81.88	26.12	20.046 0.092	0.466 0.148
8–21	233.92	233.48	20.242 0.103	0.662 0.175
8–25	43.84	468.33	20.436 0.122	0.370 0.185
8–26	194.47	291.09	20.492 0.124	0.368 0.186
8–30	138.86	452.49	21.103 0.184	-0.047 0.234
9–01	166.26	52.66	15.058 0.043	0.388 0.055
9–02	61.93	55.32	16.890 0.044	0.381 0.056
9–03	184.87	220.10	16.899 0.044	0.324 0.057
9–04	114.96	399.90	17.048 0.044	0.404 0.056
9–05	75.33	166.36	17.428 0.044	0.606 0.057
9–06	97.70	433.51	18.311 0.048	0.459 0.062
9–07	206.49	192.51	18.446 0.049	0.457 0.065
9–08	236.07	398.08	19.001 0.055	0.386 0.071
9–09	293.06	385.48	19.030 0.056	0.520 0.076
9–10	268.59	290.10	19.564 0.071	0.347 0.094
9–11	93.71	223.67	19.647 0.080	0.869 0.115
9–12	17.61	357.11	19.943 0.100	0.855 0.165
9–13	35.57	15.74	19.976 0.094	0.469 0.132
9–14	179.35	86.41	20.066 0.110	0.294 0.146
10–01	296.28	374.79	15.048 0.042	0.414 0.054
10–02	35.74	228.19	15.434 0.042	0.427 0.054
10–03	287.43	150.40	16.059 0.042	0.691 0.054
10–04	148.49	344.98	16.676 0.042	0.745 0.054
10–06	266.74	447.65	17.866 0.043	0.600 0.057
10–07	227.01	358.46	18.092 0.044	1.256 0.064
10–08	58.62	213.62	18.251 0.045	1.112 0.070
10–09	168.36	264.87	18.733 0.047	1.109 0.082
10–10	186.89	22.95	18.986 0.050	1.013 0.087
10–11	193.87	164.59	19.084 0.052	0.459 0.074
10–12	228.16	304.55	19.110 0.051	0.473 0.077
10–13	212.45	443.63	19.172 0.053	0.483 0.077
10–14	38.66	138.53	19.234 0.054	0.555 0.084
10–15	54.63	127.22	19.246 0.053	0.926 0.094

ID No.	x (pix)	y (pix)	R / σ_R	$V-R$ / σ_{V-R}
10–16	66.61	316.19	19.328 0.058	0.454 0.085
10–17	300.68	50.93	19.503 0.058	0.441 0.092
10–18	60.27	277.30	19.599 0.062	0.657 0.104
11–01	169.97	64.81	15.369 0.047	0.396 0.062
11–02	33.43	420.52	15.436 0.047	0.381 0.062
11–03	50.50	127.33	16.281 0.048	0.521 0.063
11–04	21.27	166.74	16.406 0.048	0.441 0.063
11–05	313.57	143.13	16.893 0.048	0.653 0.063
11–06	235.81	436.86	17.064 0.048	0.575 0.063
11–07	192.96	324.85	17.225 0.048	0.556 0.063
11–08	187.83	453.56	17.276 0.048	1.061 0.066
11–09	134.87	480.50	18.040 0.049	0.966 0.068
11–10	247.33	52.53	18.619 0.052	0.380 0.071
11–11	251.31	240.30	19.204 0.058	0.478 0.089
11–12	237.62	57.41	19.336 0.065	0.491 0.094
11–13	21.18	228.11	19.376 0.069	0.458 0.101
11–15	35.56	316.41	19.493 0.066	1.160 0.138
11–16	296.72	305.04	19.620 0.066	0.926 0.123
11–18	301.27	204.82	19.791 0.074	0.557 0.116
11–20	66.35	433.99	19.998 0.084	0.327 0.123
11–25	72.09	140.96	20.553 0.131	0.255 0.192
12–01	4.82	210.99	15.137 0.078	0.635 0.114
12–02	62.36	168.88	16.219 0.078	0.593 0.114
12–03	240.99	52.63	18.079 0.079	0.716 0.117
12–04	102.48	233.02	18.419 0.080	0.315 0.116
12–05	90.38	499.51	18.788 0.082	0.906 0.126
12–06	107.30	14.81	19.166 0.084	0.282 0.124
12–07	177.23	64.09	19.241 0.085	0.080 0.124
12–08	78.57	159.46	19.263 0.086	1.012 0.152
12–09	221.65	287.69	19.590 0.092	0.048 0.132
12–11	16.17	457.87	19.906 0.102	0.265 0.153
12–12	294.36	412.26	19.967 0.110	0.268 0.159
12–18	56.81	69.76	20.326 0.116	0.166 0.175
12–19	254.62	127.61	20.433 0.122	0.103 0.185
12–20	238.43	181.01	20.434 0.122	0.457 0.230
12–22	235.87	94.33	20.533 0.124	0.129 0.217
12–24	256.20	444.65	20.571 0.133	0.359 0.211
12–25	222.71	103.24	20.752 0.151	-0.165 0.216
13–01	317.67	173.96	15.196 0.037	0.689 0.065
13–02	88.07	191.69	15.977 0.036	0.962 0.064
13–03	137.27	48.42	17.157 0.036	0.467 0.065
13–04	34.19	169.53	17.839 0.037	0.614 0.067

ID No.	x (pix)	y (pix)	R / σ_R	$V-R$ / σ_{V-R}
13–05	273.26	339.65	18.220 0.038	0.426 0.067
13–06	245.39	315.87	18.578 0.038	0.500 0.069
13–07	44.79	164.71	18.606 0.040	0.539 0.071
13–08	175.29	171.69	18.793 0.040	0.324 0.070
13–09	270.19	3.45	18.821 0.040	0.508 0.072
13–10	37.95	381.38	18.951 0.041	0.577 0.074
13–11	65.25	376.18	19.202 0.045	0.528 0.079
13–12	53.98	492.91	19.429 0.047	0.742 0.094
13–13	277.80	28.33	19.476 0.048	0.813 0.095
13–14	219.39	412.04	19.481 0.051	0.912 0.096
13–15	204.63	472.93	19.754 0.062	0.573 0.116
13–16	262.10	78.98	19.790 0.054	0.314 0.090
13–17	283.89	466.88	19.896 0.061	1.055 0.131
13–19	74.05	182.22	19.970 0.073	0.854 0.142
13–20	175.31	116.09	20.029 0.068	0.078 0.102
13–21	142.71	372.98	20.218 0.071	0.333 0.119
13–22	188.31	54.35	20.487 0.081	0.085 0.126
13–23	312.37	461.01	20.528 0.084	0.043 0.127
13–25	141.20	199.13	20.650 0.097	0.060 0.141
13–29	77.82	322.27	20.851 0.113	-0.018 0.164
13–33	194.33	454.25	21.213 0.175	0.107 0.236
14–01	107.38	385.04	15.300 0.070	0.987 0.092
14–02	57.88	386.63	16.127 0.071	0.488 0.092
14–03	257.79	10.57	16.361 0.071	0.390 0.092
14–04	72.33	78.66	17.015 0.070	0.603 0.092
14–05	310.46	457.47	18.573 0.072	0.615 0.096
14–06	242.90	365.56	18.820 0.072	0.603 0.098
14–07	81.96	79.41	18.998 0.074	0.260 0.104
14–08	61.15	416.86	19.069 0.074	0.507 0.100
14–09	114.79	320.83	19.143 0.074	0.511 0.103
14–10	99.00	103.49	19.168 0.075	0.817 0.111
14–11	197.27	332.94	19.179 0.076	0.400 0.103
14–12	314.17	365.74	19.185 0.073	0.883 0.109
14–13	40.89	386.07	19.414 0.079	0.555 0.111
14–14	296.46	464.11	20.225 0.091	0.815 0.174
14–15	117.01	289.24	20.227 0.093	0.387 0.143
14–16	11.99	213.53	20.235 0.093	0.052 0.132
14–17	180.20	398.07	20.239 0.091	0.556 0.150
14–20	296.05	437.82	20.347 0.097	0.258 0.133
14–21	281.86	387.07	20.393 0.101	0.411 0.156
14–25	306.44	400.63	20.809 0.123	0.086 0.176
15–01	185.19	211.36	16.007 0.036	0.566 0.051

ID No.	x (pix)	y (pix)	R / σ_R	$V-R$ / σ_{V-R}
15–02	162.33	256.24	16.623 0.069	0.110 0.074
15–03	92.73	266.80	17.420 0.037	0.384 0.046
15–04	266.66	255.69	17.773 0.037	1.075 0.049
15–05	21.61	454.95	17.910 0.038	0.412 0.048
15–06	83.73	402.06	17.926 0.037	0.895 0.049
15–09	266.76	89.87	18.361 0.038	0.983 0.055
15–10	205.66	240.32	18.414 0.039	0.503 0.052
15–11	29.63	482.12	18.660 0.041	0.458 0.054
15–12	173.85	292.61	18.702 0.041	0.778 0.059
15–13	42.73	191.89	18.787 0.041	0.398 0.055
15–14	47.00	470.69	18.994 0.045	0.961 0.070
15–15	197.53	368.58	19.053 0.045	1.298 0.094
15–16	270.55	341.99	19.271 0.047	0.675 0.077
15–18	201.27	403.26	19.540 0.058	0.411 0.082
15–19	181.97	101.26	19.770 0.067	0.975 0.132
15–20	147.28	134.48	19.840 0.069	0.957 0.136
15–22	293.24	9.99	20.096 0.067	0.331 0.105
15–23	187.84	31.51	20.128 0.073	0.244 0.109
15–24	292.48	162.70	20.292 0.077	0.375 0.129
15–25	315.35	177.53	20.388 0.086	0.542 0.139
15–26	254.74	292.45	20.459 0.098	0.322 0.153
15–27	164.53	221.90	20.539 0.098	0.168 0.145
15–29	305.39	362.97	20.612 0.098	0.009 0.133
15–30	163.09	406.73	20.673 0.113	0.545 0.187
16–01	141.83	381.25	15.547 0.036	0.486 0.044
16–02	198.51	276.81	16.482 0.036	0.886 0.045
16–03	317.97	75.28	16.769 0.036	0.615 0.045
16–04	121.06	102.74	18.092 0.037	0.620 0.048
16–05	45.26	298.53	18.155 0.038	0.355 0.047
16–06	312.55	503.48	18.525 0.045	0.409 0.055
16–07	283.53	350.32	18.916 0.040	0.449 0.055
16–08	202.88	251.30	18.974 0.044	0.507 0.063
16–09	180.66	29.12	18.998 0.042	0.385 0.058
16–10	255.29	463.32	19.085 0.044	0.836 0.064
16–11	309.95	353.97	19.203 0.045	0.366 0.064
16–12	212.67	438.44	19.585 0.051	0.204 0.071
16–13	5.03	31.24	19.606 0.050	0.837 0.106
16–14	180.41	182.30	19.720 0.057	0.418 0.089
16–15	121.65	480.87	19.911 0.064	0.043 0.089
16–16	46.38	152.90	19.927 0.063	0.558 0.104
16–17	232.25	31.38	19.948 0.064	0.630 0.108
16–21	251.52	373.26	20.674 0.112	0.049 0.156
16–23	246.42	236.34	20.763 0.118	0.496 0.213

Appendix G: — Coordinates for RR-Lyrae Candidates

The RA, DEC (1950) coordinates and R-band magnitudes of 95 likely RR-Lyrae variables in Field 51 (see Chapter 8) are presented here. The coordinates are accurate to within a few arcsec.

ID	*RA* (1950)	*DEC* (1950)	*R* (mag)
1	00 56 29.5	-67 16 55	19.39
2	00 51 13.2	-67 19 22	19.39
3	00 39 32.0	-67 26 53	19.34
4	01 01 02.2	-67 31 55	19.13
5	00 32 42.6	-67 42 51	19.57
6	00 58 35.1	-67 49 54	19.15
7	00 52 30.2	-67 58 29	19.27
8	01 11 25.9	-67 56 24	19.68
9	00 44 26.0	-68 09 36	19.39
10	00 53 21.4	-68 12 50	19.03
11	00 40 02.8	-68 12 22	19.26
12	00 31 09.4	-68 14 14	19.18
13	00 28 09.8	-68 13 03	19.34
14	00 43 33.9	-68 20 18	19.11
15	00 36 38.3	-68 22 00	19.28
16	00 58 25.1	-68 28 04	19.22
17	00 57 37.7	-68 30 43	19.38
18	00 44 13.8	-68 32 34	19.31
19	01 03 58.6	-68 34 52	19.24
20	00 31 29.4	-68 36 40	19.34
21	00 46 09.9	-68 50 29	19.17
22	01 16 55.9	-68 50 09	19.50
23	00 55 17.5	-68 56 17	19.21
24	01 11 55.7	-68 54 22	19.06
25	00 27 33.2	-68 53 31	19.36
26	01 11 01.8	-69 05 23	19.39
27	00 49 06.3	-69 08 45	19.32
28	00 47 42.6	-69 10 09	19.55
29	00 54 30.3	-69 13 56	19.35
30	00 47 31.5	-69 14 56	19.46
31	01 10 09.9	-69 11 49	19.19
32	00 46 55.1	-69 18 17	19.62

ID	*RA* (1950)	*DEC* (1950)	*R* (mag)
33	01 04 13.3	-69 18 42	19.27
34	00 59 56.3	-69 22 42	19.58
35	00 45 24.1	-69 27 38	19.45
36	01 13 25.5	-69 28 04	19.38
37	00 47 47.9	-69 35 01	19.22
38	00 28 08.4	-69 33 21	19.28
39	01 16 26.2	-69 34 28	19.27
40	01 01 41.2	-69 42 25	19.55
41	01 15 35.2	-69 39 24	19.35
42	00 27 59.9	-69 39 06	19.28
43	00 36 10.7	-69 45 00	19.23
44	00 35 47.8	-69 46 21	19.17
45	00 47 34.0	-69 49 46	19.49
46	00 37 47.3	-69 49 35	19.21
47	01 18 25.7	-69 49 19	19.00
48	01 16 47.5	-69 53 02	19.20
49	01 02 26.4	-69 58 33	19.32
50	00 46 15.3	-70 00 16	19.65
51	00 36 20.9	-69 59 30	19.45
52	01 01 19.1	-70 05 22	19.30
53	01 04 48.1	-70 09 18	19.33
54	00 30 14.9	-70 10 11	19.36
55	00 25 05.0	-70 10 42	19.31
56	00 57 13.8	-70 19 12	19.10
57	00 43 20.9	-70 25 55	19.28
58	00 29 02.3	-70 20 53	19.52
59	00 56 16.5	-70 30 00	19.46
60	01 14 05.4	-70 31 38	19.47
61	01 17 22.6	-70 31 06	19.36
62	00 48 27.4	-70 38 14	19.13
63	01 02 33.7	-70 37 17	19.04
64	00 35 42.8	-70 36 49	19.62

ID	*RA* (1950)	*DEC* (1950)	*R* (mag)
65	00 34 59.8	-70 37 20	19.49
66	00 29 31.9	-70 35 45	19.24
67	00 58 39.2	-70 42 04	19.29
68	00 42 43.8	-70 43 00	19.32
69	00 59 37.1	-70 44 04	19.42
70	00 39 09.6	-70 42 39	19.40
71	00 29 23.2	-70 44 48	19.37
72	00 28 37.6	-70 44 36	19.51
73	01 11 09.0	-70 48 58	19.22
74	01 06 16.0	-70 49 50	19.43
75	01 14 37.9	-70 49 05	19.36
76	00 57 47.2	-70 54 18	19.47
77	01 12 20.6	-70 51 32	19.18
78	00 43 22.2	-70 55 17	19.52
79	01 10 12.8	-70 55 24	19.17
80	01 13 20.8	-70 54 54	19.31
81	01 05 50.3	-70 57 18	19.56
82	00 25 59.8	-70 51 00	19.45
83	01 12 45.9	-70 57 49	19.23
84	00 49 45.2	-71 00 57	19.41
85	00 41 24.7	-71 00 29	19.52
86	00 49 33.0	-71 05 38	19.40
87	00 44 45.4	-71 06 08	19.55
88	00 45 12.1	-71 07 03	19.39
89	00 30 01.1	-71 03 38	19.54
90	01 04 54.9	-71 08 29	19.62
91	00 48 08.4	-71 10 16	19.41
92	00 47 16.4	-71 10 16	19.46
93	00 25 04.6	-71 07 23	19.39
94	01 19 16.3	-71 09 19	19.43
95	00 57 17.0	-71 20 21	19.05

List of References

Aaronson, M. & Mould, J.R., 1982. *Astrophys.J.Suppl.*, **48**, 161.

Abbe, C., 1867. *Mon.Not.R.astr.Soc.*, **27**, 262.

Andersen, J., Blecha, A. & Walker, M.F., 1984. *IAU Symp.No.108*, eds van den Bergh, S. & de Boer, K.S., p.41, Reidel, Dordrecht, Holland.

Arp, H., 1966. *Atlas of Peculiar Galaxies*, Pasadena: California Institute of Technology, USA.

Ashman, K.M. & Zepf, S.E., 1992. *Astrophys.J.*, in press.

Avni, Y., 1976. *Astrophys.J.*, **210**, 642.

Azzopardi, M. & Rebeirot, E., 1991. *IAU Symp.No.148*, eds Haynes, R. & Milne, D., p.71, Kluwer, Dordrecht, Holland.

Bajaja, E. & Loiseau, N., 1982. *Astr.Astrophys.Suppl.*, **48**, 71.

Beard, S.M., MacGillivray, H.T. & Thanisch, P.F., 1990. *Mon.Not.R.astr.Soc.*, **247**, 311.

Bertelli, G., Bressan, A.G. & Chiosi, C., 1985. *Astr.Astrophys.*, **150**, 33.

Binney, J. & Tremaine, S., 1987. *Galactic Dynamics*, p.452, Princeton University Press, Princeton, New Jersey, USA.

Bok, B.J., 1966. *Ann.Rev.Astr.Astrophys.*, **4**, 95.

Bolte, M., 1987. *Astrophys.J.*, **315**, 469. (GC6)

Bothun, G.D., 1986. *Astron.J.*, **91**, 507.

Bothun, G.D., Impey, C.D. & Malin, D.F., 1991. *Astrophys.J.*, **376**, 404.

Brück, M.T., 1975. *Mon.Not.R.astr.Soc.*, **173**, 327.

Brück, M.T., 1978. *Astr.Astrophys.*, **68**, 181.

Brück, M.T., 1980. *Astr.Astrophys.*, **87**, 92.

Brück, M.T., Cannon, R.D. & Hawkins, M.R.S., 1985. *Mon.Not.R.astr.Soc.*, **216**, 165.

Brück, & Hawkins, M.R.S., 1983. *Astr.Astrophys.*, **124**, 216.

Brück, M.T. & Marsoglu, A., 1978. *Astr.Astrophys.*, **68**, 193.

Buttress, J., Cannon, R.D. & Griffiths, W.K, 1988. *IAU Symp.No.126*, eds Grindlay, J.E. & Davis Philip, A.G., p.575, Kluwer, Dordrecht, Holland. (GC8)

Caldwell, J.A.R. & Coulson, I.M., 1985. *Mon.Not.R.astr.Soc.*, **212**, 879.

Caldwell, J.A.R. & Coulson, I.M., 1986. *Mon.Not.R.astr.Soc.*, **218**, 223.

Cannon, R.D., 1970. *Mon.Not.R.astr.Soc.*, **150**, 111. (C70)

Cannon, R.D., 1983. *Highlights astr.*, **6**, 109.

Carrozzi, N., Peyrin, Y. & Robin, A., 1971. *Astr.Astrophys.Suppl.*, **4**, 231.

Da Costa, G.S., 1991. *IAU Symp.No.148*, eds Haynes, R. & Milne, D., p.183, Dordrecht, Holland.

Da Costa, G.S. & Mould, J.R., 1986.*Astrophys.J.*, **305**, 214. (GC1)

Da Costa, G.S., Mould, J.R. & Crawford, M.D., 1985. *Astrophys.J.*, **297**, 582.

Davies, R.D. & Wright, A.E., 1977. *Mon.Not.R.astr.Soc.*, **180**, 71.

Demers, S., Grondin L., Irwin, M.J. & Kunkel, W.E., 1991a. *Astron.J.*, **101**, 911.

Demers, S., Grondin L., Irwin, M.J. & Kunkel, W.E., 1991b. *IAU Symp.No.148*, eds Haynes, R. & Milne, D., p.473, Kluwer, Dordrecht, Holland.

Dopita, M.A., 1991. *IAU Symp.No.148*, eds Haynes, R. & Milne, D., p.393, Kluwer, Dordrecht, Holland.

Einasto, J., Haud, U., Joeveer M. & Kaasik, A., 1976. *Mon.Not.R.astr.Soc.*, **177**, 357.

Faulkner, D.J. & Cannon, R.D., 1973. *Astrophys.J.*, **180**, 435.

Faulkner, D.J. & Iben, I., 1966. *Astrophys.J.*, **144**, 995.

Feast, M.W., 1989. *Recent Developments of Magellanic Cloud Research*, eds de Boer, K.S., Spite, F. & Stasinska, G., p.75, Observatoire de Paris.

Freedman, W.L., Madore, B.F., 1991. *IAU Symp.No.148*, eds Haynes, R. & Milne, D., p.471, Kluwer, Dordrecht, Holland.

Freeman, K.C., 1984. *IAU Symp.No.108*, eds van den Bergh, S. & de Boer, K.S., p.107, Reidel, Dordrecht, Holland.

Freeman, K.C., Illingworth, G., & Oemler, A., 1983. *Astrophys.J.*, **272**, 488.

Frenk, C.S. & White, S.D.M., 1980. *Mon.Not.R.astr.Soc.*, **193**, 295.

Frogel, J.A., 1984. *Publs astr.Soc.Pacific*, **96**, 856.

Fujimoto, M. & Kumai, Y., 1991. *IAU Symp.No.148*, eds Haynes, R. & Milne, D., p.469, Kluwer, Dordrecht, Holland.

Fujimoto, M. & Murai, T., 1984. *IAU Symp.No.108*, eds van den Bergh, S. & de Boer,

K.S., p.115, Reidel, Dordrecht, Holland.

Fujimoto M. & Sofue Y., 1976. *Astr.Astrophys.*, **47**, 263.

Fujimoto M. & Sofue Y., 1977. *Astr.Astrophys.*, **61**, 199.

Gallagher, J.S. & Hunter, D.A., 1984. *Ann.Rev.Astr.Astrophys.*, **22**, 37.

Gardiner, L.T. & Hawkins, M.R.S., 1991. *Mon.Not.R.astr.Soc.*, **251**, 174.

Gardiner, L.T. & Hatzidimitriou, D., 1991. *Mon.Not.R.astr.Soc.*, submitted.

Gatley, Hyland & Jones, 1982. *Mon.Not.R.astr.Soc.*, **200**, 521.

Gerola, H., Seiden, P. & Schulman L., 1980. *Astrophys.J.*, **242**, 517.

Graham, J.A., 1975. *Publs.astr.Soc.Pacif.*, **87**, 641.

Graham, J.A., 1981. *Publs astr.Soc.Pacific*, **93**, 29.

Graham, J.A., 1982. *Publs astr.Soc.Pacific*, **94**, 244.

Green, E.M., Demarque, P. & King, C.R., 1987. *The Revised Yale Isochrones and Luminosity Functions*, Yale University Observatory, New Haven, USA.

Grondin, L., Demers, S., Kunkel, W.E. & Irwin, M.J., 1990. *Astron.J.*, **100**, 663.

Grondin, L., Demers, S., Kunkel, W.E. & Irwin, M.J., 1991. *IAU Symp.No.148*, eds Haynes, R. & Milne, D., p.478, Kluwer, Dordrecht, Holland.

Hardy, E., Buonanno, R., Corsi, C.E., James, K.A. & Schommer, R.A., 1984. *Astrophys.J.*, **278**, 592.

Hardy, E. & Durand, D., 1984. *Astrophys.J.*, **279**, 567.

Hardy, E., Suntzeff, N.B., Azzopardi M., 1989. *Astrophys.J.*, **344**, 210.

Hatzidimitriou D., 1989, *PhD. thesis*, Univ. of Edinburgh. (H-thesis)

Hatzidimitriou D., 1991. *Mon.Not.R.astr.Soc.*, **251**, 545. (H91)

Hatzidimitriou, D., Cannon, R.D. & Hawkins, M.R.S., 1991. *IAU Symp.No.148*, eds Haynes, R. & Milne, D., p.107, Kluwer, Dordrecht, Holland.

Hatzidimitriou, D., Cannon, R.D., Hawkins, M.R.S. & Teo, A.C.Y., 1991, in preparation.

Hatzidimitriou, D. & Hawkins, M.R.S., 1989. *Mon.Not.R.astr.Soc.*, **241**, 667.

Hatzidimitriou, D., Hawkins, M.R.S. & Gyldenkerne, K., 1989. *Mon.Not.R.astr.Soc.*, **241**, 645.

Hawkins, M.R.S., 1983. *Mon.Not.R.astr.Soc.*, **202**, 571.

Hawkins, M.R.S., 1984. *Mon.Not.R.astr.Soc.*, **206**, 433. (H84)

Hawkins, M.R.S & Brück, M.T., 1982. *Mon.Not.R.astr.Soc.*, **198**, 935.

Hawkins, M.R.S & Brück, M.T.,1984. *IAU Symp.No.108*, eds van den Bergh, S. & de Boer, K.S., p.101, Reidel, Dordrecht, Holland.

Hesser, J.E., Harris, W.E., VandenBergh, D.A., Allwright, J.W.B., Shott, P. & Stetson, P., 1987. *Publ.astr.Soc.Pacif.*, **99**, 739.

Hindman, J.V., 1964. *Nature*, **202**, 377.

Hindman, J.V., 1967. *Austr.J.Physics*, **20**, 147.

Hodge, P.W., 1962. *Astron.J.*, **67**, 125.

Hodge, P.W., 1983. *Astrophys.J.*, **264**, 470.

Hodge, P.W., 1984. *IAU Symp.No.108*, eds van den Bergh, S. & de Boer, K.S., p.7, Reidel, Dordrecht, Holland.

Hodge, P.W., 1987a. *Publs astr.Soc.Pacif.*, **99**, 724.

Hodge, P.W., 1987b. *Publs astr.Soc.Pacif.*, **99**, 730.

Hodge, P.W., Smith, T.R., Eskridge, P.B., MacGillivray, H.T., 1991. *Astrophys.J.*, **369**, 372.

Hubble, E., 1926. *Astrophys.J.*, **64**, 321.

Hughes, S.M.G., Wood, P.R. & Reid, N., 1991. *Astron.J.*, **101**, 1304. (HWR)

Hunter, D.A., 1982. *Astrophys.J.*, **260**, 81.

Hunter, D.A. & Gallagher, J.S., 1986. *Publs astr.Soc.Pacific*, **98**, 5.

Iben, I., 1984. *IAU Symp.No.105*, eds. A.Maeder & A.Renzini, p.3, Reidel, Dordrecht, Holland.

Irwin, M.J., 1991. *IAU Symp.No.148*, eds Haynes, R. & Milne, D., p.453, Kluwer, Dordrecht, Holland.

Irwin, M.J., Bunclark, P.S., Bridgeland, M.T. & McMahon, R.G., 1990. *Mon.Not.R. astr.Soc.*, **244**, 16P.

Irwin, M.J., Demers, S. & Kunkel, W.E., 1990. *Astron.J.*, **99**, 191. (IDK)

James, P., 1991. *Mon.Not.R.astr.Soc.*, **250**, 544.

Jarvis, J.F. & Tyson, J.A., 1981.*Astron.J.*, **86**, 476.

Johnson, H., 1961. *Publs.astr.Soc.Pacific*, **73**, 20.

Kennicutt, R.C., 1989. *Astrophys.J.*, **344**, 685.

Kennicutt, R.C., 1991. *IAU Symp.No.148*, eds Haynes, R. & Milne, D., p.139, Kluwer, Dordrecht, Holland.

King, I. 1962. *Astron.J.*, **67**, 471.

Kunkel, W.E., 1980. *IAU Symp.No.85*, ed. Hesser, J., p.353, Reidel, Dordrecht, Holland.

Landolt, A.U., 1983. *Astron.J.*, **88**, 439.

Laney, C.D. & Stobie, R.S., 1986. *Mon.Not.R.astr.Soc.*, **222**, 449.

Larson, R.B., 1972. *Nature Phys.Sci.*, **236**, 7.

Larson, R.B. & Tinsley, B.M., 1978. *Astrophys.J.*, **219**, 46.

Leavitt, H.S., 1912. *Harvard Obs.Circ.*, No.173.

Lee, Y.-W., & Demarque, P., 1990. *Astrophys.J.Suppl.*, **73**, 709.

Lequeux, J., 1984. *IAU Symp.No.108*, eds van den Bergh, S. & de Boer, K.S., p.67, Reidel, Dordrecht, Holland.

Lin, D.N.C. & Lynden-Bell, D., 1977. *Mon.Not.R.astr.Soc.*, **181**, 59.

Lin, D.N.C. & Lynden-Bell, D., 1982. *Mon.Not.R.astr.Soc.*, **198**, 207.

Lindsay, E.M. & McFarland, J., 1970. *Irish Astron.J.*, **9**, 219.

Lynden-Bell, D., 1982. *Observatory*, **102**, 7.

MacGillivray, H.T. & Stobie, R.S., 1984. *Vistas Astr.*, **27**, 433.

Mackay, C.D., 1986. *Ann.Rev.Astr.Astrophys.*, **24**, 255.

Martin, N., Maurice, E., Lequeux, J, 1989. *Astr.Astrophys.*, **215**, 219.

Mateo, M., 1988. *Astrophys.J.*, **331**, 261.

Mateo, M. & Hodge, P., 1985. *Publs astr.Soc.Pacific*, **97**, 753.

Mateo, M. & Hodge, P., 1986. *Astrophys.J.Suppl.*, **60**, 893.

Mateo, M., Nemec, J., Irwin, M. & McMahon, R., 1991. *Astron.J.*, **101**, 892.

Mathewson, D.S., 1985. *Proc.astr.Soc.Aust.*, **6**, 104.

Mathewson, D.S., Cleary, M.N. & Murray, J.D., 1974. *Astrophys.J.*, **190**, 291.

Mathewson, D.S. & Ford, V.L., 1970. *Astron.J.*, **75**, 778.

Mathewson, D.S. & Ford, V.L., 1984. *IAU Symp.No 108*, eds van den Bergh, S. & de Boer, K.S., p.125, Reidel, Doldrecht, Holland.

Mathewson, D.S., Ford, V.L. & Visvanathan, N., 1986. *Astrophys.J.*, **301**, 664.

Mathewson, D.S., Ford, V.L. & Visvanathan, N., 1988. *Astrophys.J.*, **333**, 617.

Mathewson, D.S., Wayte, S.R., Ford, V.L. & Ruan, K., 1987. *Proc.astr.Soc.Aust.*, **7**, 19. (MWFR)

Matteucci, F. & Chiosi, C., 1983. *Astr.Astrophys.*, **123**, 121.

McGee, R.X. & Newton, L.M., 1986. *Proc.astr.Soc.Aust.*, **6**, 471. (MN)

Melcher, N. & Richtler, T., 1989. *Recent Developments of Magellanic Cloud Research*, eds de Boer, K.S., Spite, F. & Stasinska, G., p.87, Observatoire de Paris. (GC7)

Menzies, J.W., 1990. *South African Astron.Obs.CCD Bull.*, **1**.

Menzies, J.W., Banfield, R.M. & Laing, J.D., 1980. *South African Astron.Obs.Circ.*, **1**, 149.

Menzies, J.W., Cousins, A.W.J., Banfield, R.M. & Laing, J.D., 1989. *South African Astron.Obs.Circ.*, **13**, 1.

Mermilliod, J.C., 1981a. *Astr.Astrophys.Suppl.*, **44**, 467.

Mermilliod, J.C., 1981b. *Astr.Astrophys.*, **97**, 235.

Mould, J.R., 1991. *IAU Symp.No.148*, eds Haynes, R. & Milne, D., p.7, Kluwer, Dordrecht, Holland.

Mould, J. & Aaronson, M., 1980. *Astrophys.J.*, **240**, 464.

Mould, J. & Aaronson, M., 1985. *Astrophys.J.*, **288**, 551.

Mould, J.R., Da Costa, G.S. & Crawford, M.D., 1984. *Astrophys.J.*, **280**, 595. (GC2)

Murai, T. & Fujimoto, M., 1980. *Publ.Astron.Soc.Japan*, **32**, 581. (MF)

Murai, T. & Fujimoto, M., 1986. *Astrophys. and Space Science*, **119**, 169.

Noguchi, M., 1987. *Mon.Not.R.astr.Soc.*, **228**, 635.

Noguchi, M., 1988. *Astr.Astrophys.*, **203**, 259.

Noguchi, M., 1990. *The Interstellar Medium in Galaxies*, eds Thronsen, H. & Shull, J.M., Kluwer, Dordrecht, Holland.

Noguchi, M. & Ishibashi, S., 1986. *Mon.Not.R.astr.Soc.*, **219**, 305.

Norris, J.E. & Hawkins, M.R.S., 1991, in preparation.

Olszewski, E.W., 1988. *I.A.U. symposium 126*, eds. Grindlay, J.E. & Davis Philip, A.G., p.159, Kluwer Academic Publishers, Doldrecht, Holland.

Olszewski, E.W., Schommer, R.A. & Aaronson, M., 1987. *Astron.J.*, **93**, 565. (GG4)

Pagel, P.E.J. & Patchett, B.E, 1975. *Mon.Not.R.astr.Soc.*, **172**, 13.

Penny, A.J. & Dickens, R.J., 1986. *Mon.Not.R.astr.Soc.*, **220**, 845.

Preston, G.W., Schectman, S.A. & Beers, T.C., 1991. *Astrophys.J.*, **375**, 121.

Ratnatunga, K.U. & Bahcall, J.N., 1985. *Astrophys.J.suppl.*, **59**, 63.

Reid, N. & Freedman, W.L., 1991. *IAU Symp.No.148*, eds Haynes, R. & Milne, D., p.365, Kluwer, Dordrecht, Holland.

Renzini, A. 1991. *IAU Symp.No.148*, eds Haynes, R. & Milne, D., p.165, Kluwer, Dordrecht, Holland.

Rich, R.M., Da Costa, G.S. & Mould, J.R., 1984. *Astrophys.J.*, **286**, 517. (GC3)

Sagar, R. & Pandey, A.K., 1989. *Astr.Astrophys.Suppl.*, **79**, 407.

Sandage, A.R., 1958. *Astrophys.J.*, **127**, 513.

Sarajedini, A. & King, C.R., 1989. *Astron.J.*, **98**, 1264.

Scalo, J.M., 1986. *Fund.Cosmic Phys.*, **11**,1.

Schmidt, Th., 1970. *Astr.Astrophys.*, **6**, 294.

Searle, L. & Sargent, W.L.W., 1972. *Astrophys.J.*, **173**, 25.

Searle, L. & Zinn, R., 1978. *Astrophys.J.*, **225**, 357.

Seidel, E., Da Costa, G.S., & Demarque, P., 1987. *Astrophys.J.*, **313**, 192. (SDD)

Seidel, E., Demarque, P. & Weinberg, D., 1987. *Astrophys.J.Suppl.*, **63**, 917. (SDW)

Shanks, T., Stevenson, P.R.F., Fong, R. & MacGillivray, H.T., 1984. *Mon.Not.R.astr. Soc.*, **206**, 767.

Shapley, H. 1940. *Harvard Obs.Bull.*, **914**, 8.

South African Astronomical Observatory Facilities Manual, 1987. South African Astronomical Observatory, Sutherland, Cape Province, South Africa.

Stetson, P.B., 1987. *Publs astr.Soc.Pacif.*, **99**, 191.

Stobie, R.S., 1986. *Pattern Recognition Letters*, **4**, 317.

Stryker, L.L., 1984a. *Astr.Astrophys.Suppl.*, **55**, 127.

Stryker, L.L., 1984b. *IAU Symp.No.108*, eds van den Bergh, S. & de Boer, K.S., p.79, Reidel, Doldrecht, Holland.

Stryker, L.L. & Butcher, H.R., 1981. *IAU Coll.No.68*, eds A.G.D. Philip & D.S.Hayes,

p.255, L.Davis Press, New York, USA.

Stryker, L.L., Da Costa, G.S. & Mould J.R., 1985. *Astrophys.J.*, **298**, 544. (GC5)

Stryker, L.L., Nemec, J.M., Hesser, J.E. & McClure, R.D., 1984. *IAU Symp.No.108*, eds van den Bergh, S. & de Boer, K.S., p.43, Reidel, Dordrecht, Holland.

Suntzeff, N.B., Friel, E., Kremola, A., Kraft, R.P. & Graham, J.A., 1986. *Astron.J.*, **91**, 275.

Thanisch, P., McNally, B.V. & Robin, A., 1984. *Image and Vision Computing*, **2**, 191.

Toomre, A. & Toomre, J., 1972. *Astrophys.J.*, **178**, 623.

Torres, G. & Carranza, G.J., 1987. *Mon.Not.R.astr.Soc.*, **226**, 513.

Tremaine, S.D., 1976. *Astrophys.J.*, **203**, 72.

Tucholke, H.-J. & Hiesgen, M., 1991. *IAU Symp.No.148*, eds Haynes, R. & Milne, D., p.491, Kluwer, Dordrecht, Holland.

Twarog, B.A., 1980. *Astrophys.J*, **242**, 242.

UK Schmidt Unit handbook, 1983, Royal Observatory, Edinburgh.

vandenBerg, D., 1985. *Astrophys.J.Suppl.*, **58**, 711.

van den Bergh, S., 1991. *IAU Symp.No.148*, eds Haynes, R. & Milne, D., p.161, Kluwer, Dordrecht, Holland.

de Vaucouleurs, G., 1955. *Astron.J.*, **60**, 219.

de Vaucouleurs, G. & Freeman, K.C., 1972. *Vistas Astr.*, **14**, 163.

Walborn, N.R., 1991. *IAU Symp.No.148*, eds Haynes, R. & Milne, D., p.145, Kluwer, Dordrecht, Holland.

Walker, A.R., 1984. *Mon.Not.R.astr.Soc.*, **209**, 83.

Wannier, P. & Wrixon, G.T., 1972. *Astrophys.J.*, **173**, 119.

Wayte, S.R., 1991. *IAU Symp.No.148*, eds Haynes, R. & Milne, D., p.447, Dordrecht, Holland.

Welch, D.L., McLaren, R.A., Madore, B.F. & McAlary, C.W., 1987. *Astrophys.J.*, **321**, 162.

Westerlund, B.E.. 1970. *Vistas Astr.*, **12**, 335.

Westerlund, B.E., 1989. *Recent Developments of Magellanic Cloud Research*, eds de Boer, K.S., Spite, F. & Stasinska, G., p.159, Observatoire de Paris.

Westerlund, B.E., 1990. *Astr.Astrophys.Rev.*, **2**, 29.

Westerlund, B.E., 1991. *IAU Symp.No.148*, eds Haynes, R. & Milne, D., p.15, Kluwer, Dordrecht, Holland.

Westerlund, B.E. & Danziger, I.J., 1985. *Proceedings of the ESO-IRAM-Onsals Workshop on '(Sub)millimeter Astronomy'*, p.107, Aspenäs, Swenden.

Westerlund, B.E. & Glaspey, J. 1971. *Astr.Astrophys.*, **10**, 1.

Yamagata, T. & Yoshii, Y., 1991. *Astron. J*, in press.